Muonium states in semiconductors

Bruce D. Patterson

Physics Institute, University of Zurich, CH-8001 Zurich, Switzerland

Positive muons implanted into diamond and zincblende-structured semiconductors often form hydrogen-like paramagnetic muonium ($\mu^+ - e^-$) states whose characteristics can be investigated with the "muon spin rotation" (μSR) technique. In contrast to the case of hydrogen, which is not known to form a paramagnetic state in semiconductors, two coexisting types of muonium states are seen. "Mu" with a large isotropic hyperfine interaction, and "Mu*" with a small [111]-axially symmetric hyperfine interaction. Both "spectroscopic" properties of these states, such as the electronic g factors and the nuclear hyperfine interactions, and "dynamic" properties, such as their diffusion rates and their rates of interconversion, are accessible with μSR. Direct information about the site of the muonium states is available using the channeling effect of the positron from muon decay in a crystalline host. The techniques for probing semiconductors with positive muons are described in this review, and the results they have provided to date are critically discussed. The considerable amount of theoretical work that has been invested in microscopic models of Mu and Mu* is also summarized.

CONTENTS

I. INTRODUCTION

During the thermalization process, a positive muon implanted into a semiconducting material may capture an electron from the host, forming a paramagnetic "muonium" defect state. The positive charge and relatively large mass ($m_\mu \sim 207 m_e$) of the muon imply that muonium will be closely analogous to hydrogen. This analogy is useful.

An isolated hydrogen atom represents conceptually one of the simplest defect centers possible in a crystalline semiconductor. Hydrogen is believed to be a ubiquitous impurity in, for example, as-grown silicon, but with a solubility which is too low to allow its detailed study. Irradiation of silicon with protons produces infrared absorption bands close to the Si—H stretch modes of the SiH_4 silane molecule, indicating occupation of Si bonds broken during the implantation. This is similar to the case of hydrogen-doped *amorphous* silicon, where hydrogen also saturates dangling bonds. The infrared absorption experiments yield no information on the nature of the isolated hydrogen impurity.

By far the most informative technique used in the study of (paramagnetic) defects in semiconductors is electron spin resonance (ESR). The position of the absorption lines identifies a defect according to its electronic g value and hyperfine interactions, the strength of the absorption yields the concentration of the center, and the relaxation rate of the signals gives information on the dynamic interactions of the center with the host. It is an unfortunate fact that up to the present, no as-grown or proton-irradiated semiconductor sample has yielded an unambiguous resonance from a hydrogen impurity. This is in sharp contrast to, for example, the alkali halides, where many detailed ESR studies of interstitial hydrogen have been performed. The conclusion is that the stable state of hydrogen in semiconductors is diamagnetic.

Positive muons can be implanted into semiconductors with negligible radiation damage. By observing the radioactive decay of individual, fully polarized muons, the muon spin rotation technique provides the same information as would ESR, but with a sensitivity far in excess of that possible with standard resonance techniques.

A study of how muons and muonium behave in a host is unavoidably limited to a time window extending from implantation to at most several muon lifetimes (2.2 μs). We are thus dealing with the "early history" of a hydrogenlike impurity. Contact with the problem of hydrogen in semiconductors is to be sought in the late stages of muonium evolution.

But it should be emphasized that because of their conceptual simplicity, paramagnetic muonium centers in semiconductors are interesting in their own right. As it turns out, these centers are in fact far from simple, and several of their unexpected characteristics present intriguing challenges to defect theorists.

The purpose of this review is to describe the present state of knowledge of the behavior of implanted positive muons in crystalline semiconductors. The overall field of muon probes in matter has been treated in several excellent review articles (Brewer *et al.*, 1975; Schenck, 1976, 1977; Brewer and Crowe, 1978; Gurevich and Nikolskii, 1981), conference proceedings (Gygax *et al.*, 1979; Brewer and Percival, 1981; Yamazaki and Nagamine, 1984; Hartmann *et al.*, 1986), and books (Chappert and Grynszpan, 1984; Schenck, 1985). Several shorter articles that specifically treat muons in semiconductors have appeared (Meier, 1980; Patterson, 1984c), and the muon- and pion-decay-blocking techniques, used to obtain direct site information on implanted positive muons and pions, have been reviewed by Patterson (1987).

In this review, I have attempted to at least mention all published work in the field of muons in semiconductors up to December 1986. I apologize in advance for any omissions. The review also contains a considerable amount of previously unpublished material, principally from the μSR physics groups at the University of Zurich, Switzerland and the University of Konstanz, West Germany.

A. Properties of the positive muon and vacuum muonium

The pertinent properties of the positive muon and of muonium in vacuum are compared with those of the proton and of hydrogen in Table I. Several points should be emphasized: (1) The mass of the muon is sufficiently large compared to that of the electron that the Born-Oppenheimer approximation is valid. (2) This validity leads to very similar properties for vacuum muonium and hydrogen. (3) The muon lifetime is sufficiently short that high implantation rates are possible with only a single muon present in the sample at a time. (4) The muon gyromagnetic ratio is such that the muon precesses once in its lifetime in 3.4 mT, an applied field of convenient magnitude. (5) The vacuum muonium hyperfine frequency implies a muon oscillation period of approximately

TABLE I. Properties of muonium and hydrogen. From Particle Data Group (1984) and Holzschuh *et al.* (1982).

	Muon	Proton
Mass (m_e)	206.7683	1836.15
Spin	$\frac{1}{2}$	$\frac{1}{2}$
Gyromagnetic ratio γ (s^{-1} T^{-1})	8.51607×10^8	2.67520×10^8
Lifetime τ (μs)	2.19709	Stable
	Muonium	Hydrogen
Reduced electron mass (m_e)	0.995187	0.999456
Ground-state radius (Å)	0.531736	0.529465
Ground-state energy (eV)	−13.5403	−13.5984
Hyperfine frequency (GHz)	4.46330	1.42041

220 ps, which is comparable to the timing resolution that can be achieved, with effort, using conventional plastic scintillators and photomultipliers.

B. Historical perspective

Muons were discovered in cosmic rays by Anderson and Neddermeyer (1973a, 1937b, 1938) and Street and Stevenson (1937), and they were first artificially produced at the 184-in. Cyclotron at Berkeley (Gardner and Lattes, 1948). The use of the spin of the muon to study its behavior in materials began with the discovery of parity violation in muon decay by Garwin *et al.* (1957) at Columbia. Besides demonstrating an important property of the muon, this experiment represented the first use of the technique later to be called "muon spin rotation" (μSR) to probe a solid. It was found that polarized muons which thermalize in graphite and copper retain their spin polarization, but that approximately half of the muons in nuclear emulsion are very rapidly depolarized. Friedmann and Telegdi (1957a, 1957b) soon proposed that the depolarization in emulsion is due to the formation of a bound μ^+-e^- system which they named "muonium." This was verified in an experiment by Orear *et al.* (1957) in which a large magnetic field was applied, which quenched the hyperfine interaction of muonium and inhibited the depolarization.

The first muon experiment in a semiconductor was one by Swanson (1958). He observed only a small muon polarization in diamond and quartz (indicating muonium formation), but a large polarization in silicon and SiC (data presented later in this review indicate that these last two samples were quite impure). Systematic studies of the temperature- and doping-dependent muon polarization (Feher *et al.*, 1960) and muonium quenching (Eisenstein *et al.*, 1966) were then made, which demonstrated the formation of muonium in weakly doped silicon and at low temperature in germanium. Andrianov *et al.* (1970) published the first value for the isotropic muonium (Mu) hyperfine interaction in silicon, which they determined from a room-temperature quenching experiment.

The spin precession of Mu was observed in a small applied magnetic field in gaseous argon (Hughes *et al.*, 1960) and later in quartz, frozen CO_2, and ice (Myasisheva *et al.*, 1967) and in cold germanium (Andrianov *et al.*, 1969). In larger applied fields, the two intratriplet Mu precession frequencies become resolvable, and measurements of the resulting beat frequency were used to determine the Mu hyperfine interval in quartz (Gurevich *et al.*, 1969), germanium (Gurevich *et al.*, 1971), silicon (Brewer *et al.*, 1973), and diamond (Holzschuh *et al.*, 1982).

The simultaneous existence of an additional paramagnetic muonium state with a reduced hyperfine interaction was suggested by Eisenstein *et al.* (1966) to explain their quenching curves in cold silicon. Precession of this state, Mu*, was seen in silicon by Brewer *et al.* (1973), and the axially symmetric spin Hamiltonian describing this anisotropic state was independently put forward by Ivanter (1977), Belousov *et al.*, (1978a, 1978b), and Waldner (Patterson *et al.*, 1978). Analogous anisotropic states were subsequently observed in germanium (Weidinger *et al.*, 1981), diamond (Holzschuh *et al.*, 1982), GaAs, and GaP (Kiefl *et al.*, 1985). Much effort has been devoted to investigating the properties of Mu and Mu* in silicon and germanium. Noteworthy here are studies of the motion of Mu in germanium (Döring *et al.*, 1983), the determination of the electronic *g*-factor anisotropy for Mu* (Blazey *et al.*, 1984), and a demonstration of the nuclear hyperfine interaction of Mu* in germanium (Estle, Rudaz *et al.*, 1984).

The Mu state is not always stable. Kudinov *et al.* (1975), in studies of the initial phase of the muon precession signal in germanium, found that Mu makes a thermally activated transition to a diamagnetic muon state. A thermally activated transition of another kind, from Mu to Mu*, was found in diamond by Holzschuh *et al.* (1982). The Mu→Mu* transition in diamond permitted Odermatt *et al.* (1986) to determine the absolute signs of the Mu* hyperfine parameters.

A major advance in the ability to determine accurately the hyperfine interval of Mu in matter came with the observation of the direct hyperfine transition using a μSR spectrometer with high timing resolution (Holzschuh *et al.*, 1981a). The subsequent inclusion in this apparatus of a compact magnet with low fringe field allowed high-field observations of Mu precession (Kiefl, Holzschuh *et al.*, 1984). Since the large field quenches the nuclear hyperfine interaction between muonium and host nuclei with spin, the apparatus permits muonium studies in materials with nuclear moments such as GaAs and GaP (Kiefl *et al.*, 1985), the zincblende cuprous halides (Kiefl, Odermatt *et al.*, 1986), and the alkali halides (Baumeler *et al.*, 1987).

The nuclear hyperfine interaction has recently been transformed from an undesirable source of line broadening to a sensitive indicator of the distribution of the bound-electron wave function among neighboring host ions. This has been achieved with the ability to resolve the nuclear hyperfine interaction using the novel "level-crossing resonance" technique (referred to in this review as "avoided level crossing") proposed by Abragam (1984) and realized by Kiefl, Kreitzman *et al.* (1986).

Direct site information on muon (and pion) states in semiconductors is beginning to become available from the observation of the blocking of the decay positron (or muon) by the crystal lattice. Pion-decay experiments have been performed in germanium and GaAs (Maier, 1984; Sigle *et al.*, 1984; Flik *et al.*, 1986), and a muon-decay experiment has been done in silicon (Patterson *et al.*, 1984a).

The first theoretical attempt to account for the hyperfine frequency of Mu in a semiconductor was the use of cavity and dielectric function models by Wang and Kittel (1973). Successively more detailed simulations of the muon states followed, based principally on the molecular cluster approach. In this way a plausible description of interstitial Mu in diamond was achieved (Sahoo *et al.*, 1983), and at long last what may well be the correct model for the Mu* state has been constructed (Claxton *et al.*, 1986).

C. Organization of the review

Section II of this review gives a theoretical description of the time evolution of the muon polarization in the isotropic and anisotropic muonium states. The reversible or "spectroscopic" behavior of these spin systems is treated first, followed by a discussion of irreversible or "dynamic" interactions with the host.

Experimental aspects of muon studies of semiconductors are presented in Sec. III, beginning with a brief description of how polarized muon beams are produced. The remainder of the section describes the various experimental techniques used to study muon states in matter.

Section IV.A addresses the question of how the implanted muon becomes thermalized and to what extent the lattice-ion vacancies produced during implantation can influence the later behavior of the muon states formed. Section IV.B contrasts the muon situation with that of implanted hydrogen and includes a discussion of the properties of lattice vacancies in silicon and germanium.

Section V is a review of experimental studies of muon states in semiconductors. After presenting the formation probabilities and regions of thermal stability of the states in tabular form and briefly discussing the site information that has been obtained from blocking and channeling experiments, we review the "spectroscopic" measurements of Mu and Mu*. The diffusion of the isotropic Mu state in semiconducting hosts is treated next, followed by a discussion of the Mu→Mu* transition observed in diamond and the determination of the absolute signs of the Mu* hyperfine parameters. The effects of temperature, doping, electric fields, illumination, and particle irradiation on the dynamics of the muon states in silicon, germanium, and GaAs are summarized in Sec. V.G, and the final subsections treat the special case of the zincblende cuprous halides and other miscellaneous semiconducting hosts.

A brief review of theoretical models of hydrogen and muon states in semiconductors is given in Sec. VI, including calculations of their energy and electronic structure. The final section offers a summary and my conclusions.

II. THEORETICAL DESCRIPTIONS OF MUONIUM SPECTROSCOPY AND DYNAMICS

The measured quantity in a μSR experiment is the time-dependent muon spin polarization. In a muonium atom, the spin magnetic moments of the positive muon and electron interact with one another via the hyperfine interaction, and they both interact with an applied magnetic field via the Zeeman interaction. Muonium in a solid-state host may in addition experience a nuclear hyperfine interaction with neighboring host nuclei with spin. All these interactions are nondissipative, hence the resulting muon polarization consists of a sum of undamped oscillating components. The oscillation frequencies for a particular set of interactions can be calculated using elementary quantum mechanics, and a comparison with experiment yields the hyperfine and nuclear hyperfine interaction tensors and the electron g value. The term "muonium spectroscopy" is used in this review to describe the analysis of these nondissipative interactions.

Muonium in a solid host can, however, also experience interactions that lead to a loss of polarization. These dissipative effects arise from the random motion of the muonium and the atoms or electrons of the host. Various theoretical models have been developed which treat these effects in terms of perturbations of either the Zeeman or the hyperfine interaction, i.e., either as a randomly fluctuating magnetic field or as a persistent or an irreversible change in the hyperfine interaction. Comparison of the results of these theories with experiment yields information about the stability of muonium and the perturbing effects of its environment. In this review the term "muonium dynamics" is used to describe such dissipative phenomena.

A. Muonium spectroscopy

In the absence of depolarizing interactions with the surroundings, the evolution of the muon spin polarization is governed by the spin Hamiltonian, which is the sum of the hyperfine interaction and the muon and electron Zeeman interactions:

$$\mathcal{H}=h\mathbf{S}_\mu\cdot\tilde{\mathbf{A}}\cdot\mathbf{S}_e-g_\mu\mu_\mu\mathbf{S}_\mu\cdot\mathbf{B}-g_e\mu_B\mathbf{S}_e\cdot\mathbf{B}\ , \tag{2.1}$$

where $\mathbf{S}_\mu$ and $\mathbf{S}_e$ are the muon and electron spin operators, respectively, and $\tilde{\mathbf{A}}$ is the hyperfine tensor.

All the paramagnetic muonium states observed to date in semiconductors have either an isotropic hyperfine interaction or one with axial symmetry. For an "isotropic muonium" or "Mu" state, $\tilde{A}$ is a c-number A times the unit matrix. In several cubic semiconductors, an additional muonium state is observed with a hyperfine interaction that is axially symmetric about any of the [111] crystal axes. This state has been named "anomalous muonium," "anisotropic muonium," or simply "Mu*." For a state of this type, $\tilde{A}$ is diagonal with elements $A_\parallel$ and $A_\perp$.

1. The hyperfine levels of isotropic muonium (Mu)

The spin Hamilton (2.1) for an isotropic muonium state with the magnetic field along the z axis can be written

$$\mathcal{H}(Mu)=\frac{\hbar}{4}\omega_0\sigma\cdot\tau-\frac{\hbar}{2}\omega_\mu\sigma_z+\frac{\hbar}{2}\omega_e\tau_z\ . \tag{2.2}$$

Here $\omega_0=2\pi A=-(2/3\hbar)\mu_0 g_\mu \mu_\mu g_e \mu_B\,|\psi^\uparrow(0)|^2$ is the hyperfine frequency, $|\psi^\uparrow(0)|^2$ is the unpaired electron density at the muon, $\boldsymbol{\sigma}$ and $\boldsymbol{\tau}$ are the Pauli spin operators for the muon and electron, respectively, and

$$\begin{aligned}\omega_\mu&=g_\mu\mu_\mu B/\hbar=2\pi\times 135.53\ \text{MHz/T}\times B\ ,\\ \omega_e&=-g_e\mu_B B/\hbar=2\pi\times 28\,024.21\ \text{MHz/T}\times B\ ,\end{aligned} \tag{2.3}$$

are the precession frequencies of isolated muons and electrons, respectively. It has become standard practice to define the frequencies

$$\omega_\pm=(\omega_e\pm\omega_\mu)/2 \tag{2.4}$$

and the dimensionless magnetic field

$$x=2\omega_+/\omega_0=B/B_0\ , \tag{2.5}$$

where

$$B_0=\hbar\omega_0/(g_\mu\mu_\mu-g_e\mu_B)\ . \tag{2.6}$$

The value of B_0 for Mu in vacuum is 0.1585 T.

It is straightforward to determine the eigenvalues $E_n=\hbar\omega_n$ of the Hamiltonian (2.2) using as a basis the spin eigenfunctions $|\chi_\alpha\rangle=|m_\alpha^\mu m_\alpha^e\rangle$, where m_α^μ and m_α^e are the muon and electron magnetic quantum numbers. Expressions for E_n for Mu are given in Table II.

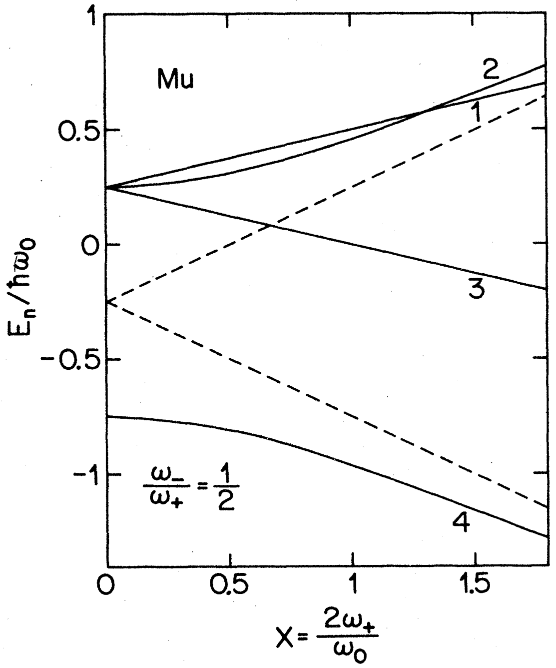

FIG. 1. The hyperfine energy-level (Breit-Rabi) diagram for isotropic 1s-Mu as a function of the dimensionless magnetic field $x=B(g_\mu\mu_\mu-g_e\mu_B)/(hA)$. A fictitious value for the quantity ω_-/ω_+ has been used for clarity; its true value is 0.9904. The dashed lines are the high-field asymptotes for levels 2 and 4.

The dependence of the energy eigenvalues on applied magnetic field is represented in the so-called "Breit-Rabi diagram," an example of which is shown in Fig. 1. In generating the figure a fictitious ratio ω_-/ω_+ has been used for clarity. Note that in zero applied field the energy splitting between the triplet and singlet is directly $\hbar\omega_0$ and that the energy-level differences E_1-E_2 and E_3-E_4 pass through a maximum and minimum, respectively, as the field is increased. The "magic" field (Ehrlich *et al.*, 1972) at which these differences are field independent to first order (see Table II) is given by

$$B_{\text{mag}}=B_0/[(\omega_+/\omega_-)^2-1]^{1/2}=7.155\ B_0\ . \tag{2.7}$$

The expansion of the Mu energy eigenvectors

$$|n\rangle=\sum_\alpha\langle\chi_\alpha|n\rangle\,|\chi_\alpha\rangle \tag{2.8}$$

in spin eigenfunctions is given in Table III.

2. The hyperfine levels of anisotropic muonium (Mu*)

The spin Hamiltonian for anisotropic muonium can be written

$$\begin{aligned}\mathcal{H}(Mu^*)=&\frac{\hbar}{4}\omega_0\boldsymbol{\sigma}\cdot\boldsymbol{\tau}+\frac{\hbar}{4}\omega^*(\boldsymbol{\sigma}\cdot\mathbf{n})(\boldsymbol{\tau}\cdot\mathbf{n})\\ &-\frac{\hbar}{2}\omega_\mu\sigma_z+\frac{\hbar}{2}\omega_e\tau_z\ ,\end{aligned} \tag{2.9}$$

where $\omega_0=2\pi A_\perp$ is now the transverse hyperfine frequency, $\omega^*=2\pi(A_\parallel-A_\perp)$ is the anisotropic part of the hyperfine interaction, and $\mathbf{n}$ is a unit vector along the symmetry axis of the Mu* state. As in Eq. (2.2), several potentially significant interactions have been neglected here. The nuclear hyperfine interaction between the Mu* electron and neighboring host nuclei with spin will be treated in Sec. II.A.4, and Meier (1987) has discussed the *dipolar* interaction of Mu* with neighboring nuclei. The effects of an anisotropic electronic *g* factor will be treated in Sec. V.D.2. A possible interaction between a quadrupole moment associated with the Mu* electronic cloud and an electric field gradient has been brought up by Baryshevskii *et al.* (1982). Finally, a more general anisotropic spin Hamiltonian has been considered by Iwasaki (1974) and Schenck (1985).

The energy eigenvalues and eigenvectors for Mu* are orientation dependent, and their determination generally requires the numerical solution of a fourth-order algebraic equation. However, simple analytical expressions can be obtained in several interesting cases (Hintermann *et al.*, 1980). Breit-Rabi diagrams for Mu* with the applied field parallel ($\theta=0$) and perpendicular ($\theta=\pi/2$) to $\mathbf{n}$ are shown in Figs. 2 and 3. In addition, formulas for the eigenvalues and eigenvectors are given in Tables II and III for zero applied field, for parallel and perpendicular fields, and in the limit of a large applied field. In the high-field limit, the electron Zeeman interaction is much larger than the hyperfine interaction, and the electron

TABLE II. Hyperfine energy eigenvalues for muonium.

Case	$\cot 2\zeta$	$\cot 2\eta$	$\omega_1 = E_1/\hbar$	$\omega_2 = E_2/\hbar$	$\omega_3 = E_3/\hbar$	$\omega_4 = E_4/\hbar$	Comments
Mu	$\frac{2\omega_+}{\omega_0}$		$\frac{\omega_0}{4} + \omega_-$	$-\frac{\omega_0}{4} + \frac{\omega_+}{\cos 2\zeta}$	$\frac{\omega_0}{4} - \omega_-$	$-\frac{\omega_0}{4} - \frac{\omega_+}{\cos 2\zeta}$	
Mu* $(B=0)$			$\frac{\omega_0 - \omega^*}{4}$	$\frac{\omega_0 + \omega^*}{4}$	$\frac{\omega_0 + \omega^*}{4}$	$-\frac{(3\omega_0 + \omega^*)}{4}$	
Mu* $(\theta = 0)$	$\frac{2\omega_+}{\omega_0}$		$\frac{\omega_0 + \omega^*}{4} + \omega_-$	$-\frac{(\omega_0 + \omega^*)}{4} + \frac{\omega_+}{\cos 2\zeta}$	$\frac{\omega_0 + \omega^*}{4} - \omega_-$	$-\frac{(\omega_0 + \omega^*)}{4} - \frac{\omega_+}{\cos 2\zeta}$	
Mu* $(\theta = \pi/2)$	$\frac{4\omega_+}{2\omega_0 + \omega^*}$	$\frac{4\omega_-}{\omega^*}$	$\frac{\omega_0}{4} + \frac{\omega_-}{\cos 2\eta}$	$-\frac{\omega_0}{4} + \frac{\omega_+}{\cos 2\zeta}$	$\frac{\omega_0}{4} - \frac{\omega_-}{\cos 2\eta}$	$-\frac{\omega_0}{4} - \frac{\omega_+}{\cos 2\zeta}$	
Mu* (high B)	$\frac{\omega_+^H}{\omega_\theta}$	$\frac{\omega_-^H}{\omega_\theta}$	$\frac{\omega_e}{2} + \frac{\omega_-^H}{4\cos 2\eta}$	$\frac{\omega_e}{2} - \frac{\omega_-^H}{4\cos 2\eta}$	$-\frac{\omega_e}{2} + \frac{\omega_+^H}{4\cos 2\zeta}$	$-\frac{\omega_e}{2} - \frac{\omega_+^H}{4\cos 2\zeta}$	$\omega_\pm^H = \omega_0 + \omega^* \cos^2\theta \pm 2\omega_\mu$ $\omega_\theta = \omega^* \sin\theta \cos\theta$
Mu $(B = B_{\text{mag}} + \Delta B)$			$\omega_2 + \frac{\omega_0}{2}(1-f)$ $+O(\Delta B^2)$	ω_2	$\omega_4 + \frac{\omega_0}{2}(1+f)$ $+O(\Delta B^2)$	ω_4	$\omega_\mu^{\text{mag}} \omega_e^{\text{mag}} = \left[\frac{\omega_0 \omega_-}{2\omega_+}\right]^2$ $f = 2(\omega_\mu/\omega_e)^{1/2}$
Mu* $(B = B^*_{\text{mag}})$	$\cot 2\theta$		$\frac{\omega_e}{2} + \frac{\omega^*}{8}$	$\frac{\omega_e}{2} - \frac{\omega^*}{8}$			$\omega_\mu^{\text{mag}} = \frac{2\omega_0 + \omega^*}{4}$

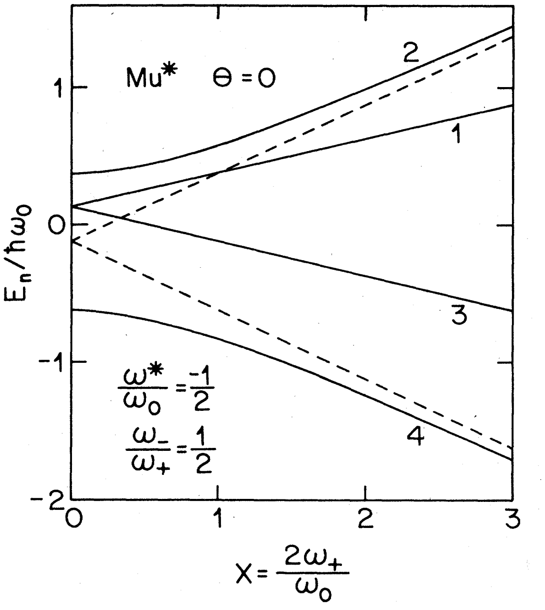

FIG. 2. The hyperfine energy-level diagram for anisotropic Mu* for the case $\theta=0$ ([111] symmetry axis parallel to the applied field). Fictitious values of both ω^*/ω_0 and ω_-/ω_+ have been assumed. The dashed lines are the high-field asymptotes for levels 2 and 4.

spin operator $\boldsymbol{\tau}$ in Eq. (2.9) can be replaced by its z component $\tau_z \mathbf{e}_z$. The final entry in Table II gives Mu* energy eigenvalues in the high-field approximation at the so-called "Mu* magic field"

$$B^*_{\text{mag}} = \hbar(2\omega_0+\omega^*)/(g_\mu \mu_\mu) \,, \tag{2.10}$$

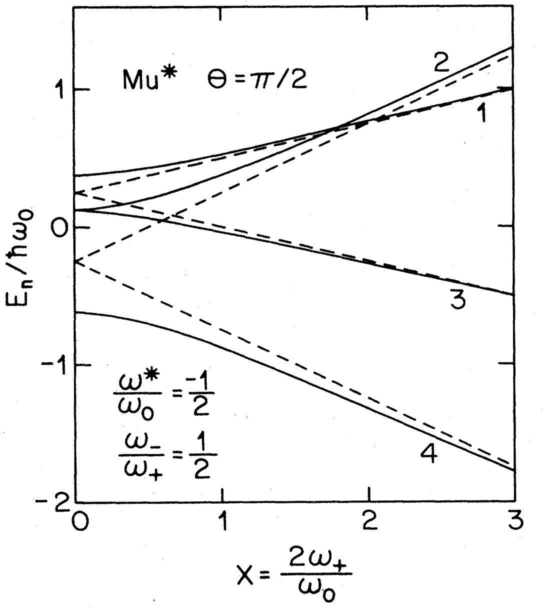

FIG. 3. The hyperfine energy-level diagram for anisotropic Mu* for the case $\theta=\pi/2$ ([111] symmetry axis perpendicular to the applied field). The dashed lines are high-field asymptotes.

TABLE III. Hyperfine energy eigenvectors for muonium in terms of the spin eigenfunctions $|m^\mu m^e\rangle$.

Case	$\|1\rangle$	$\|2\rangle$	$\|3\rangle$	$\|4\rangle$
Mu	$\|++\rangle$	$\sin\zeta\|+-\rangle+\cos\zeta\|-+\rangle$	$\|--\rangle$	$\cos\zeta\|+-\rangle-\sin\zeta\|-+\rangle$
Mu* ($\theta=0$)	$\|++\rangle$	$\sin\zeta\|+-\rangle+\cos\zeta\|-+\rangle$	$\|--\rangle$	$\cos\zeta\|+-\rangle-\sin\zeta\|-+\rangle$
Mu* ($\theta=\pi/2$)	$\cos\eta\|++\rangle+\sin\eta\|--\rangle$	$\sin\zeta\|+-\rangle+\cos\zeta\|-+\rangle$	$-\sin\eta\|++\rangle+\cos\eta\|--\rangle$	$\cos\zeta\|+-\rangle-\sin\zeta\|-+\rangle$
Mu* (high B)	$\cos\eta\|++\rangle+\sin\eta\|-+\rangle$	$-\sin\eta\|++\rangle+\cos\eta\|-+\rangle$	$-\sin\zeta\|+-\rangle+\cos\zeta\|--\rangle$	$\cos\zeta\|+-\rangle+\sin\zeta\|--\rangle$

where the energy difference $E_1-E_2=\hbar\omega^*/4$ is independent of the field orientation.

3. The time-dependent muon polarization in muonium

Having determined the energy eigenvalues and eigenvectors for the muonium spin Hamiltonian, we can now compute the time-dependent spin polarization $\mathbf{p}(t)$ of a muon in a muonium state. We shall discuss the two standard configurations: the longitudinal-field case ($B_{\parallel}$), in which the initial muon polarization $\mathbf{p}(0)$ is parallel to $\mathbf{B}$, and the transverse-field case ($B_{\perp}$) in which $\mathbf{p}(0)$ is perpendicular to $\mathbf{B}$. The angles involved in the two cases are defined in Fig. 4. Furthermore we shall assume an initial polarization $|\mathbf{p}(0)|=1$ and we shall restrict ourselves to computing the "forward" component of the muon polarization $p_f(t)=\mathbf{p}(0)\cdot\mathbf{p}(t)=p_z(t)[p_{x'}(t)]$ for $B_{\parallel}[B_{\perp}]$.

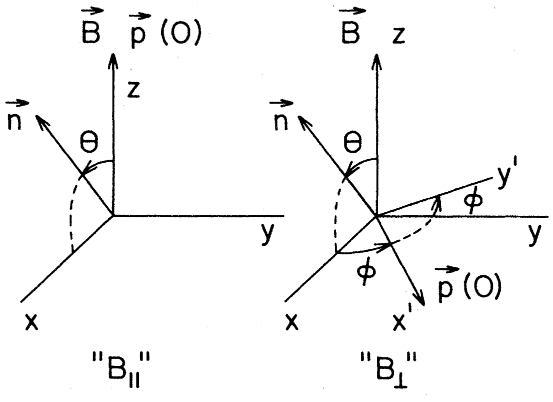

FIG. 4. Definitions of the parallel ("$B_{\parallel}$") and perpendicular ("$B_{\perp}$") geometries for μSR experiments. $\mathbf{B}$ is the applied magnetic field, $\mathbf{p}(0)$ is the initial muon polarization, and $\mathbf{n}$ is the Mu* symmetry axis.

Because we shall be dealing with mixed states, it is convenient to use the density matrix

$$\rho(t)=\tfrac{1}{4}\left[1+\mathbf{p}(t)\cdot\boldsymbol{\sigma}+\mathbf{p}_e(t)\cdot\boldsymbol{\tau}+\sum_{j,k}P^{jk}(t)\sigma^j\tau^k\right], \tag{2.11}$$

where

$$\begin{aligned}\mathbf{p}(t)&=\mathrm{Tr}[\rho(t)\boldsymbol{\sigma}],\\ \mathbf{p}_e(t)&=\mathrm{Tr}[\rho(t)\boldsymbol{\tau}],\\ P^{jk}(t)&=\mathrm{Tr}[\rho(t)\sigma^j\tau^k],\end{aligned} \tag{2.12}$$

are the time-dependent muon, electron, and mixed polarizations, respectively. As it is normally assumed that in forming muonium the muon binds electrons of each spin direction with equal probability (thus forming a mixed state), the initial electron and mixed polarizations are zero:

$$\rho(0)=\tfrac{1}{4}[1+\mathbf{p}(0)\cdot\boldsymbol{\sigma}]. \tag{2.13}$$

The time evolution of the density matrix is governed by the equation of motion

$$i\hbar\frac{d\rho}{dt}=[\mathcal{H},\rho], \tag{2.14}$$

which may be formally integrated to yield $\rho(t)$. Upon insertion into Eq. (2.12), this yields for the muon polarization

$$\mathbf{p}(t)=\mathrm{Tr}[\exp(-i\mathcal{H}t/\hbar)\rho(0)\exp(i\mathcal{H}t/\hbar)\boldsymbol{\sigma}]. \tag{2.15}$$

Using $\rho(0)$ from Eq. (2.13) and evaluating the trace in terms of the energy eigenstates $|n\rangle$, we find that the forward component of the muon polarization is given by a sum of undamped oscillations:

$$\begin{aligned}p_f(t)&=\mathbf{p}(0)\cdot\mathbf{p}(t)\\ &=\tfrac{1}{2}\sum_{n<m}\left|\sum_{\alpha,\beta}\langle n|\chi_\alpha\rangle\mathbf{p}(0)\cdot\langle\chi_\alpha|\boldsymbol{\sigma}|\chi_\beta\rangle\langle\chi_\beta|m\rangle\right|^2\cos\omega_{nm}t+\tfrac{1}{4}\sum_{n}\left|\sum_{\alpha,\beta}\langle n|\chi_\alpha\rangle\mathbf{p}(0)\cdot\langle\chi_\alpha|\boldsymbol{\sigma}|\chi_\beta\rangle\langle\chi_\beta|n\rangle\right|^2\\ &=\sum a_{nm}\cos\omega_{nm}t,\end{aligned} \tag{2.16}$$

where the precession frequencies $\omega_{nm}=\omega_n-\omega_m=(E_n-E_m)/\hbar$ correspond to energy-level separations in the Breit-Rabi diagram.

Table IV gives analytic expressions derived from Eq. (2.16) for the precession amplitudes a_{nm} for various special cases of Mu and Mu*. The precession component with zero frequency is designated by the subscripts $\parallel$ and 0 for the $B_{\parallel}$ and $B_{\perp}$ cases, respectively.

Figure 5 shows a logarithmic representation of the observable transverse-field Mu and Mu* precession frequencies $\nu_{nm}=\omega_{nm}/2\pi$ for the hyperfine constants pertinent to silicon (Mu: $\omega_0=2\pi\times2006$ MHz; Mu*: $\omega_0=2\pi\times92.6$ MHz and $\omega^*=-2\pi\times75.8$ MHz). Note the region of field-independent Mu precession frequencies ν_{12} and ν_{34} at the Mu magic field $B_{\mathrm{mag}}=0.510$ T and the crossing of the Mu* lines ν_{12}^* at the Mu* magic field $B_{\mathrm{mag}}^*=0.202$ T.

4. The nuclear hyperfine interaction

For muonium in a solid host, the muonium electron may show a significant probability density at the site of neighboring host nuclei. If these nuclei have spin, a so-called "nuclear hyperfine interaction" (NHFI) (also called "super hyperfine interaction") arises. This interaction and the nuclear Zeeman interaction add two terms

TABLE IV. Muonium precession amplitudes.

Case	a_{12}	a_{34}	a_{14}	a_{23}	a_{24}	$a_{\parallel}$, a_0	Comments
Mu $B_{\parallel}$	0	0	0	0	$\frac{\sin^2 2\zeta}{2}$	$\cos^2 2\zeta+\frac{\sin^2 2\zeta}{2}$	
Mu $B_{\perp}$	$\frac{\cos^2\zeta}{2}$	$\frac{\cos^2\zeta}{2}$	$\frac{\sin^2\zeta}{2}$	$\frac{\sin^2\zeta}{2}$	0	0	
Mu* $(B=0)$	1/3	1/3	1/6	0	0	1/6	Average over 4 [111] axes
Mu* $(\theta=0)$ $B_{\perp}$	$\frac{\cos^2\zeta}{2}$	$\frac{\cos^2\zeta}{2}$	$\frac{\sin^2\zeta}{2}$	$\frac{\sin^2\zeta}{2}$	0	0	
Mu* $(\theta=\pi/2)$ $B_{\perp}$	$=1/2-a_{14}$	$=1/2-a_{14}$	$[\sin^2(\zeta+\eta)\sin^2\varphi$ $+\sin^2(\zeta-\eta)\cos^2\varphi]/2$	$=a_{14}$	0	0	
Mu* (high B) $B_{\parallel}$	$\frac{\sin^2 2\eta}{2}$	$\frac{\sin^2 2\zeta}{2}$	0	0	0	$\frac{\cos^2 2\zeta+\cos^2 2\eta}{2}$	
Mu* (high B) $B_{\perp}$	$\frac{1-\cos^2\varphi\sin^2 2\eta}{2}$	$\frac{1-\cos^2\varphi\sin^2 2\zeta}{2}$	0	0	0	$\cos^2\varphi(\sin^2 2\zeta$ $+\sin^2 2\eta)/2$	
Mu* $(B=B^*_{\text{mag}})$	$\frac{35}{72}\le\bar{a}_{12}\le\frac{1}{2}$	0	0	0	0		Average over 4 [111] axes

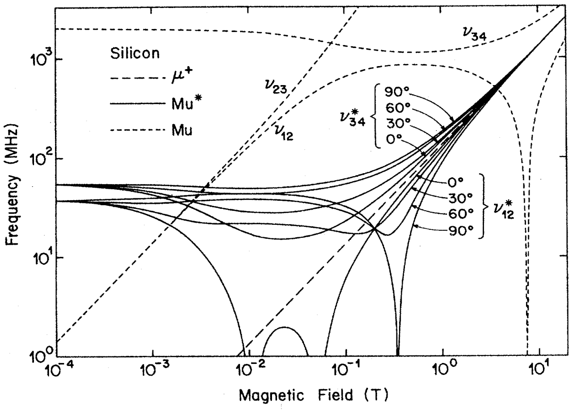

FIG. 5. A log-log plot of the observed transverse-field precession frequencies for the three muon states in silicon. The angles given refer to θ, the angle between the applied field and the Mu* symmetry axis.

to the muonium spin Hamiltonian (2.1):

$$\mathcal{H}(\text{NHFI}) = h\mathbf{S}_\mu\cdot\tilde{A}\cdot\mathbf{S}_e - g_\mu\mu_\mu\mathbf{S}_\mu\cdot\mathbf{B} - g_e\mu_B\mathbf{S}_e\cdot\mathbf{B} + h\sum_{n=1}^{N}\mathbf{S}_n\cdot\tilde{A}_n\cdot\mathbf{S}_e - \sum_{n=1}^{N} g_n\mu_n\mathbf{S}_n\cdot\mathbf{B}\ . \qquad (2.17)$$

We have neglected here the possible quadrupole interaction of the neighboring nuclei with a local electric field gradient (see Iwasaki, 1974, and Kiefl, Odermatt *et al.*, 1986). The NHFI causes energy-level splittings which in general lead to a complex μSR frequency spectrum with many weak and/or poorly resolved lines. Examples of this complexity are shown in Figs. 6 and 7, where numerically simulated transverse-field μSR spectra are presented for Mu in GaAs interacting with two spin-$\frac{3}{2}$ ^{69}Ga nuclei and for Mu* in Ge interacting with one spin-$\frac{9}{2}$ ^{73}Ge nucleus.

Nuclear hyperfine interactions play an important role in the study of organic muonic radicals, where the paramagnetic electron may interact with one or more constituent hydrogen nuclei. The effects of NHFI on μSR spectra for radicals in the liquid state, where rapid tumbling averages the anisotropic part of the hyperfine and nuclear hyperfine interactions to zero, have been investigated theoretically and experimentally by Roduner and Fischer (1981). Many of the μSR lines fall together for a system with equivalent nuclei in zero applied field. Roduner and Fischer give analytical expressions for the precession frequencies and amplitudes for the case of isotropic hyperfine and nuclear hyperfine interactions, and with the aid of NHFI strengths from hydrogen electron spin resonance they interpret an experimental 16-line zero-field spectrum of a muonic radical with six

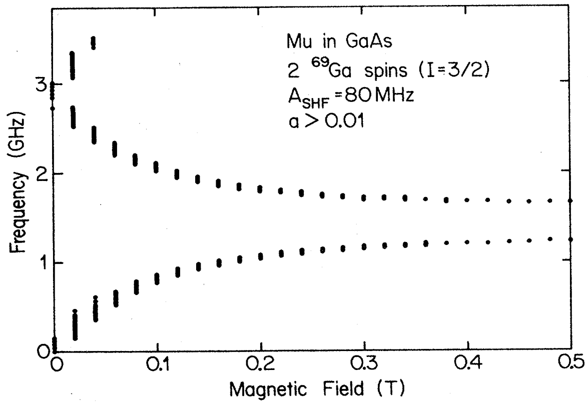

FIG. 6. Calculated precession frequencies for Mu in GaAs interacting with two equivalent ^{69}Ga spins with a nuclear hyperfine interaction of 80 MHz. Only lines with amplitude greater than 0.01 are shown.

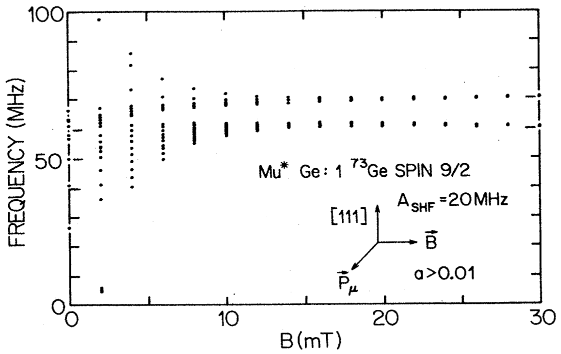

FIG. 7. Calculated precession frequencies for Mu* ($\theta=\pi/2$) in germanium interacting with a single ^{73}Ge spin with an isotropic nuclear hyperfine interaction of 20 MHz. Only lines with amplitude greater than 0.01 are shown.

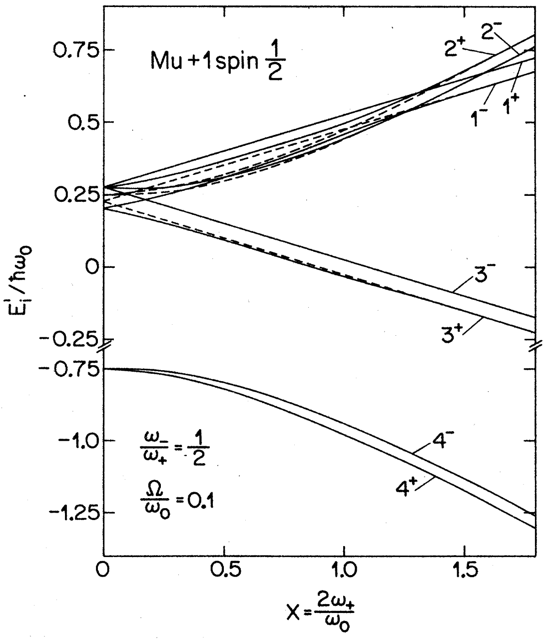

FIG. 8. The nuclear hyperfine energy-level diagram for isotropic Mu interacting with a single nuclear spin $\frac{1}{2}$. The nuclear Zeeman interaction has been neglected. Note the crossing of the first-order perturbation levels 1^- and 2^+ (dashed curves) near $x=1$ and the "avoided crossing" of the exact levels (solid curves).

equivalent protons.

For an arbitrary applied field, the numerical diagonalization of large matrices is required to determine the energy eigenvalues of the Hamiltonian (2.17) and to predict the μSR spectrum for a particular assumed NHFI along the lines of Eq. (2.16). The results of such a numerical calculation for Mu interacting with a single spin-$\frac{1}{2}$ nucleus are shown in Fig. 8. Such calculations, however, rapidly become unwieldy for many nuclei, for large nuclear spins, for a distribution of NHFI, or for NHFI that are anisotropic. The situation again becomes simple in the limit of large applied fields, where the electron Zeeman interaction dominates the Hamiltonian (2.17). The electron spin is then decoupled from the muon and the nuclei; the nuclear hyperfine interaction is said to be "quenched."

Roduner and Fischer (1981) have performed a perturbation calculation of the Mu energy levels in the limit of a small, isotropic NHFI. With the applied field along the z axis and in the notation of Eq. (2.2), the Hamiltonian (2.17) can be rewritten

$$\mathcal{H}(\mathrm{NHFI})=\frac{\hbar\omega_0}{4}\boldsymbol{\sigma}\cdot\boldsymbol{\tau}-\frac{\hbar}{2}\omega_\mu\sigma_z+\frac{\hbar}{2}\omega_e\tau_z+\mathcal{H}_N\ ,$$
$$\mathcal{H}_N=\sum_{n=1}^{N}\frac{\hbar\Omega_n}{2}\mathbf{S}_n\cdot\boldsymbol{\tau}-\sum_{n=1}^{N}\hbar\omega_n S_{n_z}\ . \tag{2.18}$$

The NHFI terms ($\mathcal{H}_N$) of this Hamiltonian are to be treated as a small perturbation. One now collects the N nuclei with which Mu interacts into N_G groups of equivalent nuclei, where the group index k runs from 1 to N_G, and where each group has total spin and magnetic quantum numbers S_k and M_k. The zeroth-order eigenstates of energy are then simply products of the form

$$|\varphi_1\rangle=|++\rangle\prod_{k=1}^{N_G}|S_k,M_k\rangle,\quad |\varphi_2\rangle=(\sin\zeta\,|+-\rangle+\cos\zeta\,|-+\rangle)\prod|S_k,M_k\rangle\ ,$$
$$|\varphi_3\rangle=|--\rangle\prod|S_k,M_k\rangle,\quad |\varphi_4\rangle=(\cos\zeta\,|+-\rangle-\sin\zeta\,|-+\rangle)\prod|S_k,M_k\rangle\ , \tag{2.19}$$

in the notation of Table III. The corresponding first-order energies are

$$E_1'/\hbar=\frac{\omega_0}{4}+\omega_--\sum_{k=1}^{N_G}\omega_k M_K+\tfrac{1}{2}\sum_{k=1}^{N_G}\Omega_k M_k,\quad E_2'/\hbar=-\frac{\omega_0}{4}+\frac{\omega_+}{\cos 2\zeta}-\sum\omega_k M_k+\frac{\cos 2\zeta}{2}\sum\Omega_k M_k\ ,$$
$$E_3'/\hbar=\frac{\omega_0}{4}-\omega_--\sum\omega_k M_k-\tfrac{1}{2}\sum\Omega_k M_k,\quad E_4'/\hbar=-\frac{\omega_0}{4}-\frac{\omega_+}{\cos 2\zeta}-\sum\omega_k M_k-\frac{\cos 2\zeta}{2}\sum\Omega_k M_k\ . \tag{2.20}$$

The dashed curves in Fig. 8 show the perturbation solutions for Mu plus one spin-$\frac{1}{2}$ nucleus.

The approximate time-dependent muon polarization can now be obtained along the lines of Eq. (2.16). In the transverse-field geometry in high field, the electron and nuclear spins remain stationary, and muon precession occurs at frequencies ω_{12}' and ω_{34}':

$$\omega_{12}'=\frac{\omega_0}{2}+\omega_--\frac{\omega_+}{\cos 2\zeta}+\sin^2\zeta\sum_{k=1}^{N_G}\Omega_k M_k\ ,$$
$$\omega_{34}'=\frac{\omega_0}{2}-\omega_-+\frac{\omega_+}{\cos 2\zeta}-\sin^2\zeta\sum_{k=1}^{N_G}\Omega_k M_k\ . \tag{2.21}$$

Thus each of the lines ω_{12} and ω_{34} is split into a number of components, where each component is weighted by the number of ways the nuclear magnetic quantum numbers can combine to produce a given total. This structure of the NHFI-split lines is shown in Fig. 9, where numerical simulations of transverse-field spectra for Mu with two equivalent spin-$\frac{3}{2}$ neighbors are presented. Note the clear component structure at high field with weightings 1-2-3-4-3-2-1, corresponding to $M=-3,-2,-1,0,1,2,3$. The factor $\sin^2\zeta$ in Eq. (2.21) implies that at high field the components of each line lie very close together; the frequency scales in the figure have been expanded for each field by the inverse of this factor. Thus with a finite-frequency resolution, the high-field NHFI splitting is not visible, and the lines appear sharp. But as the field is decreased, a broadening proportional to $\sin^2\zeta$ occurs. Finally, as the field is decreased still further, the high-field approximation breaks down, and the component

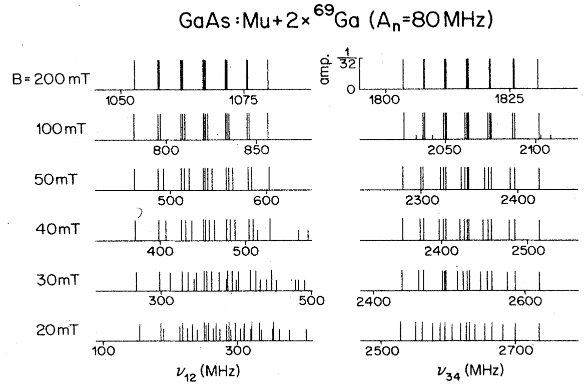

FIG. 9. Calculated precession frequency spectra for Mu in GaAs interacting with two equivalent ^{69}Ga spins. The frequency scales have been expanded by the factor $\sin^{-2}\zeta$.

structure disappears.

For a single shell of equivalent spins ($N_G=1$), the second moment of the ω_{12} and ω_{34} lines is given by Kiefl, Odermatt *et al.* (1986):

$$M_2=\Omega^2\sin^4\zeta \sum_M W(M)M^2 , \tag{2.22}$$

where $W(M)$ is the probability of finding the N spins of the shell with a total z component of nuclear spin M. For N spins S_n,

$$\sum_M W(M)M^2=\frac{NS_n(S_n+1)}{3} . \tag{2.23}$$

Interesting effects of the NHFI also appear in the longitudinal-field geometry. Beck *et al.* (1975) have investigated how the NHFI affects the zero-frequency muon amplitude $a_\parallel$. They demonstrate that large, characteristic reductions occur in $a_\parallel$ in low applied fields when compared with the value for unperturbed Mu given in Table IV. These reductions can in principle be used to determine the type and strength of the NHFI.

However, it is in *large* longitudinal fields that the most dramatic effects of the nuclear hyperfine interaction appear. These become evident in a continuation of our perturbation treatment of the NHFI term $\mathcal{H}_N$. In terms of the zeroth-order eigenstates $|\varphi_k\rangle$ [Eq. (2.19)] and the first-order energies E'_k [Eq. (2.20)], the first-order eigenstates are given by

$$|\varphi'_j\rangle=|\varphi_j\rangle+\sum_k \frac{\langle\varphi_k|\mathcal{H}_N|\varphi_j\rangle}{E'_j-E'_k}|\varphi_k\rangle . \tag{2.24}$$

The correction terms in Eq. (2.24) diverge for $E'_j=E'_k$ and $\langle\varphi_k|\mathcal{H}_N|\varphi_j\rangle\neq 0$. The simple perturbation treatment breaks down at such a first-order degeneracy, and *degenerate* perturbation theory is required. The result is a local mixing of states j and k and an "avoided level crossing" (ALC; Kiefl, Kreitzman *et al.*, 1986; Kiefl, 1986; Heming, Roduner *et al.*, 1986; Heming, Roduner, and Patterson, 1986).

To investigate such an avoided level crossing in more detail we consider the case of Mu interacting via a weak, isotropic NHFI with a single spin-$\frac{1}{2}$ nucleus. The perturbation term in Eq. (2.18) can then be written

$$\mathcal{H}_N=\frac{\hbar\Omega}{4}\boldsymbol{\tau}\cdot\boldsymbol{\Sigma}-\frac{\hbar\omega_n}{2}\Sigma_z , \tag{2.25}$$

where $\boldsymbol{\Sigma}$ is the Pauli spin operator for the nucleus. The zeroth-order eigenstates have the form

$$\begin{aligned}
|\varphi_{1^+}\rangle&=|+++\rangle ,\\
|\varphi_{1^-}\rangle&=|++-\rangle ,\\
|\varphi_{2^+}\rangle&=\sin\zeta|+-+\rangle+\cos\zeta|-++\rangle ,\\
|\varphi_{2^-}\rangle&=\sin\zeta|+--\rangle+\cos\zeta|-+-\rangle ,\\
|\varphi_{3^+}\rangle&=|--+\rangle ,\\
|\varphi_{3^-}\rangle&=|---\rangle ,\\
|\varphi_{4^+}\rangle&=\cos\zeta|+-+\rangle-\sin\zeta|-++\rangle ,\\
|\varphi_{4^-}\rangle&=\cos\zeta|+--\rangle-\sin\zeta|-+-\rangle ,
\end{aligned} \tag{2.26}$$

with the spin states written as $|m^\mu m^e m^n\rangle$, and with the Mu mixing angle ζ defined in Table II. For sufficiently small Ω, only the levels 1^- and 2^+ show an avoided level crossing, and that at high applied field ($\cos 2\zeta\simeq 1$). The first-order energies of these states are then

$$\begin{aligned}
E'_j/\hbar&=E_j+\langle\varphi_j|\mathcal{H}_N|\varphi_j\rangle ,\\
E'_{1^-}/\hbar&=\frac{\omega_0}{4}+\omega_- -\frac{\Omega}{4}+\frac{\omega_n}{2} ,\\
E'_{2^+}/\hbar&=-\frac{\omega_0}{4}+\omega_+ +\frac{\Omega}{4}-\frac{\omega_n}{2} ,
\end{aligned} \tag{2.27}$$

and a first-order degeneracy occurs for

$$\omega_x\equiv(\omega_\mu-\omega_n)-\left[\frac{\omega_0-\Omega}{2}\right]=0 . \tag{2.28}$$

For applied fields in the vicinity of this degeneracy the two states mix, and we must apply degenerate perturbation theory (e.g., Baym, 1978). Accordingly, the mixed states and their energies are

$$\begin{aligned}
|\psi_+\rangle&=\sin\alpha|\varphi_{1^+}\rangle+\cos\alpha|\varphi_{2^-}\rangle ,\\
|\psi_-\rangle&=\cos\alpha|\varphi_{1^+}\rangle-\sin\alpha|\varphi_{2^-}\rangle ,\\
E_\pm&=\tfrac{1}{2}\{E'_{1^-}+E'_{2^+}\pm[(E'_{1^-}-E'_{2^+})^2+\hbar^2\omega_G^2]^{1/2}\}\\
&=\frac{\hbar}{2}[\omega_e\pm(\omega_x^2+\omega_G^2)^{1/2}] ,
\end{aligned} \tag{2.29}$$

where the NHFI mixing angle α is given by

$$\cot 2\alpha=\omega_x/\omega_G , \tag{2.30}$$

and the perturbation matrix element ω_G is

$$\omega_G=\frac{2}{\hbar}\langle\varphi_{1^-}|\mathcal{H}_N|\varphi_{2^+}\rangle=\Omega\sin\zeta\simeq\frac{\Omega\omega_0}{2\omega_e} . \tag{2.31}$$

An energy gap of width $\hbar\omega_G$ thus opens up between the levels ψ_+ and ψ_- at the avoided crossing. Such an avoided level crossing is apparent near $x=1.0$ in Fig. 8, where the first-order energies (dashed curves) for the states 1^- and 2^+ intersect but the exact energies (solid curves) repel one another.

The time-dependent muon polarization in the vicinity of the avoided crossing can now be calculated in a fashion similar to that described in the previous section. Note, however, that the factors $\frac{1}{2}$ and $\frac{1}{4}$ occurring in Eq. (2.16) are now replaced by $\frac{1}{4}$ and $\frac{1}{8}$ due to the addition of the nuclear spin. The resulting expression for the forward component of the muon polarization in high field ($\cos 2\zeta\simeq 1$) is

$$p_f(t)=1-a(1-\cos\omega t)\ ,$$
$$a=\tfrac{1}{4}\sin^2 2\alpha\ , \qquad (2.32)$$
$$\omega=\frac{1}{\hbar}[E_+-E_-]=\sqrt{\omega_x^2+\omega_G^2}\ .$$

The nonoscillating part of the polarization shows a dip at the avoided crossing with a depth of 25% and a full width at half maximum of $\Delta\omega_x=2\omega_G$.

Figure 10 shows the results of an exact calculation of the $1^- - 2^+$ energy difference and the nonoscillating polarization amplitude as a function of the applied field for the case of vacuum Mu interacting with one ^{19}F spin-$\frac{1}{2}$ nucleus. Curves are given for NHFI strengths of 100 and 500 MHz. The large muon-electron hyperfine interaction causes the avoided level crossings to occur at the (inaccessibly) large fields of 22.8 and 20.7 T, respectively.

If a muonium state interacts with a nucleus with spin larger than $\frac{1}{2}$ or with several nuclei with spin, multiple avoided level crossings occur. The situation is shown schematically in Fig. 11 for interaction with a spin-$\frac{3}{2}$ nucleus (or with the $S_k=\frac{3}{2}$ subspace of a multinucleus problem). Note that three (unresolved) avoided level crossings now occur ($2S_k$ in general) at approximately the same value of the applied field. The splitting is due to the difference from unity of the factors $\cos 2\zeta$ in Eq. (2.20). It is remarkable that even for a system of many spins, each group of nuclear spins with equivalent NHFI contributes (in the approximation $\cos 2\zeta=1$) to a single avoided-level-crossing resonance. Besides the $(1,M_k-1)-(2,M_k)$ crossing, for larger NHFI a $(3,M_k)-(4,M_k-1)$ crossing may occur, and the approximate crossing conditions are obtained by equating the corresponding first-order energies in Eq. (2.20):

$$\omega_\mu-\omega_k=\pm\frac{(\omega_0-\Omega_k)}{2}\ . \qquad (2.33)$$

Here the positive sign corresponds to a $(1,M_k-1)-(2,M_k)$ crossing and the negative sign to a $(3,M_k)-(4,M_k-1)$ crossing.

For a large muonium hyperfine interaction typical of the isotropic Mu states in semiconductors, the ALC occur at inaccessibly large fields, but not so for the more weakly coupled anisotropic Mu* state. It is therefore of interest to extend the ALC treatment to the case of anisotropic hyperfine and nuclear hyperfine interactions. This has been done by Kiefl (1986). For isotropic interactions, the only states that mix are those with the same z component of the total spin angular momentum ($\Delta=0$). A principal result of the anisotropy is the appearance of two new types of ALC, the $\Delta=1$ and $\Delta=2$ cases, in which the z component of the total spin angular momentum changes by one and two units, respectively (the finely dashed lines in Fig. 11).

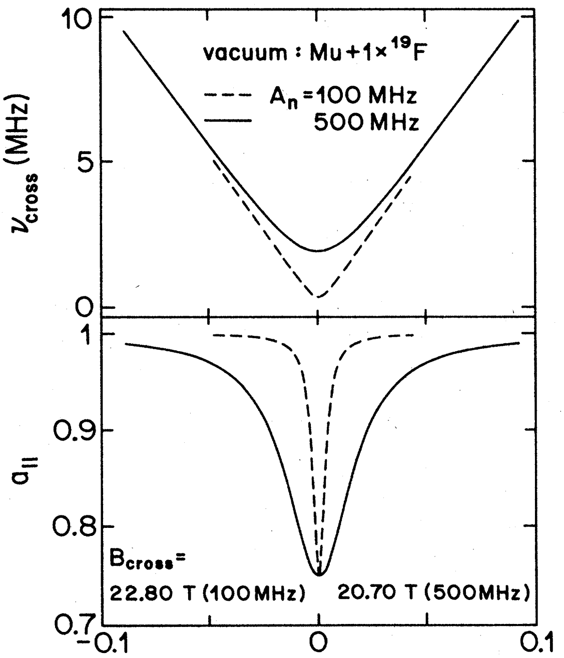

FIG. 10. The results of numerical calculations of avoided level crossing in the system vacuum Mu plus one ^{19}F spin-$\frac{1}{2}$ nucleus ($\omega_n=2\pi 40.055$ MHz/T$\times B$). The splitting of the mixed energy levels $\nu_{\rm cross}=\omega/(2\pi)$ and the nonoscillating polarization amplitude $(1-a)$ are shown as a function of applied field for NHFI strengths of 100 and 500 MHz.

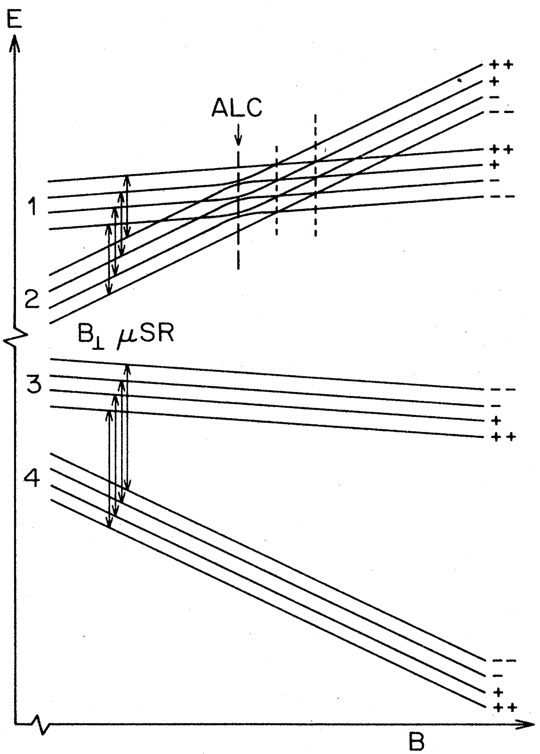

FIG. 11. A schematic representation of nuclear hyperfine levels for a multispin system with $S_k=\frac{3}{2}$. The ν_{12} and ν_{34} transverse-field μSR transitions are indicated by vertical arrows and the $\Delta=0$ avoided level crossing by the coarsely dashed line. The finely dashed lines indicate the positions of the $\Delta=1$ and 2 avoided level crossings which occur for anisotropic hyperfine and nuclear hyperfine interactions.

Besides causing dips in the longitudinal polarization, the avoided level crossing also makes itself felt in the transverse-field μSR transitions (the vertical arrows in Fig. 11). As shown above, these precession signals are composed of many individual NHFI lines which are unresolved in high field. The avoided level crossing causes a local increase in the multiplet splitting which may be observable as a line broadening. Such a broadening could be used to determine which muonium transitions are undergoing avoided level crossing.

The avoided-level-crossing effect has been experimentally observed for paramagnetic muon-electron-nuclear states in several chemical and solid-state hosts, and some results are shown in Sec. III.F.

B. Muonium dynamics

The solid-state environment of a muonium state exerts random perturbations which influence the evolution of the muon spin polarization. I shall assume that such perturbations are either "persistent" or "irreversible." Persistent random perturbations of muonium in a semiconductor fall into two categories: (1) fluctuating local magnetic fields arising from the relative motion of muonium and a paramagnetic species such as free electrons/holes or bound donors/acceptors and (2) modulation of the muonium hyperfine interaction, for example, by muonium diffusion among inequivalent sites or by repeated changes of the muonium charge state. An irreversible perturbation could be a sudden change of the muonium hyperfine interaction such as would occur when the muonium undergoes a permanent change to a diamagnetic charge state or when diffusing muonium becomes trapped at a crystal defect. When considering persistent or irreversible changes in the hyperfine interaction, it is important to consider whether or not the polarization of the muonium electron is conserved during the change.

With the inclusion of such dissipative dynamic effects, the muon polarization no longer follows Eq. (2.16), but rather takes the form of a sum of damped, phase-shifted oscillations:

$$p_f(t)=\sum_{n,m} a_{nm}\exp(-\lambda_{nm}t)\cos(\omega_{nm}t+\varphi_{nm}) \ . \tag{2.34}$$

1. Depolarization by fluctuating magnetic fields

Due to its 207 times larger magnetic moment, the muonium electron is much more sensitive to a fluctuating magnetic field than is the muon, hence the muon interaction is generally neglected. A theory that treats the effect of fluctuating magnetic fields on the muonium electron was presented by Nosov and Yakovleva (1962) and further developed by Ivanter and Smilga (1968a, 1968b). They assume that the result of such a fluctuating field is to damp the electron polarization in muonium exponentially, with a characteristic "electron flip rate" 2ν, and they investigate the effects of this damping on the muon polarization.

A more complete theory of the fluctuating electron Zeeman interaction has been developed using the Master Equation approach by Celio and Meier (1983). These authors derive a formula that describes the effect on the muon polarization of a fluctuating electron Zeeman interaction of strength δ_{ex}, which is describable by a correlation time τ_c. For sufficiently rapid fluctuations, the theory reduces to that of Nosov and Yakovleva with $\nu=\delta_{\mathrm{ex}}^2\tau_c$.

The starting point for both the Nosov-Yakovleva and Celio-Meier theories is the time-dependent density matrix and its unperturbed equation of motion given in Eqs. (2.11) and (2.14) above. The unperturbed spin Hamiltonian will be taken to be that for Mu* [Eq. (2.9)], since the case of isotropic Mu can be regained simply by letting $\omega^*=0$. In contrast with the unperturbed case, it is now necessary to follow the time-dependence of the electron polarization $\mathbf{p}_e(t)$ and the mixed polarizations $P^{jk}(t)$ as well as the muon polarization $\mathbf{p}(t)$. It is convenient to collect these polarizations into a single 15-component vector $P^{jk}(t)$ with the definitions

$$\begin{aligned} p^j(t)&=P^{j0}(t), \quad j=1,2,3 \ ,\\ p_e^k(t)&=P^{0k}(t), \quad k=1,2,3 \ ,\\ P^{jk}(t)&=P^{jk}(t), \quad j,k=1,2,3 \ . \end{aligned} \tag{2.35}$$

Following Meier (1982), we evaluate the commutator in Eq. (2.14) and the trace in Eq. (2.12) to obtain equations of motion:

$$\begin{aligned} \dot P^{j0}&=\sum_{k,l}\varepsilon_{jkl}\left[\frac{\omega_0}{2}P^{lk}+\sum_m\frac{\omega^*}{2}P^{lm}n_kn_m-\omega_\mu^kP^{l0}\right] ,\\ \dot P^{0j}&=\sum_{k,l}\varepsilon_{jkl}\left[\frac{\omega_0}{2}P^{kl}+\sum_m\frac{\omega^*}{2}P^{ml}n_kn_m+\omega_e^kP^{0l}\right] ,\\ \dot P^{jk}&=\sum_{l,m,n}\varepsilon_{nlm}\left[\left[\delta_{j,m}\delta_{k,n}\frac{\omega_0}{2}(P^{l0}-P^{0l})\right]\right.\\ &\qquad -\delta_{j,n}\left[\frac{\omega^*}{2}n_mn_kP^{l0}-\omega_\mu^mP^{lk}\right]\\ &\qquad \left.+\delta_{k,n}\left[\frac{\omega^*}{2}n_jn_lP^{0m}+\omega_e^lP^{jm}\right]\right] , \end{aligned} \tag{2.36}$$

where $\boldsymbol{\omega}_\mu$ and $\boldsymbol{\omega}_e$ are vectors of length ω_μ and ω_e with the direction of the applied field $\mathbf{B}$. We can abbreviate these unperturbed equations of motion as

$$\dot P^{jk}=\sum_{l,m}Q_{jk/lm}P^{lm} \ . \tag{2.37}$$

Such equations are solved numerically by finding the matrix U which diagonalizes Q:

$$\sum_{j,k,l,m}U^{-1}_{\alpha\beta/jk}Q_{jk/lm}U_{lm/\gamma\delta}=D_{\alpha\beta}\delta_{\alpha,\gamma}\delta_{\beta,\delta} \tag{2.38}$$

in terms of which the time-dependent muon polarization has the form

$$P^{jk}(t) = \sum_{\alpha,\beta,l,m} U^{-1}_{\alpha\beta/lm} U_{jk/\alpha\beta} \exp(D_{\alpha\beta}t) P^{lm}(0) \ . \tag{2.39}$$

For the unperturbed case, Q is antisymmetric, and the eigenvalues $D_{\alpha\beta}$ are purely imaginary, yielding undamped precession components.

In the Nosov-Yakovleva theory, account is taken of the loss of the electron polarization by the addition of relaxation terms to the equations for the electron and mixed polarizations:

$$\begin{gathered} \dot{P}^{jk} = \sum_{l,m} Q^{\mathrm{NY}}_{jk/lm} P^{lm} \ , \\ Q^{\mathrm{NY}}_{jk/lm} = Q_{jk/lm} - 2\nu(1-\delta_{k,0})\delta_{j,l}\delta_{k,m} \ . \end{gathered} \tag{2.40}$$

The matrix Q^{NY} is no longer antisymmetric, hence the polarization components obtained by diagonalization show damped oscillations. The quantities in Eq. (2.34) of principal interest are the zero-frequency amplitude $a_{\parallel}$ and relaxation rate $\lambda_{\parallel}$ in the longitudinal-field geometry and the precession amplitudes, frequencies, and relaxation rates in the transverse-field geometry. The Nosov-Yakovleva theory has been applied to Mu* by Belousov *et al.* (1981). In our presentation of the Nosov-Yakovleva results we shall restrict ourselves to isotropic Mu, and for the transverse-field case we shall focus our attention on the low-frequency precession components ω_{12} and ω_{23}.

The restriction to isotropic Mu allows substantial simplification of the equations of motion (2.40) (Ivanter and Smilga, 1968a; Brewer *et al.*, 1975; Schenck, 1985). If the applied field is longitudinal, there are only six nonzero polarization components: P^{03}, P^{11}, P^{12}, P^{21}, P^{22}, and P^{30}. For the case of Mu in a transverse applied field, it is convenient to rewrite the equations of motion in terms of the four nonzero, complex polarization components $(P^{10}+iP^{20})$, $(P^{01}+iP^{02})$, $(P^{13}+iP^{23})$, and $(P^{31}+iP^{32})$.

Approximate analytic expressions for the limits of very slow and very fast electron relaxation have been derived by several authors, and these are collected in Table V. Figures 12–16 show the results of numerical calculations as a function of the dimensionless applied field x. Note that in the limit of very fast electron relaxation, the muon in muonium behaves as if it were in a diamagnetic environment.

An example of the Nosov-Yakovleva theory applied to avoided-level-crossing resonance in a three-spin system is given in Sec. III.F. A further development of the Nosov-Yakovleva theory due to Ivanter (1969) takes account of a possible anisotropy in the electron polarization damping rate with respect to the direction of the applied field (see also Belousov *et al.*, 1981). We shall not discuss this extension here.

Since most of the work on the Nosov-Yakovleva model has been done by Soviet groups, a few comments regarding the notation conventions used in their publications

TABLE V. Limiting cases of the Nosov-Yakovleva theory for Mu depolarization.

		$\nu \ll \omega_e \ll \omega_0$	$\nu \gg \omega_0, \omega_e$
$B_{\parallel}$:	$a_{\parallel}$	$\frac{\omega_0^2+2\omega_e^2}{2\omega_0^2+2\omega_e^2}$ [a]	1 [a]
	$\lambda_{\parallel}$	$\frac{\nu\omega_0^2}{\omega_0^2+\omega_e^2}$ [a]	$\frac{\nu\omega_0^2}{4\nu^2+\omega_e^2}$ [d]
$B_{\perp}$:	a_{12}	$\frac{1}{4}\left\lvert 1+\frac{1}{Z}\left[\frac{\nu}{2}+\frac{2i\omega_+^3}{\omega_0^2}\right]\right\rvert$ [c]	1 [b]
	ω_{12}	$\omega_- - \mathrm{Im}Z$ [c]	$-\omega_\mu - \frac{\omega_e\omega_0^2}{16\nu^2}$ [b]
	λ_{12}	$\frac{3\nu}{2} - \mathrm{Re}Z$ [c]	$\frac{\omega_0^2}{4\nu}\left[\frac{8\nu^2+\omega_e^2}{8\nu^2+2\omega_e^2}\right]$ [d]
	a_{23}	$\frac{1}{4}\left\lvert 1-\frac{1}{Z}\left[\frac{\nu}{2}+\frac{2i\omega_+^3}{\omega_0^2}\right]\right\rvert$ [c]	0 [b]
	ω_{23}	$\omega_- + \mathrm{Im}Z$ [c]	
	λ_{23}	$\frac{3\nu}{2} + \mathrm{Re}Z$ [c]	2ν [b]
	Z	$\left[\frac{\nu^2}{4}-\frac{\omega_+^4}{\omega_0^2}+\frac{2i\omega_+^3\nu}{\omega_0^2}\right]^{1/2}$ [c]	

[a] Nosov and Yakovleva (1962).
[b] Ivanter and Smilga (1968a).
[c] Gurevich *et al.* (1971).
[d] Ivanter and Smilga (1968b).

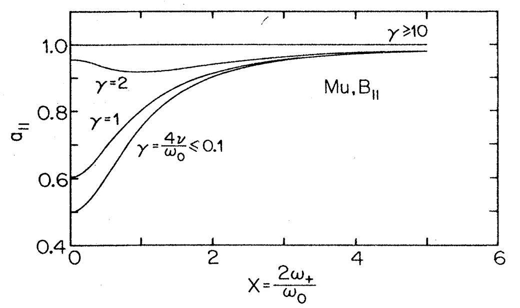

FIG. 12. Predictions by the Nosov-Yakovleva theory of the nonoscillating Mu polarization amplitude in the longitudinal-field geometry as a function of the dimensionless electron spin-flip rate $\gamma=4\nu/\omega_0$ and the reduced magnetic field x.

are in order here. (1) In the transverse-field geometry, they generally choose to orient the initial muon polarization along the x axis, to put the applied magnetic field along the y axis, and to define a complex muon polarization to be p_x+ip_z. Since we follow the convention in which $\mathbf{p}(0)$ is along the x′ axis, $\mathbf{B}$ is along the z axis, and $p_{x'}+ip_{y'}$ is the complex polarization, the frequencies of precession they find have the opposite sign from those here. (2) Two slightly different conventions are used for the dimensionless magnetic field x, namely, that $x=\omega_e/\omega_0$ (see, for example, Nosov and Yakovleva, 1962; Ivanter and Smilga, 1968a, 1971b; Ivanter, 1969; Gurevich *et al.*, 1971, 1975) and, as used here, $x=2\omega_+/\omega_0$ (e.g., Nosov and Yakovleva, 1965; Ivanter and Smilga, 1968b, 1971a). (3) A dimensionless time

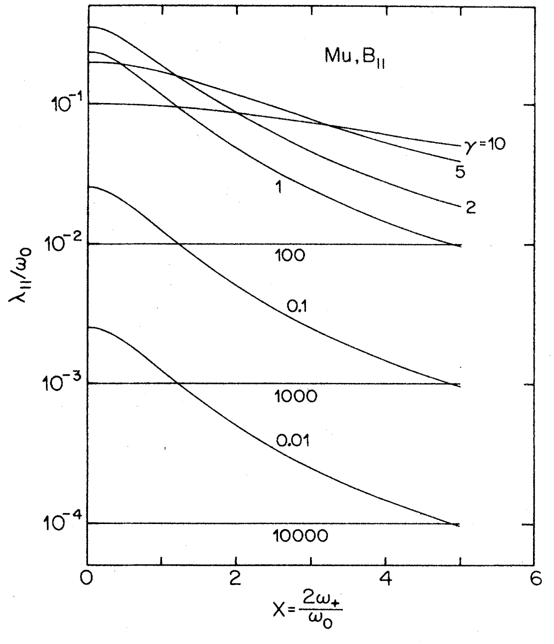

FIG. 13. Predictions by the Nosov-Yakovleva theory of the zero-frequency Mu relaxation rate in the longitudinal-field geometry as a function of the dimensionless electron spin-flip rate $\gamma=4\nu/\omega_0$ and the reduced magnetic field x.

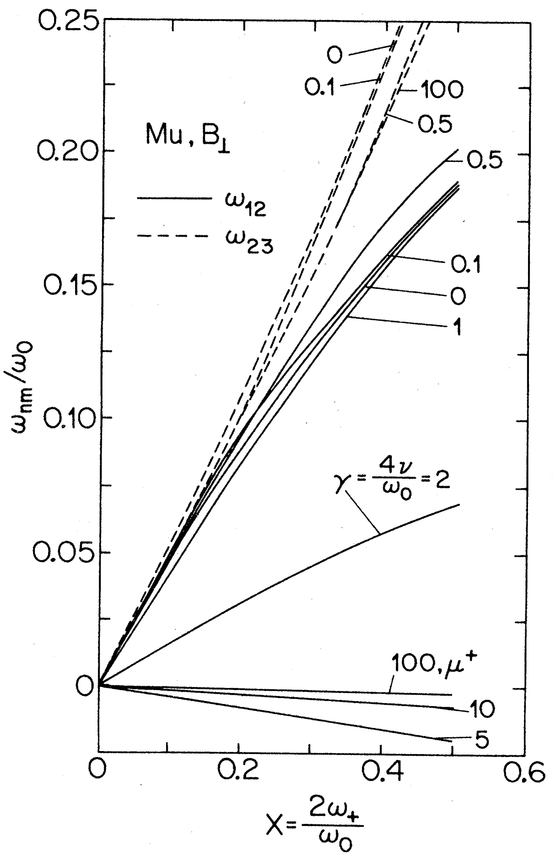

FIG. 14. Predictions by the Nosov-Yakovleva theory of the low- and intermediate-field Mu precession frequencies in the transverse-field geometry as a function of the dimensionless electron spin-flip rate $\gamma=4\nu/\omega_0$ and the reduced magnetic field x. The symbol μ^+ signifies the diamagnetic muon frequency.

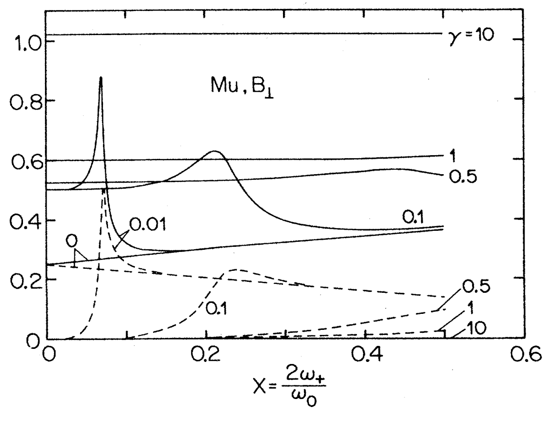

FIG. 15. Predictions by the Nosov-Yakovleva theory of the low- and intermediate-field Mu precession amplitudes in the transverse-field geometry as a function of the dimensionless electron spin-flip rate $\gamma=4\nu/\omega_0$ and the reduced magnetic field x.

equal to $\omega_0 t/2$ is occasionally used (Ivanter and Smilga, 1968a; Ivanter, 1969).

Celio and Meier (1983) used a Master Equation approach to treat the effects of a fluctuating magnetic field at the electron. Under the assumption of isotropic, Markovian fluctuations with x, y, and z components equal to $\pm\delta_{\mathrm{ex}}/(g_e\mu_B)$ and a correlation time τ_c, Celio and Meier obtained an equation of motion for the polarizations of the form [Eq. (3.21) of their paper]

$$\begin{aligned} \dot{P}^{jk} &= \sum_{l,m} Q^{\mathrm{CM}}_{jk/lm} P^{lm} , \\ Q^{\mathrm{CM}}_{jk/lm} &= Q_{jk/lm} \\ &\quad - \sum_{\alpha,\beta=1}^{4} \sum_{\kappa=1}^{3} \frac{\delta^2_{\mathrm{ex}}}{4} \left[\left(\frac{1}{\tau_c} E - Q \right)^{-1} \right]_{\alpha\beta/0\kappa} G^{\kappa\alpha\beta}_{jk/lm} , \end{aligned} \tag{2.41}$$

where E is the unit matrix,

$$G^{\kappa\alpha\beta}_{jk/lm} = \sum_{i,n} F^{0\kappa}_{jk/in} F^{\alpha\beta}_{in/lm} , \tag{2.42}$$

and the matrices F describe the commutation properties of the spin operators:

$$F^{\alpha\beta}_{in/lm} \sigma^i \tau^n = (\sigma^\alpha \tau^\beta , \sigma^l \tau^m) . \tag{2.43}$$

In Eq. (2.43), σ^0 and τ^0 are taken to be unit operators. Evaluation of the commutators (not explicitly done by Celio and Meier) yields the following expression for $G^{\kappa\alpha\beta}_{jk/lm}$:

$$\begin{aligned} G^{\kappa\alpha\beta}_{jk/lm} = {} & -4(1-\delta_{k,0})(1-\delta_{\kappa,0}) \\ & \times \{ (\delta_{k,\beta}\delta_{\kappa,m} - \delta_{k,m}\delta_{\kappa,\beta})(1-\delta_{\beta,0})(1-\delta_{m,0})[\delta_{j,l}\delta_{\alpha,0} + (\delta_{j,\alpha}\delta_{l,0} + \delta_{\alpha,l}\delta_{j,0})(1-\delta_{\alpha,0})] \\ & + \varepsilon_{\alpha lj}[\varepsilon_{\kappa mk}\delta_{\beta,0}(1-\delta_{m,0}) + \varepsilon_{\kappa\beta k}\delta_{m,0}(1-\delta_{\beta,0})](1-\delta_{\alpha,0})(1-\delta_{l,0})(1-\delta_{j,0}) \} . \end{aligned} \tag{2.44}$$

As for the unperturbed and Nosov-Yakovleva cases, the matrix Q^{CM} can be diagonalized and the polarization computed [Eqs. (2.38) and (2.39)]. Predicted $B_{\parallel}$ and $B_{\perp}$ damping rates for Mu in silicon using the Celio-Meier theory with a particular choice for δ_{ex} and τ_c are compared with results from the Nosov-Yakovleva theory in Fig. 17.

One sees from Eq. (2.41) that, for sufficiently short correlation times τ_c, the matrix Q can be neglected compared with $1/\tau_c$, and with the matrix $G^{\kappa 0\kappa}_{jk/lm}$ from Eq. (2.44) $Q^{\mathrm{CM}}_{jk/lm}$ takes the form

$$Q^{\mathrm{CM}}_{jk/lm} \simeq Q_{jk/lm} - 2\delta^2_{\mathrm{ex}}\tau_c \delta_{j,l}\delta_{k,m}(1-\delta_{j,0}) \quad \left[\frac{1}{\tau_c} \gg Q \right] , \tag{2.45}$$

which is equivalent to the Nosov-Yakovleva result [Eqs. (2.40)] with $\nu = \delta^2_{\mathrm{ex}}\tau_c$.

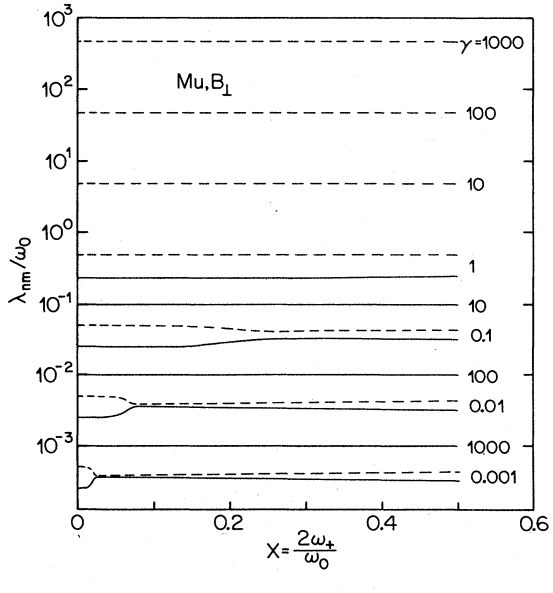

FIG. 16. Predictions by the Nosov-Yakovleva theory of the low- and intermediate-field Mu relaxation rates in the transverse-field geometry as a function of the dimensionless electron spin-flip rate $\gamma = 4\nu/\omega_0$ and the reduced magnetic field x.

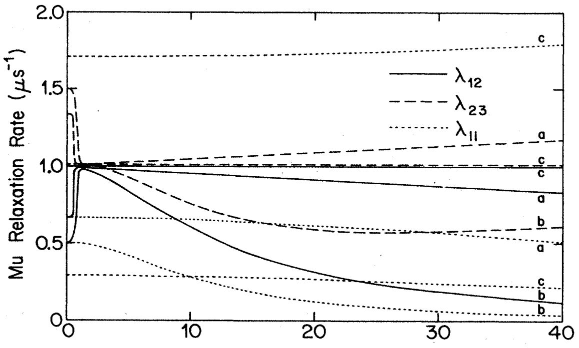

FIG. 17. Comparisons of Mu relaxation rates in silicon in the longitudinal- and transverse-field geometries predicted by (a) the Nosov-Yakovleva theory with $\nu = 6.67 \times 10^5$ s^{-1}, (b) the Celio-Meier theory with $\delta_{\mathrm{ex}} = 3.16 \times 10^7$ s^{-1} and $\tau_c = 10^{-9}$ s, and (c) the Celio theory for recurring muon jumps from the Mu state to the μ^+ state at a rate $\Lambda = 10^6$ s^{-1}. For case c in the longitudinal-field geometry, there are two zero-frequency components 1 and 2 with, respectively, low and high relaxation rates. In zero field the amplitudes of these components are in the ratio $a_1/a_2 = (1+2^{1/2})/(1-2^{1/2})$.

2. Depolarization by modulation of the hyperfine interaction

A persistent modulation of the muonium hyperfine interaction represents a further possible mechanism for muonium depolarization. Such a modulation could be the result of hopping of the muonium atom among inequivalent sites in the solid or of the repeated capture and loss of an electron. A theory that treats a general modulation has not been formulated, and we shall limit ourselves to discussing a model developed by Celio (1985) in which muonium jumps among a finite number of states, each of which is characterized by a particular hyperfine interaction. A version of the model for two states will be presented here but there is no essential difficulty in extending it to more states.

A special case of the Celio model is one in which the hyperfine interaction of muonium jumps between a particular value and zero. If one further assumes that the electron polarization is lost with each muonium formation, this limit corresponds to the "charge exchange" theory of Ferrel *et al.* (1960), Ivanter and Smilga (1971a, 1971b), and Nosov and Yakovleva (1965).

We assume that muonium repeatedly jumps from a state I to a state II and back at a rate Λ. Celio (1985) shows that Eq. (2.37), in which the equations of motion of the muon (P^{j0}), electron (P^{0k}), and mixed (P^{jk}) polarizations are given in terms of the matrix Q, can be rewritten for the polarizations in the two states, $P_{\rm I}$ and $P_{\rm II}$, as

$$\begin{aligned}\dot{P}_{\rm I}^{jk} &= (Q^{\rm I}_{jk/lm} - \Lambda E_{jk/lm})P_{\rm I}^{lm} + \Lambda R_{jk/lm} P_{\rm II}^{lm} \ , \\ \dot{P}_{\rm II}^{jk} &= \Lambda R_{jk/lm} P_{\rm I}^{lm} + (Q^{\rm II}_{jk/lm} - \Lambda E_{jk/lm})P_{\rm II}^{lm} \ ,\end{aligned} \tag{2.46}$$

where the $Q^{\rm I}$ and $Q^{\rm II}$ are the Q matrices for the unperturbed states I and II and where $E_{jk/lm} = \delta_{j,l}\delta_{k,m}$ is the unit matrix. Celio distinguishes between two cases. If the electron polarization is conserved during the jump, then the matrix

$$R_{jk/lm} = \delta_{j,l}\delta_{k,m} = E_{jk/lm} \quad (\mathbf{p}_e \text{ kept}) \tag{2.47}$$

is also the unit matrix. If, however, the electron polarization is lost during the jump, then only the *muon* polarization of state II is carried into state I and vice versa, and the matrix R has the form

$$R_{jk/lm} = \delta_{k,0}\delta_{m,0}\delta_{j,l} \quad (\mathbf{p}_e \text{ lost}) \ . \tag{2.48}$$

This system of coupled equations is conveniently solved numerically by representing the polarizations as a vector $\mathbf{P}_T$ of length 30 whose first 15 components are the $P_{\rm I}^{jk}$ and whose second 15 components are the $P_{\rm II}^{jk}$. In schematic form the equation of motion for $\mathbf{P}_T$ is then

$$\dot{\mathbf{P}}_T = \begin{bmatrix} Q^{\rm I} - \Lambda E & \Lambda R \\ \Lambda R & Q^{\rm II} - \Lambda E \end{bmatrix} \mathbf{P}_T \tag{2.49}$$

and the solution for $\mathbf{P}_T(t)$ is obtained by diagonalization, in analogy with Eq. (2.38). Finally, the total muon polarization is obtained by summing the contributions $P_{\rm I}^{j0}(t)$ and $P_{\rm II}^{j0}(t)$.

It is clear that with simple changes the theory can be applied to Mu* states, a Nosov-Yakovleva electron depolarization can be included, different jump rates from I to II and from II to I can be incorporated, or the theory can be extended to more than two states. Note that, for the case of isotropic Mu states, simplifications of the equations of motion of the polarizations can again be performed for the longitudinal- and transverse-field cases as described in the discussion of Eq. (2.40) above. For example, an application involving jumps between a $\text{Mu}^{\rm I}$ state and a $\text{Mu}^{\rm II}$ state in a transverse field can be reduced from a 30×30 matrix diagonalization to a (complex) 8×8 problem, and jumps between Mu and a diamagnetic μ^+ state reduce to a 5×5 problem.

The results of the Celio theory for the case of jumps between two isotropic muonium states I and II are shown in Fig. 18. The indices i,j in the figure can take either the values 1, 2, or 3, 4. Here it has been assumed that the difference between the hyperfine frequencies for the two Mu states is much less than the individual hyperfine frequencies, that the initial populations of the two states are equal, and that the electron polarization is conserved during the jumps. At low jump rates Λ, each of the Mu hyperfine transitions ω_{12} and ω_{34} is split into two lines corresponding to Mu frozen at the two inequivalent sites. As the jump rate increases, these two lines move together, until at a critical value of Λ they coalesce into a single line. A further increase in the jump rate causes a narrowing of the single line. Figure 18 shows a "universal" plot of the Λ-dependent line separation and linewidth obtained by normalizing these quantities to $\Delta\omega_{ij}^0$, the line separation without jumps, and plot-

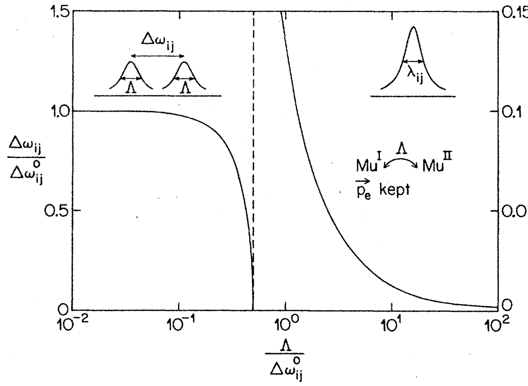

FIG. 18. Calculations using the Celio theory of the splittings and widths of the transverse-field precession lines for muons that undergo repeated jumps between two isotropic muonium states $\text{Mu}^{\rm I}$ and $\text{Mu}^{\rm II}$ at a rate Λ. The hyperfine transitions considered are those seen in high field ($\omega_{ij} = \omega_{12}$ and ω_{34}), and the results and jump rate scales are normalized to the precession frequency difference $\Delta\omega_{ij}^0$ for $\Lambda = 0$. For Λ below the critical value $\Delta\omega_{ij}^0/2$, two Lorentzian lines of width Λ and variable splitting are seen, while for Λ above the critical value, a single Lorentzian line appears whose width depends on the jump rate. It is assumed here that the electron polarization $\mathbf{p}_e$ is conserved during the jumps.

ting these dimensionless quantities against the normalized jump rate $\Lambda/\Delta\omega_{ij}^{0}$. As seen in the figure a merging of the split lines occurs at the critical normalized jump rate $\Lambda/\Delta\omega_{ij}^{0}=0.5$. Note that, since $\Delta\omega_{12}=(d\omega_{12}/d\omega_0)\Delta\omega_0$ is always smaller than $\Delta\omega_{34}$, the ω_{12} precession signal will not only be narrower than the ω_{34} signal, but with increasing jump rate Λ its narrowing will show an onset at a lower value of Λ than will that for ω_{34}.

The phenomenon of charge exchange can also be investigated using Celio's theory. This is done by setting the hyperfine frequency in state II to zero and by assuming no conservation of the electron polarization during the jumps. Thus we have a muon jumping between a paramagnetic Mu state and a diamagnetic μ^+ state, each time binding a new electron. The resulting Mu damping rates in longitudinal and transverse magnetic fields for the hyperfine frequency of Mu in Si are also shown in Fig. 17. Note that, for the jumping rate and range of applied field considered, lines ω_{12} and ω_{23} relax at the same rate in a transverse field and that in a longitudinal field there are both a rapidly and a slowly relaxing component at zero frequency.

The charge exchange phenomenon was treated by an early theory of Ferrel *et al.* (1960). This was later improved by Nosov and Yakovleva (1965), who gave an analytical solution for the case of slow jumping. Ivanter and Smilga (1971a, 1971b) extended the work of Nosov and Yakovleva to include electron spin flips in the Mu state and a second, stable diamagnetic state. The charge exchange limit of Celio's theory is identical to the charge exchange theory of Nosov and Yakovleva.

Another interesting limit to take in the muonium jumping model of Celio is that in which the two states have the same hyperfine frequency. In this case, $Q^{\rm I}=Q^{\rm II}=Q$ and

$$\dot P^{jk}=\dot P^{jk}_{\rm I}+\dot P^{jk}_{\rm II}=[Q_{jk/lm}-\Lambda(E_{jk/lm}-R_{jk/lm})]P^{lm} . \tag{2.50}$$

For the case of conserved electron polarization, this is the equation of motion for unperturbed muonium [Eq. (2.37)], and for electron nonconservation it is the Nosov-Yakovleva electron spin-flip equation (2.40) with $2\nu=\Lambda$. Alternatively, one can again set $Q^{\rm I}=Q^{\rm II}=Q$ but require that the electron spin be flipped by 180° with each change of state, i.e.,

$$R_{jk/lm}=[\delta_{k,0}\delta_{m,0}-(1-\delta_{k,0})\delta_{k,m}]\delta_{j,l} \quad (180^\circ\ e\ \text{flip}) . \tag{2.51}$$

This again results in the Nosov-Yakovleva equation (2.40), but now with $\nu=\Lambda$.

3. Irreversible change in the hyperfine interaction

In the last section we discussed the time evolution of the muon polarization when the hyperfine frequency jumps repeatedly between two different values. It is also possible that a muonium state I undergoes an *irreversible* change to a state II at an average rate Λ.

An important example of such an irreversible change of state is that from isotropic Mu to a μ^+ state, such as when Mu chemically reacts to leave the muon in a diamagnetic environment. If the reaction is sufficiently rapid, the precursor Mu state cannot be directly observed, and its existence can only be inferred by the effect of the transition on the "residual" amplitude ($t \gg 1/\Lambda$) and phase of the daughter μ^+ state. Analytical expressions for the polarization $\mathbf{p}(\infty)$ in the μ^+ state have been obtained for the transverse-field $[p_{x'}(\infty)+ip_{y'}(\infty)]$ and longitudinal-field $[p_z(\infty)]$ configurations, even including the effects of a Nosov-Yakovleva electron relaxation rate 2ν (Ivanter and Smilga, 1968a, 1968b; Brewer, 1975; Schenck, 1985). With our geometry conventions (Fig. 4), these are

$$p_{x'}(\infty)+ip_{y'}(\infty)=\left[1-\frac{i\omega_0}{2\Lambda}\,\frac{B(A+B)}{[AB^2-(A+B)]}\right]^{-1} , \tag{2.52}$$

where

$$A=\frac{-2i}{\omega_0}(\Lambda+2\nu),\quad B=A-2x , \tag{2.53}$$

and

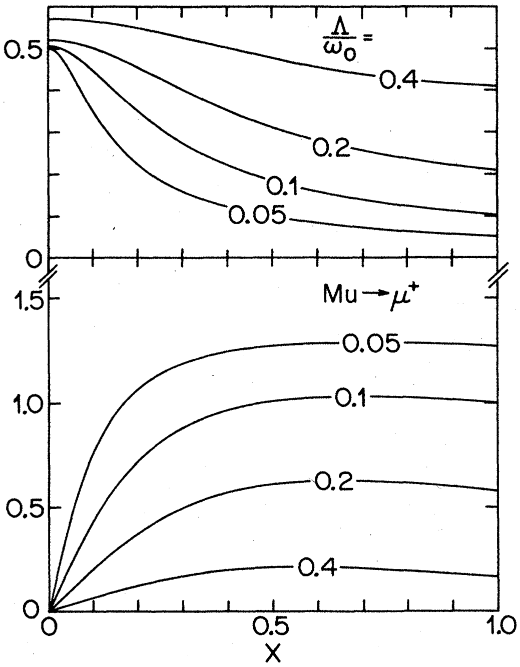

FIG. 19. The calculated amplitude and phase of the "residual" μ^+ signal after an irreversible Mu→μ^+ transition at the rate Λ, as a function of the reduced field x. This figure is a corrected version of Fig. 2 of Meier (1982).

$$p_z(\infty)=1-\left[\frac{\omega_0}{\Lambda}\right]^2\left[\frac{1}{2}+\frac{\nu}{\Lambda}\right]\times\left[\left[1+\frac{2\nu}{\Lambda}\right]^2+\left[\frac{\omega_0}{\Lambda}\right]^2\left[1+\frac{\nu}{\Lambda}+x^2\right]\right]^{-1} . \tag{2.54}$$

The reduced field x has been defined in Eq. (2.5). It should be noted that there are several errors in the expression corresponding to (2.52) in Schenck (1985). Figure 19 shows the amplitude and phase of the diamagnetic muon signal after an irreversible transition from isotropic Mu to a diamagnetic muon state in a transverse magnetic field (with $\nu=0$).

A more complex situation arises when the final state is paramagnetic. An example is the trapping of mobile muonium (state I) at a defect site to form a muonium defect state (state II). As for repeated jumps, in this case it is important to specify whether or not the electron spin polarization is conserved. Such irreversible changes of muonium state have been treated by Percival and Fischer (1976) in chemical systems and by Meier (1982) in solid-state systems.

The expression for the muon polarization $\mathbf{p}(t)=\mathrm{Tr}[\rho(t)\boldsymbol{\sigma}]$ can easily be extended to account for a decaying probability of finding a muon in state I and a transition of the muon from state I to state II at a time t' distributed between time zero and time t:

$$\mathbf{p}(t)=\exp(-\Lambda t)\mathbf{p}_{\mathrm{I}}(t)+\Lambda\int_0^t \mathrm{Tr}[\rho^{\mathrm{II}}(t,t')\boldsymbol{\sigma}]\exp(-\Lambda t')dt' . \tag{2.55}$$

Here $\mathbf{p}_{\mathrm{I}}(t)$ is the muon polarization in an undisturbed muonium state I given in Eq. (2.15):

$$\mathbf{p}_{\mathrm{I}}(t)=\mathrm{Tr}[\exp(-i\mathcal{H}^{\mathrm{I}}t/\hbar)\rho(0)\exp(i\mathcal{H}^{\mathrm{I}}t/\hbar)\boldsymbol{\sigma}] , \tag{2.56}$$

and $\rho^{\mathrm{II}}(t,t')$ is the density matrix at time t for the muonium state II, assuming that a transition to this state occurred from state I at the time t':

$$\rho^{\mathrm{II}}(t,t')=\exp[-i\mathcal{H}^{\mathrm{II}}(t-t')/\hbar]\rho^{\mathrm{II}}(t')\times\exp[i\mathcal{H}^{\mathrm{II}}(t-t')/\hbar] . \tag{2.57}$$

The spin Hamiltonians for states I and II are denoted by $\mathcal{H}^{\mathrm{I}}$ and $\mathcal{H}^{\mathrm{II}}$, and since the electron and mixed polarizations are zero at time zero,

$$\rho(0)=\tfrac{1}{4}[1+\mathbf{p}(0)\cdot\boldsymbol{\sigma}] . \tag{2.58}$$

If the electron polarization is conserved during the irreversible change at time t', the density matrix $\rho^{\mathrm{II}}(t')$ is given by

$$\rho^{\mathrm{II}}(t')=\exp(-i\mathcal{H}^{\mathrm{I}}t'/\hbar)\rho(0)\exp(i\mathcal{H}^{\mathrm{I}}t'/\hbar)\quad(\mathbf{p}_e\ \text{kept}) . \tag{2.59}$$

If, on the other hand, the muon polarization is conserved at t', but the electron and the mixed polarizations are lost, the density matrix at the time of the transition has the form

$$\rho^{\mathrm{II}}(t')=\tfrac{1}{4}[1+\mathbf{p}_{\mathrm{I}}(t')\cdot\boldsymbol{\sigma}]\quad(\mathbf{p}_e\ \text{lost}) . \tag{2.60}$$

It is now a straightforward task to calculate the time-dependent muon polarization with and without conservation of the electron polarization along the lines of Eq. (2.16). Performing the integration over t' and ignoring the damped signals from state I, we find that the forward component of the muon polarization is given by

$$p_f(t)=\mathbf{p}(0)\cdot\mathbf{p}(t)=\Lambda\sum_{k,l,m,n}S^{klmn}\left[\frac{\Lambda-i(\omega_{nm}^{\mathrm{I}}-\omega_{lk}^{\mathrm{II}})}{\Lambda^2+(\omega_{nm}^{\mathrm{I}}-\omega_{lk}^{\mathrm{II}})^2}\right]\exp(-i\omega_{lk}^{\mathrm{II}}t) , \tag{2.61}$$

where $\omega_{lk}^{\mathrm{II}}=(E_l^{\mathrm{II}}-E_k^{\mathrm{II}})/\hbar$ is a precession frequency of state II, and the factor S^{klmn} has the forms

$$S^{klmn}=\langle \mathrm{II},l\mid \mathrm{I},n\rangle\langle \mathrm{I},m\mid \mathrm{II},k\rangle T^{klmn}\quad(\mathbf{p}_e\ \text{kept}) \tag{2.62}$$

for conserved electron polarization and

$$S^{klmn}=\tfrac{1}{4}\sum_{i=1}^{3}\langle \mathrm{II},l\mid\sigma_i\mid \mathrm{II},k\rangle\times\langle \mathrm{I},m\mid\sigma_i\mid \mathrm{I},n\rangle T^{klmn}\quad(\mathbf{p}_e\ \text{lost}) \tag{2.63}$$

for nonconserved electron polarization. Here $\mid \mathrm{I},n\rangle$, for example, represents the nth energy eigenlevel of the muonium state I, and T^{klmn} is given by

$$T^{klmn}=\tfrac{1}{4}\langle \mathrm{I},n\mid\mathbf{p}(0)\cdot\boldsymbol{\sigma}\mid \mathrm{I},m\rangle\langle \mathrm{II},k\mid\mathbf{p}(0)\cdot\boldsymbol{\sigma}\mid \mathrm{II},l\rangle . \tag{2.64}$$

It is clear from the works of Percival and Fischer and of Meier that several of the most interesting examples of irreversible muonium changes of state can be treated as special cases of a transition from isotropic Mu (state I) to anisotropic Mu* (with $\theta=\pi/2$) (state II) in the transverse-field geometry. The corresponding expressions for the nonzero elements of S^{klmn} are given in Table VI for the cases of conservation and nonconservation of the electron polarization. The expressions for E_n^{I} and E_n^{II} and the eigenvector mixing angles ζ^{I}, ζ^{II}, and η^{II} are given in Table II.

Figure 20 shows the dependence of the Mu* amplitudes on magnetic field and transition rate Λ for an irreversible transition from isotropic Mu to anisotropic Mu* (with $\theta=\pi/2$) in diamond. At the top of the figure is a plot of the Mu and Mu* precession frequencies, showing the various crossings that occur between the Mu and Mu* frequencies. Due to the frequency-difference denominator in Eq. (2.61), one expects resonantly large Mu* amplitudes to occur at such crossings. The field-dependent Mu* amplitudes in the lower part of Fig. 20 demonstrate such resonance effects; a single-peaked structure occurs for electron polarization conservation, and a double-peaked structure occurs for nonconserva-

TABLE VI. The nonzero coefficients S^{klmn} defined in Eqs. (2.62) and (2.63) for the polarization transfer in a Mu→Mu* ($\theta=\pi/2$) transition.

For electron polarization *kept*

$$S^{1212}=S^{4343}=\tfrac{1}{4}\cos\zeta^{\mathrm{I}}\cos\eta^{\mathrm{II}}\cos(\zeta^{\mathrm{I}}-\zeta^{\mathrm{II}})\varphi_{-}c_{+}$$
$$S^{1214}=S^{4323}=\tfrac{1}{4}\sin\zeta^{\mathrm{I}}\cos\eta^{\mathrm{II}}\sin(\zeta^{\mathrm{I}}-\zeta^{\mathrm{II}})\varphi_{-}c_{+}$$
$$S^{1232}=S^{4341}=\tfrac{1}{4}\sin\zeta^{\mathrm{I}}\sin\eta^{\mathrm{II}}\cos(\zeta^{\mathrm{I}}-\zeta^{\mathrm{II}})\varphi_{+}c_{+}$$
$$S^{1234}=S^{4321}=-\tfrac{1}{4}\cos\zeta^{\mathrm{I}}\sin\eta^{\mathrm{II}}\sin(\zeta^{\mathrm{I}}-\zeta^{\mathrm{II}})\varphi_{+}c_{+}$$
$$S^{2321}=S^{1434}=-\tfrac{1}{4}\cos\zeta^{\mathrm{I}}\sin\eta^{\mathrm{II}}\cos(\zeta^{\mathrm{I}}-\zeta^{\mathrm{II}})\varphi_{+}s_{+}$$
$$S^{2323}=S^{1414}=\tfrac{1}{4}\sin\zeta^{\mathrm{I}}\cos\eta^{\mathrm{II}}\cos(\zeta^{\mathrm{I}}-\zeta^{\mathrm{II}})\varphi_{-}s_{+}$$
$$S^{2341}=S^{1432}=-\tfrac{1}{4}\sin\zeta^{\mathrm{I}}\sin\eta^{\mathrm{II}}\sin(\zeta^{\mathrm{I}}-\zeta^{\mathrm{II}})\varphi_{+}s_{+}$$
$$S^{2343}=S^{1412}=-\tfrac{1}{4}\cos\zeta^{\mathrm{I}}\cos\eta^{\mathrm{II}}\sin(\zeta^{\mathrm{I}}-\zeta^{\mathrm{II}})\varphi_{-}s_{+}$$
$$S^{lknm}=S^{klmn*}$$

For electron polarization *lost*

$$S^{1212}=S^{1243}=S^{4312}=S^{4343}=\tfrac{1}{8}\cos^2\zeta^{\mathrm{I}}\cos\zeta^{\mathrm{II}}\cos\eta^{\mathrm{II}}\varphi_{-}c_{+}$$
$$S^{1214}=S^{1223}=S^{4314}=S^{4323}=\tfrac{1}{8}\sin^2\zeta^{\mathrm{I}}\cos\zeta^{\mathrm{II}}\cos\eta^{\mathrm{II}}\varphi_{-}c_{+}$$
$$S^{1221}=S^{1234}=S^{4321}=S^{4334}=\tfrac{1}{8}\cos^2\zeta^{\mathrm{I}}\sin\zeta^{\mathrm{II}}\sin\eta^{\mathrm{II}}\varphi_{+}c_{+}$$
$$S^{1232}=S^{1241}=S^{4332}=S^{4341}=\tfrac{1}{8}\sin^2\zeta^{\mathrm{I}}\sin\zeta^{\mathrm{II}}\sin\eta^{\mathrm{II}}\varphi_{+}c_{+}$$
$$S^{2312}=S^{2343}=S^{1412}=S^{1443}=\tfrac{1}{8}\cos^2\zeta^{\mathrm{I}}\sin\zeta^{\mathrm{II}}\cos\eta^{\mathrm{II}}\varphi_{-}s_{+}$$
$$S^{2314}=S^{2323}=S^{1414}=S^{1423}=\tfrac{1}{8}\sin^2\zeta^{\mathrm{I}}\sin\zeta^{\mathrm{II}}\cos\eta^{\mathrm{II}}\varphi_{-}s_{+}$$
$$S^{2321}=S^{2334}=S^{1421}=S^{1434}=-\tfrac{1}{8}\cos^2\zeta^{\mathrm{I}}\cos\zeta^{\mathrm{II}}\sin\eta^{\mathrm{II}}\varphi_{+}s_{+}$$
$$S^{2332}=S^{2341}=S^{1432}=S^{1441}=-\tfrac{1}{8}\sin^2\zeta^{\mathrm{I}}\cos\zeta^{\mathrm{II}}\sin\eta^{\mathrm{II}}\varphi_{+}s_{+}$$
$$S^{lknm}=S^{klmn*}$$

where

$$\varphi_{\pm}=\cos\varphi\pm i\sin\varphi$$
$$c_{\pm}=\cos(\zeta^{\mathrm{II}}-\eta^{\mathrm{II}})\cos\varphi\pm i\cos(\zeta^{\mathrm{II}}+\eta^{\mathrm{II}})\sin\varphi$$
$$s_{\pm}=\sin(\zeta^{\mathrm{II}}-\eta^{\mathrm{II}})\cos\varphi\pm i\sin(\zeta^{\mathrm{II}}+\eta^{\mathrm{II}})\sin\varphi$$

tion.

A treatment of irreversible changes in the muonium hyperfine interaction is also contained as a special case of the Celio theory for repeated jumps between muonium states discussed in the previous section. One simply defines different rates for jumps in different directions and sets one of them to zero. Indeed, in an extended Celio theory, one can treat very complex combinations of states and reversible or irreversible transitions among them, with varying degrees of electron polarization conservation, and including Nosov-Yakovleva-type electron relaxation effects. However, unless one is able to reduce the number of polarization components by considerations such as those discussed in Sec. II.B.1, the amount of computer time required can grow very large.

III. MUON MEASUREMENT TECHNIQUES

A. Muon production and decay

This section presents a brief description of the production of polarized muon beams and gives some of their specifications. For a more detailed discussion the reader is referred to the book of Schenck (1985).

Positive muons for μSR experiments are obtained from

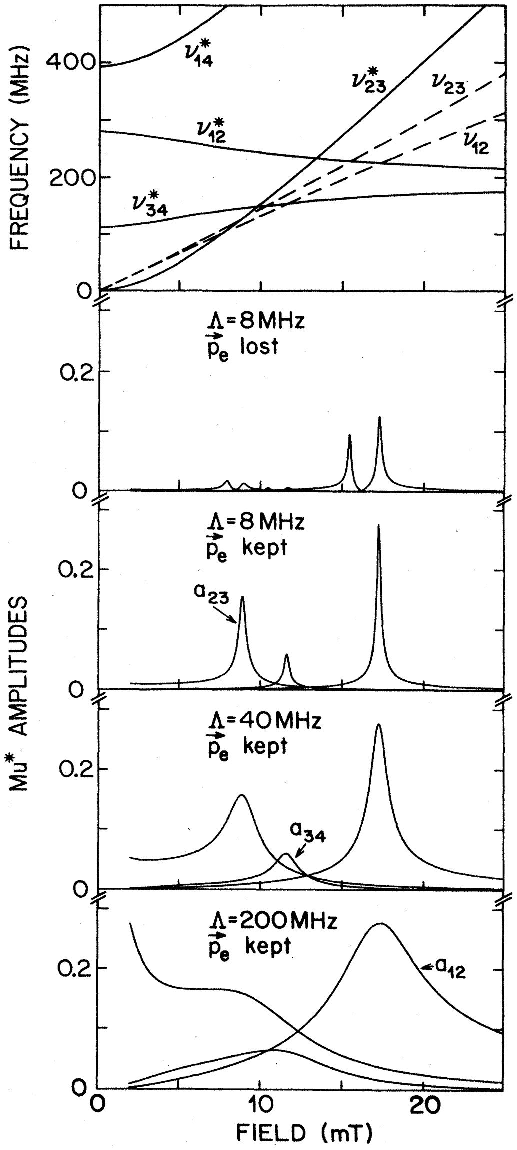

FIG. 20. The calculated Mu* ($\theta=\pi/2$) amplitudes following an irreversible Mu→Mu* transition in diamond. At the top of the figure, the Mu (dashed curves) and Mu* (solid curves) precession frequencies are shown. The transition produces double or single-peaked resonances at crossovers between Mu and Mu* frequencies, depending upon whether the electron polarization $\mathbf{p}_e$ is lost or conserved during the transition. This figure is a corrected and extended version of Fig. 4 of Meier (1982).

the decay of positive pions, which are in turn produced in the high-energy collisions of an accelerated proton beam with the nuclei in a "production target." The protons, with a typical energy of 600 MeV and an intensity between 1 and 1000 μA, produce positive pions via the two reactions

$$p+p \rightarrow p+n+\pi^+ , \quad p+n \rightarrow n+n+\pi^+ . \tag{3.1}$$

Pions that leave the production target with typically 150 MeV/c momentum are focused and momentum selected to form secondary beams with a momentum spread of 10% and an intensity of $10^5-10^8 \pi$/s. These pions pass a long, straight "decay section" of quadrupole magnets or a superconducting solenoid where they decay (with a rest-frame mean lifetime of 26 ns) to positive muons via the reaction

$$\pi^+ \rightarrow \mu^+ + \nu_\mu . \tag{3.2}$$

This decay is an example of a parity-violating weak interaction, the result being a neutrino with negative helicity and a muon which in the pion rest frame is 100% polarized antiparallel to the muon momentum. The (relativistic) transformation to the laboratory frame produces two groups of partially polarized muons: "forward" muons, whose momentum is higher than the pion momentum and whose polarization is antiparallel to direction of flight, and "backward" muons, with a lower momentum than that of the pions and a parallel polarization. After the decay section, a final momentum selection is made between these two groups, producing a polarized muon beam. Although of lower intensity than forward muons, backward muon beams have the advantages of lower pion contamination and higher polarization. A typical backward muon beam has a polarization of 80%, a momentum of 70 MeV/c, a momentum spread of 15%, a range width of 1 g cm^{-2}, a spot size of 20 cm^2, and an intensity of 10^4-10^7 μs^{-1}.

The "conventional" mode of muon production described above yields a high-momentum muon beam, which is used when samples of sufficient thickness are available and when the beam must penetrate significant material in front of the sample, or when a large transverse magnetic field is applied. An alternative mode of muon production is the "surface" muon beam. Here muons are used that arise from pion decay at rest near the surface of the production target. Such muons are 100% polarized and have a maximum momentum of 29.8 MeV/c, corresponding to a total range of approximately 140 mg cm^{-2}. A typical surface muon beam with a 10% momentum spread has an intensity of 10^5-10^8 μs^{-1} into a 10-cm^2 spot, with a range width of 10 mg cm^{-2}. A disadvantage of surface muons is the large positron contamination from pair creation by the photons from π^0 decay, but these positrons can be removed by a filter using crossed electric and magnetic fields. Such a velocity filter can also simultaneously rotate the muon polarization by 90° for high-transverse-field experiments.

The muon beam thus delivered to the experimenter passes through one or more plastic scintillation counters and typically a thermostat window before entering the sample. A discussion of the muon thermalization process in a semiconducting sample is given in Sec. IV.A. Regardless of the electromagnetic interactions experienced by the muon in the sample, it decays with a mean lifetime of 2.2 μs according to the scheme

$$\mu^+ \rightarrow e^+ + \nu_e + \bar{\nu}_\mu . \tag{3.3}$$

The energy of the decay positron lies between zero and a cutoff value of 52.3 MeV. The distribution rises gradually from zero and reaches a maximum at the cutoff. Muon decay also violates parity, with the result that positron emission occurs preferentially along the direction of the muon spin; the probability of emission at an angle θ with respect to the muon spin is given by

$$W(\theta)d\theta \propto (1+A_0 \cos\theta)d\theta , \tag{3.4}$$

where the asymmetry constant $A_0=\frac{1}{3}$, when averaged over the positron spectrum. The high-energy decay positrons exit from the sample and thermostat and are detected by additional scintillation counters. The experimentally determined asymmetry constant A_e differs from A_0 due to factors such as incomplete muon polarization, detector solid angle, and imperfect averaging over the positron spectrum.

The various muon spin rotation (μSR) techniques make use of the facts that the incoming muons are polarized and that the muon decay is anisotropic to follow the evolution of the muon polarization in the internal and applied magnetic fields experienced by the implanted muon. In the remainder of this section various experimental configurations are described that have been devised to study different aspects of this evolution.

B. The longitudinal-field technique

The first experiments to demonstrate the formation of Mu in solids were performed in a longitudinal magnetic field (Fig. 21). As discussed in Sec. II.A, in this case the muon polarization consists of a time-independent component $a_\parallel$ and a component a_{24} oscillating at the frequency ω_{24}. In zero applied field, where $\mathbf{F}=\mathbf{S}_\mu+\mathbf{S}_e$ is a good quantum number, the two components have equal strength: half of the Mu atoms are in the $m_F=+1$ stationary state, and half make transitions between the ($F=0$, $m_F=0$) and ($F=1$, $m_F=0$) states at the hyperfine frequency ω_0. In the high-field Paschen-Back region, Mu is in the $m_\mu, m_e=+\frac{1}{2},\pm\frac{1}{2}$ stationary states, and the muon retains its full polarization. The hyperfine interaction has been "quenched." Since the large frequency ω_{24} is generally not observed, what one sees in an experiment is the rise in the amplitude of the zero-frequency component from 50% at zero field to 100% at high field. This rise is shown in Fig. 22 and, after rewriting from Table IV, has the form

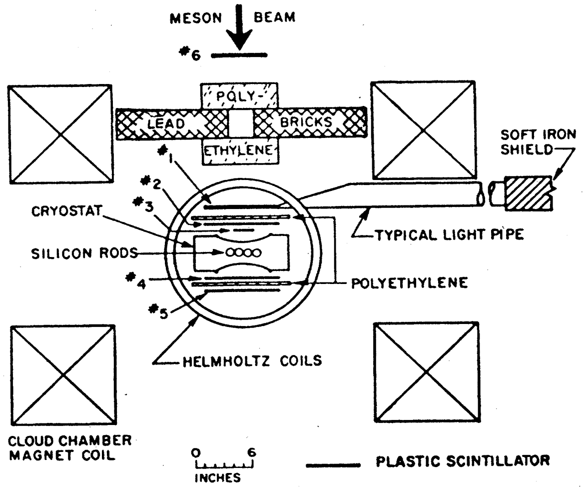

FIG. 21. Plan of a longitudinal-field μSR apparatus showing the detector telescopes for the incoming muon M (counters 1, 2, 3, and 6), the forward positrons F (counters 4 and 5), and the backward positrons R (counters 1 and 2). The longitudinal field is produced by the "cloud chamber magnet coils"' the Helmholtz coils provide a small transverse field. From Eisenstein *et al.* (1966).

$$a_{\parallel}=\tfrac{1}{2}[1+x^2/(1+x^2)] \ . \tag{3.5}$$

Mu quenching occurs when the electron Zeeman interaction greatly exceeds the hyperfine interaction. Hence measurement of a quenching curve allows a determination of the Mu hyperfine frequency and formation probability. In principle, anisotropic Mu* states can also be investigated in this way (see Fig. 22).

In the absence of spin relaxation, $a_{\parallel}$ is simply the time-averaged muon polarization, and a quenching curve can be rapidly measured by observing the average detection rates of muon-decay positrons emitted parallel (F) and antiparallel (R) to the initial muon polarization. It is generally necessary to calibrate the apparatus by measuring the corresponding rates F_s and R_s in a material (such as graphite or clean aluminum) where no Mu is formed and no muon depolarization occurs. For example, assuming Mu and diamagnetic muon fractions f_{Mu} and f_{μ^+},

$$f_{\mathrm{Mu}}a_{\parallel}(B_{\parallel})+f_{\mu^+} =(F-R)/(F+R)\times(F_s+R_s)/(F_s-R_s) \ . \tag{3.6}$$

Such a "time-integral" measurement of average counting rates avoids the necessity of following the time-dependent muon polarization and hence was used in the first determinations of the Mu parameters in Ge, Si, and α-SiC.

This type of measurement is presently experiencing a rebirth as a way of capitalizing on the extremely high muon fluxes now becoming available (see Secs. III.F and G). More accurate hyperfine parameter determinations are possible with the "time-differential" precession techniques to be described shortly. A time-differential approach is also required to follow the longitudinal spin relaxation of the muon.

In a time-differential experiment, repeated measurements are made of the time interval between the entrance of the muon into the sample (a pulse in detectors 1, 2, 3, and 6 in Fig. 21) and the detection of the decay positron in a particular direction (e.g., a pulse in detectors 4 and 5). These intervals are then collected into a "time histogram" $N_f(t)$, which has the form

$$N_f(t_j)=B+N_0\exp(-t_j/\tau_\mu)[1+A_e p_f(t_j)] \ ,$$
$$t_j=j\Delta t \quad (j=1,N) \ , \tag{3.7}$$

where B is a time-independent background, N_0 is a normalization constant, and N and Δt are the number and width of the time histogram bins. Assuming Mu and diamagnetic fractions and an exponential Mu relaxation, the forward component of the muon polarization $p_f(t)$ has the form

$$p_f(t)=f_{\mathrm{Mu}}\exp(-\lambda_{\parallel}t)a_{\parallel}+f_{\mu^+} \ . \tag{3.8}$$

The real value of the longitudinal-field technique is for Mu studies in the presence of static and dynamic random disturbances. An example of a static random disturbance is that arising from a nuclear hyperfine interaction (NHFI) of Mu with the magnetic moments of the host nuclei (see Sec. II.A.4).

The Nosov-Yakovleva theory treats the effects of a particular dynamic disturbance, namely, that represented by spin flips of the Mu electron on the Mu polarization, in both the longitudinal- and transverse-field geometries (see Sec. II.B.1). A comparison of the predicted relaxation rates for the two geometries (Figs. 13 and 16 and Table V) indicates an advantage of the longitudinal-field technique over the transverse-field technique for studying Mu relaxation: for the interesting case where the electron flip rate ν is less than the hyperfine frequency, the predicted longitudinal relaxation rate $\lambda_{\parallel}$ approaches zero in a sufficiently large applied field. This quenching of the longitudinal relaxation finds use in studies of dynamically

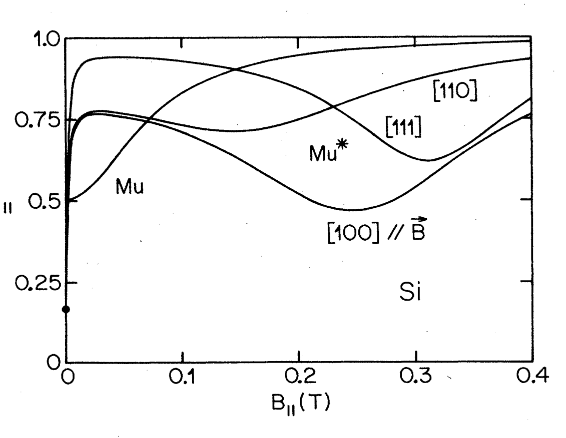

FIG. 22. Longitudinal-field quenching curves $a_{\parallel}(B_{\parallel})$ for isotropic Mu and Mu* in silicon. The results for Mu* are averaged over the four possible [111] symmetry axes.

perturbed muonium in semiconductors. Predictions of the Nosov-Yakovleva theory (but not of the Celio-Meier theory—see Fig. 17) for the transverse-field relaxation rates λ_{12} and λ_{23} are always greater than ν.

In Fig. 23, calculations using the Nosov-Yakovleva theory of the quenching of the longitudinal relaxation for Mu and Mu* in silicon are presented. For isotropic Mu, a single, damped contribution to $a_{\parallel}$ is predicted which quenches above a few hundred mT. The weaker hyperfine interaction of anisotropic Mu* would lead one to expect quenching to occur for this state at a much lower field than for Mu. However, the anisotropy of the hyperfine interaction produces two contributions (a and b) to $a_{\parallel}$ and the b component of the relaxation persists to higher fields than for Mu.

Another dynamic disturbance of muonium whose effects can to some degree be eliminated in the longitudinal-field geometry is the change in the muonium hyperfine interaction that occurs during a transition from a muonium state Mu^{I} to a state $\mathrm{Mu}^{\mathrm{II}}$. In a transverse field the states in general precess at different frequencies, and only for a sufficiently rapid transition is muon polarization transferred from I to II. In a longitudinal field, on the other hand, both states I and II have a (field-dependent) zero-frequency component $a_{\parallel}$ that can be coherently transferred. This effect has been used to study unstable muonium states in semiconductors.

C. The transverse-field technique

As shown in Sec. II.A.3, in a geometry where the muons are initially polarized perpendicular to the applied field, muonium precession occurs at the frequencies ω_{12}, ω_{23}, ω_{34}, and ω_{14} given by differences of the hyperfine energy levels. In the transverse-field technique (Fig. 24), a time-differential measurement of the muon polarization is performed, and the resulting time histogram [Eq. (3.7)] is modulated by these precession frequencies (see Fig. 25). The precession lines are best seen in a μSR frequency spectrum generated by the Fourier analysis of the time histogram (after correcting for the time-independent background, the normalization, and the muon decay):

$$a(\omega_k)=\frac{1}{A_e N}\sum_{j=0}^{N-1}\left[\frac{[N(t_j)-B]}{N_0}\exp(t_j/\tau_\mu)-1\right]\times\exp(-i\omega_k t_j)\,, \qquad (3.9)$$

$$\omega_k=\frac{2\pi k}{N\Delta t}\quad [k=-(N/2-1),N/2]\,.$$

The maximum frequency observable in such a spectrum

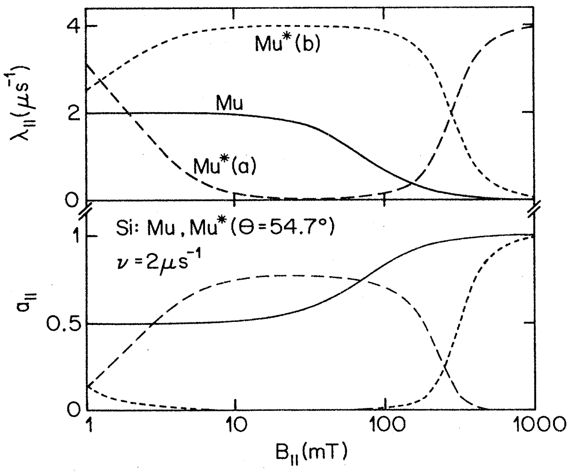

FIG. 23. Longitudinal-field relaxation rates and amplitudes fo Mu and Mu* in silicon calculated with the Nosov-Yakovleva theory with $\nu=2\ \mu s^{-1}$. The orientation of Mu* in the field is taken to be $\theta=54.7°$, corresponding to a [100]-oriented crystal. Note that there are two nonoscillating components, labeled (a) and (b), to the Mu* polarization.

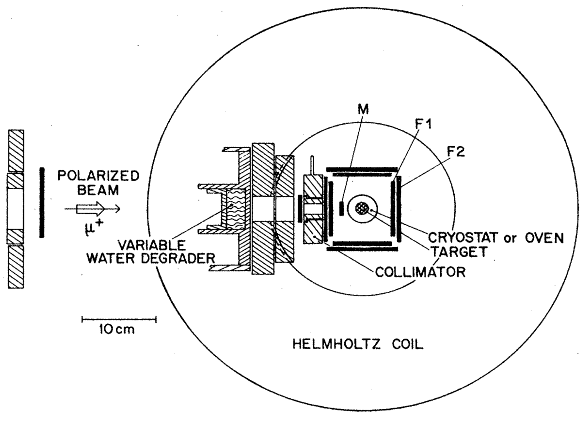

FIG. 24. Plan of a transverse-field μSR apparatus used (among others) by the Zurich group with conventional muons at the Swiss Institute for Nuclear Research.

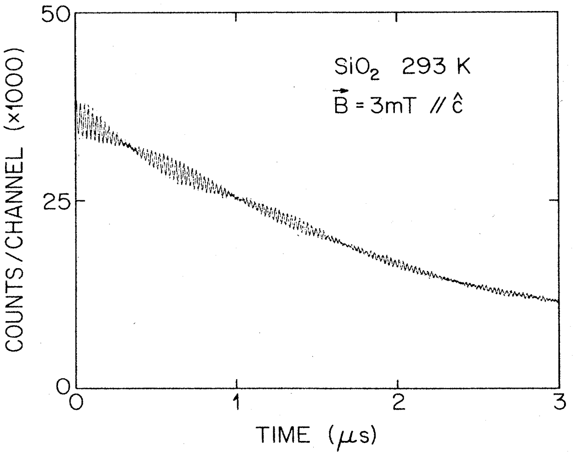

FIG. 25. A high-statistics transverse-field μSR time histogram taken by the Zurich group in a quartz crystal at room temperature. Note the beats that occur between the intermediate-field frequencies ν_{12} and ν_{23}. The smooth curve is a fit to the data.

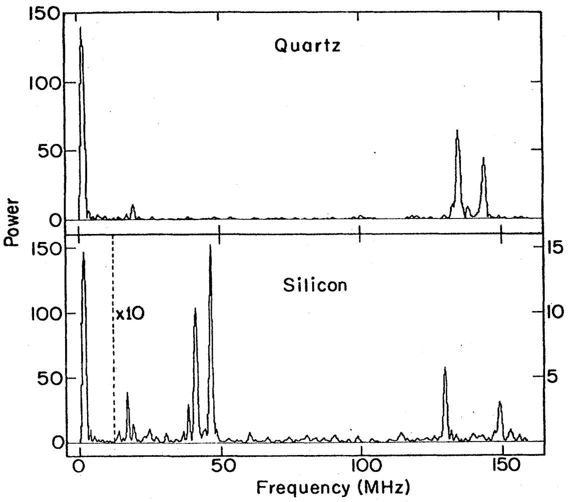

FIG. 26. Transverse-field μSR frequency spectra taken at 10 mT in quartz at room temperature and [111] Si at 77 K showing the precession components from diamagnetic μ^+ ($\nu_{\mu^+}=1.36$ MHz) and isotropic Mu (the pair ν_{12} and ν_{23} centered on 140 MHz). Note the larger Mu splitting in Si, indicating a weaker hyperfine interaction and the presence in Si but not in quartz of Mu* precession lines (ν_{12} and ν_{34}, $\theta=70.5°$, at 41 and 46 MHz). From Brewer *et al.* (1973).

is limited either by the histogram time channel width Δt or by the time resolution of the apparatus. The frequency resolution of the spectrum, on the other hand, is determined by the data collection time window $N\Delta t$ or by the muon lifetime. A comparison of μSR frequency spectra for quartz and Si is shown in Fig. 26.

The transverse-field technique avoids two important drawbacks of the longitudinal-field technique. First, it generally provides a more accurate determination of the muonium hyperfine parameters, since the systematic errors involved in a frequency measurement are smaller than those in an amplitude measurement. Second, the μSR frequency spectrum allows the individual identification and investigation of simultaneously occurring muonium states. This "μSR spectroscopy" has made the transverse-field technique by far the most practiced of the μSR techniques.

A technical problem that arises with all time-differential frequency measurements is the linearity of the time scale. Until recently, most μSR experiments made use of a time-to-amplitude converter (TAC) and an amplitude-to-digital converter (ADC) to digitize the time of a decay event. Such a combination typically has an integral nonlinearity of 10^{-3}, which must be accounted for during accurate measurements. This is normally done by calibrating with a quartz clock. The measured spectrum is then corrected according to a fitted polynomial which relates true time to channel number. The time resolution of digital clocks is steadily improving, however, and the TAC-ADC combination may soon be a thing of the past.

We consider the behavior of an unperturbed isotropic Mu state in a transverse field. An expression for the time-dependent muon polarization has been given in Eq. (2.16) and Table IV, which we rewrite here using a more convenient notation:

$$
\begin{aligned}
&p_f(t)=\sum a_{nm}\cos(\omega_{nm}t)\quad\text{(transverse field)}\,,\\
&\omega_{12}=+\frac{\omega_0}{2}+\omega_- -\frac{\omega_0}{2}\sqrt{1+x^2},\quad a_{12}=\tfrac{1}{4}\left[1+\frac{x}{\sqrt{1+x^2}}\right],\\
&\omega_{23}=-\frac{\omega_0}{2}+\omega_- +\frac{\omega_0}{2}\sqrt{1+x^2},\quad a_{23}=\tfrac{1}{4}\left[1-\frac{x}{\sqrt{1+x^2}}\right],\\
&\omega_{34}=+\frac{\omega_0}{2}-\omega_- +\frac{\omega_0}{2}\sqrt{1+x^2},\quad a_{34}=\tfrac{1}{4}\left[1+\frac{x}{\sqrt{1+x^2}}\right],\\
&\omega_{14}=+\frac{\omega_0}{2}+\omega_- +\frac{\omega_0}{2}\sqrt{1+x^2},\quad a_{14}=\tfrac{1}{4}\left[1-\frac{x}{\sqrt{1+x^2}}\right],\quad x=\frac{2\omega_+}{\omega_0}\,.
\end{aligned}
\tag{3.10}
$$

Precession frequencies of the order of the Mu hyperfine frequency ω_0 (typically 2–4 GHz $\times 2\pi$) are too large to be easily observed experimentally. It is standard practice, therefore, to use the transverse-field technique with "low" or "intermediate" applied fields. At low field (typically 1 mT) we neglect the terms x^2 in Eq. (3.10). This causes the two observable low-frequency lines ω_{12} and ω_{23} to coincide, and we obtain

$$p_f(t)\simeq\tfrac{1}{2}\cos(\omega_- t)\quad\text{(low field)}\,. \tag{3.11}$$

The observation of this strong line at 13.94 MHz/mT serves as a quick demonstration of the existence of Mu in the sample, but gives no information about the hyperfine frequency ω_0.

At somewhat higher fields in the intermediate-field region (typically 10–20 mT) we expand the square roots in

Eq. (3.10) to split the lines ω_{12} and ω_{23}:

$$p_f(t) \simeq \tfrac{1}{4}(1+x)\cos\left[\omega_- - \frac{\omega_+^2}{\omega_0}\right]t + \tfrac{1}{4}(1-x)\cos\left[\omega_- + \frac{\omega_+^2}{\omega_0}\right]t \quad \text{(intermediate field)} . \tag{3.12}$$

The hyperfine frequency is inversely proportional to the splitting of the two intratriplet precession lines. The hyperfine frequency $A=\omega_0/(2\pi)$ and the electronic g value can be determined (beyond the intermediate-field approximation) from the measured Mu frequencies and the diamagnetic muon frequency ν_μ according to

$$A=\frac{1}{2}\left[\frac{(\nu_{12}+\nu_{23}+2\nu_\mu)^2-(\nu_{23}-\nu_{12})^2}{\nu_{23}-\nu_{12}}\right] ,$$

$$g_e=-g_\mu\frac{m_e}{m_\mu}\left[\frac{\nu_{12}+\nu_{23}+\nu_\mu}{\nu_\mu}\right] . \tag{3.13}$$

This "two-frequency" technique of determining ω_0 is substantially more accurate than with longitudinal-field quenching. Although the relative accuracy of a frequency determination increases with increasing frequency, the weakening of the higher-frequency line together with the limited experimental time resolution (typically 2 ns full width at half maximum) places an upper limit on the field at which such an ω_0 determination can be made.

The concept of statistical noise, i.e., uncertainty arising from the finite number of muon-decay events recorded, is important in connection with the transverse-field technique, since it produces a white background in the Fourier transform in Eq. (3.9) (Brewer *et al.*, 1982; Burkhard *et al.*, 1984). From the uncorrelated Poisson statistics in the time channels t_i and t_j we have

$$\overline{N(t_i)N(t_j)}=\overline{N(t_i)}\,\overline{N(t_j)}+\delta_{i,j}\overline{N(t_i)} . \tag{3.14}$$

It is then a straightforward calculation to find the average power level in a Fourier spectrum of pure noise:

$$\bar{P}=\overline{|a(\text{noise})|^2} = \frac{\tau_\mu}{N^2A_e^2N_0\Delta t}[\exp(N\Delta t/\tau_\mu)-1] . \tag{3.15}$$

In the absence of a precession signal at ω_k, the successive partial sums in the expression for $a(\omega_k)$ [Eq. (3.9)] fall at points corresponding to a random walk in the complex $a(\omega)$ plane. The Nth partial sum gives $a(\omega_k)$, which thus scatters about the origin with a Gaussian distribution. The noise peaks in a Fourier power spectrum, therefore, have an exponential distribution:

$$W(P_k)=\frac{1}{\bar{P}}\exp(-P_k/\bar{P}) . \tag{3.16}$$

One can then define a "confidence level" $\text{CL}(P_k,N,\bar{P})$ of a Fourier peak with power P_k as the probability that none of the $N/2$ peaks in a Fourier power spectrum of pure noise with average noise power $\bar{P}$ exceeds P_k:

$$\text{CL}(P_k,N,\bar{P})=[1-\exp(-P_k/\bar{P})]^{N/2} . \tag{3.17}$$

Note that the expression for $\text{CL}(P_k,N,\bar{P})$ given by Brewer *et al.* (1982) is only valid for $P_k \ll \bar{P}$.

The analysis of a transverse-field μSR experiment involves a determination of the precession frequencies contained in the frequency spectrum, their amplitudes, their linewidths, and their initial phases. This determination can be made by least-squares fitting of the time histogram to Eq. (3.7) with $p_f(t)$ given by a sum of damped oscillations:

$$p_f(t)=\sum_j a_j\exp(-\lambda_j t)\cos(\omega_j t+\varphi_j) . \tag{3.18}$$

Alternatively, one may fit the isolated peaks in the experimental Fourier spectrum to the theoretical line shape for an exponentially damped oscillation:

$$\overline{a(\omega_k)}=\left[\frac{a_j\exp(i\varphi_j)}{2N\Delta t}\right]\frac{1-\exp[(i\omega_j-\lambda_j)N\Delta t]}{\lambda_j-i(\omega_j-\omega_k)} ,$$

$$\overline{|\Delta a(\omega_k)|^2}=\bar{P} . \tag{3.19}$$

Each type of fitting has its advantages and disadvantages. In Fourier space one need fit only the precession line of interest, but low, rapidly damped frequencies show up poorly in a Fourier spectrum, and one is limited in the choice of theoretical line shapes. In time space, low frequencies are less of a problem, and arbitrary lineshapes can be used, but a good χ^2 (and hence a reliable error estimate) is only achievable if all strong precession components (and any instrumental distortions) are fitted.

D. The zero-field technique

Certainly the most elegant experimental demonstration of Mu is the observation of the hyperfine oscillation in zero applied field at the frequency ω_0 (see Fig. 27). Because for isotropic Mu states this frequency is high (of the order of GHz), this "Mu heartbeat" can only be seen if special precautions are taken to optimize the timing resolution of the μSR apparatus (Holzschuh and Kündig, 1984). These include a small-diameter muon beam, fast scintillator material, short or nonexistent light guides, selected photomultiplier tubes and bases, low-loss signal cables, constant-fraction discriminators, and a temperature-stabilized environment for the sensitive electronics.

The effect of a Gaussian time-resolution function with full width at half maximum (FHWM) δt on a μSR precession line with frequency ν (Holzschuh, 1983) is an amplitude reduction:

$$a_{\text{obs}}/a=\exp[-(\pi\nu\delta t)^2/(4\ln 2)] . \tag{3.20}$$

The zero-field technique has been used to determine the

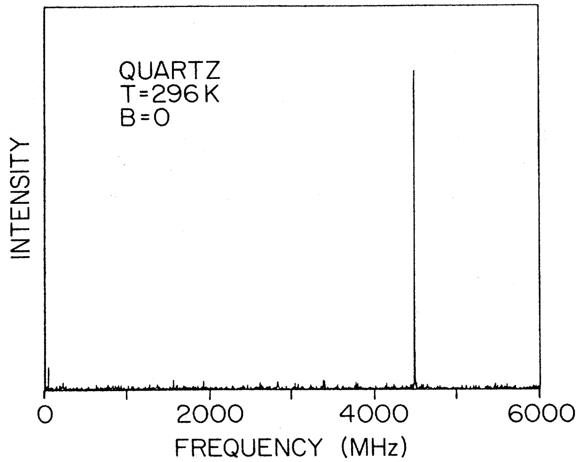

FIG. 27. A zero-field μSR spectrum of quartz at room temperature. The Mu hyperfine frequency is close to the vacuum value ($\omega_0 = 2\pi 4.463$ GHz). The FWHM time resolution is $\delta t = 110$ ps. From Holzschuh *et al.* (1981b).

temperature and pressure dependence of ω_0 for isotropic Mu in several semiconductors (Holzschuh, 1983). The observation of the direct hyperfine transition at several GHz in Si and Ge implies that the Mu state forms within 100 ps after implantation. The ability to observe very-high-frequency muon spin oscillations allows one to study Mu under conditions of rapid damping, since a large number of oscillations can still be seen before the signal disappears.

E. The high-transverse-field technique

The zero-field technique discussed above permits very accurate determinations of the Mu hyperfine frequency. However, Mu measurements at zero field are only possible when line broadening from the nuclear hyperfine interaction (NHFI) is small. This requires that there be few host nuclei with spin or that Mu be moving sufficiently rapidly to motionally average the NHFI to zero. The study of Mu in materials with a large concentration of nuclei with spin, e.g., type III-V and type I-VII semiconducting compounds, requires a different approach.

The NHFI of Mu is quenched in a sufficiently large applied field (of the order of 1 T). This quenching results in a narrowing of the transverse-field precession lines, but the precession frequencies are then of the order of GHz. In the high-transverse-field technique (Kiefl, Holzschuh *et al.*, 1984), a special low-fringe-field magnet and counters with high timing resolution are used to observe GHz Mu precession frequencies in applied fields of approximately 1 T. The low fringe field is required in order to allow the operation of the sensitive photomultiplier tubes with short light guides.

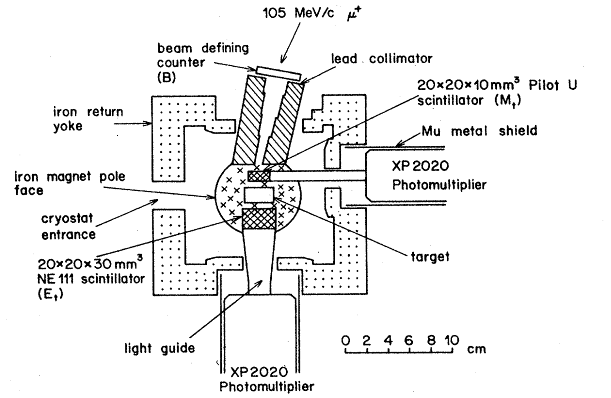

FIG. 28. A plan of the high-field, high-time resolution μSR apparatus. From Kiefl, Odermatt *et al.* (1986).

Figure 28 shows a plan of the high-field, high-timing-resolution μSR apparatus of the Zurich group. Note the massive iron return yoke, the magnetic shielding of the photomultiplier tubes, and the short light guides. The magnet has a 2.4-cm gap, a maximum field of 1.2 T, a homogeneity of 10^{-4} over a volume of 2 cm^3, and a fringe field at the photomultipliers (10 cm from the magnet center) of less than 0.01 mT. The FWHM time resolution of the apparatus is typically 220 ps.

A μSR frequency spectrum of GaAs taken with this apparatus is shown in Fig. 29. The sum of the two Mu precession frequencies

$$\nu_{12} + \nu_{34} = A = \omega_0/(2\pi) \tag{3.21}$$

is just the Mu hyperfine frequency. A simultaneous measurement of the free-muon precession frequency ν_μ yields the g factor for the Mu electron,

$$g_e = -g_\mu \frac{m_e}{m_\mu} \frac{2\nu_{12}\nu_{34} + (\nu_{34} - \nu_{12})\nu_\mu}{(\nu_{34} - \nu_{12} - 2\nu_\mu)\nu_\mu} . \tag{3.22}$$

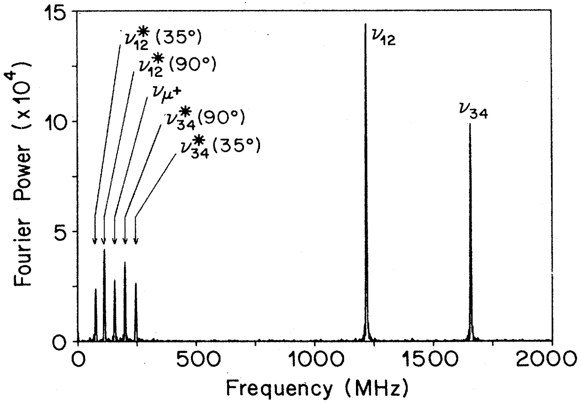

FIG. 29. A μSR frequency spectra taken with the high-field, high-time-resolution apparatus in high-resistivity GaAs at 10 K with a 1.15-T field applied along the [110] axis. Note the two Mu lines ν_{12} and ν_{34}, the Mu* lines $\nu^*_{ij}(\theta)$ (θ is the angle between the [111] Mu* symmetry axis and the applied field), and the diamagnetic muon line ν_{μ^+}. From Kiefl *et al.* (1985).

In order to avoid inhomogeneous broadening of the ν_{12} and ν_{34} Mu lines, it is advantageous to measure close to the "magic" field $B_{\text{mag}}=7.155B_0$ [Eq. (2.7)] at which these frequencies are to first order field independent.

The precession amplitudes of the ν_{12} and ν_{34} Mu signals should be equal (see Table IV). In Fig. 29, however, the higher-frequency Mu line is significantly weaker than the lower-frequency line. This is a result of the finite-time resolution of the apparatus, which causes a reduction of the observed amplitude described by Eq. (3.20). This effect can be used to determine the experimental time resolution:

$$\delta t\ (\text{FWHM})=2/\pi[\ln 2\ln(a_{12}/a_{34})/(\nu_{34}^2-\nu_{12}^2)]^{1/2}\ . \tag{3.23}$$

As with the zero-field technique, the high precession frequencies seen at high field allow Mu observations even under conditions of rapid damping. The real value of the high-field technique, however, is the quenching of the NHFI. In Sec. II.A.4 we saw how a NHFI produces a broadening of the μSR lines. In the high-field limit, the lines are approximately Gaussian, with second moments M_2 given by Eq. (2.22). Following Kiefl, Odermatt *et al.* (1986), we define a Gaussian linewidth σ:

$$\begin{aligned}\sigma=\left[\frac{M_2}{2}\right]^{1/2}&=\left[\frac{NS_n(S_n+1)}{6}\right]^{1/2}\Omega\sin^2\zeta\\ &=\left[\frac{NS_n(S_n+1)}{6}\right]^{1/2}\frac{\Omega}{2}\left[1-\frac{x}{\sqrt{1+x^2}}\right]\\ &\simeq\left[\frac{NS_n(S_n+1)}{6}\right]^{1/2}\frac{\Omega}{4x^2}\quad(x\gg 1)\ .\end{aligned} \tag{3.24}$$

The quenching effect of an applied field on the NHFI-broadened Mu precession lines is obvious from the B^{-2} dependence of σ.

For Mu at rest with respect to the nuclear spins, one thus expects a Gaussian relaxation of the precession frequencies of the form $\exp(-\sigma^2t^2)$. If, on the other hand, Mu is moving sufficiently rapidly with respect to the neighboring spins (Mu jump time $\tau_c\ll\sigma$), the broadening is "motionally narrowed," and an exponential damping $\exp(-\lambda t)$ results (Abragam, 1961) with the rate

$$\lambda=2\sigma^2\tau_c\ . \tag{3.25}$$

Note that the damping rate (λ) in the motional narrowing regime has a stronger field dependence than the rate (σ) in the static limit. Hence measurements of the field-dependent NHFI broadening at several temperatures can yield, in addition to the NHFI strength Ω, the Mu hopping rate $1/\tau_c$.

F. The avoided-level-crossing technique

It was shown in Sec. II.A.4 that muonium nuclear hyperfine energy states with equal z components of total spin angular momentum strongly mix with one another near the value of the applied field at which their energy levels show a first-order degeneracy. These "avoided level crossings" (ALC) produce pronounced minima in $a_{\parallel}(B_{\parallel})$, the nonprecessing component of the muon polarization in a longitudinal-field μSR experiment (Fig. 10). If the nuclear species and the hyperfine frequency A are known, a determination of the position of an avoided-level-crossing resonance is equivalent to a determination of Ω, the strength of the nuclear hyperfine interaction (NHFI). The NHFI strength is in turn related to the density of the muonium electron at the neighboring nuclear site and hence yields important information on the local structure of the muonium state.

The ALC resonances can in principle be observed using the standard time-differential μSR technique. In this case, one would look for polarization components oscillating at frequencies comparable to the ALC gap ω_G. However, these oscillations will in general be both weak and slow, requiring a careful experiment with low background and high statistics. A very elegant method for searching for the ALC resonances is to look instead for the decrease in the nonoscillating amplitude with the time-integral μSR technique (Kiefl, Kreitzman *et al.*, 1986). This avoids the necessity of following the muon polarization in time and hence of registering individual muons, thus allowing the experimenter to use the full muon beam intensity.

As in Sec. III.B we define the time-integral signal s as the normalized difference in the forward (F) and backward (R) positron detection rates:

$$s=\frac{F-R}{F+R}=\frac{A_e}{\tau_\mu}\int_0^\infty\exp(-t/\tau_\mu)p_f(t)dt\ . \tag{3.26}$$

With $p_f(t)$ given by Eq. (2.32) (i.e., in the absence of dynamic effects) we obtain

$$s=A_e\left[1-\frac{a\omega^2\tau_\mu^2}{1+\omega^2\tau_\mu^2}\right] \tag{3.27}$$

with the ALC amplitude a and frequency ω given in Eq. (2.32). Thus an ALC will produce a resonant dip in the time-integral signal s with an amplitude

$$1-s_{\min}/A_e=\tfrac{1}{4}(\omega_G^2\tau_\mu^2)/(1+\omega_G^2\tau_\mu^2) \tag{3.28}$$

and a FWHM $\Delta\omega_x=2(\omega_G^2+1/\tau_\mu^2)^{1/2}$. Note that a sufficiently weak NHFI will lead to a slow ALC oscillation frequency, making the resonant dip in s unobservable.

Measurements with the ALC resonance technique have been made to date on several muonic radical systems in liquids (Heming, Roduner *et al.*, 1986; Kiefl, Kreitzman *et al.*, 1986) and on the Mu* states in GaP and GaAs (Kiefl, Kreitzman *et al.*, 1986). Results for

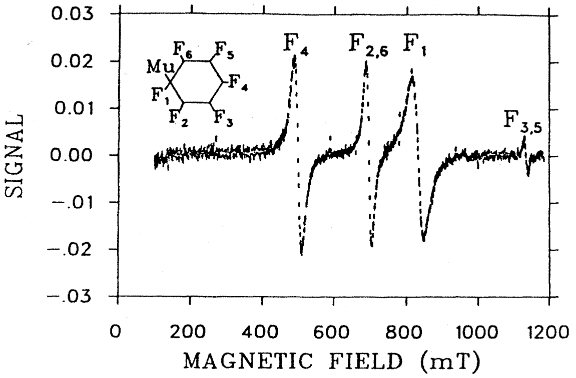

FIG. 30. The field derivative of the avoided-level-crossing signal from the muonic radical formed by adding Mu to the C_6F_6 molecule. The four dips are attributable to the four sets of equivalent fluorine spins. The hyperfine and nuclear hyperfine interactions are isotropic due to rotational averaging in the liquid state. From Kiefl, Kreitzman *et al.* (1986).

C_6F_6 are shown in Fig. 30.

We consider briefly the effects of muonium dynamics on the ALC signal (Heming, Roduner, and Patterson, 1986). By extending the treatment of Sec. II.B.1 to include the nuclear spins, one can investigate the effect of a Nosov-Yakovleva electron spin-flip rate ν on the ALC dip. For a single spin-$\frac{1}{2}$ nucleus, this implies a polarization vector analogous to Eq. (2.35) with 63 components. The numerical analysis of the resulting equations of motion leads to a time-dependent muon polarization of the form

$$p_f(t)=\sum_j a_j \exp(-\lambda_j t)\cos(\omega_j t) \tag{3.29}$$

and hence to a time-integral signal

$$s=\frac{A_e}{\tau_\mu}\sum_j a_j \frac{\lambda_j+1/\tau_\mu}{\omega_j^2+(\lambda_j+1/\tau_\mu)^2} \; . \tag{3.30}$$

Figure 31 shows the effect of an electron spin-flip rate ν on the time-integral signal in the vicinity of the ALC for vacuum Mu interacting with a single ^{19}F nucleus with an isotropic $A_n=\Omega/(2\pi)=500$ MHz. As the electron flip rate is increased from zero, the resonant dip increases in width and, aside from a small initial deepening, decreases in amplitude.

It is also interesting to consider the effect of an irreversible muonium change of state on the ALC resonance. Because the ALC technique is performed in a large longitudinal field where the muonium states are quenched, a large fraction of the muon polarization is stationary and hence will be coherently transferred from one state to the other. The only requirement for seeing an ALC dip is that the muon spend a significant fraction of its lifetime in the ALC resonant state, be it the precursor or the final state.

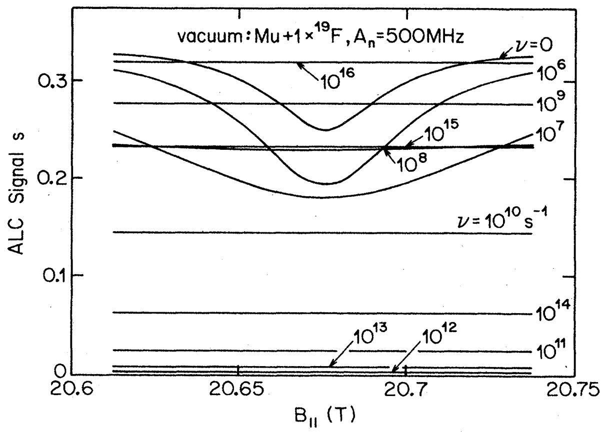

FIG. 31. The calculated effect of a Nosov-Yakovleva electron spin flip with rate ν on the avoided-level-crossing signal s. The system is vacuum Mu interacting with a single ^{19}F spin with an isotropic NHFI of strength 500 MHz, and the experimental asymmetry A_e is taken to be 1/3. The decrease and subsequent increase of the flat signal level at very high flip rates is a feature of the standard Nosov-Yakovleva model that occurs when ν becomes comparable to ω_e, the electron precession frequency.

G. Muon and muonium resonance techniques

Many experiments have been performed in which the time-dependent muon polarization is influenced by an applied oscillating magnetic field. Coffin *et al.* (1958) used the muon-decay asymmetry to detect the resonant absorption of radio-frequency (rf) energy in an early measurement of the muon magnetic moment. In this experiment a 12-kV ringing pulse was triggered upon detecting a stopped muon with a rate of 20 events/min. With a pulsed muon beam, this "muon spin resonance" technique becomes much more attractive and can be applied to the study of muons in solids (Kitaoka *et al.*, 1982), although the instantaneous rf power required is still high (20 kW).

An interesting variation of muon resonance by Nishiyama *et al.* (1985) allows the study of slow transitions from a muonium state to a diamagnetic muon state. In this "decoupling field muon spin resonance" technique, the muon polarization is held stationary during a time interval Δt in a longitudinal field sufficient to quench the precursor muonium state. At the end of this period, a 90°-rf pulse rotates the final-state diamagnetic muons perpendicular to the field. The amplitude of the subsequent muon precession is then measured as a function of the delay Δt to determine the transition rate of muonium to diamagnetic muons. This technique holds promise for several semiconducting systems in which a paramagnetic to diamagnetic transition occurs.

Due to the large magnetic moment of the bound electron, much less rf power is required if one performs a resonance experiment on *muonium* instead of the diamagnetic muon. Many muonium rf resonance experiments have been performed, generally in noble gases, with the aim of accurately determining the Mu hyperfine frequency as a test of quantum electrodynamics. Such measurements have used continuous microwave excitation in zero applied field (Thompson *et al.*, 1969), at the 1.13-T "Mu magic field" (Ehrlich *et al.*, 1972) where the interesting Mu hyperfine transition frequencies are field independent [see Eq. (2.7)] and with surface muons (Mariam *et al.*, 1982). A clever technique based on multiple microwave pulses has also been used in zero applied field (Favart *et al.*, 1971). All these Mu resonance techniques detect the resonance absorption with a time-integral counting measurement of the forward-backward muon-decay asymmetry.

It is also interesting to follow the *time dependence* of the muon polarization in a muonium resonance experiment. Basically one performs a time-differential μSR experiment of the type described in Secs. III.B or III.C, while at the same time applying rf or microwave radiation to the sample. This technique has been named "double electron muon resonance" or simply "DEMUR," and its first demonstration was on Mu in quartz (Brown *et al.*, 1983). In these experiments, a transverse field of 12.5 mT was applied, and an oscillating B_1 field perpendicular to both the static field and the initial muon polarization was applied at resonance with the observable μSR hyperfine transition ω_{12} or ω_{23}. Resulting frequency spectra are shown in Fig. 32.

The spectra in Fig. 32 demonstrate a general feature of DEMUR: if one drives a particular muonium hyperfine transition at resonance, the corresponding line in the μSR frequency spectrum is split into a triplet, while a μSR transition that shares a single energy level with the driven transition is split into a doublet. The general theory of DEMUR based on a perturbation treatment has been given by Estle and Vanderwater (1983). I present here an exact treatment due to Meier (1981) for the case of a circularly polarized B_1 field oscillating in the plane perpendicular to the applied field.

We begin with $\mathcal{H}_0$, the unperturbed spin Hamiltonian for Mu with a static magnetic field along the z direction [Eq. (2.2)]:

$$\mathcal{H}_0=\frac{\hbar\omega_0}{4}\sigma\cdot\tau-\frac{\hbar\omega_\mu}{2}\sigma_z+\frac{\hbar\omega_e}{2}\tau_z \ . \tag{3.31}$$

The energy eigenvalues and eigenvectors of $\mathcal{H}_0$ were given in Tables II and III:

$$\mathcal{H}_0\,|\,n\,\rangle=\hbar\omega_n\,|\,n\,\rangle \ . \tag{3.32}$$

We now add the effect of a circularly polarized magnetic field B_1 oscillating in the x-y plane with frequency ω:

$$\mathcal{H}_1(t)=\frac{\hbar}{2}[(\tilde{\omega}_e\tau_x-\tilde{\omega}_\mu\sigma_x)\cos(\omega t+\delta)+(\tilde{\omega}_e\tau_y-\tilde{\omega}_\mu\sigma_y)\sin(\omega t+\delta)] \ , \tag{3.33}$$

where

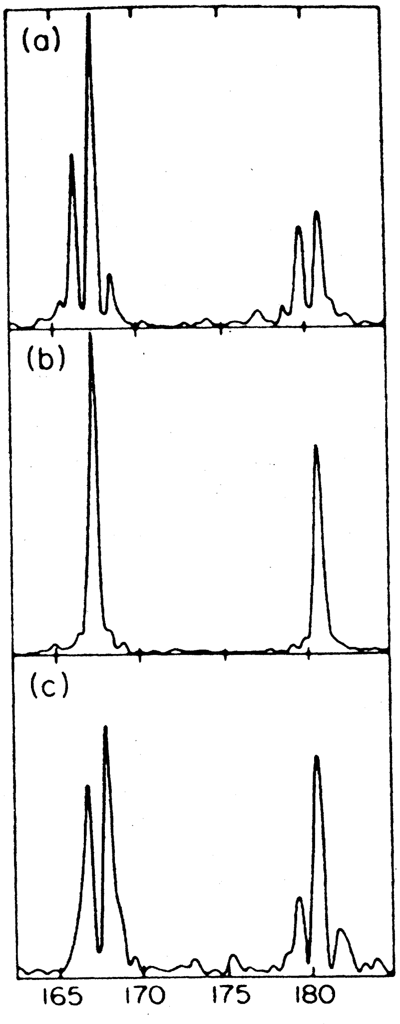

FIG. 32. Double electron muon resonance (DEMUR) spectra for Mu in quartz in a transverse field of 12.48 mT and a B_1 field of 0.1 mT. The rf field was applied (a) at 167.30 MHz near the ν_{12} transition, (b) at 173.90 MHz midway between the ν_{12} and ν_{23} transitions, and (c) at 180.51 MHz near the ν_{23} transition. From Brown *et al.* (1983).

$$\tilde{\omega}_\mu=g_\mu\mu_\mu B_1/\hbar, \quad \tilde{\omega}_e=-g_e\mu_B B_1/\hbar \ . \tag{3.34}$$

We now attempt to solve the time-dependent Schrödinger equation,

$$i\hbar\,|\,\dot{\psi}(t)\rangle=[\mathcal{H}_0+\mathcal{H}_1(t)]\,|\,\psi(t)\rangle \ , \tag{3.35}$$

with the Ansatz

$$|\,\psi(t)\rangle=\sum_j c_j(t)\,|\,j\,\rangle \ . \tag{3.36}$$

We thus obtain a set of coupled differential equations for the expansion coefficients $c_j(t)$:

$$i\dot{c}_j=\omega_j c_j+\frac{1}{\hbar}\sum_k\langle j\,|\mathcal{H}_1(t)\,|\,k\,\rangle c_k \ . \tag{3.37}$$

Now making the transformation suggested by Meier,

$$\begin{aligned} c_1(t)&=\exp(-i\omega t-i\delta)d_1(t)\ ,\\ c_2(t)&=d_2(t)\ ,\\ c_3(t)&=\exp(i\omega t+i\delta)d_3(t)\ ,\\ c_4(t)&=d_4(t)\ , \end{aligned} \tag{3.38}$$

we obtain a simpler set of equations for the coefficients $d_j(t)$:

$$i\dot{d}_j=\sum_k \mathcal{M}_{jk}d_k\ . \tag{3.39}$$

Here the time-independent matrix $\mathcal{M}$ has the form

$$\mathcal{M}=\begin{bmatrix} \omega_1-\omega & M_{12} & 0 & M_{14}\\ M_{12} & \omega_2 & M_{23} & 0\\ 0 & M_{23} & \omega_3+\omega & M_{43}\\ M_{14} & 0 & M_{43} & \omega_4 \end{bmatrix}\ , \tag{3.40}$$

where the elements M_{jk} are given by

$$\begin{aligned} M_{12}&=\tfrac{1}{2}(\tilde{\omega}_e\sin\zeta-\tilde{\omega}_\mu\cos\zeta)\ ,\\ M_{14}&=\tfrac{1}{2}(\tilde{\omega}_e\cos\zeta+\tilde{\omega}_\mu\sin\zeta)\ ,\\ M_{23}&=\tfrac{1}{2}(\tilde{\omega}_e\cos\zeta-\tilde{\omega}_\mu\sin\zeta)\ ,\\ M_{43}&=\tfrac{1}{2}(-\tilde{\omega}_e\sin\zeta-\tilde{\omega}_\mu\cos\zeta)\ , \end{aligned} \tag{3.41}$$

and ζ is the Mu mixing angle from Table II.

We proceed to diagonalize $\mathcal{M}$ (in general, numerically),

$$\sum_{k,l} U_{jk}^{-1}\mathcal{M}_{kl}U_{lm}=\delta_{j,m}\lambda_m\ , \tag{3.42}$$

whereby the time-dependent coefficients $d_j(t)$ are obtained:

$$d_j(t)=\sum_{k,l} U_{jk}\exp(-i\lambda_k t)U_{kl}^{-1}d_l(0)\ . \tag{3.43}$$

The muon polarization is computed from

$$\begin{aligned} \mathbf{p}(t)&=\mathrm{Tr}[\rho(t)\boldsymbol{\sigma}]\\ &=\sum_{n,m}\langle n\,|\rho(t)|\,m\rangle\langle m\,|\boldsymbol{\sigma}|\,n\rangle\ , \end{aligned} \tag{3.44}$$

and since the incoming muon binds spin-up and spin-down electrons with equal probability, we are dealing with a mixed state whose density matrix has the form

$$\rho(t)=\tfrac{1}{2}[\,|\psi^{\uparrow}(t)\rangle\langle\psi^{\uparrow}(t)|+|\psi^{\downarrow}(t)\rangle\langle\psi^{\downarrow}(t)|\,]\ . \tag{3.45}$$

We take as initial states (a) the muon spin along $+x$ and the electron spin along $+z$ and (b) the muon spin along $+x$ and the electron spin along $-z$:

$$\begin{aligned} |\psi^{\uparrow}(0)\rangle&=\frac{1}{\sqrt{2}}[\,|++\rangle+|-+\rangle]\ ,\\ |\psi^{\downarrow}(0)\rangle&=\frac{1}{\sqrt{2}}[\,|+-\rangle+|--\rangle]\ , \end{aligned} \tag{3.46}$$

thus

$$\begin{aligned} c^{\uparrow}(0)&=\frac{1}{\sqrt{2}}(1,\cos\zeta,0,-\sin\zeta)\ ,\\ c^{\downarrow}(0)&=\frac{1}{\sqrt{2}}(0,\sin\zeta,1,\cos\zeta)\ . \end{aligned} \tag{3.47}$$

It is now a straightforward task to transform the $c_j(0)$ to $d_j(0)$ for each initial electron state, to insert these into Eq. (3.43) to obtain $d_j(t)$, to transform back to the $c_j(t)$, and finally to evaluate $\mathbf{p}(t)$.

To illustrate this computation we investigate the case of Mu with DEMUR at the resonance $\omega=\omega_{12}$ in low applied field ($\omega_e\ll\omega_0$). We furthermore assume a weak B_1 field, implying a significant coupling by the perturbation only between the states $|1\rangle$ and $|2\rangle$. This example has been given by Patterson *et al.* (1981).

Our assumption of only 1,2 coupling implies that we can disregard the elements M_{14}, M_{23}, and M_{43} in the matrix (3.40). This makes it easy to diagonalize the matrix $\mathcal{M}$, and we find for the coefficients $c_j(t)$

$$c_j(t)=\exp(-i\omega_j t)\sum_k Q_{jk}(t)c_k(0),\quad Q(t)=\begin{bmatrix} \cos(\Delta\omega t) & -ie^{-i\delta}\sin(\Delta\omega t) & 0 & 0\\ -ie^{i\delta}\sin(\Delta\omega t) & \cos(\Delta\omega t) & 0 & 0\\ 0 & 0 & 1 & 0\\ 0 & 0 & 0 & 1 \end{bmatrix}\ , \tag{3.48}$$

where, since in low field $\sin\zeta\simeq\cos\zeta\simeq 2^{-1/2}$,

$$\Delta\omega=M_{12}=\frac{\tilde{\omega}_e-\tilde{\omega}_\mu}{\sqrt{8}}\ . \tag{3.49}$$

With the initial conditions

$$c^{\uparrow}(0)=\left[\frac{1}{\sqrt{2}},\frac{1}{2},0,-\frac{1}{2}\right],\quad c^{\downarrow}(0)=\left[0,\frac{1}{2},\frac{1}{\sqrt{2}},\frac{1}{2}\right]\ , \tag{3.50}$$

the forward component of the muon polarization becomes

$$p_f(t)=\tfrac{1}{8}[\cos(\omega_{12}t)+\cos(\omega_{12}t+2\delta)]+\tfrac{1}{16}\{\cos[(\omega_{12}+2\Delta\omega)t]+\cos[(\omega_{12}-2\Delta\omega)t]\}$$
$$+\tfrac{1}{16}\{\cos[(\omega_{12}+2\Delta\omega)t+2\delta]+\cos[(\omega_{12}-2\Delta\omega)t+2\delta]\}+\tfrac{1}{8}\{\cos[(\omega_{23}+\Delta\omega)t]+\cos[(\omega_{23}-\Delta\omega)t]\}\ . \qquad (3.51)$$

Here the polarization components oscillating at the high frequencies ω_{14} and ω_{34} have been omitted.

In their DEMUR experiment, Brown *et al.* did not maintain a particular phase relationship between the incoming muons and the rf field. Hence one should average over the phase δ, thus eliminating those terms with δ from Eq. (3.51). We are left with the five-line spectrum seen by Brown *et al.* for ω_{12} resonance [Fig. 32(a)]. Patterson *et al.* (1981) have performed an experiment in which the phase δ had definite values, resulting in the phase-dependent amplitudes of the ω_{12} satellites predicted by Eq. (3.51). Note that minor errors in the paper by Patterson *et al.* (1981) are corrected in the present Eq. (3.48).

The DEMUR technique has been applied to the study of the Mu* state in silicon (Blazey *et al.*, 1986b), and it is to be expected that this and the other resonance techniques will continue to yield information on muonium centers in semiconductors. This is particularly true for the time-integral resonance techniques, which place no limit on the incoming muon intensity.

H. The muon-decay-blocking technique

The muon-decay-blocking technique is distinct from the muon-spin-rotation techniques discussed until now in three important respects. First, it is based on the steering of the trajectory of the decay positron by the crystal lattice and not on the time evolution of the muon spin polarization. Muon-decay blocking would work equally well with unpolarized muons. Second, while the μSR techniques provide some degree of indirect information as to the muon site, e.g., from the symmetry of the muonium hyperfine interaction, the muon-decay-blocking technique yields *direct* information about the site of the muon in the host crystal. Third, the history of the muon's interaction with the crystal prior to its decay is important to preserving phase coherence in μSR but is irrelevant muon-decay blocking. The positron blocking pattern depends only on the position of the muon in the crystal at the instant of decay. A disadvantage of blocking or channeling techniques in general is that they are nonspectroscopic, that is, they do not differentiate between different electronic states. This drawback can to a large extent be removed for muon-decay blocking by conducting blocking and μSR experiments on the same sample under the same conditions. The muon-decay- (and pion-decay-) blocking techniques have been described by Patterson (1987). Conventional blocking and channeling techniques have been reviewed by Gemmel (1974).

In the muon-decay-blocking technique, the angular distribution of positrons from the decay of muons implanted in a crystal is measured with a high angular resolution. A positron traveling approximately parallel to an atomic row or plane in a crystal will undergo many correlated collisions with the positively charged ion cores, thus introducing characteristic features into the angular distribution. Along a crystal direction in which the site of the decaying muon is hidden by a crystal row or plane, the positron path is "blocked," and a minimum is observed in the distribution. Along a direction in which the muon site is open, the positron is "channeled," and a maximum is observed. Measurements of such dips and peaks along several axes and planes are compared with computer-simulated patterns to determine the site of the muon. This technique is identical in principle to those used to determine the site of β-emitting nuclei in crystals (Gemmel, 1974).

It is instructive to estimate the angular width of a typical feature in a muon-decay-blocking experiment. In his treatment of the classical channeling effect, Lindhard (1965) uses the "continuum" approximation to describe the potential seen by a positively charged particle traveling at a small angle to a crystal row. Since such a particle is deflected by correlated collisions with many ions of the host crystal, the continuum potential is constructed by averaging the particle-ion interaction energy along the direction of the row. Lindhard shows that if the kinetic energy of the particle's motion perpendicular to the row remains less than the critical value

$$V\simeq\frac{2Ze^2}{4\pi\varepsilon_0 d}\ , \qquad (3.52)$$

then the continuum approximation is valid. For larger transverse energies, the distance of closest approach between the particle and a host ion is so small that a large-angle collision will result and strongly deflect the particle from the channel direction. In the expression for V, Z is the atomic number of the host and d is the distance between neighboring ions along the row. We consider in the following discussion the two-dimensional problem of channeling between atomic planes, and we take the continuum potential to be harmonic with a maximum height V (see Fig. 33).

We follow the trajectory of a positron initially at the midpoint between the atomic planes and traveling with a velocity $\mathbf{v}$ at an angle ψ with respect to them. The perpendicular component of the velocity is

$$v_\perp=v\sin\psi\simeq v\psi\ . \qquad (3.53)$$

We now make a (relativistic) transformation to a frame of reference moving with the parallel component of the velocity. In this primed frame, the atomic spacing along the row is $d'=d/\gamma$ due to the Lorentz contraction, hence the primed critical transverse potential energy is γV. Furthermore, the time dilation implies a

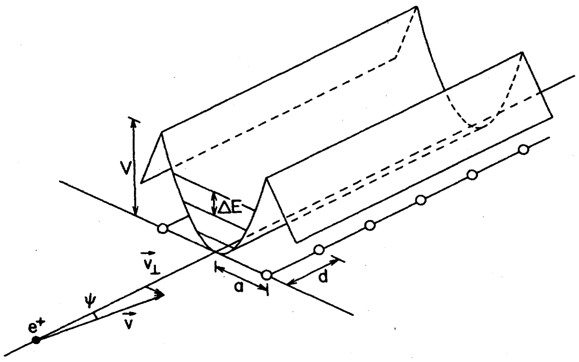

FIG. 33. A schematic diagram that defines the quantities used in the present discussion of planar channeling.

transformed transverse velocity $v'_\perp = \gamma v_\perp$. We assume the transverse motion to be nonrelativistic, and we obtain the critical angle for channeling by setting the transverse kinetic energy equal to γV:

$$\tfrac{1}{2} m v'^2_\perp = \tfrac{1}{2} m \gamma^2 v^2 \psi^2_{\rm cr} = \gamma V , \tag{3.54}$$

yielding

$$\psi_{\rm cr} = \left[\frac{2V}{m \gamma v^2} \right]^{1/2} . \tag{3.55}$$

For the example of a positron with the average energy of 37 MeV ($\gamma = 73$) moving along the (111) plane in silicon ($Z = 14$, $d = 1.57$ Å), $\psi_{\rm cr} \simeq 0.2°$. A muon-decay-channeling apparatus should have an angular resolution significantly better than this.

We have applied the *classical* channeling theory to the positron. To what extent is it valid to ignore the wavelike properties of the positron and the discreteness of the energy states in the continuum potential? In addition to its deflection, due to its wave nature, the positron will be diffracted by the crystal planes (with a separation of $2a$) at the Bragg angle:

$$\psi_B = \sin^{-1} \frac{\lambda}{4a} \simeq \frac{h}{4ap} = \frac{h}{4am\gamma v} . \tag{3.56}$$

Diffraction can be neglected if the critical angle is large compared to the Bragg angle, i.e., if

$$\frac{\psi_{\rm cr}}{\psi_B} = \frac{4a}{h} \sqrt{2m\gamma V} \gg 1 . \tag{3.57}$$

Under the assumption of a harmonic transverse potential, the bound positron states will be separated by an energy

$$\Delta E = \hbar\omega = \frac{\hbar}{a} \left[\frac{2V}{m\gamma} \right]^{1/2} . \tag{3.58}$$

The discreteness of these energy states can be ignored if there is a large number n of such bound states:

$$n = \frac{V}{\Delta E} = \frac{\pi a}{h} \sqrt{2m\gamma V} \gg 1 . \tag{3.59}$$

We thus see that

$$\frac{\psi_{\rm cr}}{\psi_B} = \frac{4}{\pi} n \tag{3.60}$$

and hence that the condition for ignoring diffraction is identical to that for ignoring quantum effects. For our example of a 37-MeV positron channeling along the (111) plane of silicon (with a taken equal to d), $n = 55$ and the conditions are well fulfilled. Note that without the relativistic mass increase γ, n would be 6, and the conditions would be only marginally met.

We have found the approximate width of the channeling peak arising from positron emission at the center of the harmonic planar valley in Fig. 33 to be $\psi_{\rm cr}$. The calculation of the *shape* of the channeling peak for this potential has been given by Patterson (1980) and is reproduced in the upper part of Fig. 34. As indicated, the channeling profile is the sum of a contribution from the bound particles, with a transverse kinetic energy less than V, and a contribution from particles with transverse energy greater than V. The lower part of Fig. 34 shows the blocking dip that occurs from positron emission at the top of the potential ridge in Fig. 33. More realistic forms for channeling peaks and blocking dips require a more realistic continuum potential, and, in practice, multiple scattering effects will round out the sharp features in Fig. 34. It is generally true, however, that channeling

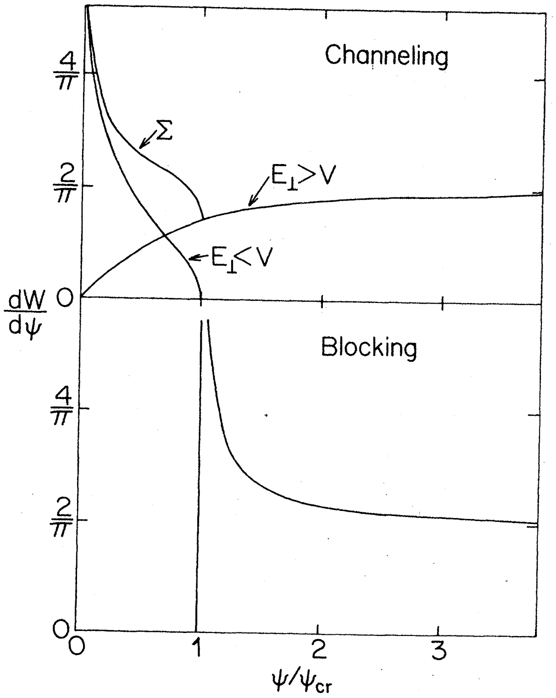

FIG. 34. Calculated differential particle detection probabilities for the case of a channeling peak (top) and blocking dip (bottom) for harmonic planar continuum potentials. From Patterson (1980).

peaks are narrower than blocking dips.

Muon-decay-channeling experiments have been performed on the semiconductors silicon (Patterson *et al.*, 1984a) and germanium. Such experiments require the following components: (1) an intense, low-energy muon beam, (2) a sample crystal of sufficient area with a mosaic spread significantly less than $\psi_{\rm cr}$, (3) an evacuated, magnetically shielded positron flight path, and (4) a high-resolution position-sensitive detector. We now discuss each of these components and how it has been realized.

An intense muon beam is required due to the necessity of obtaining a statistically meaningful number of positrons within the tiny critical solid angle in a reasonable length of time. Multiple scattering of the decay positron with electrons in the crystal will lead to dechanneling, and this limits the muon implantation depth from which blocking effects can be seen. A small implantation depth requires the use of surface muons (see Sec. III.A). In the experiments described below, $2\times10^{6}\ {\rm s}^{-1}$ surface muons were slowed down by degrader foils and implanted into a 3-inch silicon wafer to an average depth of 14 μm.

High-quality crystals are an obvious requirement of this technique. This presents no problem for the cases of silicon and germanium, which can be obtained as dislocation-free 5-inch-diameter ingots. Although much worse by comparison, many zincblende materials are presently available with sufficient quality over an area of 2 cm^{2}.

Scattering or deflection of the emitted decay positrons must be kept well below $\psi_{\rm cr}$. If cold, the sample must be free of condensed oil or water, and the positrons cannot pass a vacuum window or a detector while still in the vicinity of the sample. The flight path to the position-sensitive detector must be evacuated, shielded from the Earth's magnetic field, and sufficiently long to provide the required angular resolution. In the present experiments, the sample was at room temperature in a roughing vacuum that was continuous with a 3.4-m positron flight path. Magnetic shielding reduced the field felt by the positrons to less than 0.01 mT.

A reasonable position-sensitive detector for a muon-decay-channeling experiment is a multiwire proportional chamber (MWPC) or a drift chamber. The position resolution of a MWPC is of the order of the signal wire spacing, and that of a drift chamber is determined by the accuracy with which the arrival time of the drifting ions at a signal wire can be determined (typically 10 μm). In the present experiment, a MWPC was used with two perpendicular planes of 128 wires, each with a 2-mm wire separation.

Figure 35 shows the apparatus used in the present experiments. To avoid degrading the angular resolution by the finite sample size, the crystals were bent to the form of spherical caps whose center of curvature coincided with the center of the MWPC. For details of the apparatus and its performance the reader is referred to Patterson *et al.* (1984b).

Muon-decay-blocking patterns taken on high-purity float-zone silicon and on silicon containing 20 ppm interstitial oxygen (Czochralski) are shown in Fig. 36. Samples of each type of material cut perpendicular to the [110] and the [111] axes were investigated at room temperature. The intersecting bands of enhanced and diminished positron counting rates are the result of planar channeling and blocking by the indicated crystal planes. The axial effect can be seen at the intersection of the planar features. An interpretation of these features, and in particular their sensitivity to oxygen impurities, will be given in Sec. V.B. At this point the method of interpreting such muon-decay-blocking data to determine the muon site will be demonstrated using the Czochralski silicon data.

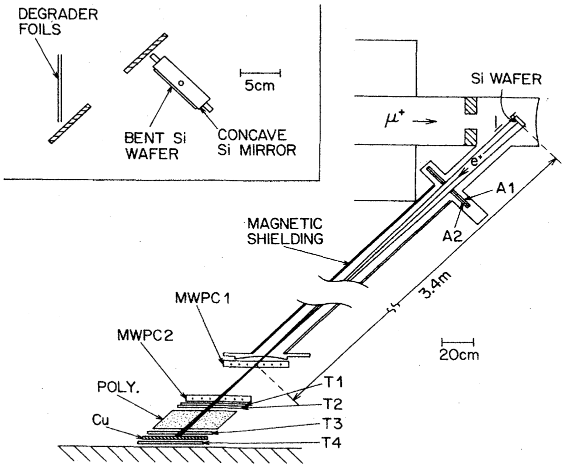

FIG. 35. A plan of the muon-decay-blocking apparatus used by Patterson *et al.* (1984a) showing the degrader foils, the bent sample wafer, the evacuated positron flight path, and the MWPC detectors.

The site analysis is performed by comparing the experimental planar and axial features with those calculated for various assumed muon sites until agreement is obtained. Instead of computing the direct process of positron emission, it is generally easier to treat the fictitious inverse process of positron injection. Lindhard's "rule of reversibility" (Lindhard, 1965; Patterson, 1980) states that the angular dependence of the probability that an *injected* positron of energy E *strikes* the muon is the same as the angular dependence of the probability of *detecting* an *emitted* positron of energy E. What follows is a nonrelativistic treatment. It can be made relativistic by replacing the kinetic energy E by the quantity $m\gamma v^{2}/2$.

The method used here is the so-called "analytic multirow continuum" method described by Picraux (1976). In this method, the multistring (multiplane) potential $U(x,y)$ $[U(x)]$ pertinent to the axis (plane) under consideration is first constructed by superposing individual string or plane continuum potentials in, for example, the Molière approximation (Molière, 1947; see Gemmel, 1974). Next a muon site is assumed, and its projected po-

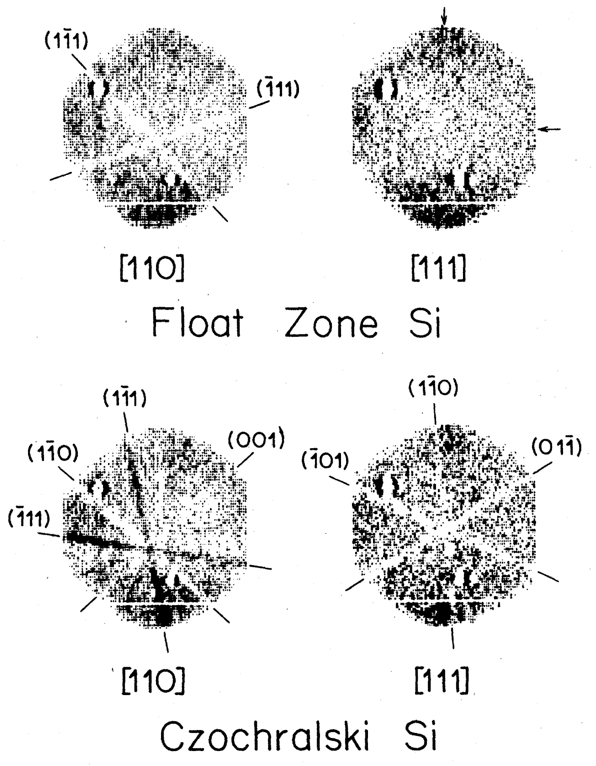

FIG. 36. Muon-decay-blocking patterns for high-purity (float-zone) and oxygen-doped (Czochralski) silicon samples. Dark and light features correspond, respectively, to enhanced and diminished positron detection probability. Each pattern spans an angular width of approximately 2.5°. The two localized areas of disturbed counting efficiency seen in the patterns were caused by dust on the MWPC wires. No blocking features were observed in the float-zone [111] sample; the arrows mark the known position of the [111] axis. From Patterson *et al.* (1984a).

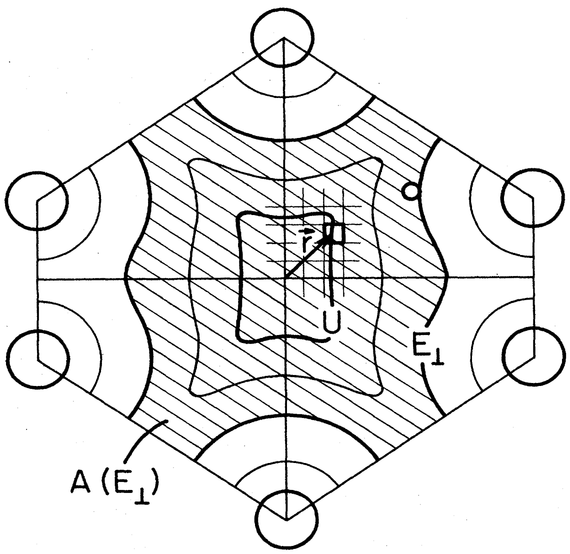

FIG. 37. A schematic multistring continuum potential for the [110] axis in silicon. The six large circles represent silicon-ion rows. The small circle represents the projected muon site $\mathbf{r}_\mu$, $\mathbf{r}$ is the assumed initial location of the injected positron [with potential energy $U(\mathbf{r})$ and traveling at an initial angle ψ with respect to the [110] axis], $E_\perp = U(\mathbf{r}) + E\psi^2$ is the total transverse energy of the injected positron, and $A(E_\perp)$ is the (crosshatched) area within the $E_\perp$ energy contour.

sition $\mathbf{r}_\mu$ in the potential is determined (e.g., the small open circle in Fig. 37).

Next the incident position $\mathbf{r}$ of the injected positron is assumed and the corresponding potential energy $U(\mathbf{r})$ is evaluated. The total transverse energy of the injected positron is found by assuming an initial injection angle ψ with respect to the string direction and summing

$$E_\perp = U(\mathbf{r}) + E\psi^2 \ . \tag{3.61}$$

The assumption is now made that sufficient transverse movement of the injected positron occurs on its way into the crystal that it uniformly samples the area of the channel that is energetically accessible. The probability that this positron will strike the muon is thus inversely proportional to the accessible area $A(E_\perp)$, hence the striking probability for this incident angle and this $\mathbf{r}_\mu$, averaged over all possible initial positron positions $\mathbf{r}$, is

$$\frac{dW(\mathbf{r}_\mu,\psi)}{d\psi} = \int \frac{d^2r}{A(E_\perp)} \tag{3.62}$$

with the condition

$$E_\perp \geq U(\mathbf{r}_\mu) \ . \tag{3.63}$$

This procedure is repeated for various values of ψ, and an average is taken over all the crystallographically equivalent sites for the muon.

Two details regarding the calculation of the blocking pattern should be noted. First, the Molière expression for the axial string continuum potential is infinite at the string itself (Molière, 1947; see Gemmel, 1974). This implies an infinitely wide blocking dip for a muon position located on such an axial string. To circumvent this problem in the present calculations, a cutoff distance from the string was assumed, within which the string potential was taken to be constant. For the Molière potential of silicon, the cutoff distance was determined to be 0.1 Å by requiring the width of the blocking dip to agree with that given by the empirical formulas of Barrett (see Gemmel, 1974). Second, the zero-point motion of the muon will cause a distribution of muon sites and thus influence the blocking pattern. One should account for this, for example, by performing an average over a Gaussian distribution of muon sites. Since this is costly, in the present calculation zero-point motion was accounted for by performing an average over the eight corners of a cube centered on the equilibrium muon site. It was found that the orientation of the cube had negligible importance. For the fit to the Czochralski data presented below, the edge length of this zero-point motion cube was taken to be 0.5 Å.

Figure 38 presents a comparison of experimental and theoretical blocking patterns for the Czochralski silicon data assuming that the muon is at the tetrahedral interstitial site. A displacement of the muon equilibrium position by 0.6 Å along the [111] axis is sufficient to worsen the agreement significantly.

A technique has also been developed to use the blocking of *muons* from positive *pion* decay to determine the site of the implanted pion (Sigle *et al.*, 1984). Since the pion is only 32% heavier than the muon, one would expect the two particles to behave similarly when implanted into a host. It should be kept in mind, however, that due to the 84 times shorter lifetime of the pion, a pion-decay-blocking experiment samples a different time scale than a muon-decay experiment. The absence of a pion spin unfortunately makes a comparison of pion-decay-blocking results with "πSR" impossible.

IV. THE STOPPED MUON AND ITS IMMEDIATE ENVIRONMENT

On a microscopic scale, muon implantation is a very violent process. This fact combined with the high mobility of the light muon and the short time scale of a μSR experiment implies that the quantities measured with μSR may to some extent reflect transient phenomena. This section addresses the question of the possible influence of the lattice defects and electronic excitation produced by the stopping muon on its subsequent behavior. The similarity of muonium and hydrogen (Table I) suggests that these two atoms will behave similarly in a solid host. Hence the large existing literature on hydrogen, in particular *implanted* hydrogen, in semiconductors is of interest to the μSR physicist. Much of this literature involves the interaction of hydrogen and lattice-ion vacancies, defects that are created during the muon and proton implantation.

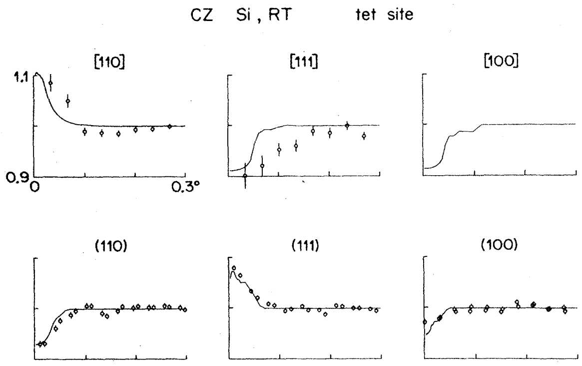

FIG. 38. A comparison of measured and calculated muon-decay-blocking patterns for Czochralski silicon under the assumption that the muon occupies the tetrahedral interstitial site and has a zero-point motion amplitude of 0.5 Å. The amplitudes of all the theoretical features have been reduced by a factor of 10, reflecting the importance of scattering of the positrons by electrons in the sample. The finite angular resolution of the apparatus (Patterson *et al.*, 1984a) has not been taken into account in this figure.

A. The muon stopping process

A general treatment of muon stopping in matter has been given by Brewer *et al.* (1975), and Fleming *et al.* (1982) have considered the problem by concentrating on processes in the gas phase. Here we consider the specific problem of muon stopping in a semiconductor.

The *accumulated* radiation damage caused by muon implantation and decay during a μSR experiment is negligible. For example, in a surface-muon μSR experiment in Si, 4-MeV muons with a typical dose of 2×10^9 cm^{-2} are implanted and allowed to decay to $\sim$40-MeV positrons. As will be seen, such a muon has a range of 0.07 cm and produces approximately 15 lattice defects. Data for the defect production rate by electrons (Cahn, 1959) indicate that a decay positron produces approximately two defects within the muon range. This implies a total defect concentration produced during an experiment of $\sim5\times10^{11}$ cm^{-3}. The mobility of Mu in semiconductors will be the subject of Sec. V.B, but even assuming Mu motion at the adiabatic limit for over-barrier motion, several hundred μs are required to find defects with this dilution.

As we shall see, the process of muon deceleration in solids lasts approximately 10 ps. This is sufficiently rapid on the time scale of a time-differential μSR experiment (given by the width of a time bin, typically 1 ns) to consider it instantaneous. It is also too rapid to allow any significant loss of the muon polarization during the stopping process. Polarization loss *does*, however, occur during muon stopping in gases, where thermalization is a much slower process (Fleming *et al.*, 1982).

Measurements of the (unchanneled) proton range in crystalline silicon have been performed by Ross and Terreault (1986) at energies down to 0.72 keV, and, using theoretical arguments supported by comparisons with such data, empirical models for the electronic and nuclear proton stopping power dE/dx have been constructed (Ziegler *et al.*, 1985). For the case of silicon, the formulas of Ziegler *et al.* show maxima in the electronic and nuclear proton stopping powers of 134 and 2.5 keV/μm occurring at proton energies of 80 and 0.4 keV, respectively, and maxima in the electronic and nuclear muon stopping powers of 134 and 0.29 keV/μm occurring at muon energies of 8 and 0.4 keV, respectively. Electronic stopping depends to a good approximation only on the *velocity* of the proton or muon and is much more important than nuclear stopping at all energies. In their book, Ziegler *et al.* provide a Monte Carlo FORTRAN program called TRIM85 that makes use of the electronic stopping power to simulate the implantation of an ion in a solid. Figure 39 demonstrates the agreement between the simulated proton range and range straggling in silicon with the measurements of Ross and Terreault.

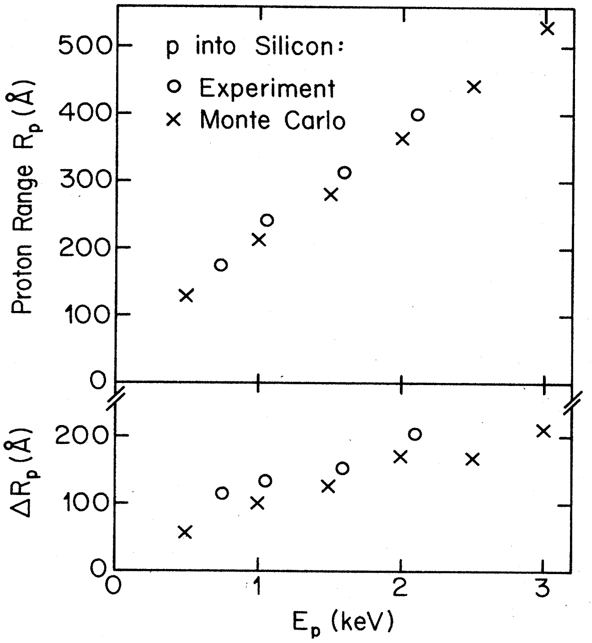

FIG. 39. The measured (circles) and simulated (crosses) proton range and its standard deviation in silicon as a function of E_p, the initial proton energy. The measurements are from Ross and Terreault (1986) on a crystalline sample, and the simulation was made by the present author using the TRIM85 program of Ziegler *et al.* (1985). For the simulation, a final energy of $0.001\times E_p$, a 0.05-eV minimum transferred energy in a nuclear scattering event, and a lattice-ion displacement energy E_d of 15 eV were assumed. Each point is an average over 100 simulations.

During the stopping process, a primary lattice-ion vacancy is produced by a nuclear scattering event for which the host-ion recoil energy exceeds the displacement energy E_d. Values of E_d for diamond, Si, and Ge of 50–80, 25, and 14 eV, respectively, have been determined experimentally (see Palmer, 1977). If the recoiling atom is of sufficient energy, it in turn creates secondary vacancies (Kinchin and Pease, 1955). Nuclear scatters with recoil energies below E_d result in energy loss by phonons.

Vacancy creation according to a modified Kinchin-Pease model is included in the TRIM85 program. I have used the program to investigate vacancy production by hydrogenlike ions in group-IV semiconductors. In each case, 500 implantations were simulated, and the average range of the particle, the average number of vacancies (primary plus secondary) produced per ion, and the average distance from the stopped implanted ion to the last created vacancy were calculated. The ion had an initial energy of 4 MeV (as do surface muons) and was assumed to be stopped when its energy fell below 4 keV. The displacement energy E_d was taken to be 15 eV in each case, and only nuclear scattering events with an energy transfer of at least 5 eV were considered.

If we accept the modeling for the proton by Ziegler *et al.* down to the 0.72-keV point measured by Ross and Terreault, then the TRIM85 simulation applies to muon energies down to 80 eV. The maximum fraction of the muon's energy that can be transferred in a collision with a host atom of mass M is

$$\Delta E_{\max}/E = 4m_\mu M/(m_\mu + M)^2 , \tag{4.1}$$

so barring "subthreshold" effects (Palmer, 1977) and assuming an E_d of 15 eV, a muon whose energy is below 960 eV can create no further vacancies in silicon.

The TRIM85 results are summarized in Table VII. (No significant change in the distance to the last vacancy formed by muons in silicon was found when the implantation was followed to a final energy of 5 eV and a minimum nuclear collision energy transfer of 0.05 eV was assumed.) Mean distances between the stopped muon and its last created vacancy of the same order of magnitude have been predicted in several metals by Brice (1978).

We can compute an effective *density* of self-created vacancies seen by a stopped muon in silicon by taking 24 μm as the radius of a spherical volume per vacancy. This yields approximately 2×10^7 cm^{-3}, a value more than 4 orders of magnitude smaller than the accumulated vacancy density. We conclude that the vacancies created by the muon during its own deceleration also play no role in a μSR experiment.

Further results of the simulation of 4 MeV muons into silicon with TRIM85 are presented in Fig. 40. The upper section shows a typical muon stopping track, and the lower two sections show the average distribution of phonon and electronic energy loss per implanted muon. Note that the total time for the muon to come to rest is approximately 12 ps, a result which is unchanged when the muon energy is followed down to 5 eV.

Measurements of the neutral fraction of protons passing through matter and theoretical studies of charge-changing processes in gases are cited by both Brewer *et al.* (1975) and Fleming *et al.* (1982) as evidence that the muon undergoes a rapid succession of electron captures and losses below 35 keV, the energy at which the muon velocity is comparable to that of the valence electrons of the host. The neutral charge state is believed to dominate as the energy decreases. It is thus remarkable that, in their analysis of low-velocity proton stopping

TABLE VII. Simulated results for implantation in semiconductors of protonlike particles with an initial kinetic energy of 4 MeV using the TRIM85 program of Ziegler *et al.* (1985).

Particle	Host	Mean range (μm)	Vacancies implanted ion	Mean distance to last vacancy (μm)
μ^+	Diamond	447	18.1	19.3
μ^+	Si	733	16.5	24.4
μ^+	Ge	406	20.0	9.7
p	Si	147	43.5	0.13
d	Si	94.2	68.1	0.020

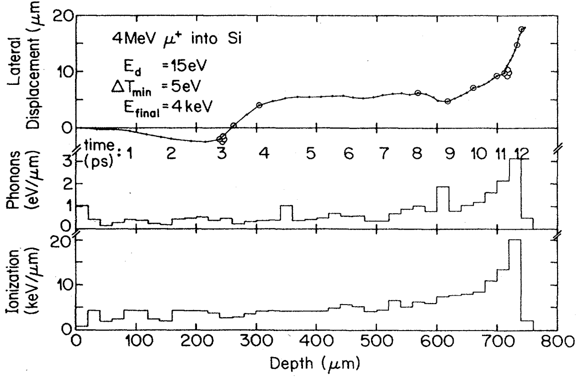

FIG. 40. Stimulated results of the stopping of 4-MeV muons in silicon using the TRIM85 program of Ziegler *et al.* (1985). A typical stopping track is shown in the top section. Dots represent nuclear scattering events with a transferred energy greater than 5 eV, and open circles represent primary and secondary lattice-ion vacancies. The center and lower sections show the average phonon and electronic energy-loss distributions for 500 implantations.

data down to 10 keV in silicon and down to 300 eV in carbon, Mann and Brandt (1981) find no evidence of an effective proton charge less than one. A proton of energy 300 eV has approximately the same velocity as a 35-eV muon.

Regardless of where one sets its upper energy limit, the final phase of the muon thermalization process in matter is the scene of a substantial amount of "radiation-induced" chemistry. The terms "hot-atom reactions" (Brewer *et al.*, 1975; Fleming *et al.*, 1982) and "spur model" (Arseneau *et al.*, 1984; Percival *et al.*, 1984) are used in the gaseous and liquid states, but no general theory exists for the solid state. One cannot attempt to explain the distribution of thermalized muons among the μ^+, Mu, and Mu* states in a semiconductor without microscopic models of these states. All that can be done at present is to point out several radiation-induced effects that may be relevant.

Can the implanted muon interact with the ionization from its own deceleration? Consider first the instant of stopping. A simulation with TRIM85 indicates that an 8-keV muon in silicon (at the peak of its electronic stopping power) that is followed to a final energy of 0.025 eV has a range of 0.06 μm and a stopping time of 0.12 ps. It loses only 20 eV to phonons, with the remainder going into electronic excitation and ionization. The mean energy lost by a charged particle per direct electron-hole pair creation event in silicon is estimated by Palmer (1977) to be 2 eV, implying that approximately seven electron-hole pairs (broken or weakened bonds) per Å of muon track are created at the stopped muon. According to Palmer, the primary electronic excitation is localized along the track to within the order of an atomic radius. Distributing seven electrons uniformly throughout a cylinder of radius 2 Å and length one Å yields an instantaneous electron density at the muon of the order of 5×10^{23} cm^{-3}, or approximately six times the conduction-electron density in copper. The *instantaneous* effects of the muon's ionization can thus be appreciable. Note that this electron density is also far in excess of that in an electron-hole liquid ($\sim3\times10^{17}$ cm^{-3}).

The motion of the electrons and holes will ultimately be governed by their diffusivity D, typically 40 cm^2 s^{-1} in room-temperature silicon (see Kittel, 1968). A diffusion equation for the electron density n has the form

$$dn/dt = D\nabla^2 n - n/\tau \ . \tag{4.2}$$

Assuming for the moment that the recombination rate $1/\tau$ may be neglected, we arrive at an expression for $n(r,t)$:

$$n(r,t) = N/(4\pi Dt)^{3/2}\exp[-r^2/(4Dt)] \ , \tag{4.3}$$

where N is the number of electrons produced at $r=0$ and $t=0$. As we shall see in Sec. V.G.1.b, a doping concentration of 5×10^{12} electrons cm^{-3} is required in order to produce a Mu* relaxation rate in silicon of 1 μs^{-1}. According to Eq. (4.3) with $N=4000$, the electron density at the muon ($r=0$) from ionization falls below 5×10^{12} cm^{-3} already within 2 ns after the muon stop. Since this is short compared to the electron-hole recombination lifetime in room-temperature silicon, $\tau\simeq20$ μs (Haynes and Hornbeck, 1953), we are justified in neglecting recombination.

Under these assumptions we conclude that the muon has no direct, persistent interaction with its ionization cloud on the time scale of a μSR experiment. This conclusion would be invalid if the muon were to remain in or near an electron-hole droplet. (A droplet with a density of $\sim3\times10^{17}$ electrons cm^{-3} containing 4000 electrons has a radius of 1500 Å.) Such drops in silicon at 4-K decay, both by electron-hole recombination and by thermionic emission of excitons, with a lifetime of approximately 150 ns (Hensel *et al.*, 1977).

The abundant supply of free electrons produced by ionization *can*, however, influence the initial charge state of the muon and that of any defect with which the muon may interact. The ionization may also influence the motion and even the type of lattice defects formed. The activation energy for vacancy migration in silicon is known to depend sensitively on the charge state of the vacancy (Watkins, 1975). There are also several possible mechanisms by which ionization can accelerate the motion of defects (see Palmer, 1977). The "Bourgoin" mechanism (Bourgoin and Corbett, 1975) is one such possibility that has been much discussed but not yet experimentally observed. It calls for a defect whose position in the lattice is a strong function of its charge state. Alternating changes of its charge state could then provide an athermal driving force for motion of the defect.

Palmer (1977) discusses the possibility that electronic excitation promotes defect production because of weakened bonds or the mutual repulsion of multiply ionized lattice ions. And it has been suggested by Pooley (1966) that in some alkali halides, lattice-ion vacancies (*F* centers) can be created by the nonradiative recombination of electron-hole pairs. It is believed (A. M. Stoneham, private communication) that this direct process is energetically unfeasible in the case of the group-IV semiconductors, but it may play a role in the large-gap II-VI compounds and the marginally stable cuprous halides. An intriguing possibility is that in the presence of a muon, electron-hole recombination could produce a lattice-ion vacancy even in a material like silicon. The muon could either be the supplier of the missing energy difference or, through its bonding to the lattice ions involved, it could lower the energy barrier of the vacancy formation process. An interesting observation in this respect is the subthreshold production of damage by electron irradiation in germanium containing hydrogen (Chen and MacKay, 1968).

How long does the muon require to truly thermalize? Nothing serious happens when we ask TRIM85 to follow the muon down to 0.025 eV, but the program was not designed to treat such low energies. It has been suggested by Emin (1981) that because of the muon's small mass, a reasonable picture of a thermalized positive muon in a solid is that of a self-trapped "small polaron." According to this model, an energy barrier must be overcome before a suitable local lattice distortion is established. This energy barrier could produce a significant "delay to self-trapping." The self-trapping process will be accelerated by the presence of impurities and lattice defects, but in a sufficiently perfect host the muon may not thermalize in its lifetime. A two-component model in which a fraction of the muons quickly self-trap at impurities while a non-self-trapped fraction continues to move ballistically has been proposed to explain the low, temperature-independent plateau in the muon spin-relaxation rate in very pure niobium (Hartmann *et al.*, 1983).

The initially disturbed environment of the implanted muon may also require a significant fraction of a muon lifetime to come to thermal equilibrium. In spite of their rapid dispersal, electrons and holes in silicon demonstrate this by their 20-μs recombination lifetime for the case of electronic excitations. A related process is the approach of various defect centers to the equilibrium distribution of charge states dictated by the position of the Fermi level. Finally, although a defect such as the silicon self-interstitial in a close Frenkel pair may nominally be mobile, it may still require a significant amount of time to move to its final position and annihilate the vacancy. Many of the phenomena important in μSR may involve metastable configurations far from equilibrium.

B. Lattice-ion vacancies and hydrogen in semiconductors

An energetic collision between an incoming implanted particle and a lattice-ion can eject the ion from its lattice site to produce a vacancy interstitial or Frenkel pair. Approximate rates of vacancy production for several protonlike particles were given in the last section. Unless the interstitial is trapped or otherwise immobilized, it may recombine with the vacancy. It is found that the production rate of stable vacancies in electron-irradiated silicon is dramatically increased by the presence of boron traps for the mobile interstitials (Watkins, 1975). Vacancies can exist in a variety of charge states; four different states have been identified for the vacancy in silicon (Watkins, 1975).

Above its "annealing" temperature, the vacancy is unstable, either because it becomes mobile and can move to the surface or form complexes with other defects or because the interstitial becomes free to recombine. The annealing behavior of vacancies and related defects in silicon and germanium is shown schematically in Figs. 41 and 42. Once free to migrate, the vacancy in impure silicon may trap at an impurity such as boron, phosphorus, or oxygen, and these complexes break up at still higher temperatures (300, 400, and 600 K for B, P, and O, respectively) (Corbett *et al.*, 1977). The annealing behavior of vacancies and vacancy complexes often proceeds at a rate described by an Arrhenius law. The measured annealing and reorientation rates for defects in silicon are shown in terms of process half-times in Fig. 43. The vacancy in diamond is stable to at least 700 °C (Loubser and van Wyk, 1978). Vacancies in compound semiconductors are less mobile than in elemental hosts because it is the next nearest neighbor that must jump into the vacancy in order for it to move (Watkins, 1973).

A large literature exists on hydrogen (and deuterium) impurities in semiconductors. Hydrogen is known to bind to phosphorus, boron (Johnson *et al.*, 1986), and oxygen (Johnson and Hahn, 1986) impurities in silicon, thereby "passivating" the otherwise electrically active donor or acceptor. It is believed that hydrogen may bind to an interstitial silicon atom in the silicon lattice (Kleinhenz *et al.*, 1979). Further, hydrogen in ultrapure germanium is known to form tunneling states around carbon and silicon impurities, in this case *activating* the impurities to acceptor states (Haller *et al.*, 1980).

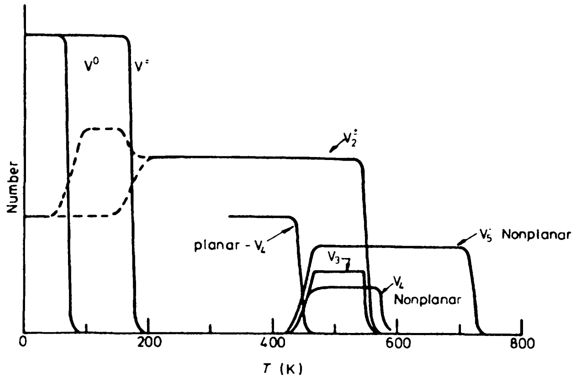

FIG. 41. The schematic annealing behavior of vacancies and vacancy clusters in silicon. From Corbett *et al.* (1977). The labels for the neutral vacancy and the doubly negative vacancy should be interchanged (Watkins, 1973).

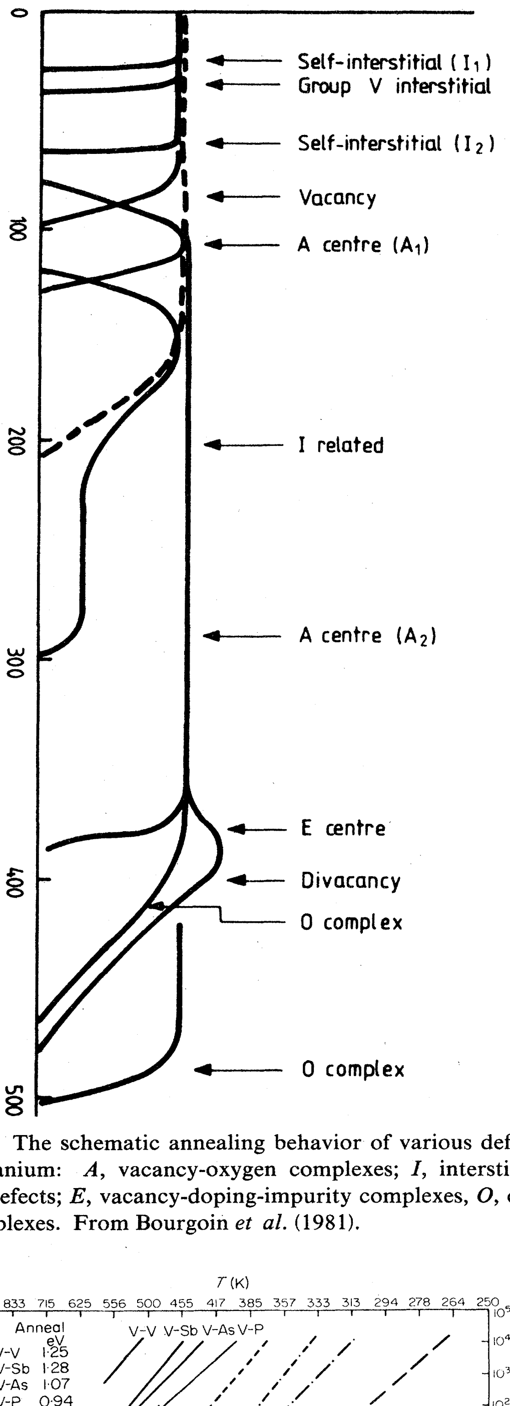

FIG. 42. The schematic annealing behavior of various defects in germanium: *A*, vacancy-oxygen complexes; *I*, interstitial-related defects; *E*, vacancy-doping-impurity complexes, *O*, oxygen complexes. From Bourgoin *et al.* (1981).

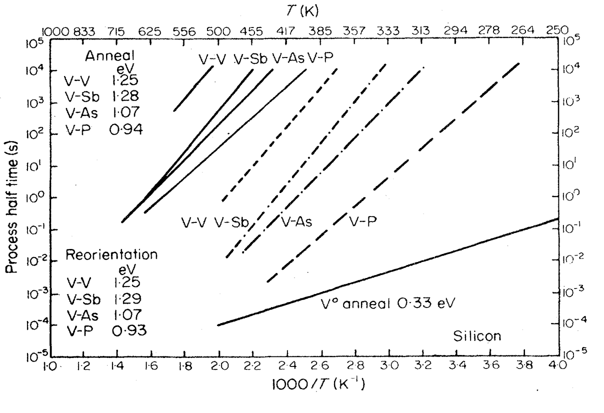

FIG. 43. Measured annealing and reorientation half-times for vacancy complexes in silicon. From Vook (1973).

But in the large majority of observations, hydrogen in semiconductors, particularly when implanted, is found to saturate one or more of the dangling bonds in a vacancy or an aggregate of vacancies. Hydrogen in such a configuration is not paramagnetic, implying that an alternate technique to electron paramagnetic resonance, such as infrared absorption, must be used for its study. Shi *et al.* (1982) have published theoretical predictions of the infrared absorption frequencies for 70 complexes of hydrogen with defects and impurities in silicon.

A number of infrared absorption bands are observed in proton-implanted silicon (typical dose 6×10^{15} protons cm^{-2} at 50–100 keV) that lie close to the Si-H stretch modes observed in the silane molecule (SiH_4) (Picraux *et al.*, 1979). These are attributed to various configurations of hydrogen atoms in vacancy clusters, an assignment that is supported by the fact that the bands show a partial annealing corresponding to the divacancy stage at 570 K. The bands anneal completely only above 1000 K.

Recently the sensitive "deep-level transient spectroscopy" (DLTS) technique has permitted the study of implanted silicon at a much lower dose (typically 10^{10} protons cm^{-2} at 300 keV; Irmscher *et al.*, 1984). The most interesting observation is of the so-called $E3'$ electron trap seen after proton implantation at 80 K. Irmscher *et al.* suggest that this defect is a single hydrogen atom at the vacancy of a close Frenkel pair, and they propose a charge-state effect to explain the different annealing temperatures seen in *n*- and *p*-type silicon (120 and 300 K, respectively).

The saturation of dangling bonds by hydrogen is also observed by infrared absorption in proton-implanted GaAs and GaP corresponding to Ga—H modes at As and P vacancies (Newman and Woodhead, 1980). The absorption in GaAs anneals out in the temperature region 200–250 °C. No absorption attributable to hydrogen was seen in InP. Similar experiments on the 6H polytype of SiC show a C—H mode from hydrogen at a Si vacancy which *increases* in strength upon raising the sample temperature to 800 °C (Choyke and Patrick, 1972). Infrared absorption in unimplanted type-I diamonds shows a C—H mode that is interpreted as hydrogen on the surface of a submicroscopic cavity or at a diamond-inclusion interface (Woods and Collins, 1983). Finally, Hall-effect and conductivity measurements have revealed the presence of a hydrogen-divacancy center in high-purity germanium (Haller *et al.*, 1977).

Two channeling experiments have been performed that directly determine the site of implanted deuterium in silicon using the $d(^3\mathrm{He},p)\,^4\mathrm{He}$ nuclear reaction. A room-temperature measurement with a high deuterium implantation dose (3×10^{15} cm^{-2} at 13 keV) yielded a deuterium site 1.6 Å from a silicon ion in the [111] antibonding direction (Picraux and Vook, 1978). A recent series of experiments, in which a milder dose of deuterium (8×10^{14} cm^{-2} at 10 keV) was implanted at 30 K, has determined the deuterium site as a function of annealing temperature (Nielsen, 1986). Here it is found that a fraction of the deuterium occupies the bond-center site and a fraction the tetrahedral interstitial site. In the temperature range 30–120 K the bond-center site is preferentially occupied, while in the range 140–400 K the tetrahedral site is preferred, and the bond-center site gains in importance again above 400 K. Nielsen suggests that the 120- and 400-K site changes are associated with the annealing of mono- and divacancies, respectively (see Fig. 42). Note that, as in the majority of implanted hydrogen and deuterium studies, there is severe radiation damage in the vicinity of the stopped deuteron; in the latter study the estimated peak implanted deuterium concentration is 0.05 atomic%, implying a 20-Å mean deuteron-deuteron distance. This is a tenth of the mean distance between a deuteron and the last vacancy it created (Table VII).

V. MUON EXPERIMENTS IN SEMICONDUCTORS —RESULTS AND DISCUSSION

A. Formation probabilities of muon states and their limits of stability

A μSR experiment on a semiconductor at low temperature typically shows the existence of three muon states: the diamagnetic or μ^+ state and the two paramagnetic states Mu and Mu*. Field- and orientation-dependent measurements of the various precession frequencies yield the symmetry and strength of the muonium hyperfine interactions. In general, some part of the muon polarization is unobserved, implying the formation of a collective "missing fraction." Careful experiments in which few muons stops in the sample holder and which include a calibration of the experimental muon-decay asymmetry (e.g., by measuring a copper sample in the same experimental geometry) allow a quantitative determination of the fractions of muons initially in each muon state.

Temperature-dependent measurements yield the limits of stability of the states. Here transitions from one muon state to another are often observed; a transition from a state I to a state II is characterized by an increase in the relaxation rate of state I with increasing temperature, followed by an increase in the amplitude of state II by the amount lost with the disappearance of state I. After these basic properties have been determined, more specialized experiments can be designed to further elucidate the nature of the various states and their relationship to one another.

Results of the low-temperature formation probabilities of muon states in the diamond and zincblende-structure semiconductors studied to date are listed in Table VIII.

TABLE VIII. Fractions of incoming muons forming the various muon states in undoped diamond and zincblende semiconductors at low temperatures.

Sample	f_{μ^+} (%)	f_{Mu^*} (%)	f_{Mu} (%)	f_{missing} (%)
Diamond	8.1 (3.0)	22.7 (8)	68.9 (1.0)	0.3 (3.3)
Si	7.5 (4)	36.8 (1.8)	61.0 (7.6)	−5.3 (7.8)
Ge[a]	10 (2)	8 (4)	72 (10)	10 (11)
β—SiC[b]	65 (12)		30 (5)	5 (19)
α—Sn[c]	~100			
GaP[d]	11 (1)	18 (3)	72 (10)	−1 (11)
GaAs[d]	9 (1)	35 (5)	63 (6)	−7 (8)
GaSb[e]	56 (1)			44 (1)
InP[e]	75 (3)			25 (3)
InAs[e]	106 (2)			−6 (2)
InSb[e]	72 (2)			28 (2)
ZnS	20 (1)		19 (3)	61 (3)
ZnSe	36 (1)		11 (2)	53 (2)
CdS	92 (3)			8 (3)
CdTe	69 (2)			36 (2)
CuCl[f]	16 (4)		66 (3)$^{\mathrm{I}}$	
			9.9 (8)$^{\mathrm{II}}$	8 (5)
CuBr[f]	23 (4)		66 (5)$^{\mathrm{I}}$	
			5.8 (8)$^{\mathrm{II}}$	5 (6)
CuI[f]	18 (8)		72 (3)	10 (9)

[a] Döring *et al.* (1984).
[b] Patterson *et al.* (1986).
[c] Andrianov *et al.* (1978b).
[d] Kiefl *et al.* (1985).
[e] Schneider (1984).
[f] Kiefl, Odermatt *et al.* (1986).

TABLE IX. Low-temperature hyperfine parameters for anisotropic Mu* ($A_{\parallel}, A_{\perp}$) and isotropic Mu (A) in diamond and zincblende semiconductors, the maximum temperatures of their observation, and observed transitions among the muon states. The hyperfine parameters for the III-V and II-VI compounds refer to 10 K, and the other values are extrapolations to 0 K. The hyperfine frequency of Mu in vacuum is 4463.302 88 (16) MHz (Mariam *et al.*, 1982).

Sample	$A_{\parallel}$ (MHz)^{a}	$A_{\perp}$ (MHz)^{a}	A (MHz)	$T^{\max}_{\mathrm{Mu}^*}$ (K)	$T^{\max}_{\mathrm{Mu}}$ (K)	Transitions
C	$+167.983$ (57)^{b}	-392.586 (55)^{b}	3711 (21)^{b}	$\geq 1000^{b}$	405^{c}	$\mathrm{Mu} \rightarrow \mathrm{Mu}^{*c}$
Si	16.819 (11)^{d}	92.59 (5)^{d}	2006.3 (2.0)^{e}	165	300^{f}	$\mathrm{Mu}^* \rightarrow \mu^{+g}$ $\mathrm{Mu} \rightarrow \mu^{+g}$
Ge	27.269 (13)^{d}	131.037 (34)^{d}	2359.5 (2)^{e}	85^{d}	120^{h}	$(\mathrm{Mu},\mathrm{Mu}^*) \rightarrow \mu^{+i}$
β—SiC					$\geq 22^{j}$	$\mu^+ \rightarrow \mathrm{Mu}?^{j}$
GaP	219.0 (2)^{k}	79.48 (7)^{k}	2914 (5)^{k}	100	240	
GaAs	217.8 (2)^{k}	87.74 (6)^{k}	2883.6 (3)^{k}	100	300	$\mathrm{Mu}^* \rightarrow \mu^+$
ZnS			3547.8 (3)		≥ 10	
ZnSe			3456.7 (3)		≥ 13	
CuCl			1334.23 (8)$^{\mathrm{I}\,l}$		60$^{\mathrm{I}\,l}$	$\mathrm{Mu}^{\mathrm{I}} \rightarrow \mathrm{Mu}^{\mathrm{III}\,l}$,
			1212.3 (1)$^{\mathrm{III}\,l}$		$\geq 300^{\mathrm{III}\,l}$	$\mathrm{Mu}^{\mathrm{II}} \rightarrow \mu^+$
CuBr			1403.66 (6)$^{\mathrm{I}\,l}$		153$^{\mathrm{I}\,l}$	$\mathrm{Mu}^{\mathrm{I}} \rightarrow \mathrm{Mu}^{\mathrm{III}\,l}$
			1250.9 (2)$^{\mathrm{III}\,l}$		$\geq 300^{\mathrm{III}\,l}$	
CuI			1670.9 (2)^{l}		102^{l}	

[a] Except for C, only the relative signs of $A_{\parallel}$ and $A_{\perp}$ are known.
[b] From Holzschuh *et al.* (1982).
[c] From Odermatt *et al.* (1986).
[d] From Blazey *et al.* (1983).
[e] From Holzschuh (1983).
[f] From Patterson, Holzschuh, Kiefl, Blazey, and Estle (1984).
[g] From Barsov *et al.* (1979).
[h] From Döring *et al.* (1983).
[i] From Kudinov *et al.* (1976).
[j] From Patterson *et al.* (1986).
[k] From Kiefl *et al.* (1985).
[l] From Kiefl, Odermatt *et al.* (1986).

For those materials in which muonium states have been observed, entries in Table IX give the low-temperature values of the hyperfine parameters of each state and the maximum temperature of its observation in the highest-purity sample studied. Also included in Table IX are the transitions between muon states that have been observed. Except for a few corrections, Tables VIII and IX are the same as those of Schneider *et al.* (1986).

The muon-state fractions given in Table VIII refer to $T < 30$ K, with the exception of diamond (300 K), silicon (μ^+ and Mu*: 110 K, Mu: 25 K), and α-Sn (77–300 K). The entries represent what in my opinion are the most reliable values. Other, often conflicting, values for diamond, silicon, and germanium have appeared in the literature. The diamond values in the table are from a type-IIa crystal (i.e., < 50 ppm N impurities). Holzschuh *et al.* (1982) give results in a IIa powder (grain size 1–6 μm) at 4.2 K: $f_{\mu^+} < 10\%$, $f_{\mathrm{Mu}^*} = 9.9$ (7)%, and $f_{\mathrm{Mu}} = 18.5$ (9)%. These are in good agreement with the 4.2-K results from a type-Ia (~ 0.1 at.% N) crystal (Holzschuh *et al.*, 1982). Spencer *et al.* (1984) measured a type-Ia crystal between 80 and 295 K and found $f_{\mathrm{Mu}} = 28$ (2)%.

The fractions for silicon given in the table are in approximate agreement with those cited for p- and n-doped samples at 78 K by Barsov *et al.* (1979, 1980). Clawson *et al.* (1981) could not detect a diamagnetic muon signal ($f_{\mu^+} < 0.003$) in an ultrapure silicon sample below 10 K with surface muons. The small value of $f_{\mathrm{Mu}} \simeq 12\%$ given by Boekema *et al.* (1981) and Boekema (1983) is probably due to the neglect of the amplitude reduction caused by a finite timing resolution [Eq. (3.20)], as are the small f_{Mu} values of Patterson, Kündig *et al.* (1978).

The diamagnetic and Mu fractions given by Kudinov *et al.* (1976) for n-type germanium (10^{14} cm^{-3} dopants) at 100 K are in approximate agreement with the values in Table VIII, but the fractions in an undoped germanium sample at 10 K found by Holzschuh *et al.* (1979) [$f_{\mu^+} = 10$ (5)%, $f_{\mathrm{Mu}^*} = 25$ (10)%, and $f_{\mathrm{Mu}} = 35$ (5)%] are not.

B. Site studies with blocking and channeling

As discussed in Sec. III.H the muon-decay-blocking technique is in principle capable of providing direct information about the muon's site at the time of its decay. To date, three semiconducting samples have been investigated at room temperature with this technique: Czochralski-grown silicon, float-zone silicon, and Czochralski-grown germanium.

The muon-decay-blocking results for [111] and [110] wafers of Czochralski and float-zone silicon (Patterson *et al.*, 1984a) are shown in Fig. 36, and as discussed in Sec. III.H, the Czochralski results indicate muon occupation of the tetrahedral interstitial site with zero-point motion of 0.5 Å amplitude. As we shall see, this site assignment differs from that in float-zone material. Since the principal difference between the two types of silicon is the 100 times larger oxygen content of the Czochralski material (10^{18} cm^{-3} versus 10^{16} cm^{-3}; Newman, 1982), we surmise that the tetrahedral site occupied by the muon is in the vicinity of an oxygen impurity. Evidence for the trapping of hydrogen at oxygen impurities in silicon has been found by Qi *et al.* (1985) and by Johnson and Hahn (1986).

Analysis of the sparse float-zone silicon data in Fig. 36 yields a different muon site (Patterson *et al.*, 1984a). If one assumes that the muon occupies a site with [111] symmetry, the data indicate a site 0.9 Å from a silicon-ion position in either the bonding or the antibonding direction. The Si—Si bond length in silicon is 2.35 Å, thus the data are marginally compatible with the bond-center site (1.18 Å from a silicon ion), as proposed by Cox and Symons (1986), Estle *et al.* (1986), and Claxton *et al.* (1986), and as found for implanted deuterium by Nielsen (1986). The Si—H bond length in the silane molecule (SiH_4) is 1.48 Å (note that $2.35-1.48\simeq0.9$). Since the blocking technique is unable to distinguish between occupied and unoccupied lattice-ion sites, the muon site could also be at the Si—H position 0.9 Å from a lattice-ion vacancy, as proposed by Sahoo *et al.* (1985) or 0.9 Å from a silicon-ion neighboring a vacancy, close to the site proposed by Singh *et al.* (1977). The muon-decay-blocking data in float-zone silicon are not compatible with the hexagonal interstitial site (Estle, 1981) or Picraux and Vook's "deuterium site" (Picraux and Vook, 1978; Rodriguez *et al.*, 1979; Patterson, 1984b), which are, respectively, 3.5 and 1.6 Å from a silicon ion in a [111] antibonding direction.

Muon-decay-blocking patterns taken at room temperature in [110], [111], and [100] Czochralski-grown germanium wafers are shown in Fig. 44. They show similarities to the Czochralski silicon data, presumably again due to tetrahedral muon trapping at an impurity such as oxygen. An analysis of these germanium data will be published at a later date.

The room-temperature site assignments made above are based on a single muon site. Although perhaps justified at room temperature, where all muonium μSR signals are rapidly damped and the muon most often decays in a (hopefully) unique daughter state, multiple sites will certainly play a role at lower temperature. There it will be necessary to correlate the temperature-dependent blocking patterns with the known formation probabilities and lifetimes of the muonium states observed with μSR. Reliable temperature-dependent muon-decay-blocking data do not yet exist. Temperature-dependent measurements on Czochralski silicon which showed a deterioration of the blocking signal at low temperatures (Patterson *et al.*, 1984b; Patterson, 1984b) are believed to have been plagued by condensation of volatiles on the sample surface. It is nonetheless interesting to compare the room-temperature blocking patterns observed in the semiconductors with low-temperature μSR spectra taken on the same samples. Such a comparison is shown in Fig. 45, together with μSR spectra from a high-purity germanium sample. The applied fields for the μSR spectra were chosen to optimize the visibility of the Mu and Mu* signals. Although all samples show the familiar Mu* signals, a strong reduction in the Mu signal strength is seen in the Czochralski samples. Also noteworthy is the lack of a diamagnetic μ^+ signal in Czochralski silicon (see Sec. V.G.1.b).

As mentioned in Sec. III.H a technique related to muon-decay blocking but based on positive pion decay to a muon has been developed to investigate the *pion* site in crystals. One would expect the pion- and muon-decay experiments to yield very similar results, but there is unfortunately as yet no direct overlap between the two techniques where a comparison can be made. Most pion-decay-blocking experiments have been performed in metals, but several results in high-purity germanium and

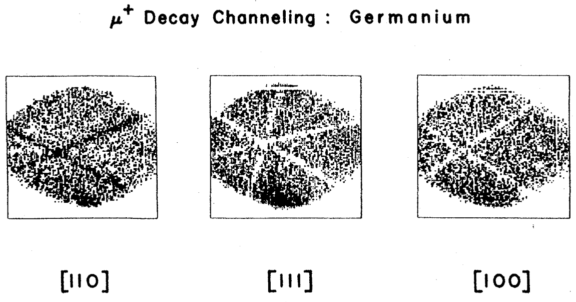

FIG. 44. Room-temperature muon-decay-blocking patterns for three Czochralski-grown germanium wafers. Dark and light features indicate, respectively, enhanced and diminished positron counting rates. The height of each pattern corresponds to 2.5°. The patterns have not been corrected for the 45° slant of the multiwire proportional chamber. The data are from the Zurich group (unpublished).

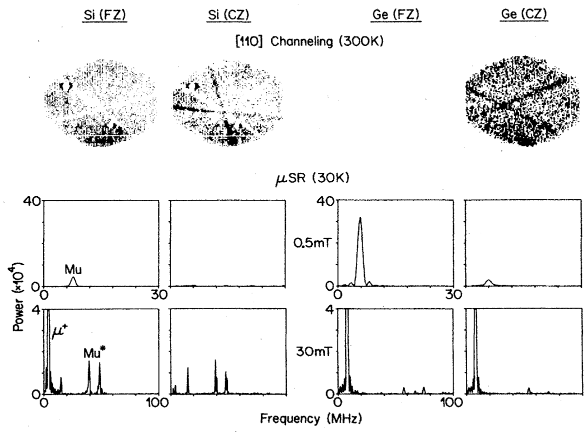

FIG. 45. A comparison of room-temperature [110] muon-decay-blocking patterns and μSR spectra at 30 K from Czochralski and float-zone silicon and germanium. The same samples were used for both types of experiment.

GaAs have been published. Two pion investigations of germanium gave somewhat different results. In the first experiment, Sigle *et al.* (1984) and Maier (1984) found a sharp central [110] peak at four temperatures between room temperature and 88 K, which became significantly broadened at three temperatures between 62 and 22 K. This was interpreted in terms of pion occupation of the tetrahedral interstitial site at high temperature and hexagonal or bond-center occupation at low temperature. In a later experiment at 100 K, Flik *et al.* (1986) found a strong side lobe on the [110] peak, which merged into a broad central peak at 200 K.

The effects on the pion site of silicon impurities in germanium and illumination of germanium and GaAs with visible light have also been investigated. It was found that adding 10^{17} cm^{-3} silicon impurities to Ge causes a side lobe to appear in the [110] muon peak below 40 K, indicating pion trapping (Maier, 1984). This indicates very rapid pion diffusion at low temperature [D ($T=20$ K) $\geq 10^{-4}$ cm^{2}s^{-1}]. The reader is referred to Sec. V.E for a comparison with muonium diffusion rates. Some of these Si-doped germanium samples have also been studied with μSR (Döring *et al.*, 1984). In the illumination experiment, a change in the pion site with illumination was observed in germanium at 100 K and in GaAs at room temperature, presumably due to the effect of free-carrier generation on the charge state of pionium (Flik *et al.*, 1986). This experiment prompted a μSR test of the effects of illumination, which is described in Sec. V.G.4.

As mentioned in Sec. IV.B channeling experiments have also been performed to determine the site of implanted deuterium in silicon.

C. Spectroscopy of the isotropic muonium state

1. The "zincblende series"

The isotropic muonium state has been observed and the hyperfine frequency $A=\hbar\omega_0$ measured in a large number of materials with the diamond and zincblende structures. In hosts with few nuclei with spin, the hyperfine frequency can be obtained from the splitting of the intratriplet Mu precession frequencies [Eq. (3.13)]. A more accurate measurement of A is possible with the high-transverse-field technique [Eq. (3.21)], and, in a host with nuclei with spin, this is the only way to observe Mu precession. Careful experiments in silicon (Bucci *et al.*, 1981) and germanium (Balzer *et al.*, 1981b) have shown that the Mu hyperfine interactions are isotropic to within 0.05 % and 0.4 %, respectively. Balzer *et al.* (1981b) have also demonstrated the doping independence of A in Ge.

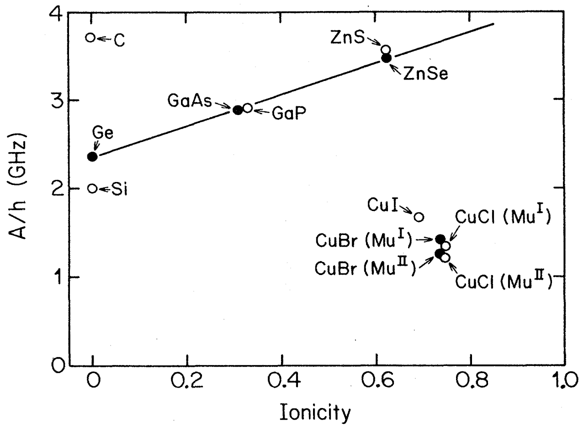

FIG. 46. Measured hyperfine frequencies for the isotropic Mu state in materials with the diamond or zincblende structure as a function of the Philips ionicity. From Schneider *et al.* (1986).

The Mu hyperfine frequencies measured in the diamond/zincblende materials are listed in Table IX and presented in Fig. 46 as a function of the ionicity of the host, according to the ionicity scale of Philips (1970). Noteworthy is the scatter of points at zero ionicity (the group-IV materials) compared to the close agreement within the III-V, II-VI, and I-VII groups. Also remarkable is the linear rise in A with increasing ionicity for the compounds in the same row of the Periodic Table (Ge, GaAs, and ZnSe), followed by a drastic drop to CuBr. Two different isotropic Mu states are observed in CuCl and CuBr. As will be discussed in Sec. V.H a thermally activated transition occurs in these materials from the Mu$^{\mathrm{I}}$ state, which predominates at low temperature, to the Mu$^{\mathrm{II}}$ state, which is the only state seen at high temperatures. Only the low-temperature Mu$^{\mathrm{I}}$ state has as yet been seen in CuI.

The status of theoretical investigations of Mu in semiconductors is presented in Sec. VI. It is fair to say that the Mu hyperfine frequency is quantitatively understood in diamond and silicon, but in spite of some interesting speculation (Cox and Symons, 1986), no convincing explanation of the trends in Fig. 46 has as yet been published.

2. The temperature dependence of the hyperfine interaction

The high precision with which the zero-field and high-transverse-field techniques (Secs. III.D and E) determine the Mu hyperfine frequency permits studies of the frequency as a function of conditions such as temperature and hydrostatic pressure. The observation of Mu precession at GHz frequencies implies that Mu is formed within a fraction of a precession period, i.e., ~100 ps (Holzschuh *et al.*, 1981a).

The temperature dependence of A for Mu in germanium as measured with the zero-field technique (Holzschuh, 1983) is shown in Fig. 47. The presence of phonons causes excited electronic states to be mixed with the Mu ground state via the orbit-lattice interaction. This admixture, and hence the change in the hyperfine interaction, is proportional to the square of the strain

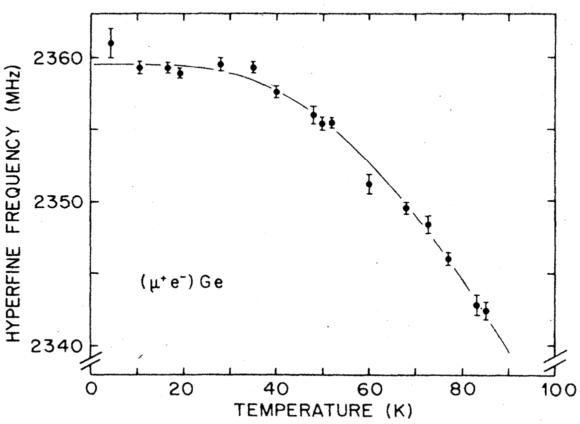

FIG. 47. The temperature-dependent hyperfine frequency of Mu in germanium as measured with the zero-field technique. The curve is a fit of the data to the Debye model (5.1). From Holzschuh (1983).

(Simánek and Orbach, 1966). Under the assumption that Mu couples to the long-wavelength part of a Debye phonon spectrum, the hyperfine frequency should then have a temperature dependence described by

$$A(T)=A(0)\left[1-C\left[\frac{T}{\Theta}\right]^4\int_0^{\Theta/T}\frac{x^3dx}{e^x-1}\right], \tag{5.1}$$

where Θ is the Debye temperature of the host. The constant C is a measure of the orbit-lattice interaction and determines the slope of $A(T)$ in the high-temperature limit:

$$dA/dT=-CA(0)/(3\Theta),\quad T\gg\Theta\ . \tag{5.2}$$

The physical significance of C has been discussed by Holzschuh (1982) and by Calvo and Orbach (1967). The curve in Fig. 47 is given by Eq. (5.1) with the fitted values

$$\begin{aligned}&A(0)=2359.5(2)\ \text{MHz}\ ,\\&C=0.27(7)\ ,\\&\Theta=273(25)\ \text{K}\ .\end{aligned} \tag{5.3}$$

This Debye temperature is in reasonable agreement with those found calorimetrically for germanium ($\Theta=250$–370 K) in the range of temperatures covered by the μSR experiment (Dolling and Cowley, 1966). An alternative expression for $A(T)$ is considered by Holzschuh (1983), which assumes that Mu couples predominantly to a single phonon mode of frequency ν_p (Doyle and Wolbarst, 1975). Although yielding an equally good fit, the resulting value of $\nu_p=3.6(3)\times10^{12}\ \text{s}^{-1}$ is a factor of 2 smaller than optical phonon frequencies in germanium.

The temperature dependence of the Mu hyperfine frequency in silicon, also measured with the zero-field technique by Holzschuh (1983), is shown in Fig. 48. The data above 80 K are again well described by the Debye formula (5.1), but the decrease in A with decreasing temperature clearly requires a modification of the theory. That this decrease in A cannot be due to the nonmonotonic thermal expansion of Si was demonstrated by Holzschuh (1983) with a room-temperature μSR experiment in silicon under hydrostatic pressure. He saw no significant change in the Mu hyperfine parameter $[1/A\ dA/da_{1c}=0.078(84)\ \text{Å}^{-1}]$ up to 1500 bar, a pressure sufficient to change the silicon lattice constant a_{1c} by approximately twice as much as from thermal expansion between 120 and 300 K.

The explanation offered by Holzschuh for the anomalous temperature dependence of A in silicon assumes that Mu hops among sites at which it experiences slightly different isotropic hyperfine interactions. At high temperatures, all sites are visited with equal probability, and an unbiased average over the distribution of hyperfine frequencies results. But as the temperature is reduced, the inequivalent sites are populated according to a Boltzmann distribution, which weights the energetically preferred sites—those with lower hyperfine frequencies. Holzschuh developed a correction to the Debye formula (5.1) assuming two Mu sites with an energy difference $k\Theta'$ and a difference in hyperfine frequency δA. The curve in Fig. 48 is Holzschuh's fit, which gave the values

$$\begin{aligned}&A(0)=2006(2)\ \text{MHz}\ ,\\&\Theta=655(25)\ \text{K}\ ,\\&C=0.68(5)\ ,\\&\Theta'=55(14)\ \text{K}\ ,\\&\delta A=31(3)\ \text{MHz}\ .\end{aligned} \tag{5.4}$$

This Debye temperature is in excellent agreement with the literature value of 625 K (de Launay, 1956). Relaxation effects of the two-state model will be discussed in Sec. V.G.1. We note here only that the zero-field precession line remains narrow ($\lambda<5\ \mu\text{s}^{-1}$) down to at least 25

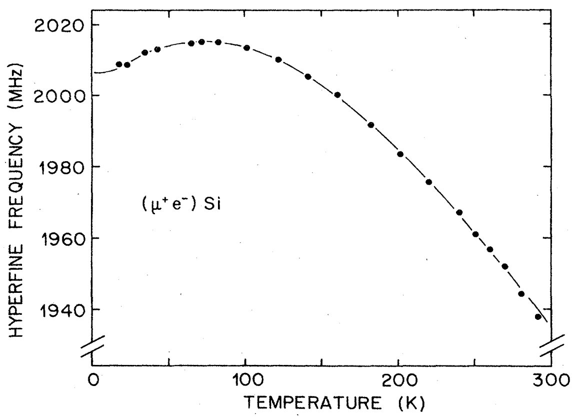

FIG. 48. The temperature-dependent hyperfine frequency of Mu in silicon as measured with the zero-field technique. The curve is a fit of the data to the Debye model modified to include the temperature-dependent occupation of two inequivalent Mu sites. From Holzschuh (1983).

K, implying a jump rate among the inequivalent Mu sites of $1/\tau_c > \delta A$.

Temperature-dependent Mu hyperfine frequencies have also been observed with the high-transverse-field technique in GaAs and GaP (Fig. 49) and in the cuprous halides (Fig. 50).

3. The electronic *g* factor

The deviation of the *g* value (g_e) of the bound electron in Mu from the vacuum value is a measure of the spin-orbit interaction and the admixture of $l > 0$ states into the ground-state wave function. An accurate measurement of the Mu precession frequencies in a known magnetic field can be used to determine g_e in low- or high-applied transverse fields [Eqs. (3.13) and (3.22)]. To date, the only published g_e values for Mu in diamond and zinc-blende materials are for silicon (Boekema *et al.*, 1981), diamond (Holzschuh *et al.*, 1982), and the cuprous halides (Kiefl, Odermatt *et al.*, 1986). These values, along with previously unpublished results for the other materials that show Mu precession, are presented in Table X.

The g_e determinations in the table made at 20 mT and below are based on the Mu precession frequencies ν_{12} and ν_{23} [Eq. (3.13)], while those at higher fields are based on ν_{12} and ν_{34} [Eq. (3.22)]. The entry "digital" in the table refers to the use of a linear time scale (time-to-digital conversion), while "analog" refers to a nonlinear time scale (time-to-analog plus analog-to-digital conversion). The integral nonlinearity in the analog mode, typically 10^{-3}, was corrected using a third-order polynomial fit to the peaks from a precision time calibrator. The agreement between the two modes for the case of germanium demonstrates the accuracy of this procedure.

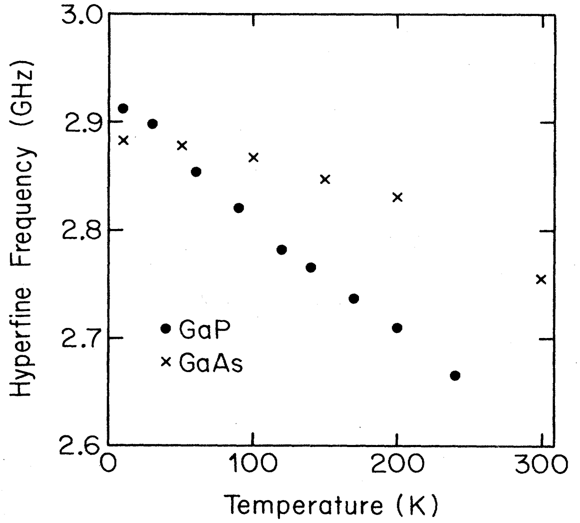

FIG. 49. The temperature-dependent hyperfine frequencies of Mu in GaP and GaAs as measured with the high-transverse-field technique. From the Zurich group (unpublished).

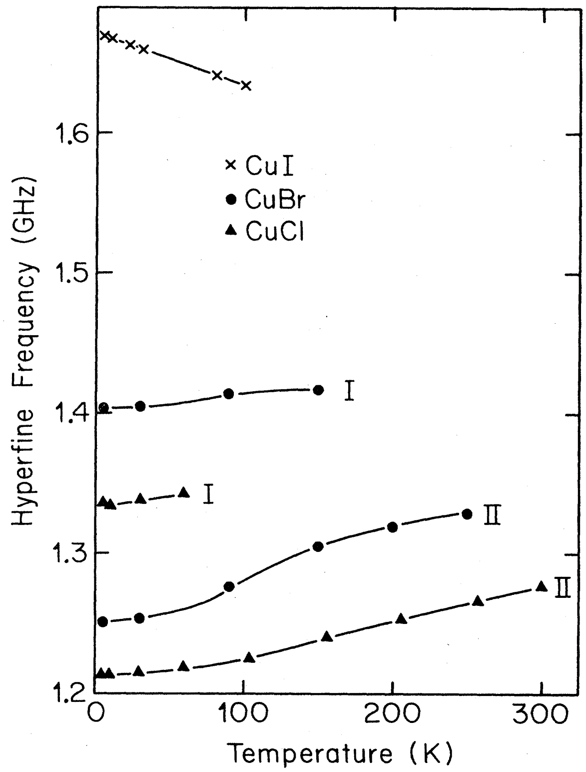

FIG. 50. The temperature-dependent hyperfine frequencies of the Mu states in the cuprous halides as measured with the high-transverse-field technique. The curves are to guide the eye. From Kiefl, Odernatt *et al.* (1986).

A more troublesome effect, however, is noticed when comparing g_e determinations made at low and at high fields for the case of silicon. A continuous decrease in the apparent magnitude of g_e is seen as the field is decreased from 1.1 to 0.1 T. This observation casts doubt on the accuracy of all high-field g_e determinations. The probable explanation is as follows. In order to use Eq. (3.13) or (3.22), one must know the applied field, through the value of ν_μ, to high precision. This diamagnetic μ^+ frequency is generally determined from the same data as are the Mu frequencies, but due to sources of background such as the sample holder or cryostat walls, the muons producing the diamagnetic signal and the Mu signals may not be at the same place and hence may not see the same magnetic field. For the case of silicon at 1.1 T, a value of the external field that is 0.5% too high causes the g_e value from Eq. (3.22) to be 1.8% too high. At 0.1 T, the effect of a 0.5% overestimate of the field is a g_e that is 0.5% too low. The small iron-core magnet used in the high-field measurements produces an inhomogeneous field that could cause the observed deviations in g_e. The error made at the magic field $B_{\text{mag}} = 0.510$ T is zero, since here the Mu precession frequencies are to first-order field independent. Indeed, measurements near this

TABLE X. Electronic g values (assumed isotropic) for the isotropic Mu state. The errors quoted are statistical, after a polynomial correction of the nonlinear time scale.

Sample	B (T)	Analog/Digital	g_e
Free e^-			$-2.002\,319\ldots$
Vacuum Mu			$-2.002\,284\ldots$
Diamond[a]	0.001–0.02	A	−2.0034 (17)
Si	0.01–0.02	A	−1.99 (1)[b]
	0.01	D	−1.9845 (70)
	0.1	A	−1.959 (15)
	0.3	A	−1.9926 (47)
	0.8	A	−2.0014 (47)
	1.1	A	−2.0069 (71)
Ge	0.01	D	−1.9996 (38)
	0.01	A	−2.0014 (16)
GaP	1.1	A	−2.007 (51)
GaAs	1.1	A	−2.0189 (24)
ZnS	1.1	A	−1.9981 (46)
ZnSe	1.2	A	−2.0236 (64)
CuCl[c]: I	1.2	A	−2.0608 (80)
II	1.2	A	−2.0694 (72)
CuBr[c]: I	1.2	A	−2.0438 (30)
II	1.2	A	−2.056 (32)
CuI[c]: I	1.2	A	−2.0650 (48)

[a] Holzschuh *et al.* (1982).

[b] Boekema *et al.* (1981).

[c] Kiefl, Odermatt *et al.* (1986).

field show reasonable agreement with the low-field technique, where a large air-core Helmholtz coil pair was used.

A suggestion for future g_e measurements would then be either to perform them with the low-field technique or, if this is not possible due to the nuclear hyperfine interaction with host spins, to perform a high-field measurement close to the magic field. At $B = B_{\text{mag}}$ we can rewrite Eq. (3.22) as

$$g_e = -g_\mu \frac{m_e}{m_\mu}\left[\frac{2-\delta^2+2\sqrt{1-\delta^2}}{\delta^2}\right],$$

$$\delta = \frac{\nu_{34}-\nu_{12}}{\nu_{34}+\nu_{12}} \quad (B = B_{\text{mag}}) . \tag{5.5}$$

Electronic g values determined in high field for Mu in 6H—SiC will be presented in Sec. V.I.1.

4. The nuclear hyperfine interaction

As discussed in Sec. III.E the nuclear hyperfine interaction broadens the precession lines of Mu. This broadening can be quenched by a sufficiently large applied field, and the field-dependent width of the ν_{12} or ν_{34} precession line yields an estimate of the nuclear hyperfine interaction strength Ω.

The measured field-dependent linewidth σ is shown for Mu in GaAs and for the low-temperature Mu$^{\text{I}}$ state in CuCl in Figs. 51 and 52. All the nuclei in these two hosts have spin $\frac{3}{2}$, and assuming an isotropic nuclear hyperfine interaction with four equivalent neighbors, we fit the data to expression (3.24) [plus a field-independent linewidth contribution $\sigma(\infty)$] to obtain Ω. This has been done for all the observed Mu states in the copper halides by Kiefl, Odermatt *et al.* (1986). The new GaAs and the previous

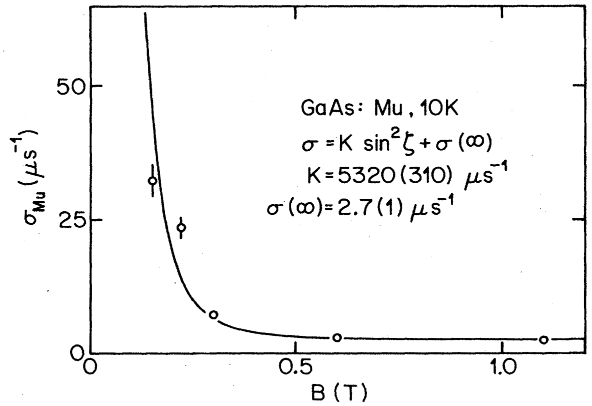

FIG. 51. The Mu linewidth in high-resistivity GaAs as a function of applied field. Each point is a weighted average of the widths of the precession lines ν_{12} and ν_{34}. The curve is a fit assuming nuclear hyperfine broadening for static Mu [Eq. (3.24)]. A bending over of the linewidth with decreasing field similar to that observed is expected to occur in the transition region between the motionally narrowed and the static cases (where $\sigma\tau_c \simeq 1$). However, the linewidth at high field should then be fit to the motional narrowing formula (3.25), and this produces an unphysically large nuclear hyperfine frequency Ω. From the Zurich group (unpublished).

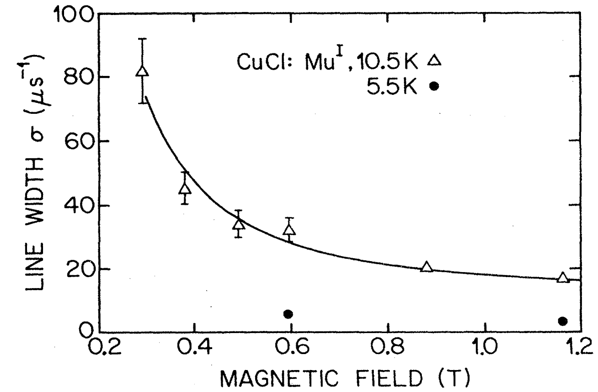

FIG. 52. The linewidth of the low-temperature Mu^{I} center in CuCl as a function of applied field. The curve is a fit to the 10.5-K data assuming static Mu [Eq. (3.24)]. From Kiefl, Odermatt *et al.* (1986).

copper halide results are summarized in Table XI.

With the exception of the Mu^{I} center in CuCl, the *nuclear* hyperfine frequency is always much smaller than the *hyperfine* parameter for the center, justifying the perturbation approach. The curves in Figs. 51 and 52 correspond to Eq. (3.24) and hence to a static Mu state; the dynamic function (3.25) gives much poorer fits to the GaAs and cuprous halide (Mu^{I}) linewidth data. The $\mathrm{Mu}^{\mathrm{II}}$ cuprous halide data is of insufficient quality to decide between the static and fast-diffusion cases. An upper limit for the rate of Mu diffusion in GaAs is derived from the data of Fig. 51 in Sec. V.E. In view of the very similar hyperfine frequencies of the Mu states in the cuprous halides, the large value of $\Omega/2\pi$ for Mu^{I} in CuCl is strikingly different from that for the other states. Much narrower Mu^{I} precession lines were observed in this sample at 5.5 K (see Fig. 52), indicating either more rapid motion or a change in the nuclear hyperfine interaction.

No nuclear hyperfine broadening of the Mu lines is detected in the elemental semiconductors silicon (with 4.70% ^{29}Si), germanium (7.76% ^{73}Ge), and diamond (1.11% ^{13}C). Dilution of the nuclear spin system decreases the strength of the effective nuclear hyperfine interaction, as does motion of Mu. Note that with a sufficiently small value of Ω, even slow Mu diffusion puts us in the motional narrowing regime.

TABLE XI. The nuclear hyperfine interaction (NHFI) strength and field-independent linewidth for Mu in GaAs (Zurich group, unpublished) and the cuprous halides (Kiefl, Odermatt, *et al.*, 1986).

Center	No. and type of spin	T (K)	$\Omega/2\pi$ (MHz)	$\sigma(\infty)$ ($\mu\mathrm{s}^{-1}$)
GaAs: Mu	$4\times\frac{3}{2}$	10	535 (31)	2.68 (12)
CuCl: Mu^{I}	$4\times\frac{3}{2}$	10.5	1010 (98)	12.3 (8)
CuCl: $\mathrm{Mu}^{\mathrm{II}}$	$4\times\frac{3}{2}$	10.5	94 (13)	0.0 (3.5)
CuBr: Mu^{I}	$4\times\frac{3}{2}$	5.5	202 (7)	0.24 (7)
CuBr: $\mathrm{Mu}^{\mathrm{II}}$	$4\times\frac{3}{2}$	5.5	169 (34)	0.80 (54)
CuI: Mu^{I}	$4\times\frac{3}{2}$	10.5	279 (7)	0.72 (10)

D. Spectroscopy of the anisotropic muonium state

1. The hyperfine interaction and its temperature dependence

The hyperfine interaction of the Mu* state differs from that of the Mu state in two respects. First, it is significantly weaker [$|A_\perp(\mathrm{Mu}^*)|/A(\mathrm{Mu})\simeq 0.05$ in Si]. The Paschen-Back regime, where only the precession lines ν_{12} and ν_{34} are observed, is already reached at approximately 3 mT. Second, it is anisotropic ($A_\parallel/A_\perp\simeq 0.2$ in Si), implying that the precession frequencies depend not only on the strength of the applied field (Figs. 53 and 54) but also on its direction with respect to the principal axes of the Mu* hyperfine tensor (Fig. 55). For an arbitrary direction of the magnetic field, a pair of precession lines is expected for each distinct Mu* orientation.

Experimentally, eight Mu* precession lines are seen with the magnetic field in an arbitrary direction. This observation and the fact that the lines collapse to two when the field is directed along the [100] direction (see Fig. 55) establish that the hyperfine interaction of Mu* has [111]-axial symmetry.

The hyperfine interaction parameters for Mu* may in principle be determined as follows. According to Table II, in sufficiently high applied fields, the sum of the two Mu* precession frequencies is field independent and given by

$$\nu_{34}+\nu_{12}=|A_\parallel\cos^2\theta+A_\perp\sin^2\theta| \ . \tag{5.6}$$

Thus high-field measurements at several angles are

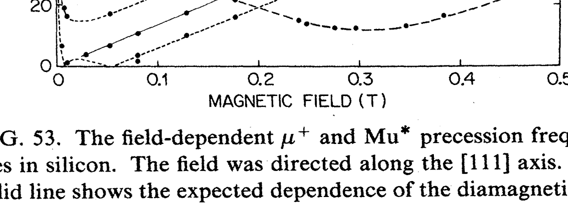

FIG. 53. The field-dependent μ^+ and Mu* precession frequencies in silicon. The field was directed along the [111] axis. The solid line shows the expected dependence of the diamagnetic μ^+ signal, and the finely and coarsely dashed curves are fits to the axially symmetric spin Hamiltonian (2.9) for angles between the field and Mu* symmetry axis of 0 and 70.5°, respectively. From Patterson, Hintermann *et al.* (1978).

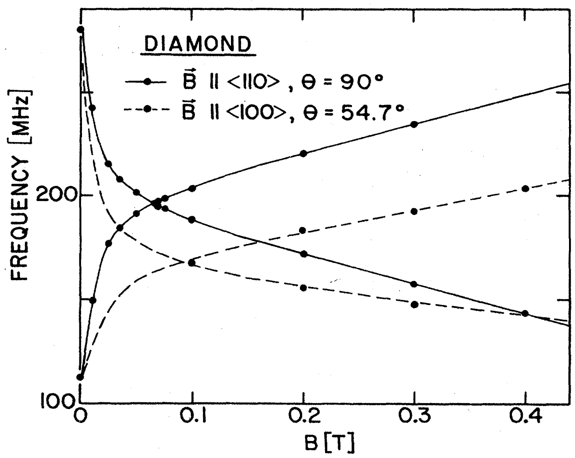

FIG. 54. Precession frequencies of Mu* in diamond as a function of the applied field for two different field directions. The curves are fits to the axially symmetric spin Hamiltonian (2.9). From Kündig *et al.* (1980).

sufficient to determine $A_{\parallel}$, $A_{\perp}$, and their relative sign. The *absolute* signs of the Mu* hyperfine parameters can only be determined via a dynamic process such as is described for diamond in Sec. V.F.

Tabulated values for the Mu* hyperfine parameters are given in Table IX for the diamond and zincblende hosts in which it has been observed: diamond, Si, Ge, GaP, and GaAs. The relative sign between $A_{\parallel}$ and $A_{\perp}$ is given correctly for all entries, and the *absolute* signs are given in the case of diamond. As with the hyperfine frequency of isotropic Mu, the values scatter for the group-IV materials, but they lie close to one another for the two III–V compounds.

With accurate transverse-field measurements at different crystal orientations, it is possible to determine the temperature dependence of the Mu* hyperfine parameters. This has been done for diamond (Holzschuh *et al.*, 1982), Si (Blazey *et al.*, 1981), and Ge (Blazey *et al.*, 1983). The results from all three materials are summarized and small errors are corrected by Blazey *et al.* (1983). The results are schematically presented in terms of the fitted Debye curves [see Eq. (5.1)] in Fig. 56. Blazey *et al.* use a "natural" representation of the hyperfine parameters in terms of $A_s=(A_{\parallel}+2A_{\perp})/3$ and $A_p=(A_{\parallel}-A_{\perp})/3$, the isotropic and axial-dipolar components of the hyperfine interaction, and they find that both $|A_s|$ and $|A_p|$ decrease with increasing temperature in all three hosts. The results of fits to the Debye formula (5.1) are shown in Table XII. The agreement between the fitted and calorimetric Debye temperatures deteriorates as one moves down the group-IV column of the Periodic Table. Blazey *et al.* also give results of fitting the Mu* hyperfine parameters to an Einstein model for the host-phonon spectrum.

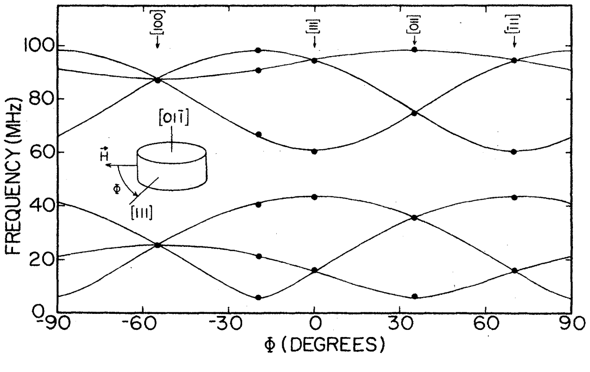

FIG. 55. The orientation dependence of the Mu* precession frequencies in silicon in an applied field of 0.383 T. Φ is the rotation angle of the sample about the [0 1 −1] axis, which in turn is perpendicular to the applied field. The curves are a fit to the axially symmetric spin Hamiltonian (2.9). From Patterson, Hintermann *et al.* (1978).

2. The electronic *g*-factor anisotropy

By fitting the experimentally determined Mu* precession frequencies to those predicted by the Hamiltonian (2.9), one can obtain the electronic *g* value for Mu*. The first such determination in silicon (Brewer *et al.*, 1973) incorrectly assumed an isotropic hyperfine interaction ($A_{\parallel}=A_{\perp}$) for Mu* and yielded $g_e=-13(3)$. With the correct anisotropic hyperfine interaction, the electron and muon *g* values for Mu* in silicon were found, respec-

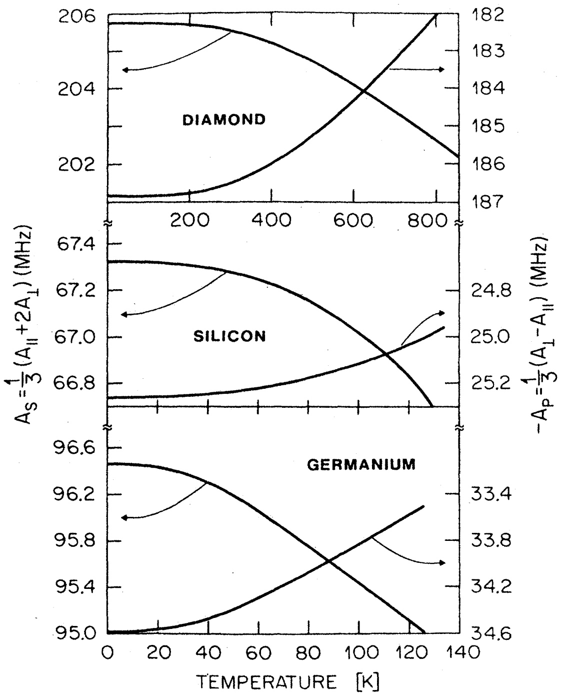

FIG. 56. Calculated curves from fits of the Debye model (5.1) to the temperature-dependent Mu* precession frequencies in diamond, silicon, and germanium. From Blazey *et al.* (1983).

TABLE XII. Fitted parameter values for the Debye model description of the temperature-dependent Mu* hyperfine frequencies. From Blazey *et al.* (1983). The literature values for the calorimetric Debye temperatures Θ_D(lit) are those cited by de Launay (1956).

	Diamond	Silicon	Germanium
Θ_D (K)	1902 (51)	425 (66)	152 (14)
Θ_D (lit) (K)	1860	625	360
A_S (0) (MHz)	205.730 (41)	67.333 (34)	96.448 (32)
A_p (0) (MHz)	−186.856 (26)	−25.257 (17)	−34.589 (12)
C_s	0.284 (26)	0.353 (136)	0.088 (18)
C_p	0.483 (17)	0.418 (181)	0.182 (26)

tively, to be −2.2(2) and 2.01(1) (Patterson, Hintermann *et al.*, 1978). A similar experiment on Mu* in diamond (Holzschuh *et al.*, 1982) yielded $g_e=-1.9932(43)$ and $g_\mu=2.0016(17)$. Finally, a DEMUR experiment (see Sec. III.G) on Mu* in silicon gave $g_e=-2.00(2)$ (Blazey *et al.*, 1986b).

The strong anisotropy of the Mu* state prompts one to ask whether the electronic *g factor* is also anisotropic. In the case of an axially symmetric g tensor (presumably also [111]), the electron Zeeman term of the spin Hamiltonian (2.1) is replaced by the expression

$$-g_\perp\mu_B\mathbf{S}_e\cdot\mathbf{B}-(g_\parallel-g_\perp)\mu_B(\mathbf{S}_e\cdot\mathbf{n})(\mathbf{B}\cdot\mathbf{n}) \ . \tag{5.7}$$

In principle, the Mu* precession frequencies predicted by Eq. (5.7) can be fit to those observed and the values of $g_\parallel$ and $g_\perp$ determined. This has been attempted for the case of silicon (Seifert, 1981), with later corrections made by myself. The experiment was performed at 30 K, at a total of 14 combinations of applied field and [110] or [111] crystal orientation in the field range 4–100 mT. Only the resolved Mu* lines with $\theta=0$ or 35.3° or the orientation-insensitive lines with $\theta=90°$ were analyzed, and the angular deviations from perfect crystal orientation were included as fitting parameters. The nonlinear time scale was corrected using a quartz calibrator. The fitting results were as follows:

$$\begin{aligned} &A_\parallel=92.5914(59)\ \text{MHz}\ ,\\ &A_\perp=16.787(14)\ \text{MHz}\ ,\\ &g_\perp=-1.9918(49)\ ,\\ &g_\parallel-g_\perp=-0.0035(19)\ ,\\ &g_\mu=2.003\,82(82)\ ,\\ &\chi^2=56.3\ \text{for 32 degrees of freedom}\ . \end{aligned} \tag{5.8}$$

Such experiments are complicated by the fact that in the high-field regime it is difficult to determine the electronic g values and the hyperfine parameters independently of one another. On the other hand, as the field is decreased, one suffers from nuclear hyperfine broadening, which damps the precession and may even shift the lines. There is an applied field, however, where a g-value *anisotropy* $g_\parallel$-$g_\perp$ causes a very noticeable effect on the Mu* precession frequencies. This is at the Mu* magic field B^*_{mag} defined in Eq. (2.10), where to a very good approximation the Mu* precession frequencies ν_{12} are equal, independent of the orientation of the Mu* states in the applied field. This frequency crossing, which can be seen for Si at approximately 0.2 T in Fig. 5, has allowed magic-field observations of Mu* in *powdered* silicon (Boekema *et al.*, 1981) and diamond (Holzschuh *et al.*, 1982). Blazey *et al.* (1986a) have demonstrated, however, that the crossing is destroyed by an anisotropy in the electronic g factor and have used this fact to determine the anisotropy for Mu* in silicon and germanium.

The Mu* ν_{12} precession frequencies in Si and Ge are shown in Fig. 57 near the respective Mu* magic fields. Note that the frequencies cross for the case of Si but not for the case of Ge. The detailed analysis of Blazey *et al.* yields the g-factor anisotropies

$$\begin{aligned} g_\parallel-g_\perp&=-0.0002(8)\ \ (\text{Si})\\ &=-0.0330(12)\ \ (\text{Ge})\ . \end{aligned} \tag{5.9}$$

Blazey *et al.* also quote fitted values of $g_\perp$ from these data [$g_\perp(\text{Si})=-2.190(85)$, $g_\perp(\text{Ge})=-1.953(85)$], but the authors state that systematic errors, for example, from the nonlinear time scale, are probably much larger than these statistical errors. In their discussion of the measured anisotropies, they point out that a larger g-factor

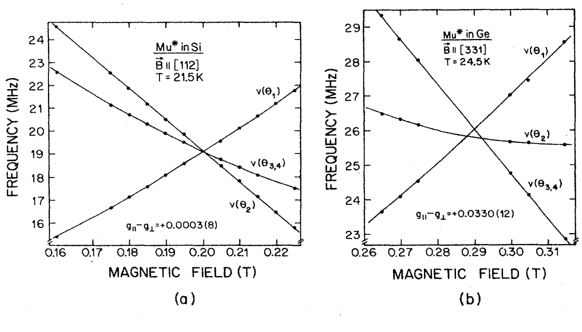

FIG. 57. The ν_{12} Mu* precession frequencies in the vicinity of the Mu* magic fields B^*_{mag} in (a) silicon and (b) germanium. The noncrossing of the lines from differently oriented Mu* centers in the case of Ge demonstrates the anisotropy of the electronic g value. From Blazey *et al.* (1986a). Note that these authors use the opposite sign convention for g_e from that used in this review.

anisotropy is to be expected in Ge than in Si due to the larger spin-orbit interaction. An empirical classification by g factor of defect types in Si has been made by Lee and Corbett (1973) and extended by Sieverts (1983), but in the absence of reliable g factors, the anisotropy is not a decisive quantity for models of Mu*.

3. The nuclear hyperfine interaction

The Mu* state is immobile, and its weak hyperfine interaction indicates that the paramagnetic electron spends much of its time *away* from the muon. One thus expects a strong *nuclear* hyperfine interaction that is not motionally averaged (De Renzi *et al.*, 1981).

Silicon (with 4.70% spin-$\frac{1}{2}$ ^{29}Si) and germanium (with 7.76% spin-$\frac{9}{2}$ ^{73}Ge) are dilute nuclear spin systems. Some small fraction of the Mu* centers formed will have a strong nuclear hyperfine interaction with a single host nucleus, but the majority will be quite distant from a spin and will experience a much reduced interaction. The effective strength of the nuclear hyperfine interaction in these materials will therefore depend on the concentration of nuclear spins.

With very high statistics, broad Mu* precession lines can be seen in silicon at zero field (Patterson, Hintermann *et al.*, 1978). Blazey *et al.* (1986b) observed a strong broadening of the $\theta=90°$ Mu* lines in applied fields of $B=1-5$ mT. The Lorentian linewidths λ were fit to the expression

$$\lambda=C/B^2+\lambda(\infty)\ . \tag{5.10}$$

For reduced field values $x=2\omega_+/\omega_0=B(\mathrm{mT})/3.29$ large compared to one, this is a good approximation to the expression for the field-dependent linewidth σ given in Eq. (3.24). To extract a nuclear hyperfine frequency Ω from these data, it remains only to convert the Lorentzian width λ to an approximate Gaussian width σ. This can be done by setting the full widths at half maximum (FWHM) of the two lineshapes equal:

$$\frac{2}{\pi}\sqrt{\ln 2}\,\sigma=\frac{\lambda}{\pi}\ . \tag{5.11}$$

Thus, for a single spin-$\frac{1}{2}$ neighbor, the fitted value $C=4.94\ (34)\ \mathrm{mT}^2\ \mu\mathrm{s}^{-1}$ implies $\Omega/2\pi=0.493\ (33)$ MHz, as entered in Table XIII.

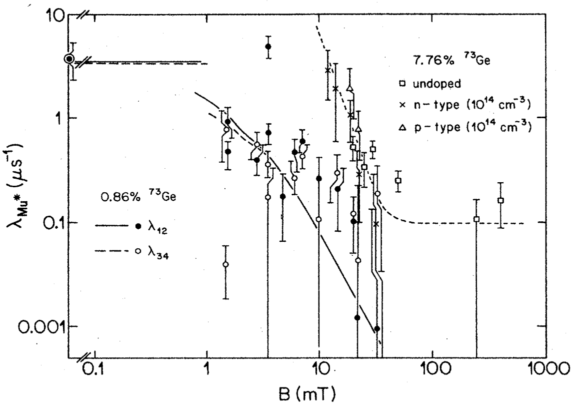

FIG. 58. Mu* linewidths as a function of the applied magnetic field in natural germanium (from Weidinger, unpublished) and a crystal isotopically enriched in the spinless nucleus ^{74}Ge (from Estle, Rudaz *et al.*, 1984). The narrower lines in the enriched sample establish that the broadening is due to the nuclear hyperfine interaction. The solid and coarsely dashed curves are model calculations in which Mu* interacts with a single ^{73}Ge spin with a NHFI of 2.5 MHz (Estle, Rudaz *et al.*, 1984). The finely dashed curve is to guide the eye.

Germanium shows a similar broadening of the Mu* lines below 50 mT (Balzer *et al.*, 1981a). Proof that this broadening is due to the nuclear hyperfine interaction is provided by the comparison of field-dependent Mu* linewidths in natural Ge and in a crystal isotopically enriched in ^{74}Ge (with 0.86% ^{73}Ge) in Fig. 58. An analysis of this data has been performed by Estle, Rudaz *et al.* (1984), using empirical relations from numerical simulations of Mu* in an environment of dilute ^{73}Ge nuclei (Estle, Warren, and Patterson, 1984). This analysis yielded the average isotropic nuclear hyperfine interactions listed in Table XIII. An observation by Balzer *et al.* (1981a) that the nuclear hyperfine broadening of the Mu* lines in Ge is doping dependent is in conflict with the doping independence seen in Fig. 58.

Numerical simulations of nuclear hyperfine structure

TABLE XIII. The effective nuclear hyperfine interaction strength for Mu*.

Host	No. and type of spin assumed	T (K)	$\Omega/2\pi$ (MHz)	$\lambda(\infty)$ (μs^{-1})
Si[a]	$1\times\frac{1}{2}$	4.2	0.493 (33)	0.200 (12)
Ge (7.76% ^{73}Ge)[b]	$1\times\frac{9}{2}$	11	20	
Ge (0.86% ^{73}Ge)[b]	$1\times\frac{9}{2}$	11	2.5	
GaP[c]	$1\times\frac{1}{2}$	10	990 (110)	0.08 (18)
GaAs[c]	$1\times\frac{1}{2}$	23	1190 (110)	0.56 (12)

[a] From Blazey *et al.* (1986b).

[b] From Estle *et al.* (1984c).

[c] From Schneider (1984).

rapidly become unwieldy for a concentrated spin system such as the III-V or I-VII hosts, hence one must resort to a perturbation calculation. In the discussion of the nuclear hyperfine interaction presented in Sec. II.A.4, the electron-nuclear interaction was treated as a small perturbation of the electron-muon hyperfine interaction. While apparently a good approximation for the isotropic Mu state, it is probably a poor description of the Mu* state in a concentrated spin system. A perturbation theory that treats the hyperfine and nuclear hyperfine interactions on equal footing in the high-field limit has been developed by Heming, Roduner *et al.* (1986), but it too becomes unwieldy if many spins are included.

A simpler approach to the problem of a strong nuclear hyperfine interaction is to assume that the Mu* electron interacts with a single spin-$\frac{1}{2}$ nucleus and to compute an "effective" nuclear hyperfine interaction for this situation. We consider the case of a Mu* center with [111] symmetry axis parallel to the applied field ($\theta=0$), and we "invert" Eq. (3.24) by setting $N=1$ (a single muon), replacing S_n with the muon spin ($\frac{1}{2}$), and replacing Ω with the hyperfine frequency $(\omega_0+\omega^*)/2\pi=2\pi A_{\parallel}$:

$$\lambda=\left[\frac{\ln 2}{8}\right]^{1/2}(\omega_0+\omega^*)\left[1-\frac{x'}{\sqrt{1+x'^2}}\right]+\lambda(\infty)\ . \tag{5.12}$$

The reduced field x' is now given by

$$x'=\frac{B}{B_0'},\quad B_0'=\frac{\hbar\Omega}{g_n\mu_n-g_e\mu_B}\ , \tag{5.13}$$

where g_n and μ_n are the nuclear g factor and nuclear magneton, respectively. In Eq. (5.12) we have included the conversion factor (5.11) between σ and λ as well as a field-independent contribution $\lambda(\infty)$.

This is the method used by Schneider (1984) to analyze the field-dependent Mu* linewidth in GaP and GaAs. The width of the ν_{34}, $\theta=0$ Mu* line in GaP and GaAs is shown as a function of applied field in Fig. 59, and the curves are Schneider's fits to the function (5.12). The fit results are given in Table XIII. Note that the nuclear hyperfine frequencies are considerably larger than the hyperfine frequencies $A_{\parallel}$ for GaP and GaAs from Table IX, namely, 219.0 and 217.8 MHz, respectively. The perturbation treatment of the *hyperfine* interaction is thus justified.

E. Motion of the isotropic muonium state

The fact that the Mu* state shows a [111]-symmetric hyperfine interaction in hosts with cubic symmetry demonstrates that it does not undergo long-range diffusion. No such statement can be made, however, for the isotropic Mu state, and the question of Mu motion must be addressed using other data.

The motion of hydrogen in silicon and germanium is describable by a diffusion constant $D(T)$ which has the dimensions cm^{2}s^{-1} and obeys an Arrhenius law with activation energy E_a:

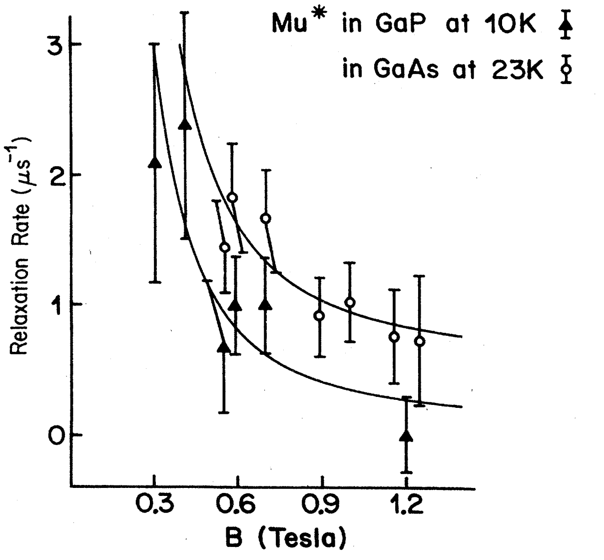

FIG. 59. Widths of the low-frequency $\theta=0$ Mu* precession line in GaP and GaAs as a function of the applied field. The curves are fits to the nuclear hyperfine broadening according to Eq. (5.12). From Schneider (1984).

$$D(T)=D_0\exp(-E_a/kT)\ . \tag{5.14}$$

High-temperature permeation measurements of the diffusion of hydrogen (van Wieringen and Warmoltz, 1956) and tritium (Ichimiya and Furuichi, 1968), in silicon and of hydrogen in germanium (Frank and Thomas, 1959) are summarized in Table XIV. Note the approximate agreement of the E_a values for hydrogen and tritium diffusion in silicon. Formation of an oxide layer may be responsible for the smaller prefactor seen in the tritium measurement. Table XIV also includes the (somewhat fantastic) extrapolations of the data for hydrogen in silicon and germanium to 20 K.

In a simple model in which Mu makes random jumps of length 1 in three dimensions with a rate $1/\tau_c$, the diffusion constant can be written

$$D=1^2/6\tau_c=a_{1c}^2/32\tau_c\ . \tag{5.15}$$

Here it is assumed that Mu jumps between neighboring tetrahedral interstitial sites in the diamond lattice, implying a jump length of $3^{1/2}/4$ times the lattice constant a_{1c}.

A lower limit for the jump rate of Mu in silicon was derived in Sec. V.C.2 from the hopping model for the anomalous temperature dependence of the hyperfine interaction. In order to produce the observed narrow zero-field precession line at 25 K, the jump rate of Mu must be greater than the difference in hyperfine frequency between the sites. In the two-state model, this implies $1/\tau_c<\delta A=3\times10^7$ s^{-1} or, using Eq. (5.15), $D(T=25$ K$)>2.5\times10^{-9}$ cm^{2}s^{-1}, as entered in Table XIV.

TABLE XIV. Diffusion constants $D(T)$ (or Arrhenius parameters for $D(T)=D_0\exp[-E_a/(kT)]$) for hydrogenlike atoms in semiconductors. See text for deviations and references.

Isotope	Host	Temperature (K)	$D(T)$ or D_0 ($\mathrm{cm}^2\ \mathrm{s}^{-1}$)	E_a (eV)	Method
Hydrogen	Si	1365–1473	9.4×10^{-3}	0.48	Permeation
		20	$D\simeq10^{-123}$		Extrapolated
Tritium	Si	675–775	4.2×10^{-5}	0.56	Permeation
Hydrogen	Ge	1073–1183	2.8×10^{-3}[a]	0.38	Permeation
		20	$D\simeq10^{-99}$		Extrapolated
Mu	Diamond	8–150	0.1	0.043	Grain surface
Mu	Si	25	$D>2.5\times10^{-9}$		Line narrowing
		20	$>10^{-4}$		C doping
		30	$>10^{-5}$		O doping
		80	$>10^{-4}$		*n* irradiation
		81	$>6\times10^{-6}$		*e* irradiation
Mu	Ge	20	$D\simeq10^{-3}$		Si doping
π^+	Ge	20	$>10^{-4}$		Si doping
Mu	GaAs	10	$D<7\times10^{-10}$		Line broadening
		20	$>1.5\times10^{-3}$ (?)		Doping
Mu^{I}	CuCl	10.5	$D<3\times10^{-9}$		Line broadening
Mu^{I}	CuBr	5.5	$D<6\times10^{-10}$		Line broadening
Mu^{I}	CuI	10.5	$D<8\times10^{-10}$		Line broadening

[a] D_0 has been computed from the measured diffusion rate at 800 °C and the activation energy for diffusion.

The rate at which Mu reaches impurities or radiation defects can also be used to estimate D. Consider a trapping model in which Mu diffuses to an impurity or defect and immediately becomes depolarized. The number of sites visited by Mu in a time t is approximately t/τ_c, and the concentration of Mu trapping sites can be taken to be $k\,n_{\mathrm{defect}}$, where n_{defect} is the concentration of impurities or defects, and k is the number of trap sites per defect. With these assumptions the Mu relaxation rate λ_{Mu} is related to the jump rate by

$$1/\tau_c = 8\lambda_{\mathrm{Mu}}/(k n_{\mathrm{defect}} a_{1c}^3)\ , \tag{5.16}$$

where it is again assumed that Mu moves among the tetrahedral interstitial sites, whose concentration in the diamond lattice is $8/a_{1c}^3$. Using Eq. (5.15), we arrive at a relation between the Mu relaxation rate measured at a particular temperature and the diffusion constant $D(T)$:

$$D(T)=\lambda_{\mathrm{Mu}}/(4k n_{\mathrm{defect}} a_{1c})\ . \tag{5.17}$$

Döring *et al.* (1983) have observed that Mu atoms at 20 K in ultrapure Si-doped germanium find silicon impurities at a concentration of $10^{16}\ \mathrm{cm}^{-3}$ at a rate of $7\times10^6\ \mathrm{s}^{-1}$. This result has been verified by Clawson *et al.* (1984). Assuming that trapping may occur at any of the four tetrahedral sites around each impurity, one obtains from Eqs. (5.16) and (5.17) a Mu jump rate $1/\tau_c=8\times10^{12}\ \mathrm{s}^{-1}$ and a diffusion constant $D=10^{-3}\ \mathrm{cm}^2\ \mathrm{s}^{-1}$, as listed in Table XIV (Döring *et al.*, 1984). Also included in the table is the pion-trapping result from pion-decay-blocking experiments in some of the same samples (Maier, 1984; see Sec. V.B).

An analysis similar to that made of Döring's data can also be made of other experiments. The nonobservance at 20 K of Mu in silicon doped with $^{13}\mathrm{C}$ (Estle, Blazey *et al.*, 1984) implies a relaxation rate λ_{Mu} exceeding 10 $\mu\mathrm{s}^{-1}$. Attributing this relaxation to trapping at carbon impurities ($10^{17}\ \mathrm{cm}^{-3}$) leads to a minimum Mu jump rate of $10^{12}\ \mathrm{s}^{-1}$ and to the lower limit for D given in Table XIV. Mu also relaxes with a rate exceeding 10 $\mu\mathrm{s}^{-1}$ in Czochralski-grown silicon at 30 K (see Fig. 45). If one attributes this relaxation to trapping at oxygen impurities (the principal impurity in this material with a concentration of the order of $10^{18}\ \mathrm{cm}^{-3}$), one arrives at somewhat less stringent limits on the Mu jump rate. Döring *et al.* (1984) have also observed an effect of carbon and oxygen impurities on the Mu relaxation rate in germanium.

As will be discussed in Sec. V.G.4 the irradiation of silicon with neutrons and electrons causes the Mu precession signals to disappear. Assuming that this disappearance is due to Mu trapping at radiation defects, we can obtain lower limits for the diffusion constant from these data. Barsov *et al.* (1983, 1984a) saw no Mu signal (implying $\lambda_{\mathrm{Mu}}>1\ \mu\mathrm{s}^{-1}$) at 80 K in a neutron-irradiated sample with 10^{16} defects cm^{-3}. Albert *et al.* (1985a) found a Mu relaxation rate greater than 20 $\mu\mathrm{s}^{-1}$ at 81 K after irradiation with 3-MeV electrons at a dose of $6\times10^{17}\ \mathrm{cm}^{-2}$. Taking as a defect production rate $dN/dx=6\ \mathrm{cm}^{-1}$ (Cahn, 1959), we obtain a defect concentration in the electron-irradiated sample of $4\times10^{18}\ \mathrm{cm}^{-3}$. Again assuming that Mu jumps among tetrahedral interstitial sites and that each defect is surrounded by four trapping sites, we arrive at jump rates $1/\tau_c$ which are greater than $10^{12}\ \mathrm{s}^{-1}$ and $6\times10^{10}\ \mathrm{s}^{-1}$ for the *n*- and *e*-irradiation experiments, respectively, and the lower limits for D quoted in Table XIV.

The presence of hydrogen impurities (approximately 10^{18} cm^{-3}) in germanium grown in a hydrogen atmosphere on the amplitude of the diamagnetic μ^+ precession signal was reported by Andrianov *et al.* (1976). In a later experiment, however, Clawson *et al.* (1981) found no unambiguous effect of hydrogen on the relaxation rate of Mu in germanium. Evidence for fast diffusion of Mu below 20 K in high-purity silicon is provided by the observation by the Zurich group of strong, sample-dependent Mu relaxation (Felber, 1984; see Sec. V.G.1.a).

Estimates for Mu jump rates can also be made on the basis of the field quenching of the nuclear hyperfine broadening. As discussed in Sec. III.E, a jump rate $1/\tau_c > \sigma$ narrows a line of width σ and changes the dependence of the linewidth on applied field from approximately B^{-2} to B^{-4} [Eqs. (3.24) and (3.25)]. As discussed in Sec. V.C.4 low-temperature fits of the Mu precession linewidth measured with the high-transverse-field technique for GaAs and the Mu^{I} state in CuCl and CuBr show B^{-2} dependences, implying static Mu states (see Figs. 51 and 52). An upper limit for the Mu jump rate can in this case be obtained from the condition

$$1/\tau_c < \sigma - \sigma(\infty) \, , \tag{5.18}$$

where σ is the smallest linewidth that is still demonstrably static. Applying this argument to the GaAs data in Fig. 51 and the cuprous halide data of Kiefl, Odermatt *et al.* (1986) and assuming jumps among both types of tetrahedral interstitial site with equal probability, we obtain the limits for D in these materials given in Table XIV. The low diffusion rate for Mu in GaAs is compatible with the observation by the Zurich group (unpublished) that Mu precession at 15 K is not affected by a defect concentration of 1.5×10^{17} cm^{-3} produced by neutron irradiation (see Sec. V.G.4). A strong reduction in the Mu diffusion rate in compounds compared to elemental hosts would result from the increased intersite distance if Mu occupation of one of the two types of tetrahedral sites in the zincblende structure were unfavorable.

A problem arises when considering the diffusion of Mu in GaAs that contains impurities. In contrast to a "high-resistivity" sample, no Mu precession could be observed in a "low-resistivity" sample with a room-temperature carrier concentration of 4×10^{16} cm^{-3} (Kiefl *et al.*, 1985). Under the assumption that this represents the concentration of Mu trapping centers, Eq. (5.17) leads to a very large diffusion constant (1.5×10^{-3} $\mathrm{cm}^2\mathrm{s}^{-1}$; see Table XIV), in strong disagreement with the upper limit for D obtained from the nuclear hyperfine quenching. It is unlikely that the carriers themselves cause Mu relaxation, since Mu* is unaffected by the doping and since the dopants are not ionized at 20 K, but the low-resistivity sample may differ from the high-resistivity sample in, for example, the amount of boron impurities introduced during growth. It is also clear that the fit of the high-resistivity linewidth data to the function (3.24) leaves much to be desired (see Fig. 51).

An unusual linewidth behavior is also observed for the Mu^{I} state in CuCl (Kiefl, Odermatt *et al.*, 1986). The lines for this state at 10.5 K are much broader than those for the muonium states in the other cuprous halides, and a drastic narrowing, due either to motion or to a change of site, is seen upon cooling to 5.5 K (see Fig. 52).

There is presently some confusion in the literature regarding the relaxation rate of the Mu precession signals in diamond (see Fig. 60). Holzschuh *et al.* (1982) studied the temperature dependence of λ_{Mu} in a high-purity type-IIa powder (containing less than 50 ppm nitrogen) with grain size of $1-6$ μm. The powder showed a relaxation rate that increased from 2 $\mu\mathrm{s}^{-1}$ at 8 K to 4.6 $\mu\mathrm{s}^{-1}$ at 150 K, and no signals could be seen above 150 K. Spencer *et al.* (1984) used a small type-Ia crystal (of the order of 1000 ppm nitrogen) and observed a *decrease* in λ_{Mu} with increasing temperature from 7.2 $\mu\mathrm{s}^{-1}$ at 6 K to 1.8 $\mu\mathrm{s}^{-1}$ at 295 K. Unpublished room-temperature data from the Zurich group on eight crystals of types Ia and IIa showed an excellent correlation between the presence of a strong Mu signal and the absence of nitrogen. In contrast to the stone of Spencer *et al.*, none of the Ia crystals showed a detectable Mu signal at room temperature. One of these type-Ia stones was used in an early study of the Mu-to-Mu* transition (Patterson, Holzschuh, Kündig, Meier, Odermatt, Sellschop, and Stemmet, 1984; see Sec. V.F). Finally, $\lambda_{\mathrm{Mu}}(T)$ was measured in one of the IIa stones during the most recent Mu-to-Mu* transition study (Odermatt *et al.*, 1986). In this high-purity stone the Mu relaxation rate, which rises to a value of 18 $\mu\mathrm{s}^{-1}$ at 405 K, is clearly associated with

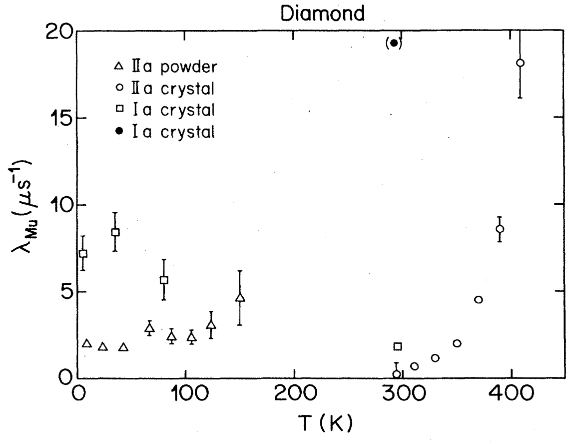

FIG. 60. Mu relaxation rates measured in various diamond samples. All points were taken in the low-field regime where ν_{12} and ν_{23} are not resolved. The measurements in high-purity IIa material were performed in powder at 0.975 mT by Holzschuh *et al.* (1982) and in a crystal at 1.25 mT by Odermatt *et al.* (1986). The Ia stones, containing of the order of 1000 ppm nitrogen, were measured at 1 mT by Spencer *et al.* (1984) (open squares) and at 0.5 mT by the Zurich group (unpublished) (solid circle).

the Mu-to-Mu* transition.

Apparently the low-temperature maximum in λ_{Mu} seen by Spencer *et al.* and the absence of Mu at room temperature found in Zurich are different consequences of the nitrogen content of type-Ia stones. A possible explanation is that the nitrogen is *dispersed* in Spencer's stone, presenting Mu with many shallow traps, which are quickly found at low temperature but from which Mu can escape at room temperature. On the other hand, in the Zurich stones the nitrogen is collected in *complexes,* forming fewer but deeper traps for Mu. Thus more rapid Mu motion is required to find the complexes, and the Mu remains trapped at room temperature.

An intriguing possibility to explain the disappearance of Mu at 150 K in the type-IIa powder is that Mu is moving rapidly enough to reach the surface of the grains. It is known that Mu rapidly reaches the surface of fine SiO_2 grains (70 Å mean diameter) at temperatures as low as 5 K (Kiefl, Patterson *et al.,* 1984). The root-mean-square distance r_{rms} a Mu atom moves in a time t is related to the diffusion constant D by

$$r_{\mathrm{rms}}=(6Dt)^{1/2} . \tag{5.19}$$

We now take t to be $1/\lambda_{\mathrm{Mu}}$ and r_{rms} to be the mean distance to the surface of a powder grain. A reasonable value for r_{rms} for an irregularly shaped grain of average diameter 3 μm is 0.3 μm. Holzschuh *et al.* (1982) found that $\lambda_{\mathrm{Mu}}(T)$ in the diamond powder could be described by an Arrhenius law with a frequency factor of 10^8 s^{-1} and an activation energy $E_a=43$ meV. This implies a diffusion prefactor for Mu in diamond $D_0 \simeq 0.015$ cm^2 s^{-1} (Table XIV), or, using Eq. (5.15), a jump rate at infinite temperature of $\sim 4\times 10^{14}$ s^{-1}. This is high, but only marginally so.

We conclude from Table XIV that Mu in silicon and germanium is vastly more mobile at low temperature than would be expected from the high-temperature hydrogen permeation measurements. An estimate for the maximum rate at which over-barrier diffusion can occur is the so-called "adiabatic limit"

$$D_{\mathrm{adiabatic}}=1^2\nu_D , \tag{5.20}$$

where 1 is again the jump distance and $\nu_D=k\Theta/h$ is the Debye frequency of the host (Seeger, 1984). Assuming jumps among neighboring tetrahedral sites, and using the calorimetric Debye temperatures Θ quoted in Table XII, we arrive at $D_{\mathrm{adiabatic}}$ values for diamond, silicon, and germanium as

$$D_{\mathrm{adiabatic}}=\begin{cases} 9.2\times 10^{-3}\ \mathrm{cm}^2\ \mathrm{s}^{-1} & (\text{diamond}), \\ 7.2\times 10^{-3}\ \mathrm{cm}^2\ \mathrm{s}^{-1} & (\text{Si}), \\ 4.5\times 10^{-3}\ \mathrm{cm}^2\ \mathrm{s}^{-1} & (\text{Ge}) . \end{cases} \tag{5.21}$$

Note the similarity of these values for diamond and germanium with those given in Table XIV.

F. The Mu-to-Mu* transition in diamond

The signs of the hyperfine parameters for a muonium state reflect the polarization of the bound electron, and hence are important in characterizing the state. By analogy with vacuum muonium, the hyperfine parameter of the isotropic Mu state is certainly positive, corresponding to a positive electron spin density at the muon. No such analogy can be made for the anisotropic Mu* state. Here the spin density at the muon is related to the isotropic part of the Mu* hyperfine interaction,

$$A_s=(A_{\parallel}+2A_{\perp})/3 . \tag{5.22}$$

A positive A_s, and hence a positive spin density, would suggest that Mu* is a distorted version of Mu. A negative spin density, on the other hand, would result from a polarization transfer effect (similar to "core polarization" in magnetic ions) exerted by an unpaired electron some distance from the muon. The similarity in the temperature dependences of the Mu* hyperfine constants for different materials (see Fig. 56) makes it plausible that the sign of A_s is the same in all of them.

Purely spectroscopic observations of the Mu* state, as described in Sec. V.D.1, can be used to determine the relative sign of the anisotropic Mu* hyperfine constants $A_{\parallel}$ and $A_{\perp}$. But a *dynamic* process is required in order to perform an *absolute* sign determination. Such a process is fortunately available in diamond, namely, a thermally activated, irreversible transition from the Mu state to the Mu* state.

A general observation in the diamond and zincblende materials is that the isotropic Mu state is unstable at elevated temperatures (see Table IX). In nitrogen-free diamonds, Mu is observed up to 405 K. The first observation of the Mu-to-Mu* transition (Holzschuh *et al.,* 1982) was in a diamond powder at zero field, where three Mu* oscillation frequencies are observed, namely, ν_{12}, ν_{14}, and ν_{34} (see Table II). A strong steplike increase was observed in the amplitude of each of these lines as the temperature was increased, but the increases did not occur at the same temperature. Points of inflection for a_{12}, a_{14}, and a_{34} occurred, respectively, at 560 K, 700 K, and 720 K. Just this behavior, namely, an increase in a_{12} followed by increases in the other two amplitudes, was predicted by Meier (1982) assuming a thermally activated Mu-to-Mu* transition in which the electron polarization is conserved. Using Meier's theory it was possible for Holzschuh *et al.* to fit the transition rate Λ from Mu to Mu* to an Arrhenius law,

$$\Lambda(T)=\Psi\exp(-E_a/kT) , \tag{5.23}$$

with the values (Richner, 1982)

$$\begin{aligned} \Psi&=1.2\ (2)\times 10^{14}\ \mathrm{s}^{-1} , \\ E_a&=0.569\ (8)\ \mathrm{eV}\ (\text{powder}) . \end{aligned} \tag{5.24}$$

The fact that this law, extrapolated to lower temperature, did not correspond to the observed Mu disappearance rate was later found to be due to Mu trapping at nitrogen impurities (see Sec. V.E).

Although establishing the existence of a transition, the zero-field data were not of sufficient quality to determine the sign of A_s, hence the experiment was repeated with a single crystal sample in an applied field. In the chosen experimental geometry, the [110] axis was oriented parallel to the applied field such that two [111] Mu* symmetry axes were at $\theta=90°$. A preliminary experiment on a nitrogen-containing (type-Ia) diamond was plagued by strong relaxation effects (Patterson, Holzschuh, Kündig, Meier, Odermatt, Sellschop, and Stemmet, 1984). Improved data are now available from a nitrogen-free (type-IIA) diamond (Odermatt *et al.*, 1986). The Mu relaxation rate and the amplitudes of the $\theta=90°$ Mu* lines in this stone are shown in Fig. 61. As in the powder experiment, with increasing temperature one sees the Mu relaxation followed by frequency-specific increases in the Mu* amplitudes.

As discussed in Sec. II.B.3 and illustrated in Fig. 20 a resonant transfer of muon polarization occurs from the Mu to the Mu* state at applied fields at which the precession frequencies of Mu and Mu* coincide. As seen in the upper part of Fig. 62 there are coincidences between ν_{12} of Mu* and ν_{12} and ν_{23} of Mu at the field values $B_+=17.2$ and $B_-=15.4$ mT, respectively. If the electron spin is conserved during the transition, a resonant transfer of muon polarization will occur at B_+ or B_-, depending on whether the isotropic part of the Mu* hyperfine interaction A_s is positive or negative, respectively. As the applied field is swept through one or the other of these values, one thus expects to observe a maximum in the a_{12} Mu* amplitude. If the electron polarization is *not* conserved during the transition, peaks should occur in the a_{12} Mu* amplitude at *both* B_+ and B_-. The width of the peak(s) reflects the transition rate Λ from Mu to Mu*; a slower transition produces a narrower peak.

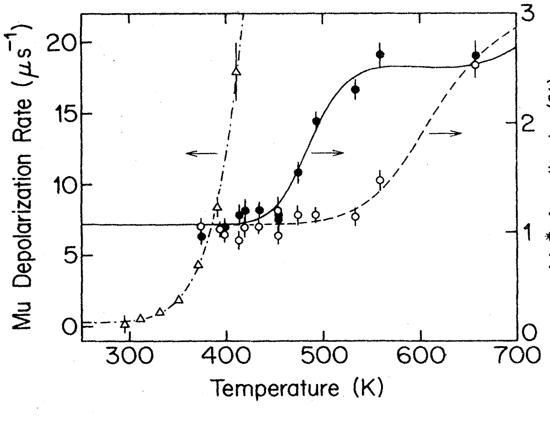

FIG. 61. The Mu relaxation rate (triangles and left-hand scale) in a nitrogen-free (type-IIa) diamond as a function of temperature in an applied field of 1.25 mT. Also shown are the Mu* precession amplitudes a_{12} (solid circles) and a_{34} (open circles) for centers with the symmetry axis perpendicular to an applied field of 16.5 mT (right-hand scale). The dot-dashed curve represents an Arrhenius law for the Mu relaxation rate (plus a temperature-independent term), and the solid and dashed curves represent fits to the Mu→Mu* transition model of Meier (1982). From Odermatt *et al.* (1986).

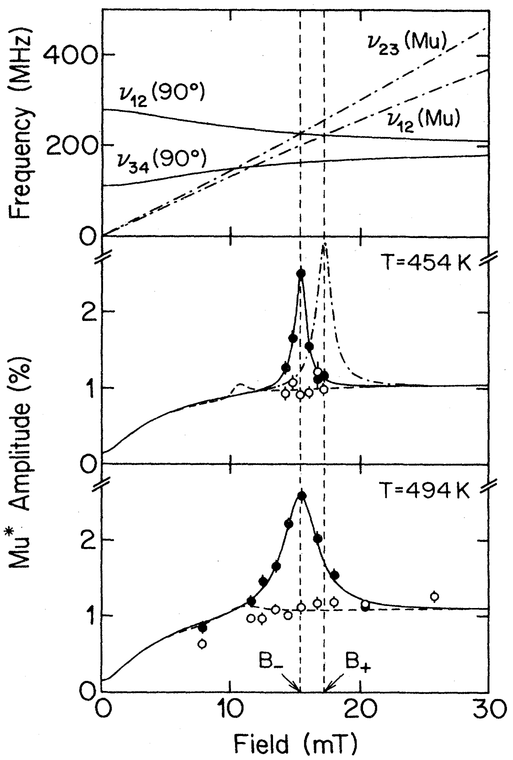

FIG. 62. The resonant transfer of muon polarization from Mu to Mu* in diamond. The upper section shows the Mu (dot-dashed curves) and Mu* (solid curves) precession frequencies as a function of applied field and indicates the field values B_- and B_+ at which coincidences occur between the Mu* frequency ν_{12} and the Mu frequencies ν_{23} and ν_{12}. The center and lower sections show the field-dependent Mu* amplitudes a_{12} (solid circles, solid curves) and a_{34} (open circles, dashed curves) at two different temperatures. The resonant polarization transfer at B_- implies that A_s, the isotropic part of the Mu* hyperfine interaction, has the opposite sign to that in Mu (i.e., it is negative). The dot-dashed curves in the center section show the expected behavior for a positive A_s. From Odermatt *et al.* (1986).

The central and lower parts of Fig. 62 show field-dependent measurements made on the type-IIa diamond. A single resonant peak in the a_{12} Mu* amplitude (solid circles) is clearly seen, while the amplitude a_{34} (open circles) shows no effect. The narrower resonance at the lower temperature indicates a lower transition rate [Λ $(T=454\text{ K})=46$ (5) μs^{-1}, Λ $(T=494\text{ K})=142$ (12) μs^{-1}].

As seen in Figs. 61 and 62, there is a prompt fraction of Mu* that is formed at $t=0$, as well as the indirect fraction that forms first as Mu. These two fractions must be added in phase for each of the two Mu* symmetry axes perpendicular to the applied field. After having determined the fractions with global fits to the data, it was possible to extract a transition rate Λ from the Mu* amplitude data of Fig. 61 for the individual temperature points. These determinations, together with the Mu relaxation rate (minus a temperature-independent constant) and the two values of Λ from the field-dependent measurements, are shown in an Arrhenius plot in Fig. 63. The data are nicely consistent, showing that no additional relaxation processes are important. The fitted parameters for the Arrhenius law (5.23),

$$\begin{aligned} \Psi &= 1.14\ (28)\times 10^{13}\ \mathrm{s}^{-1}\ , \\ E_a &= 0.476\ (9)\ \mathrm{eV}\quad (\text{crystal})\ , \end{aligned} \tag{5.25}$$

are slightly different from those from the powder experiment [Eq. (5.24)].

Thus Mu is thermally excited to cross a barrier of approximately 0.5 eV to form the more stable Mu* state, and the transition occurs without polarization loss by the bound electron. The prefactor Ψ is of the order of an optical phonon frequency (Warren *et al.*, 1967), which is approximately the highest frequency possible for thermal motion in a solid. This implies that if Mu succeeds in crossing the barrier, a *single hop* brings it to the Mu* state.

It is clear from Fig. 62 that the resonant peak in the Mu* amplitude occurs at B_-, implying a *negative* sign for A_s. Thus the correct picture of Mu* in diamond, and by extension in the other diamond and zincblende materials, is that of an approximately diamagnetic center which is "exchange polarized" by a distant paramagnetic electron.

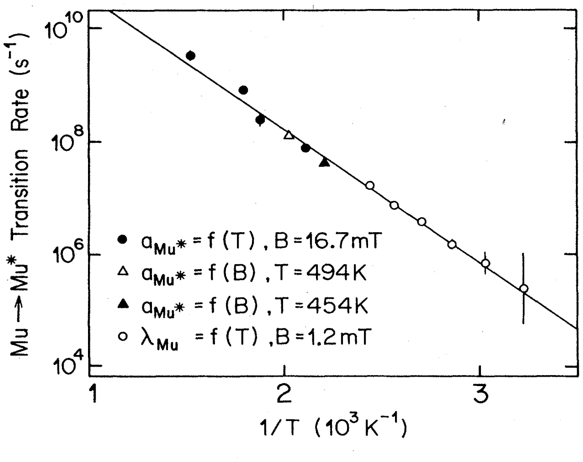

FIG. 63. An Arrhenius plot of the transition rate Λ from the Mu to the Mu* state in diamond as determined in three different ways: ○, the observed Mu relaxation rate corrected by a small temperature-independent term; ●, temperature-dependent measurements of the Mu* amplitudes; △, ▲, widths of the resonant peaks seen in field-dependent measurements of the Mu* amplitudes at two different temperatures. The line corresponds to the Arrhenius parameters in Eq. (5.25). From the Zurich group (unpublished).

G. Muonium dynamics in silicon, germanium, and gallium arsenide

Two classes of processes are important for the dynamics of muonium states in semiconductors. These involve either (a) motion of the muon or (b) interactions of muonium with free charge carriers. Particular examples of muon motion have been treated in Secs. V.E (Mu diffusion) and V.F (change of site in diamond), where it was shown that typical activation energies for muon motion range from approximately zero to 500 meV (0–6000 K). The interaction of muonium with free carriers is limited by the muonium-electron collision rate,

$$\nu_{\text{collision}} = \sigma_{\text{collision}} v_e n\ , \tag{5.26}$$

where $\sigma_{\text{collision}}$ is a typical cross section ($\sim 10^{-15}\ \mathrm{cm}^2$), v_e is a typical thermal electron velocity [$(3\ \mathrm{kT}/m_e)^{1/2} \sim 10^7\ \mathrm{cm\,s}^{-1}$], and n is the free-carrier density. We expect such collisions to produce observable effects when $\nu_{\text{collision}}$ is of the order of either the muon-decay rate ($5\times 10^5\ \mathrm{s}^{-1}$) or a muonium hyperfine frequency ($2\times 10^9\ \mathrm{s}^{-1}$), and according to Eq. (5.26) this will occur at carrier concentrations of approximately $5\times 10^{13}\ \mathrm{cm}^{-3}$ and $2\times 10^{17}\ \mathrm{cm}^{-3}$, respectively.

The carrier concentration in a semiconductor can be altered either by doping with electrically active impurities or by the intrinsic thermal creation of electrons and holes. Figure 64 shows the intrinsic electron concentration in silicon and germanium as a function of temperature, as determined by Morin and Maita (1954a, 1954b). The rate of collisions between the muon and intrinsic electrons becomes comparable to the muon-decay rate in silicon and germanium at approximately 450 and 320 K, respectively.

Numerous μSR data exist on the dynamics of muonium states, principally in silicon and germanium. These

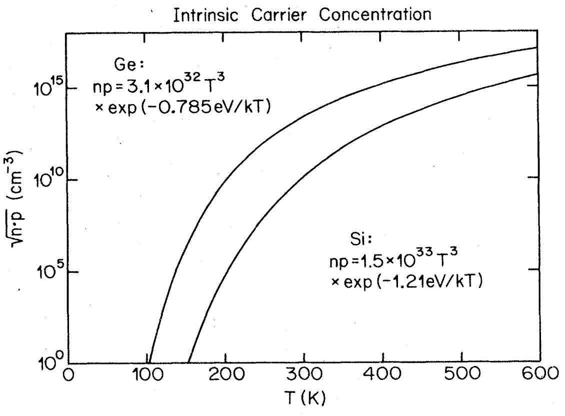

FIG. 64. Intrinsic carrier concentrations in silicon and germanium, expressed as the product of the electron and hole concentrations. From measurements by Morin and Maita (1954a, 1954b).

data are reviewed in this section, which is organized as follows. A subsection is devoted to each of the materials Si, Ge, and GaAs, and within each subsection the experimental results are classified as (a) temperature-dependent effects in high-purity samples, (b) doping-dependent effects, and (c) longitudinal-field measurements. Experience has shown that the dynamic quantities measured with μSR which depend on temperature and doping are the Mu* relaxation rate λ_{Mu^*}, the Mu relaxation rate λ_{Mu}, the diamagnetic μ^+ amplitude a_{μ^+}, and the μ^+ relaxation rate λ_{μ^+}. The temperature- and doping-dependent results are presented in this order.

A general observation for high-purity Si, Ge, and GaAs is that, with increasing temperature, λ_{Mu^*} first begins to increase due to a $\mathrm{Mu}^* \rightarrow \mu^+$ transition, followed by an increase in λ_{Mu} from a $\mathrm{Mu} \rightarrow \mu^+$ transition. The μ^+ amplitude shows stepwise increases as the corresponding transition rates become sufficiently large to prevent muon dephasing. The diamagnetic state itself becomes unstable at the highest temperatures measured, presumably due to repeated "charge exchanges" between the μ^+ state and a paramagnetic state. The relaxation rates of all three states are doping dependent, and even nominally high-purity material shows sample-dependent effects. The longitudinal-field quenching of this relaxation is helpful in determining the causes of the relaxation.

The final subsection treats dynamic effects that are induced by applied electric fields, illumination with visible light, and particle irradiation.

1. Silicon

Silicon is the semiconductor that has been most intensively studied with μSR. The first doping- and temperature-dependent studies of muonium states in silicon were the longitudinal-field quenching experiments of Feher *et al.* (1960) and Eisenstein *et al.* (1966). Figure 65 shows their time-averaged muon polarization measured at room temperature in silicon and at two temperatures in germanium. Note the metallic-like lack of depolarization at extreme *p* and *n* doping, where the carrier-muon collision frequency $\nu_{\mathrm{collision}}$ from Eq. (5.26) exceeds the Mu hyperfine frequency. Note also the sudden change in the muon polarization that occurs at approximately 10^{13} cm^{-3} *n* doping (where $\nu_{\mathrm{collision}}$ is of the same order as the muon-decay rate). A more complete picture from Patterson, Kündig *et al.* (1978) (Fig. 66) shows the observed precession amplitudes of the μ^+, Mu, and Mu* fractions at three temperatures. The sudden change in the room-temperature μ^+ amplitude with *n* doping is again observed.

a. Effects of temperature

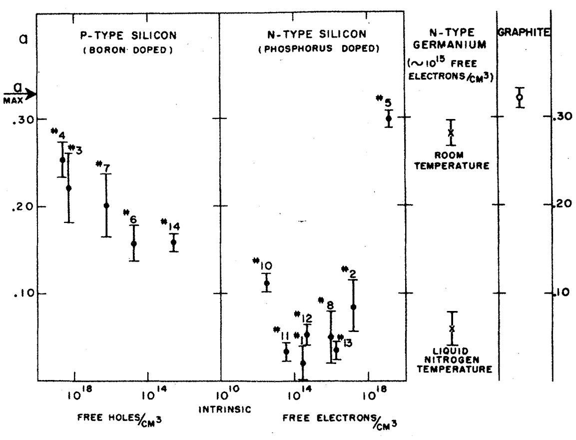

FIG. 65. The muon polarization in doped silicon at room temperature compared to that in warm and cold germanium and in graphite. The measurements were performed by comparing the forward and backward positron emission rates in transverse applied fields of zero and 4 mT. The integrated rates were recorded starting 0.6 μs after the muon stop during a 1.2-μs time window. From Feher *et al.* (1960).

It has been established in numerous experiments that the amplitudes of the Mu and Mu* states are to a good approximation temperature and doping independent in silicon and germanium; the apparent variations in Figs. 65 and 66 are due to changes in the relaxation rates of these signals. [The observation of a temperature-dependent Mu* formation probability and of Mu* precession signals above 165 K in silicon by Boekema *et al.* (1981) have not been reproduced in later work (Albert, 1986; the Zurich group, unpublished).] An overview of

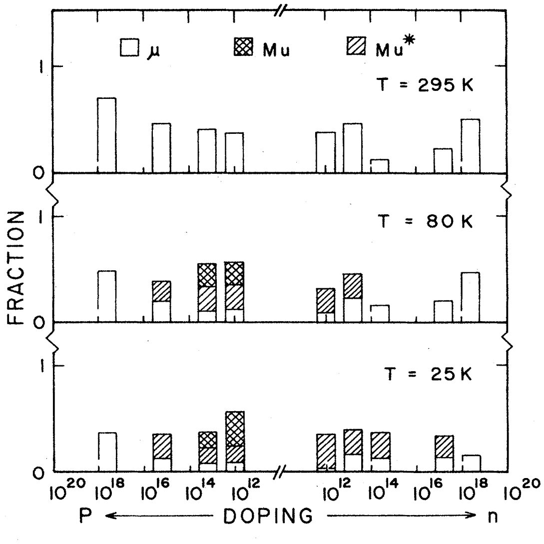

FIG. 66. The muon state formation probabilities in silicon measured in intermediate-field precession experiments as a function of temperature and doping (Patterson, Kündig *et al.*, 1978). The fractions should be taken as lower limits, since the effects of signal relaxation and finite time resolution were not accounted for.

the temperature-dependent dynamics data in silicon is presented in Fig. 67, where the relaxation rates for Mu* and Mu, the μ^+ amplitude, and the μ^+ relaxation rate are plotted for high-purity samples as a function of temperature. The data in the figure have been collected from the sources given in Table XV, and all were taken with conventional muons, with the exception of the λ_{Mu^*}, a_{μ^+}, and λ_{μ^+} measurements on p-type material with 10^{12} cm^{-3} acceptors, for which surface muons were used.

λ_{Mu^*}: The Mu* relaxation rate in silicon measured by the Zurich group (unpublished) rises sharply as the temperature is increased above 140 K, and no precession is observed above 165 K, in agreement with Blazey *et al.* (1981) and Albert *et al.* (1984). Blazey *et al.* found that λ_{Mu^*} is independent of the orientation of the sample. The Zurich group has fitted $\lambda_{\mathrm{Mu}^*}(T)$ for a 13 500-Ω cm sample to an Arrhenius law of the form

$$\lambda(T)=\Psi\exp(-E_a/\mathrm{k}T)+\lambda(0)\ , \tag{5.27}$$

with the values

$$\Psi=9.5\ (7.1)\times10^5\ \mathrm{s}^{-1}\ ,$$
$$E_a=0.168\ (10)\ \mathrm{eV}\ , \tag{5.28}$$
$$\lambda(0)=0.041\ (15)\ \mu\mathrm{s}^{-1}\ .$$

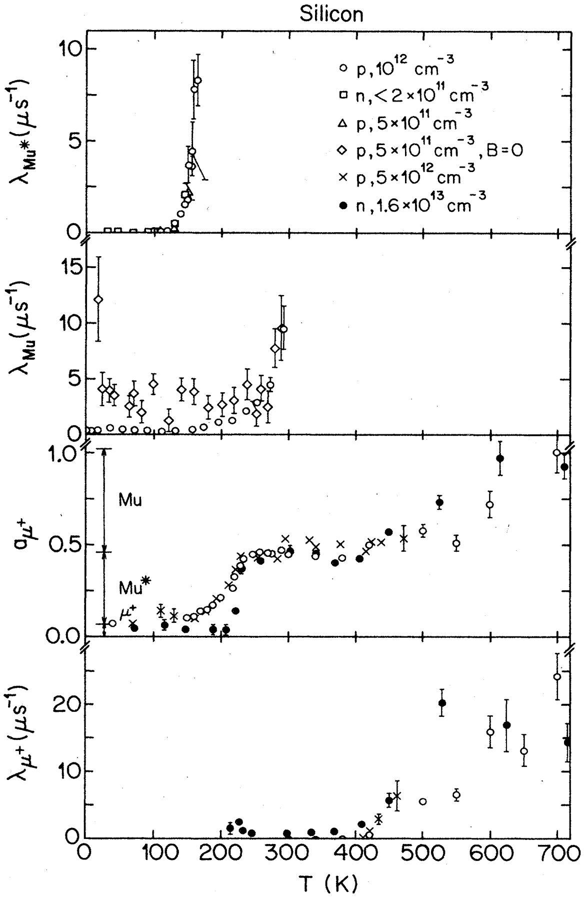

FIG. 67. Collected data on the temperature-dependent dynamics of muon states in high-purity silicon. The indicated low-temperature muon state fractions in the a_{μ^+} panel are from Table VIII. References for the individual data sets are given in Table XV.

TABLE XV. References for the transverse-field, high-purity silicon data in Fig. 67.

Doping (cm^{-3})	B (mT)	Reference
p, $10^{12}(\lambda_{\mathrm{Mu}^*})$	290	Zurich group (unpublished)
p, $10^{12}(a_{\mu^+},\lambda_{\mu^+})$	10	Zurich group (unpublished)
p, $10^{12}(\lambda_{\mathrm{Mu}})$	0.5	Patterson, Holzschuh, Kiefl, Blazey, and Estle (1984)
n, $<2\times10^{11}$	200	Albert *et al.* (1984)
p, 5×10^{11}	15	Blazey *et al.* (1981)
p, 5×10^{11}	0	Holzschuh (1983)
p, 5×10^{12}	42	Barsov *et al.* (1980)
n, 1.6×10^{13}	23.6	Barsov *et al.* (1979)

This activation energy is in disagreement with the 0.11 eV found by Blazey *et al.*, and the Zurich data are incompatible with the T^9 law cited by those authors for a Raman process.

λ_{Mu}: The relaxation of the isotropic Mu state in high-purity silicon begins rising above 140 K, and precession can no longer be observed above 300 K. The 0.5-mT data of Patterson, Holzschuh *et al.* (1984) on the 13 500-Ω cm sample is well represented below 290 K by the Arrhenius law (5.27) with the values

$$\Psi=6.54\times10^8\ \mathrm{s}^{-1}\ ,$$
$$E_a=0.114\ \mathrm{eV}\ , \tag{5.29}$$
$$\lambda(0)=0.35\ \mu\mathrm{s}^{-1}\ .$$

It should be noted that a 0.5-mT room-temperature measurement lay significantly above this curve and that the linewidth measured at 0.5 mT at 275 K agreed excellently with that of the direct transition seen with the zero-field technique.

The Mu relaxation rate in silicon appears to be sample dependent, even in nominally high-purity samples. Very-low-temperature data of Bucci *et al.* (1981) on a 2000-Ω cm sample show an increase in λ_{Mu} below 10 K, reaching a value of 4 $\mu\mathrm{s}^{-1}$ at 60 mK, and Patterson, Holzschuh *et al.* (1984) found a rate of 1.6 $\mu\mathrm{s}^{-1}$ in the temperature range 1.6–4.2 K in a 30 000-Ω cm sample. There is also a report in the literature of the sample-dependent disappearance of triplet Mu signals in ultrapure silicon at 4.2 K (Brewer, 1979). These sample-dependent low-temperature relaxation rates in silicon presumably indicate that electrically inactive impurities are trapping mobile Mu. The apparently extremely rapid motion of Mu at low temperature in silicon and germanium has been documented in Sec. V.E.

The low-temperature Mu relaxation rate in silicon also depends on the frequency ν_{ij} of the Mu precession component. A comparison of λ_{Mu} measured in the same 30 000-Ω cm sample at 1 mT (where $\nu_{12} \simeq \nu_{23} \simeq 14$ MHz) and at zero field ($\nu_{24} \simeq 2000$ MHz; Holzschuh, 1983) showed that, below 20 K, the direct transition ν_{24} is very strongly damped, while the intratriplet line remains narrow (see Fig. 67). Holzschuh interpreted this frequency-dependent relaxation in terms of the hopping of Mu among inequivalent sites with slightly varying, but still isotropic, hyperfine interactions. In contrast to the direct transition, the triplet precession is insensitive to such a variation. As discussed in Sec. V.C.2 such hopping was also used by Holzschuh to explain the nonmonotonic temperature dependence of the Mu hyperfine frequency A in silicon.

Additional measurements of λ_{Mu} and A have been performed on the 13 500-Ω cm and the 30 000-Ω cm samples by the Zurich group with the high-transverse-field technique (Felber, 1984). By varying the field, one could change the frequencies of the precession lines ν_{12} and ν_{34} over a wide range and alter their sensitivity to a variation of the hyperfine frequency A. Results of the experiment at 15 K are summarized in Table XVI.

All the A values measured by Felber at 15 K are in approximate agreement with that found by Holzschuh (2009 MHz) at zero field in the 30 000-Ω cm sample and are well below the maximum A value of 2015 MHz measured by Holzschuh at 75 K. This implies that the nonmonotonic behavior of $A(T)$ is present in *both* samples. Furthermore, the 30 000-Ω cm sample shows the expected frequency-dependent linewidth: broader lines for a higher sensitivity of the precession frequency to a variation in A [i.e., λ_{12} decreases and λ_{34} increases with increasing field; see the discussion of the Mu jump model of Celio (1985) in Sec. II.B.2]. What is surprising in Felber's data, however, are the much narrower lines observed in the 13 500-sample at all fields. This again points to sample-dependent trapping of Mu at low temperature in silicon, and it demonstrates that the nonmonotonic $A(T)$ dependence and the low-temperature Mu relaxation seen in silicon have *different* origins.

a_{μ^+}: The amplitude of the diamagnetic muon signal a_{μ^+} in silicon increases from a value of 10% or less at low temperature to virtually 100% at 700 K (see Fig. 67). This increase occurs in two distinct steps, one near 200 K and a second near 500 K, associated with polarization transfers from the disappearing Mu* and Mu states, respectively. This is obvious from the correlation of the a_{μ^+} steps with the increases in λ_{Mu^*} and λ_{Mu} on the one hand, and from the agreement between the size of the steps and the fraction of the polarization originally appearing as Mu* and Mu on the other hand (note the indicated fractions in Fig. 67).

There appear to be significant differences in the form of $a_{\mu^+}(T)$ from one experiment to another. For the case of the 200-K Mu*→μ^+ step, this may reflect the strong doping dependence of the Mu* relaxation rate, which will be discussed in the following section, or it may reflect the fact that the experiments were performed at different applied fields. The 500-K Mu→μ^+ step is difficult to measure accurately due to the simultaneous increase in the muon relaxation rate.

The 500-K step in $a_{\mu^+}(T)$ has been fit to a model in which Mu makes a transition to the μ^+ state at a rate given by an Arrhenius law (Gordeev *et al.*, 1978). Gordeev *et al.* fit their data for an *n*-type silicon sample, 1.6×10^{13} cm^{-3} [identical to that of Barsov *et al.* (1979) in Fig. 67] to Eq. (2.52), assuming a negligible spin-flip rate ν and a modified Arrhenius law for Λ, and obtained an activation energy of $E_a = 0.18$ eV. (I have performed the same analysis of their data and have obtained $E_a = 0.39$ eV.) This is not in good agreement with the activation energy of 0.114 eV obtained from $\lambda_{\mathrm{Mu}}(T)$ in sil-

TABLE XVI. High-transverse-field measurements of the Mu hyperfine frequency A and precession linewidth λ in two high-purity silicon samples. From Felber (1984).

Si sample (ohm cm)	B (T)	Mu line	Frequency (MHz)	A (MHz)	λ (μs^{-1})
30 000	0.1	ν_{12}	686.774 (56)		3.67 (36)
		ν_{34}	1321.28 (48)		20.7 (3.0)
				2008.05 (48)	
30 000	0.5	ν_{12}	863.73 (10)		5.50 (63)
		ν_{34}	1142.23 (14)		8.69 (89)
				2005.96 (17)	
13 500	0.1	ν_{12}	701.076 (47)		0.92 (30)
		ν_{34}	1307.14 (8)		1.91 (48)
				2008.22 (15)	
13 500	0.5	ν_{12}	865.131 (65)		0.85 (41)
		ν_{34}	1143.20 (7)		1.08 (45)
				2008.33 (10)	

icon [Eq. (5.29)]. Such a Mu$\rightarrow\mu^+$ transition should produce a measurable shift of the initial phase φ of the muon precession signal, and evidence of such a shift at 380 K has been mentioned by Barsov *et al.* (1980). No arrhenius analysis has yet been done of the increase of a_{μ^+} associated with the Mu$^*\rightarrow\mu^+$ transition in silicon.

λ_{μ^+}: In high-purity silicon, the relaxation rate λ_{μ^+} of the diamagnetic muon signal is negligible below 400 K (see Fig. 67). [The observation of a μ^+ component in mildly doped (5.3×10^{13} cm^{-3}) *p*-type silicon that relaxed with a rate of 30 μs^{-1} at 77 K and 0.44 T cited by Johnson (1976) and Brewer *et al.* (1975), has not been reproduced.] The rate λ_{μ^+} increases sharply above 400 K, implying that the μ^+ state becomes unstable. Note that 400 K is the temperature at which the collision rate defined in Eq. (5.26) between the muon and intrinsic carriers is of the order of the muon-decay rate.

b. Effects of doping

The effects on the muonium states of doping silicon with phosphorous donors (*n*-type doping) are summarized in Fig. 68. These are unpublished data of the Zurich group taken using conventional muons with the high-transverse-field technique at an applied field of 0.9 T. The relaxation rates of all three muon states increase with *n* doping.

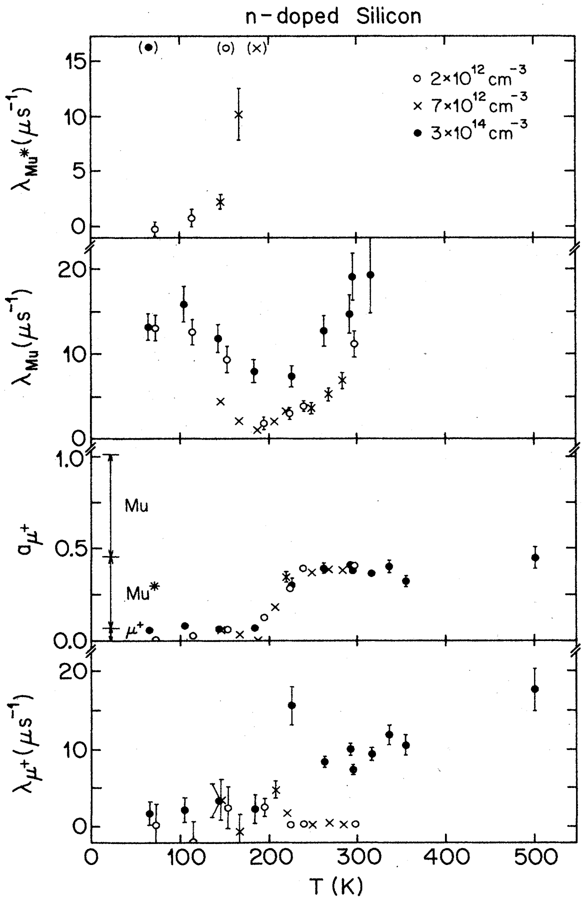

FIG. 68. Data on the dynamics of muon states in *n*-doped silicon at 0.9 T. From the Zurich group (unpublished). The indicated low-temperature muon state fractions in the a_{μ^+} panel are from Table VIII.

λ_{Mu^*}: The effect of *n* and *p* doping on the Mu* relaxation rate in silicon has been intensively studied at the magic field (B^*_{mag}) by Albert *et al.* (1984, 1985b), and these results are reproduced in Figs. 69 and 70. In both sets of data, two contributions to λ_{Mu^*} are seen, one proportional to the free-carrier concentration *n* (solid curves) and the other an activated intrinsic process (dashed curves) also seen in high-purity samples. The proportionality of λ_{Mu^*} to carrier concentration below 140 K is most dramatic in the *p*-type data of Fig. 70, where acceptors with different ionization energies were used. The authors conclude that the doping-dependent contribution λ_{Mu^*} (doping) follows the laws

$$\lambda_{\mathrm{Mu}^*}(\text{doping})=\begin{cases} n\,2\times10^{-7}\ \mathrm{cm}^3\,\mathrm{s}^{-1} & (n\text{-type})\,,\\ n\,2\times10^{-9}\ \mathrm{cm\,s}^{-1} & (p\text{-type})\,,\end{cases} \tag{5.30}$$

and they ascribe this contribution either to the scattering of carriers on Mu* or to a change of charge state resulting from the capture by Mu* of a carrier. Note that these rates are of the order of the carrier-muon collision

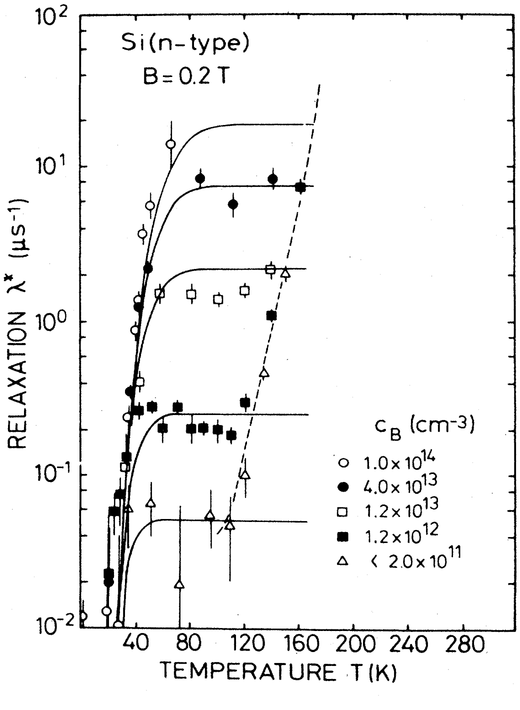

FIG. 69. Doping and temperature-dependent Mu* relaxation rates in *n*-doped silicon measured at the magic field $B^*_{\mathrm{mag}}\simeq0.2$ T. The solid curves show the relation $\lambda_{\mathrm{Mu}^*}=n2\times10^{-7}$ cm^3 s^{-1}, and the dashed curve indicates an intrinsic process. From Albert *et al.* (1984).

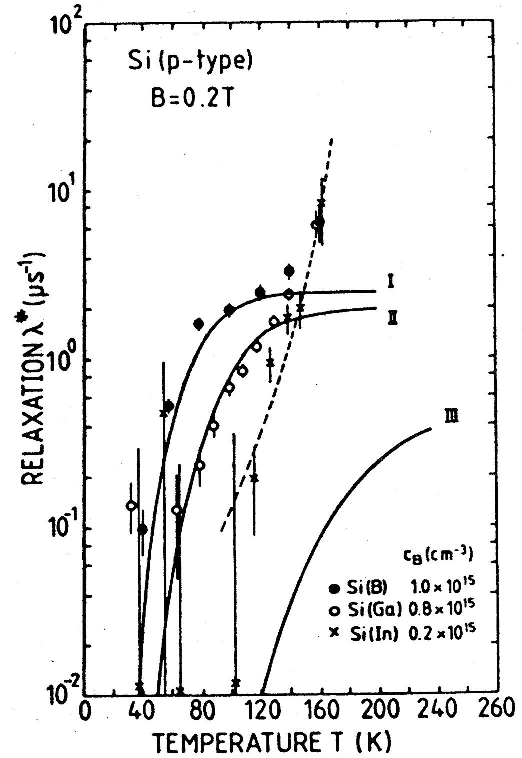

FIG. 70. Doping- and temperature-dependent Mu* relaxation rates in silicon doped with different acceptors measured at the magic field $B^*_{\mathrm{mag}} \simeq 0.2$ T. The solid curves show the relation $\lambda_{\mathrm{Mu}^*} = n 2\times 10^{-9}$ cm^3 s^{-1}, and the dashed curve indicates an intrinsic process. From Albert *et al.* (1985b).

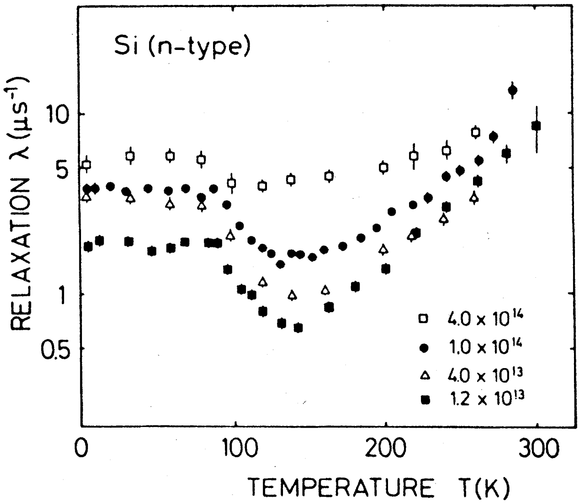

FIG. 71. Doping- and temperature-dependent Mu relaxation rates in *n*-doped silicon at 1 mT. From Weidinger *et al.* (1983).

frequency ($\nu_{\mathrm{collision}} = n\,10^{-8}$ cm^{3}s^{-1}) estimated in Eq. (5.26).

λ_{Mu}: A transverse-field study (with conventional muons at 1 mT) of the relaxation of isotropic Mu in *n*-type silicon is shown in Fig. 71 (Weidinger *et al.*, 1983). Noteworthy are (a) the temperature-independent but doping-dependent plateaus in λ_{Mu} below 90 K, (b) the approximately doping-independent rise in λ_{Mu} above 200 K, and (c) the doping- and temperature-dependent regions at intermediate temperatures.

Low-temperature plateaus similar to these have been observed in doped germanium (see Sec. V.G.2.b) by Weidinger *et al.* (1981) and tentatively explained in terms of an exchange interaction of Mu with neutral, paramagnetic dopant atoms. This mechanism cannot explain the plateaus in doped silicon (nor, by extrapolation, in doped germanium) for the following reasons.

(a) Such an exchange interaction should be quenched by an applied field of the order of 50 mT. But measurements in transverse fields up to 0.1 T by Albert (1986) and up to 1.1 T by the Zurich group (unpublished) show no significant change in λ_{Mu}.

(b) The plateau values of λ_{Mu} are not uniquely determined by the phosphorous dopant concentration, as can be seen from a comparison of the Zurich measurements (Fig. 68) with those of Weidinger *et al.* (Fig. 71).

(c) As seen in Fig. 69, the phosphorous donors in silicon are completely ionized at 50 K, whereas the λ_{Mu} plateau extends to 90 K.

In the following section longitudinal-field measurements by Weidinger *et al.* (1983) will be discussed which demonstrate that a dephasing mechanism is responsible for the plateaus and not a spin-flip process. Transverse-field μSR measurements by Boekema *et al.* (1981) on some of the same samples as in Fig. 68 indicate that the Mu relaxation rate at 20 K in *n*- and *p*-doped silicon is proportional to $n^{0.1}$, with a 2.5 times higher rate in the *n*-doped material (Boekema, 1983). Albert (1986), on the other hand, finds no significant difference between the *n*- and *p*-doping dependences of λ_{Mu} at 10 K, and he sees an $n^{0.5}$ dependence of λ_{Mu} in *n*-type silicon at 140 K. All these observations are compatible with a model in which Mu relaxes at low temperature due to trapping at impurities. Such trapping would be in accordance with the high Mu diffusion rates discussed in Sec. V.E and the sample-dependent relaxation effects discussed in Sec. V.G.1.a.

a_{μ^+}: It is clear from Fig. 68 that moderate phosphorous doping causes no dramatic change in the temperature dependence of the diamagnetic amplitude a_{μ^+}.

λ_{μ^+}: Figure 68 also shows that weak *n* doping of silicon has no marked effect on the relaxation rate λ_{μ^+} of the diamagnetic signal, except perhaps to produce a small maximum around 200 K, the temperature at which the amplitude a_{μ^+} of this signal begins to increase. Such a peak is also seen in the *n*-type data of Barsov *et al.* (1980) in Fig. 67. A strong effect is seen, however, upon doping to a phosphorous concentration of 3×10^{14}. This produces a λ_{μ^+} of approximately 10 μs^{-1} for temperatures above 230 K, implying that sufficient *n* doping also makes the μ^+ state unstable, perhaps in a similar fashion to the thermally excited carriers in undoped silicon. Note that the muonium-electron collision rate (5.26) at a doping of 3×10^{14} cm^{-3} is in approximate agreement with the μ^+ relaxation rate ($10\,\mu s^{-1}$).

It is the failure to account for this doping-dependent μ^+ relaxation which is responsible for the decreased amplitude of the μ^+ signal in the n-doping region in the early experiments of Feher *et al.* (1960) (Fig. 65) and Patterson, Kündig *et al.* (1978) (Fig. 66). The same samples were used in Fig. 68 and by Patterson, Kündig *et al.* (1978).

The comparison of μSR spectra in float-zone and Czochralski-grown silicon presented in Sec. V.B showed that the presence of the 10^{18}-cm^{-3} oxygen impurities in the Czochralski material caused the disappearance of the Mu signals. This was interpreted in Sec. V.E in terms of trapping of rapidly moving Mu. It was also shown that oxygen destroyed the diamagnetic μ^+ signal at 30 K while leaving the Mu* signals unchanged. The comparison between float-zone and Czochralski silicon is extended to room temperature in Fig. 72. Note that not only is the μ^+ signal absent in Czochralski silicon at low temperature, it is also missing at room temperature. Apparently the presence of dilute oxygen impurities inhibits the Mu*$\rightarrow\mu^+$ transition seen in float-zone material. Examination of the μSR time histograms from room-temperature Czochralski runs reveals a μ^+ signal that decays with an extremely rapid, sample-dependent rate of the order of $30\,\mu s^{-1}$. The implication of this admittedly sparse data is that the intrinsic Mu* relaxation discussed above is due to a transition to a *mobile* μ^+ state, which subsequently traps at the oxygen impurities.

c. Longitudinal-field experiments

Several studies of the longitudinal relaxation rate $\lambda_\parallel$ in n-doped silicon as a function of the applied longitudinal field are summarized in Fig. 73. The sample with 10^{14} cm^{-3} doping was studied by Ivanter *et al.* (1978), and that with 1.6×10^{13} cm^{-3} was studied by Barsov *et al.* (1980).

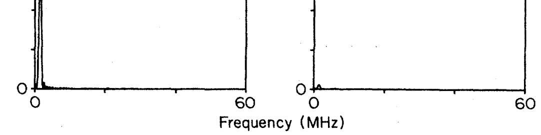

FIG. 72. Transverse-field μSR spectra in float-zone and Czochralski-grown silicon. The approximately 10^{18}-cm^{-3} oxygen impurities in the Czochralski sample have no effect on Mu*, but destroy entirely the μ^+ signal (as well as the Mu signal—see Fig. 45). From the Zurich group (unpublished).

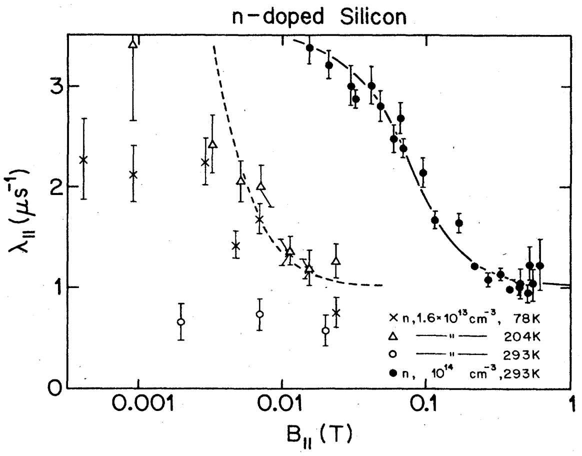

FIG. 73. Collected longitudinal-field relaxation studies in n-doped silicon. The sample with 1.6×10^{13} cm^{-3} doping was studied by Barsov *et al.* (1980), and that with 10^{14} cm^{-3} was studied by Ivanter *et al.* (1978). The dashed curve shows $\lambda_\parallel(B_\parallel)$ for Mu* ($\theta=70.5°$) undergoing Nosov-Yakovleva spin flips at a rate $\nu=10\,\mu s^{-1}$, and the solid curve is for Mu with $\nu=5\,\mu s^{-1}$. Background relaxation rates of $1\,\mu s^{-1}$ have been assumed in both cases.

At 78 and 204 K, Barsov *et al.* find a $\lambda_\parallel$ that is quenched by an applied field of 20 mT, indicating that it arises from the relaxation of the Mu* state (see Fig. 23). This is confirmed by their simultaneous observation of a rise in the polarization $a_\parallel$. In this experiment the crystal was oriented with the [111] axis parallel to the field. The dashed curve in Fig. 73 shows my calculation of $\lambda_\parallel(B_\parallel)$ assuming Nosov-Yakovleva spin flips of a Mu* state with symmetry axis at $\theta=70.5°$ to the applied field. The spin-flip rate is $\nu=10\,\mu s^{-1}$, and an additive background relaxation rate $\lambda_\parallel(\infty)=1\,\mu s^{-1}$, presumably from Mu, is assumed. The low-field data are poorly accounted for by this curve, perhaps because of the drop in the amplitude of the relaxing component (see Fig. 23). For comparison, the transverse-field relaxation rate λ_{Mu^*} at 78 K expected for this doping from the relation of Albert *et al.* [Eq. (5.30)] is $3.2\,\mu s^{-1}$. At 204 K the "intrinsic" Mu* relaxation has raised λ_{Mu^*} in excess of $100\,\mu s^{-1}$ (see Fig. 69). Barsov *et al.* find no longitudinal relaxation in the n-type sample at room temperature, either because ν exceeds the Mu* hyperfine frequency or because Mu* makes a very rapid change of state to μ^+. Finally, Barsov *et al.* fail to find longitudinal relaxation in a p-type sample with 5×10^{12} dopants cm^{-3} at any temperature, presumably due to the lower rate of Mu* relaxation [see Eq. (5.30)].

The more strongly doped sample of Ivanter *et al.* shows a faster longitudinal relaxation at room temperature, which quenches only above 0.2 T. Recall that the room-temperature transverse-field λ_{μ^+} rate is also greater

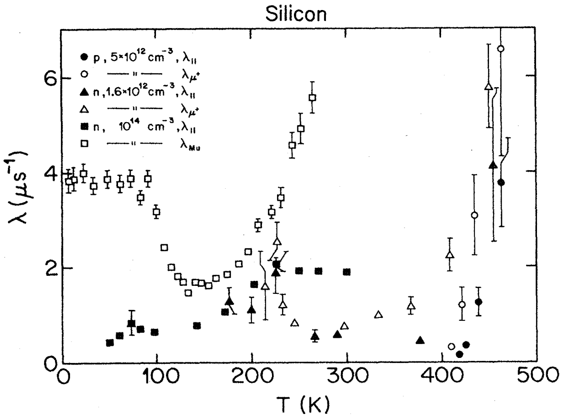

FIG. 74. Collected longitudinal- and transverse-field relaxation studies in silicon. References for the various data sets are given in Table XVII.

in an n-doped sample than in undoped material (see Fig. 68). The solid curve in Fig. 73 is my calculation of the Nosov-Yakovleva $\lambda_{\|}(B_{\|})$ assuming Mu electron spin flips with a rate $\nu=5\ \mu\text{s}^{-1}$. The background relaxation rate $\lambda_{\|}(\infty)$ was again taken to be $1\ \mu\text{s}^{-1}$, but in this case it is unexplained. Ivanter *et al.* find that the *amplitude* of the longitudinal relaxing component is also field dependent. Instead of invoking spin flipping, they propose a model involving transitions among three distinct muonium states to explain this observation:

$$\text{Mu}' \underset{\Lambda'}{\rightarrow} \text{Mu} \underset{\Lambda}{\rightarrow} \mu^+ \ . \tag{5.31}$$

A fit of the amplitude data to this model yields $A'=1580$ (80) MHz, $\Lambda'=7100\ \mu\text{s}^{-1}$, and $\Lambda=0.69\ \mu\text{s}^{-1}$, assuming negligible spin flipping in either state.

A comparison in silicon of the temperature-dependent transverse-field relaxation rates λ_{Mu} and λ_{μ^+} and the longitudinal-field rate $\lambda_{\|}$ is presented in Fig. 74. References for the data shown are given in Table XVII. The $\lambda_{\|}$ measurements were all performed at 20 mT, a field sufficient to quench a spin-flip relaxation of the Mu* state but one that leaves that of the Mu state unaffected (see Fig. 23). Two points are noteworthy.

(1) The Nosov-Yakovleva theory predicts a ratio of approximately 2/3 between $\lambda_{\|}$ and λ_{Mu} if slow electron spin flips are the principal cause of relaxation. For $\nu \ll \omega_e \ll \omega_0$,

$$(\lambda_{12}+\lambda_{23})/2=3\nu/2=3\lambda_{\|}/2 \tag{5.32}$$

(see Table V). A ratio of 2/3 between $\lambda_{\|}$ and λ_{Mu} is indeed found in the temperature range 140–220 K, indicating that Nosov-Yakovleva spin flipping of the Mu electron is responsible for the relaxation at these temperatures (Weidinger *et al.*, 1983). As for the 140-K transverse-field λ_{Mu} rate, Albert (1986) finds that $\lambda_{\|}$ in n-type silicon follows an $n^{0.5}$ doping dependence at 69, 140, and 273 K. But the low-temperature λ_{Mu} plateau in n-type silicon does not appear in $\lambda_{\|}$, implying that here the relaxation is due to dephasing, perhaps by impurity trapping, and not to spin flips. Further evidence for this conclusion was presented in the previous section. By the same argument, dephasing also causes the rise in λ_{Mu} above 220 K.

(2) Above 400 K, only a μ^+ signal is seen in transverse-field experiments in silicon, and the damping rate λ_{μ^+} and amplitude a_{μ^+} of this signal both increase with increasing temperature (see Fig. 67). The Nosov-Yakovleva theory predicts a signal at the diamagnetic μ^+ frequency for Mu which is undergoing very rapid spin flips ($\nu \gg \omega_0$). Under these circumstances, the predicted relaxation rates are

$$\lambda_{\mu^+}=\lambda_{\|}=4\omega_0^2/(4\nu) \tag{5.33}$$

(see Table V). But it is unlikely that this is the μ^+ signal seen in warm silicon for two reasons. First, the Nosov-Yakovleva theory cannot explain the gradual rise in a_{μ^+} with temperature. Second, Eq. (5.33) predicts a λ_{μ^+} rate that *decreases* with increasing spin-flip rate ν, and it is difficult to explain a decrease of ν with increasing temperature. An alternative explanation is offered by the charge exchange model of Ivanter and Smilga (1971a, 1971b; see Sec. II.B.2), in which repeated changes of state occur between Mu and a diamagnetic μ^+ state. It appears possible to find thermally activated rates for electron capture and loss that not only can account for the simultaneous rise in λ_{μ^+} and a_{μ^+} but also can explain the observed rise in $\lambda_{\|}$ (W. Odermatt, private communication).

TABLE XVII. References for the longitudinal- and transverse-field measurements or silicon presented in Fig. 74.

Doping (cm^{-3})	Measurement	B (mT)	Reference
p, 5×10^{12}	$\lambda_{\|}$	20	Barsov *et al.* (1980)
	λ_{μ^+}	42	Barsov *et al.* (1980)
n, 1.6×10^{12}	$\lambda_{\|}$	20	Barsov *et al.* (1980)
	λ_{μ^+}	23.6	Gordeev *et al.* (1978)
n, 10^{14}	$\lambda_{\|}$	20	Albert (1986)
	λ_{Mu}	1	Weidinger *et al.* (1983)

2. Germanium

In general, germanium presents a similar picture of muonium dynamics to that of silicon. Two important differences between the two hosts should be noted, however: (a) Germanium shows a much smaller Mu* formation probability than does silicon. (b) Whereas the Mu and Mu* precession signals in silicon disappear at two well-separated temperatures (165 and 300 K, respectively), both states disappear at approximately 110 K in high-purity germanium.

a. Effects of temperature

Representative measurements of the temperature-dependent quantities λ_{Mu^*}, λ_{Mu}, a_{μ^+}, and λ_{μ^+} are shown in Fig. 75 for high-purity germanium, and the references for the data are given in Table XVIII. As in the case of silicon, both muonium states disappear with increasing temperature, and their polarizations reappear in the diamagnetic μ^+ state. At still higher temperatures, the μ^+ state again shows an increased relaxation rate.

λ_{Mu^*}: The three measurements of the Mu* relaxation rate $\lambda_{\mathrm{Mu}^*}(T)$ in high-purity germanium are in agreement (Weidinger *et al.*, 1981; Blazey *et al.*, 1983; Döring *et al.*, 1983). Blazey *et al.* have analyzed their data in terms of an Arrhenius law and find an activation energy of 26 meV, compared to the values of 168 and 110 meV for $\lambda_{\mathrm{Mu}^*}(T)$ in silicon. No agreement was possible with a T^9 law typical for a Raman process. These authors also found no significant dependence of λ_{Mu^*} on the crystal orientation.

λ_{Mu}: As in the case of silicon, the relaxation rate of the isotropic Mu state λ_{Mu} in high-purity germanium also shows a monotonic rise with increasing temperature. Weidinger *et al.* (1981) have determined an activation energy of 12 (3) meV from the doping-independent rise in λ_{Mu} above 50 K. Also as for silicon, a zero-field study (Holzschuh, 1983) showed an increased relaxation rate of the direct hyperfine transition [10 (4) μs^{-1} at 4.2 K] which is not observed for the intratriplet transitions [Patterson, Holzschuh *et al.*, (1984) measured less than 0.35 μs^{-1} at this temperature]. This indicates that germanium shows a similar low-temperature Mu trapping behavior to that observed in silicon.

a_{μ^+}: Except for a small step reported by Döring *et al.* (1984) between 5 and 20 K, the diamagnetic amplitude a_{μ^+} in germanium changes only in the temperature range 150–300 K from less than 15% to virtually 100%. That this rise is associated with a Mu→μ^+ transition is most elegantly demonstrated by the measurements of the initial phase φ of the μ^+ precession signal by Kudinov *et al.* (1975, 1976; see Figs. 76 and 19). In their analysis of φ and a_{μ^+} as functions of field, these authors assumed a Mu→μ^+ transition that proceeds at the rate Λ and

TABLE XVIII. References for the transverse-field, high-purity germanium data in Fig. 75.

Doping (cm^{-3})	B (mT)	Reference
$<1.5\times10^{10}$ (λ_{Mu^*})	300–400	Weidinger *et al.* (1981)
$<1.5\times10^{10}$ (λ_{Mu})	6	Weidinger *et al.* (1981)
$<4\times10^{10}$	200	Blazey *et al.* (1983)
p, 2.2×10^{11}	6	Döring *et al.* (1983)
p, 10^{14}	5	Andrianov *et al.* (1969)
n, 10^{14} (a_{μ^+})	5	Andrianov *et al.* (1978a)
n, 10^{14} (λ_{μ^+})	12	Kudinov *et al.* (1977)

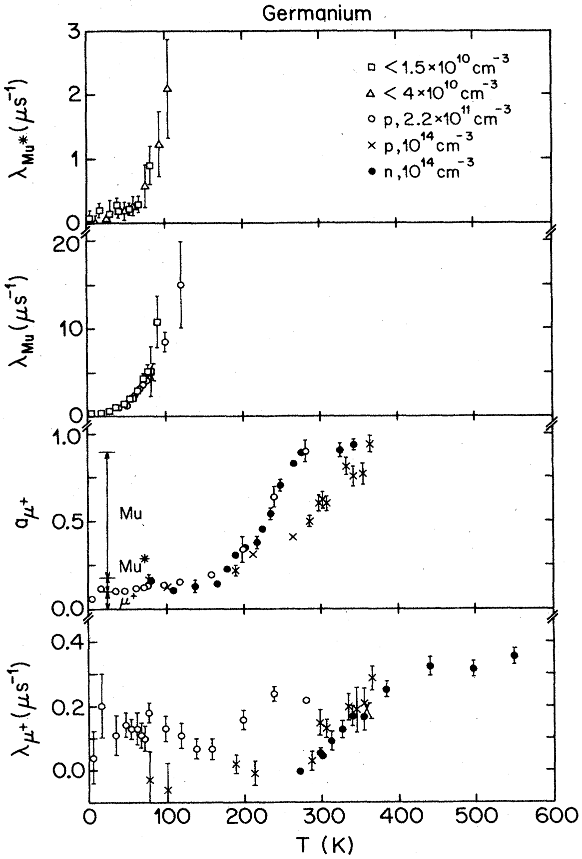

FIG. 75. Collected data on the temperature-dependent dynamics of muon states in high-purity germanium. The indicated low-temperature muon state fractions in the a_{μ^+} panel are from Table VIII. References for the individual data sets are given in Table XVIII.

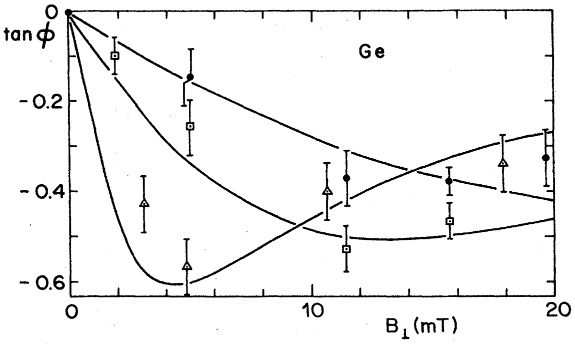

FIG. 76. The shift in the initial phase φ of the diamagnetic μ^+ signal due to the Mu→μ^+ transition in n-type germanium with 10^{14} cm^{-3} donors: measurements taken at △, 177 K; □, 187 K; ●, 198 K. The curves are fits to the expression for the residual polarization [Eq. (2.52)], and the fit results are given in Table XIX. From Kudinov *et al.* (1976). The convention used in this review implies the reversed sign for φ.

Nosov-Yakovleva spin flipping of the Mu electron at a rate ν [Eq. (2.52)]. Their results for an n-type sample with 10^{14}-cm^{-3} donors are given in Table XIX. The quantity $a(0)$ is the fraction of muons that promptly forms Mu. The approximate constancy of the ratio ν/Λ implies that the Mu$\rightarrow\mu^+$ transition and the Mu electron spin flip have a common cause.

These results and those from the temperature-dependent residual polarization a_{μ^+} at higher temperature are displayed in the modified Arrhenius plot of Λ in Fig. 77. The slope of the line, assuming a transition rate $\Lambda(T)$ of the form

$$\Lambda(T)=T^{1/2}\Psi'\exp(-E_a/kT)\ , \tag{5.34}$$

gives an activation energy $E_a=184(7)$ meV, which is much larger than the 12(3) meV determined by Weidinger *et al.* (1981) from $\lambda_{\mathrm{Mu}}(T)$. The factor $T^{1/2}$ in the modified Arrhenius law (5.34) arises from the assumption of a frequency factor proportional to the thermal velocity of Mu.

The $a_{\mu^+}(T)$ behavior observed by Andrianov *et al.* (1969) in a p-type sample with 10^{14} cm^{-3} acceptors is quite different from that observed in the high-purity and n-type material (see Fig. 75).

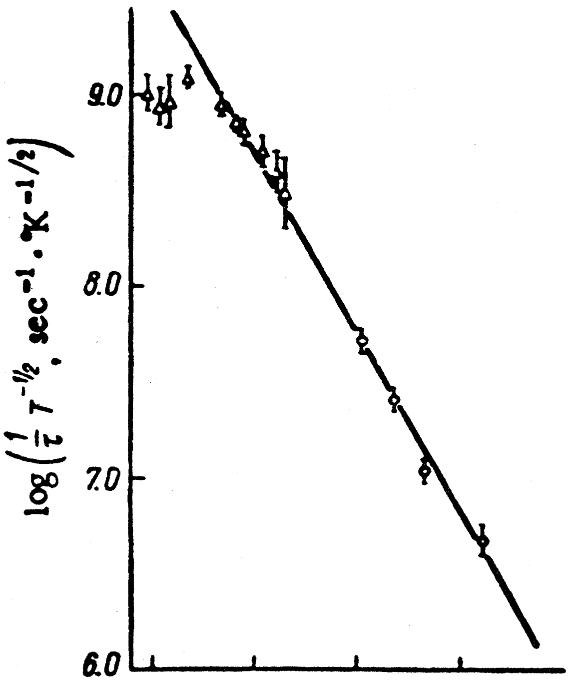

FIG. 77. The temperature-dependent rate $\Lambda=1/\tau$ for the Mu$\rightarrow\mu^+$ transition in weakly n-type germanium (10^{14}-cm^{-3} donors). The points below 200 K were obtained from analyses of the field-dependent phase and residual μ^+ polarization, where Λ and the spin-flip rate ν could be independently determined. Above 200 K, only the residual polarization $a_{\mu^+}(T)$ was used, and the ratio ν/Λ was fixed to the low-temperature value. The factor $T^{1/2}$ arises from the assumption of an Arrhenius frequency factor proportional to the thermal velocity of Mu. From Andrianov *et al.* (1978a).

λ_{μ^+}: The increase in the μ^+ relaxation rate with temperature in germanium (Fig. 75) is reminiscent of that observed in silicon, but the maximum relaxation rate reached is approximately 2 orders of magnitude smaller.

b. Effects of doping

λ_{Mu^*}: The relaxation rate of Mu* in germanium is increased by the presence of electrically active impurities (Weidinger *et al.*, 1981; see Fig. 78). The similarity between $\lambda_{\mathrm{Mu}^*}(T)$ for the p- and n-type doped samples is reasonable in view of the proportionality found in silicon between λ_{Mu^*} and carrier concentration and the similar binding energies of the Ga and Sb impurities in germanium (10.8 and 9.6 meV, respectively). A report that Mu* is observed to lower applied fields in a doped sample than in an undoped one (Balzer *et al.*, 1981a) is not supported by later measurements (see Fig. 58). Döring *et al.* (1984) have found that Mu* is unaffected by up to 10^{16} cm^{-3} electrically *inactive* impurities in Ge.

λ_{Mu}: The dependence on doping of the Mu relaxation rate λ_{Mu} has also been investigated by Weidinger *et al.* (1981; see Fig. 79). As in silicon, doping causes the appearance of a low-temperature plateau in $\lambda_{\mathrm{Mu}}(T)$ which is presumably due to the trapping of mobile Mu by the impurities (see the discussion of the analogous effect for silicon in Sec. V.G.1.b). Studies of λ_{Mu} in Ga- and Sb-doped samples by Weidinger *et al.* show an approximate $n^{0.7}$ dependence at 4.3 K and an $n^{0.95}$ dependence at 30 K. Apparently Sb is a more efficient trap than Ga, since the n-type rate is consistently a factor of 30 higher than the p-type rate. Above 50 K, a doping-independent rise

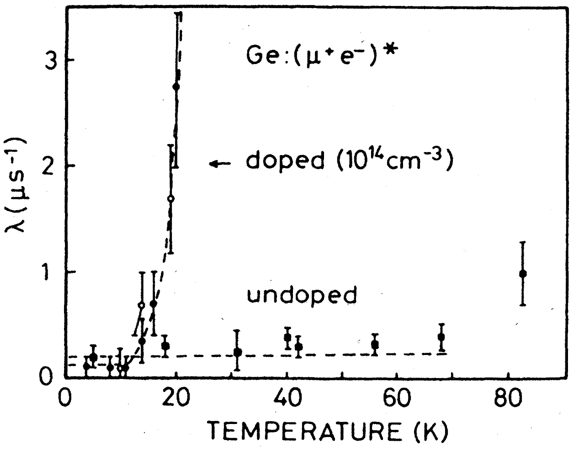

FIG. 78. The temperature-dependent Mu* relaxation rate in doped and undoped germanium at 0.3–0.4 T. The open and solid circles correspond to Ga and Sb dopants, respectively. From Weidinger *et al.* (1981).

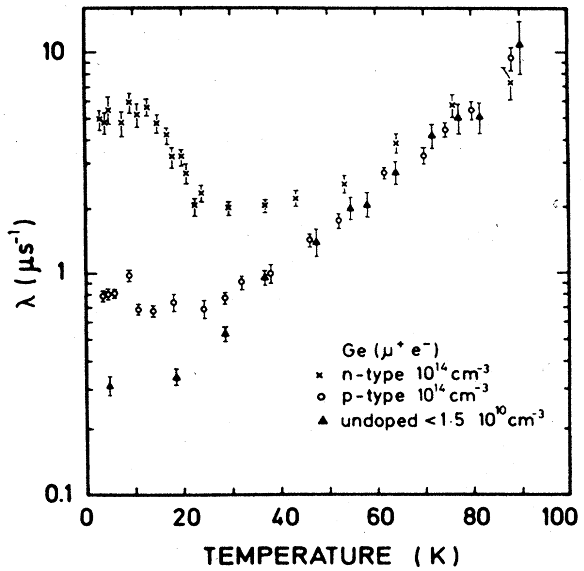

FIG. 79. The temperature-dependent Mu relaxation rate in doped and undoped germanium measured at 6 mT. From Weidinger *et al.* (1981).

in λ_{Mu} with temperature is observed, as in the case of silicon above 200 K. Measurements of λ_{Mu} in very weakly doped germanium by Döring *et al.* (1983) show only a marginally larger damping rate in n samples than in p samples. These authors further find that at 20 K the presence in ultrapure germanium of electrically inactive Si impurities causes a $\mathrm{Mu}\rightarrow\mu^+$ transition at a rate approximately proportional to $[\mathrm{Si}]^{0.75}$. The rate of this transition, as evidenced by the initial phase of the residual μ^+ precession signal, is approximately temperature independent in the temperature range 4–180 K. In contrast to the *thermally activated* $\mathrm{Mu}\rightarrow\mu^+$ transition discussed below, the Mu relaxation rate and the $\mathrm{Mu}\rightarrow\mu^+$ transition rates *agree* in the Si-doped samples, implying that spin flipping of the Mu electron is negligible (Döring *et al.*, 1984). These authors also noted that oxygen and carbon impurities increase the λ_{Mu} rate in germanium.

a_{μ^+}: The study by Andrianov *et al.* (1978a) of the temperature, field, and n-doping dependences of the amplitude a_{μ^+} and initial phase φ of the diamagnetic muon signal in germanium culminated a series of papers on the subject (Andrianov *et al.*, 1969; Kudinov *et al.*, 1975, 1976). In my opinion, this work is the most convincing argument for the existence of a Nosov-Yakovleva electron spin-flip process. The temperature-dependent $\mathrm{Mu}\rightarrow\mu^+$ transition rate found by Andrianov *et al.* (1978a) in a weakly doped sample was shown in Fig. 77. Figure 80 shows their measurements of $a_{\mu^+}(T)$ in samples with various n dopings, and the curves are fits to the data of Ivanter and Smilga's expression for the residual polarization in a $\mathrm{Mu}\rightarrow\mu^+$ transition, including an electron spin-flip rate ν in the parent state [Eq. (2.52)].

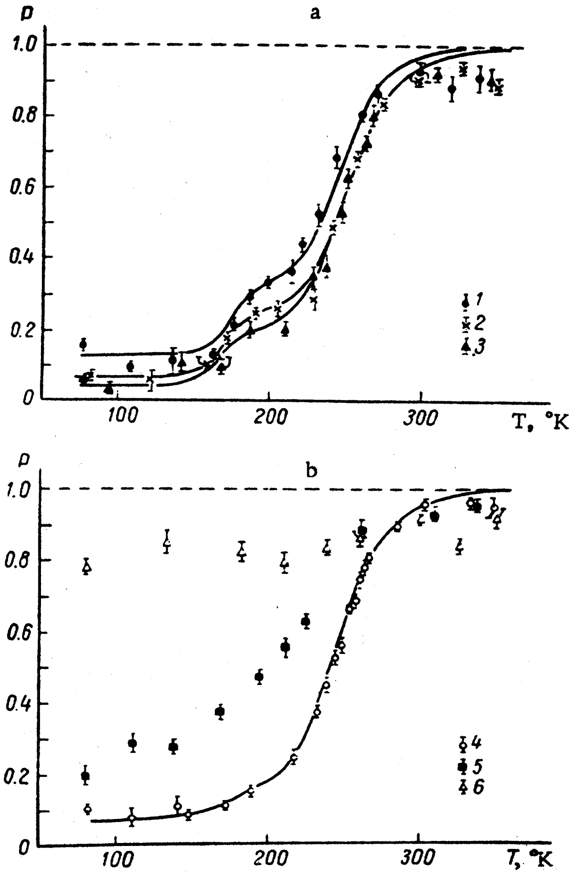

FIG. 80. Temperature-dependent measurements of the residual diamagnetic μ^+ precession amplitude in six germanium samples of different n dopings. The samples 1–6 had dopant concentration of (1) 10^{14}; (2) 1.5×10^{15}; (3) 1.5×10^{16}; (4) 1.5×10^{17}; (5) 1.8×10^{18}, and (6) 2×10^{19} cm^{-3}. The applied magnetic field was 5 mT. The curves are fits to Eq. (2.52), and the results are given in Table XX. From Andrianov *et al.* (1978a).

An interesting aspect of the data in Fig. 80 is the doping-dependent shoulder at 200 K. At 5 mT and in the absence of electron spin flips, Eq. (2.52) predicts the appearance of a shoulder at the value $a_{\mu^+}=50\%$. As mentioned above, the analysis by Kudinov *et al.* (1976) of the field-dependent initial phase and amplitude of the μ^+ signal demonstrated that the ratio ν/Λ is approximately temperature independent (see Table XIX). The

TABLE XIX. The $\mathrm{Mu}\rightarrow\mu^+$ transition (Λ) and electron spin-flip (ν) rates and the prompt μ^+ fraction $a(0)$ in germanium with 10^{14} cm^{-3} donors from field-dependent measurements of the μ^+ phase φ and amplitude a_{μ^+}. From Kudinov *et al.* (1976).

T (K)	Λ (μs^{-1})	ν/Λ	$a(0)$ (%)
161	59 (10)	0.7 (2)	12 (2)
177	140 (40)	0.6 (2)	13 (2)
187	340 (50)	1.1 (2)	13 (2)
198	715 (255)	1.2 (2)	15 (3)

TABLE XX. Results of fitting the residual μ^+ polarization amplitude to a Mu$\rightarrow\mu^+$ transition in n-doped Ge. The modified Arrhenius law (5.34) was assumed. From Andrianov *et al.* (1978a).

n doping (cm^{-3})	Ψ' (s^{-1} K$^{-1/2}$)	E_a (eV)	ν/Λ	$a(0)$ (%)
10^{14}	$2.5\ (1.1)\times10^{12}$	0.184 (7)	0.9 (2)	13 (1)
1.5×10^{15}	$1.1\ (4)\times10^{12}$	0.166 (5)	1.5 (4)	7 (1)
1.5×10^{16}	$2.1\ (1.4)\times10^{12}$	0.170 (20)	2.0 (5)	5 (1)
1.5×10^{17}	$1.4\ (7)\times10^{12}$	0.173 (8)	4.5 (1.2)	5 (1)

assumption of a constant ν/Λ has the effect of lowering the shoulder in $a_{\mu^+}(T)$ below the 50% level, in agreement with the data of Fig. 80. The results of fitting these data to Eq. (5.34) for the Mu$\rightarrow\mu^+$ transition rate $\Lambda(T)$ are given in Table XX. The ratio ν/Λ increases and the prompt μ^+ fraction $a(0)$ decreases with increasing doping. A possible alternative explanation for the low shoulders in $a_{\mu^+}(T)$ would be to assign them to a Mu*$\rightarrow\mu^+$ transition. One would still need, however, rapid electron spin flips to explain the lack of a Mu$\rightarrow\mu^+$ shoulder at $a_{\mu^+}=50\%$.

The heavy doping of samples 5 and 6 in Fig. 80 puts them in the "metallic" regime, where the collision rate of Mu with free carriers is large compared to the Mu hyperfine frequency.

A striking effect of hydrogen impurities on the $a_{\mu^+}(T)$ curve in p-type germanium has been observed by Andrianov *et al.* (1976). A crystal pulled from the melt in a hydrogen atmosphere contained approximately 10^{18} cm^{-3} hydrogen, and it showed a μ^+ amplitude which remained at approximately 20% up to 300 K and then rose sharply to 100% at 350 K. An n-type sample with the same carrier concentration (10^{14} cm^{-3}) yielded a normal $a_{\mu^+}(T)$. Investigations of ultrapure germanium crystals grown in various atmospheres by Clawson *et al.* (1981) showed no effect of hydrogen.

λ_{μ^+}: The temperature-dependent relaxation rate λ_{μ^+} of the diamagnetic signal is shown for n-type germanium samples in Fig. 81 (Kudinov *et al.*, 1977). Note that λ_{μ^+} saturates at a value much smaller than the maximum values seen in silicon and that increased doping moves the increase in λ_{μ^+} to higher temperatures.

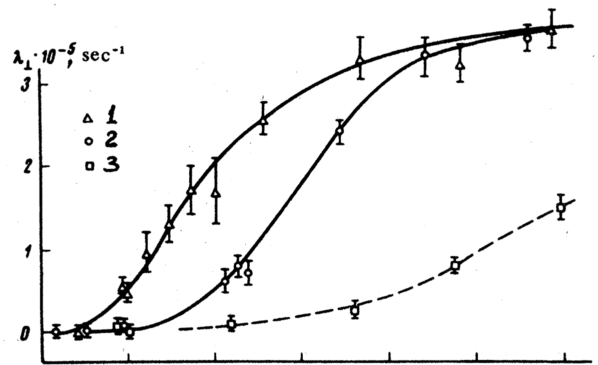

FIG. 81. The relaxation rate λ_{μ^+} of the diamagnetic signal in n-type germanium as a function of temperature. The samples 1–3 contained dopant concentrations of (1) 10^{14}; (2) 1.5×10^{15}; and (3) 1.5×10^{17} cm^{-3}. The applied field was 12 mT. From Kudinov *et al.* (1977).

c. Longitudinal-field experiments

In the only study of the longitudinal-field relaxation rate $\lambda_\parallel$ in germanium published to date, Gurevich *et al.* (1975) observed the behavior shown in Fig. 82 in a sample of unspecified doping. The amplitude of the relaxing component was constant at approximately 70%, indicating that Mu is involved, but a fit to the Nosov-Yakovleva theory gave A values far smaller than that of Mu in germanium (2359.5 MHz):

$$\begin{aligned}233\ \text{K}:&\ A=240(20)\ \text{MHz},\quad \nu=1.0(2)\times10^{10}\ \text{s}^{-1}\ ,\\ 267\ \text{K}:&\ A=154(2)\ \text{MHz},\quad \nu=2.2(1)\times10^{10}\ \text{s}^{-1}\ .\end{aligned}\tag{5.35}$$

Curves corresponding to these isotropic A values are labeled "Mu" in Fig. 82. Since the small A values are rem-

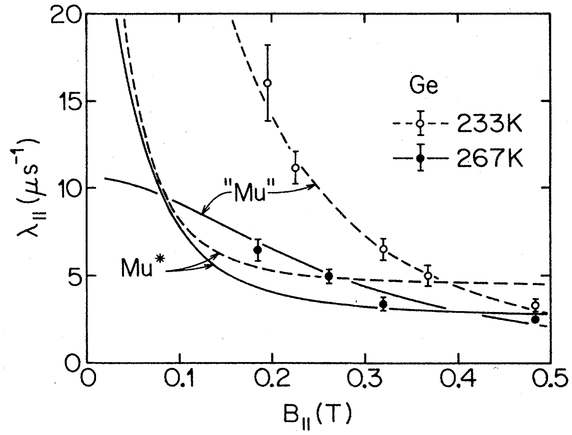

FIG. 82. The longitudinal-field relaxation rates measured in a germanium sample of unspecified doping and orientation as a function of temperature and applied field. The curves are best fits to the Nosov-Yakovleva theory for relaxation by a (temperature-dependent) electron spin-flip rate (1) of an isotropic muonium state with a fitted (temperature-dependent) hyperfine interaction (Mu) and (2) of the Mu* state seen in germanium with an assumed [100] crystal orientation. Data and Mu fits from Gurevich *et al.* (1975).

iniscent of Mu* ($A_{\parallel}=27.72$ MHz, $A_{\perp}=131.04$ MHz), I attempted to fit these data to spin-flipped Mu*. My best fits for the two temperatures are also shown in Fig. 82, and they correspond to the [100] axis parallel to the field and to spin-flip rates at 233 and 267 K of 2.8×10^9 s^{-1} and 4.8×10^9 s^{-1}, respectively. Needless to say, the Mu* fits are very bad. The fit results in Eq. (5.35) were obtained under the assumption that $\nu \gg 2\pi A$. The opposite assumption, $\nu \ll 2\pi A$, led to Mu A values of 3300 (760) MHz and 7010(360) MHz at 233 and 267 K, respectively (Gurevich *et al.*, 1975), which are also less than satisfying. Since these temperatures are in the midst of the rise in $a_{\mu^+}(T)$ (see Fig. 75), account should be taken of the Mu$\rightarrow\mu^+$ transition, but according to Ivanter and Smilga (1968b) this will only add a constant to $\lambda_{\parallel}$ equal to the transition rate Λ.

3. Gallium arsenide

The limited amount of transverse-field data presently available on muonium dynamics in gallium arsenide is summarized in Fig. 83. The data from the p-type sample with 2×10^{12} cm^{-3} acceptors was taken by Barsov *et al.* (1985) in an applied field of 28 mT, and the other two samples were investigated by the Zurich group (unpublished) with the high-transverse-field technique at 1.1 T. The strong nuclear hyperfine interactions experienced by Mu and Mu* make a large applied field necessary for muonium precession studies.

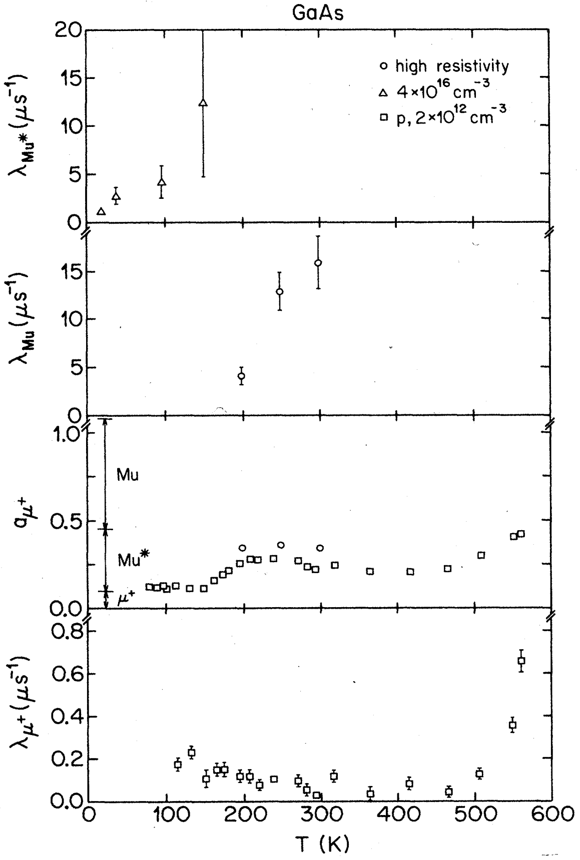

FIG. 83. Collected data on the temperature-dependent dynamics of muon states in GaAs. The indicated low-temperature muon state fractions in the a_{μ^+} panel are from Table VIII. The "high-resistivity" and 4×10^{16} cm^{-3} doped samples were measured at 1.1 T by the Zurich group (unpublished), and the 2×10^{12} cm^{-3} p-doped data were taken at 28 mT by Barsov *et al.* (1985).

The trends presented by Fig. 83 should by now be familiar. The Mu* signals show a relaxation rate that increases with increasing temperature until the signals are lost at 150 K. Above this temperature the diamagnetic muon amplitude increases in response to a Mu*$\rightarrow\mu^+$ transition. The Mu state disappears due to an increasing relaxation rate above 300 K, and above 450 K the muon amplitude increases again due to a Mu$\rightarrow\mu^+$ transition. Finally, above 500 K the diamagnetic μ^+ signal becomes unstable.

The high-field Mu precession signals were not observed in the low-resistivity sample (4×10^{16} cm^{-3} dopants), presumably due to impurity trapping, but the diamagnetic and Mu* signals were equally strong in the high- and low-resistivity material (Kiefl *et al.*, 1985).

A preliminary longitudinal-field study of GaAs has been performed by Barsov *et al.* (1984b), in which quenching experiments confirmed the presence of Mu* at 96 K and of Mu at 350 K.

4. Effects of electric fields, illumination, and radiation

a. Electric fields and illumination

The precedent for searching for effects of an applied electric field on the muon polarization in a solid is an experiment by Ivanov *et al.* (1962), in which a pulsed field was applied to emulsion plates. A reduction in the muon-decay asymmetry by a factor of 2.7 (1.4) was observed for a field of 240 kV cm^{-1}, and the authors interpreted the effect in terms of the incorporation of Mu in a molecule.

The Zurich group (unpublished) has made two attempts to observe the effect of an electric field on muonium states, both using surface muons and both unsuccessful. In the first experiment we tried to shift the position of Mu* in diamond or to alter its electronic structure with a field of 160 kV cm^{-1}. The electric field was applied along the [111] direction of a type-Ia diamond at room temperature, and the applied magnetic field was 27 mT along the [-1 2 -1] direction. Upon turning the electric field on and off, no change could be detected in the upper $\theta=0$ frequency at a level of 0.02%. Isotropic Mu was not detected in this experiment due to the presence of nitrogen impurities.

In the second experiment, muons were stopped in a silicon surface barrier detector at room temperature. The hope was to decrease the relaxation rate of Mu or Mu* by the removal of free carriers in a depleted layer. With *no* applied field a rapidly damped Mu signal was observed at 0.5 mT and no Mu* precession was seen at 290 mT, as expected for a high-purity sample (Mu* precession is normally not observed above 165 K). By applying 220 V to the detector we generated a depleted layer which extended throughout most of the volume of the silicon wafer. No change in the Mu precession was observed with the field applied, and Mu* remained unobservable.

Prompted by the results from pion-decay blocking which indicate a change of pion site upon illumination with visible light in germanium and GaAs (Flik *et al.*, 1986), the Zurich group (Simmler, 1986) attempted to observe the effect of illumination-generated free carriers on the muonium precession signals in cold germanium. Degraded surface muons were used to ensure that the stopped muons were within the diffusion depth of the created carriers. Light from a 150-W halogen bulb with reflector was carried via a fiber-optics guide into an internally reflecting sample chamber mounted in a gas-flow cryostat. We estimate that 0.1 $\mathrm{W\,cm^{-2}}$ fell on the sample. The light passed through an infrared filter and was pulsed with a mechanical chopper, and muon-decay events with and without light were routed into separate histograms. The effect of light on the pion-decay-blocking spectra in germanium was most pronounced at 100 K, although a strong effect was also observed at 50 K (K. Maier, private communication). With typically $1-4\times10^7$ good decay events, we saw no effect of light on the μ^+, Mu, or Mu* signals either at 25 K or at 70 K. Moreover, an experiment at 25 K in silicon showed no effect for any of the three states. We have no explanation for the discrepancy between the pion-decay blocking and these μSR results.

b. Irradiation

The most detailed investigations of the effect of particle irradiation on muonium states in a semiconductor are of electron-irradiated silicon (Albert *et al.*, 1983, 1985a; Albert, 1986; Westhauser *et al.*, 1986). Several important results of these studies are summarized in Figs. 84 and 85.

A lightly doped sample of silicon shows Mu precession in a low-temperature transverse-field μSR experiment. Irradiation with 3-MeV electrons produces radiation defects, principally vacancies and interstitials, which then may migrate to form defect clusters and defect-impurity complexes. Such irradiation also destroys the Mu precession signal, presumably due to trapping of the mobile Mu. Figure 84 shows the recovery of the Mu signal, as evidenced by the reduction of its relaxation rate λ_{Mu}, with increasing annealing temperature T_A. The μSR measurements were all performed at 81 K. The recovery of λ_{Mu} appears to be correlated with the annealing of phosphorous-vacancy pairs at around 400 K (see Fig. 43) and of oxygen-vacancy pairs at around 600 K in *n*- and *p*-type materials, respectively, as indicated by the shaded areas in Fig. 84.

Whereas electron irradiation of silicon degrades the Mu signal, it tends to *enhance* the Mu* signal. As seen in Sec. V.G.1.b, Mu* is normally not observed in strongly doped material at 81 K. Upon irradiation, however, narrow Mu* lines are observed, and only upon annealing do the lines broaden and finally disappear (see Fig. 85). The explanation of this effect is that the radiation defects also act as traps for free carriers. Since at 81 K the Mu* relaxation rate λ_{Mu^*} is proportional to the carrier concentration [see Eq. (5.30)], the irradiation narrows the Mu* lines. Again the recovery of the (broad) Mu* lines appears to be correlated with the *P-V* and *O-V* annealing stages (shaded areas in Fig. 85). The weakly doped sample in Fig. 85 shows no Mu* line broadening upon annealing, since too few carriers were present in the unirradiated sample to cause relaxation.

A particularly interesting observation of Mu* dynamics in irradiated silicon was made by Albert (1986). In an *n*-type sample with 5×10^{16} $\mathrm{cm^{-3}}$ dopants, Mu* was made visible by 3-MeV electron irradiation to a dose of 6×10^{17} $\mathrm{cm^{-2}}$. μSR measurements were then made at

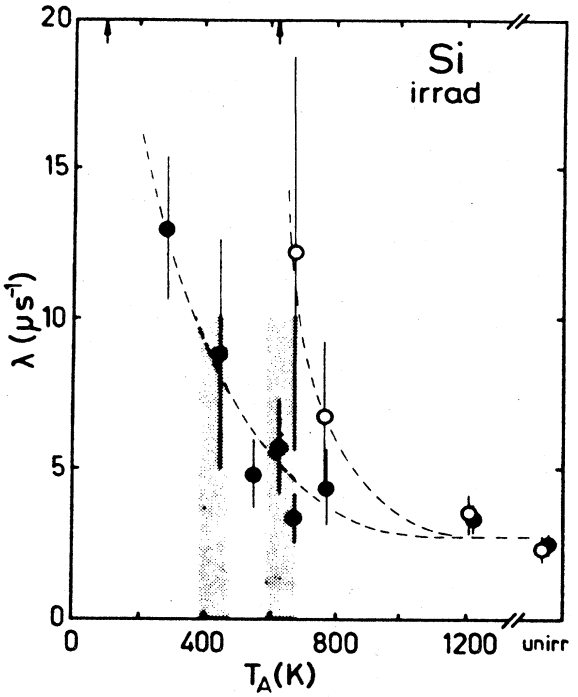

FIG. 84. The relaxation rate λ_{Mu} of isotropic Mu in electron-irradiated silicon as a function of the annealing temperature T_A. The open and closed circles refer, respectively, to initially *p*-type and *n*-type samples, each with 10^{13} $\mathrm{cm^{-3}}$ dopant concentration. Each sample was irradiated with 3-MeV electrons to a dose of 6×10^{17} electrons $\mathrm{cm^{-2}}$. The annealing time was 10 min, and the μSR measurements were performed with surface muons at 81 K in a field of 11.4 mT. Before irradiation, both samples showed long-lived Mu signals (the point labeled "unirr."). These were destroyed upon irradiation due to trapping at radiation defects, and the figure shows the recovery of the relaxation rate with annealing. From Albert *et al.* (1985a).

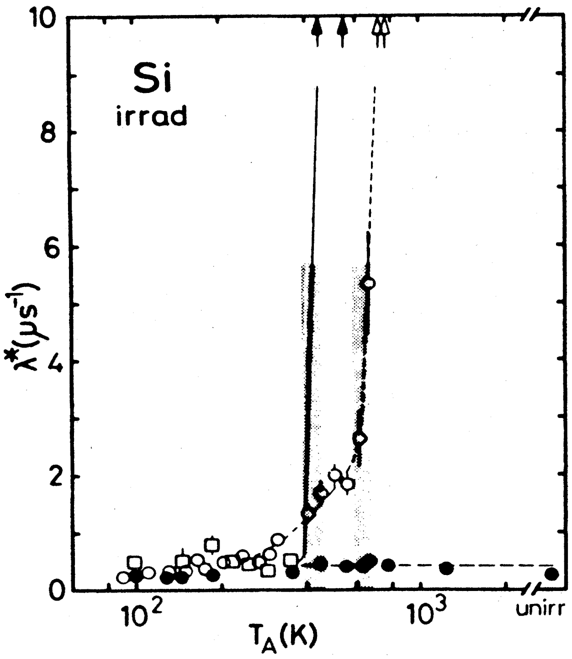

FIG. 85. The Mu* relaxation rate in three samples of electron-irradiated silicon as a function of annealing temperature T_A. The electron energy was 3 MeV, the annealing time was 10 min, and the measurements were made with surface muons at 81 K in a field of 11.4 mT. The dopant concentrations and electron doses for the three samples used: □, 5×10^{16} phosphorous cm^{-3} and 6×10^{17} electrons cm^{-2}; ○, 10^{16} boron cm^{-3} and 10^{17} electrons cm^{-2}; ●, 10^{13} boron cm^{-3} and 6×10^{17} electrons cm^{-2}. Before irradiation, only the weakly doped *p*-type sample showed Mu* (the point labeled "unirr."), and after irradiation all showed narrow Mu* lines due to the trapping of free carriers at radiation defects. The increase in λ_{Mu^*} with T_A in the strongly doped samples is coupled to the release of carriers from the annealed traps. From Albert *et al.* (1985a).

various temperatures, and it was found that the Mu* relaxation rate increased above 150 K, just as it does in *undoped* samples, due to the doping-independent "intrinsic" process seen in Fig. 69. This observation implies that the removal of free carriers by radiation defect trapping has no effect on the intrinsic Mu* relaxation process, supporting the view advanced in Sec. V.G.1.b that the relaxation involves a change of muon site.

In an investigation by Westhauser *et al.* (1986), irradiated silicon was used to test the theory that Mu* is a vacancy-associated center by presenting the incoming muons with "preformed" vacancies. The μSR measurements were performed at 15 K with surface muons in *p*-type material with 10^{16} boron cm^{-3}. In an applied field of 10 mT, no change in the Mu* amplitude was seen upon electron irradiation (with 3-MeV electrons to a dose of 10^{17} cm^{-2} and the sample kept below 90 K). However, an enhancement of the low-frequency Mu* precession line ($\theta=90°$) *was* seen in the irradiated sample in the vicinity of 3 mT, the field at which the Mu and Mu* precession frequencies coincide. Like the single-crystal diamond experiment at high temperature described in Sec. V.F, this implies that a Mu→Mu* transition occurs in the irradiated silicon at 15 K. The resonant polarization transfer disappeared after a 10-min anneal at 298 K. Annealing at 298 K removes, among other defects, monovacancies and vacancy-boron pairs, but leaves the vacancy-oxygen complexes. Westhauser *et al.* conclude that the Mu→Mu* transition is promoted by radiation defects, and it is either the decrease in their number or the removal of a particular defect type that is responsible for the absence of a transition after annealing.

A study of neutron-irradiated silicon by Barsov *et al.* (1983, 1984a) yielded effects similar to those produced by electron irradiation. A *p*-type sample (5×10^{12} cm^{-3} acceptors) was irradiated with fast neutrons to defect concentrations of 2×10^{18}, 10^{17}, and 10^{16} cm^{-3}, and longitudinal- and transverse-field μSR experiments were performed with conventional muons. No influence of irradiation was found on the diamagnetic precession signal or the longitudinal polarization (at $B_{\parallel}=25$ mT) in the temperature range 80–370 K, nor on the Mu* signals at 80 K. At all three irradiation doses, however, the Mu signals at 80 K were absent. Annealing (at an unspecified temperature) restored the Mu precession. Their observation of an unchanged longitudinal polarization $a_{\parallel}$ is consistent with a picture in which the transverse-field Mu precession is dephased by trapping at radiation defects. The immobile Mu* state in this chemically pure sample is not affected by the defects.

The *opposite* effect has been observed by the Zurich group (Schwab, 1986) in *GaAs* irradiated with fast neutrons. In this study, several 4-cm^3 pieces of high-resistivity material were exposed to neutrons of energy 0.8–1.6 MeV to a dose of 8×10^{15} cm^{-2}. Such a dose creates approximately 1.5×10^{17} cm^{-3} antisite defects (As replacing Ga) and Ga-ion vacancies (Goltzene *et al.*, 1984). As shown in the high-transverse-field μSR spectra in Fig. 86, this time the irradiation leaves the Mu signals unchanged but destroys the Mu* state by transferring its polarization to the diamagnetic μ^+. Annealing at 400° C, the temperature at which the Ga-ion vacancy anneals, has no effect, but a 600°-C anneal, which anneals the antisite defect (Weber and Schneider, 1983), restores the Mu* signals and reduces the μ^+ amplitude to approximately its unirradiated value. A possible explanation is as follows. The mobility of Mu is insufficient in GaAs to permit trapping at the defects (this is supported by the nuclear hyperfine broadening seen at low applied fields, see Sec. V.E). The antisite defect is a double donor (Weber and Schneider, 1983), which could inhibit the formation of Mu* by restricting the supply of electrons available to the stopping muon.

H. Muonium dynamics in the cuprous halides

As a class of muonium hosts, the cuprous halides are special in several respects. The group-I-VII compounds

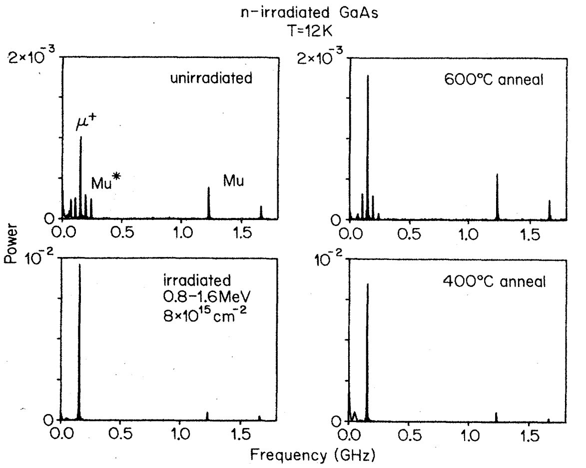

FIG. 86. High-transverse-field frequency spectra for high-resistivity GaAs samples taken at 1.1 T with the [110] crystal axis parallel to the field. The neutron irradiation leaves the ν_{12} and ν_{34} Mu signals unaffected, but the ν_{12} and ν_{34} Mu* signals (for centers with $\theta=35.3°$ and 90°) disappear with irradiation to reappear in the form of a stronger diamagnetic μ^+ signal. Annealing at 600 °C restores the unirradiated situation. From the Zurich group.

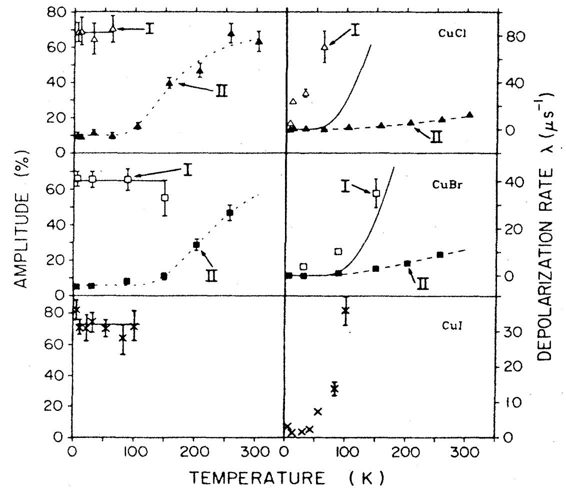

FIG. 87. Muonium dynamics in the cuprous halides. At the left are the precession amplitudes for the Mu$^{\rm I}$ and Mu$^{\rm II}$ states. At the right are the relaxation rates of the Mu states. The solid and dashed curves in the amplitude plots for Mu$^{\rm I}$ and Mu$^{\rm II}$ are the results of fits of the amplitudes to the transition model of Meier (1982), as are the solid curves in the Mu$^{\rm I}$ relaxation rate plots. The dashed curves in the Mu$^{\rm II}$ relaxation rate plots are fits to an Arrhenius law. From Kiefl, Odermatt *et al.* (1986).

CuCl, CuBr, and CuI are the most ionic of all materials with the zincblende structure. They are close to the critical ionicity for tetrahedrally coordinated compounds, and upon heating they show a phase transition to the wurtzite structure (Schwab and Goltzene, 1982). They are also special as regards the properties of implanted muons. As can be seen in Fig. 46 and Table IX, two isotropic muonium states, a low-temperature state Mu$^{\rm I}$ and a high-temperature state Mu$^{\rm II}$, are observed in CuCl and CuBr. Only the Mu$^{\rm I}$ state has as yet been observed in CuI. The isotropic hyperfine frequencies of all the Mu states are very similar and much smaller than would be expected from the high host ionicity. Indeed, they are by far the smallest observed in any diamond or zincblende material. All observations of Mu$^{\rm I}$ and Mu$^{\rm II}$ have been made using the high-transverse-field technique.

Several properties of the Mu$^{\rm I}$ and Mu$^{\rm II}$ states in CuCl, CuBr, and CuI have been presented in earlier sections: the temperature dependence of their hyperfine constants, their electronic g factors, and their nuclear hyperfine interactions in Sec. V.C, and upper limits for their diffusion rates in Sec. V.E. A comprehensive description of the properties of the muonium states in these three materials has been published by Kiefl, Odermatt *et al.* (1986).

The dynamics of these states is summarized in Fig. 87. At temperatures below 60 K, predominantly the Mu$^{\rm I}$ state is formed, together with a small fraction of Mu$^{\rm II}$. With increasing temperature, the relaxation rate of Mu$^{\rm I}$ increases until the state becomes invisible above 60 K in CuCl, 153 K in CuBr, and 102 K in CuI. At still higher temperatures in CuCl and CuBr, the Mu$^{\rm II}$ state grows in amplitude until it accounts for the entire Mu$^{\rm I}$ amplitude lost. At still higher temperatures, the relaxation rate of the Mu$^{\rm II}$ state grows.

Fits of the Mu$^{\rm II}$ amplitude data in Fig. 87 have been made to the transition model of Meier (1982) under the assumption of a transition from Mu$^{\rm I}$ to Mu$^{\rm II}$ with a rate $\Lambda(T)$ given by the Arrhenius law of Eq. (5.23). The fit results are (Kiefl, Odermatt *et al.*, 1986)

$$\Psi^{\rm I}=1.330(100)\times10^9\ {\rm s}^{-1},\quad E_a^{\rm I}=0.115(9)\ {\rm eV}\ \ ({\rm CuCl})\ ,$$

$$\Psi^{\rm I}=1.195(107)\times10^9\ {\rm s}^{-1},\quad E_a^{\rm I}=0.103(9)\ {\rm eV}\ \ ({\rm CuBr})\ . \tag{5.36}$$

The Mu$^{\rm I}$ relaxation rates predicted by Eq. (5.36) are lower than those observed (see Fig. 87). The Mu$^{\rm II}$ relaxation rates were fit to the same Arrhenius law plus a temperature-independent term. The resulting parameters are

$$\Psi^{\rm II}=6.0(1.2)\times10^7\ {\rm s}^{-1},\quad E_a^{\rm II}=0.045(4)\ {\rm eV}\ \ ({\rm CuCl})\ ,$$

$$\Psi^{\rm II}=4.8(2.2)\times10^7\ {\rm s}^{-1},\quad E_a^{\rm II}=0.038(9)\ {\rm eV}\ \ ({\rm CuBr})\ . \tag{5.37}$$

Note that the values (5.36) and (5.37) are very similar for the two hosts.

In unpublished results of the Zurich group (Schwab, 1986), clear evidence of a Mu$^{\rm II}$-to-μ^+ transition is observed in CuCl. The Mu$^{\rm II}$ state disappears above 450 K, following which the diamagnetic μ^+ fraction rises in strength, reaching 100% at approximately 700 K. There is no significant discontinuity in the μ^+ signal strength when passing the transition to the wurtzite structure in CuCl at 680 K nor upon melting at 695 K. In contrast to the rise in the μ^+ relaxation rate observed at high temperatures in Si and GaAs, λ_{μ^+} in CuCl remains constant at approximately 1.8 μs^{-1} between 500 and 750 K. Neither CuBr nor CuI has yet been studied above room temperature.

I. Miscellaneous semiconductors

1. Silicon carbide

Silicon carbide exists in a vast number of polytypes. Of principal interest to us here are the zincblende or β—SiC form and the common hexagonal 6H—SiC or α—SiC form. The present status of studies of muonium states in SiC has recently been summarized by Patterson *et al.* (1986).

It is difficult to obtain β—SiC in crystalline form. In an experiment by the Zurich group, a sample in the form of glassy, bright yellow grains obtained from the Philips Corporation, Holland, was investigated at 22 K with the transverse-field technique in applied fields between 1.25 and 30 mT. A strong, unsplit Mu signal (ν_{12} and ν_{23}) was seen at the lowest field, but as the field was increased, the amplitude of the signal decreased until it was no longer visible above 5 mT. A strong dependence of the initial phase of the Mu signal on field was also observed. A plausible interpretation of the data is that a μ^+-to-Mu transition occurs at a rate of approximately 10^8 s^{-1} at 22 K. No Mu precession in β-SiC was observed at room temperature, and no Mu* precession was seen at 22 K in a high-statistics run at zero field.

The hexagonal 6H form of SiC has a variety of interstitial sites not found in the zincblende structure. And indeed, in a high-transverse-field experiment on a mosaic of oriented crystals, two muonium states, $\mathrm{Mu^A}$ and $\mathrm{Mu^B}$, were observed at 310 K, and three states, $\mathrm{Mu^{AII}}$, $\mathrm{Mu^{AI}}$, and $\mathrm{Mu^B}$, were observed at 20 K (see Fig. 88). The hyperfine parameters and electronic g factors for these states are given in Table XXI. Due to a calculation error, the g factors given by Patterson *et al.* (1986) are all a factor of 1.003 73 too large.

The precession data are in qualitative agreement with an earlier result from Andrianov *et al.* (1978b) using longitudinal-field quenching. From the hyperfine parameters in Table XXI it is reasonable to assume that with increasing temperature the $\mathrm{Mu^{AI}}$ state disappears and that the $\mathrm{Mu^{AII}}$ state becomes the $\mathrm{Mu^A}$ state. All the precession data in the table were taken with the applied field perpendicular to the hexagonal axis. One would expect muonium in a hexagonal crystal to be anisotropic, as it is in quartz (Brewer *et al.*, 1979). But a measurement at 310 K with a tilted sample showed no significant anisotropy in the hyperfine frequency of $\mathrm{Mu^A}$ or $\mathrm{Mu^B}$.

All three Mu states appear to be undamped at 20 K, but the $\mathrm{Mu^A}$ and $\mathrm{Mu^B}$ signals at room temperature show relaxation rates of the order of 5 μs^{-1}. Measurements of the 6H—SiC crystal mosaic at room temperature in a standard surface-muon μSR apparatus gave values of the total Mu, diamagnetic μ^+, and missing fractions of 56 (13)%, 11 (2)%, and 33 (13)%, respectively.

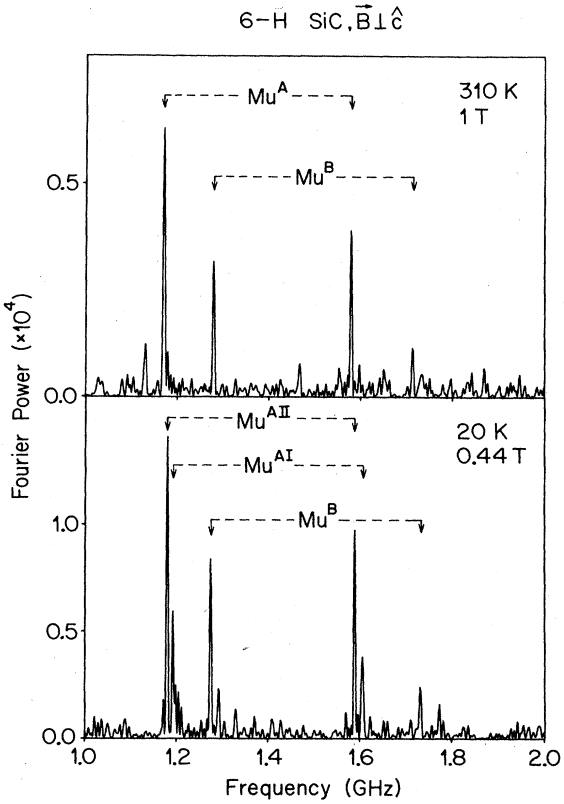

FIG. 88. High-transverse-field frequency spectra taken on an oriented mosaic of 6H—SiC crystals with surface muons. From Patterson *et al.* (1986).

It is interesting to note that the Mu hyperfine frequencies in diamond and silicon (3711 and 2006 MHz) bracket the values in 6H—SiC. No precession frequencies attributable to a Mu*-like state are seen in 6H—SiC. The observation of C—H stretching frequencies in the luminescence of proton-implanted 6H—SiC has been interpreted in terms of saturation by hydrogen of a dangling bond in a Si vacancy (Patrick and Choyke, 1973). The existence of a muonium state in SiC with hyperfine parameters similar to those for Mu* in diamond or silicon would have lent strong support to a vacancy model for Mu*.

TABLE XXI. Hyperfine frequencies A and electronic g values g_e for the isotropic Mu states in 6H—SiC. From Patterson *et al.* (1986).

Temperature (K)	Mu state	A (MHz)	g_e
20	Mu^{AII}	2767.85 (16)	2.0042 (19)
	Mu^{AI}	2797.32 (40)	2.0050 (51)
	Mu^{B}	3005.73 (20)	2.0015 (22)
310	Mu^{A}	2748.35 (42)	1.9996 (71)
	Mu^{B}	2989.69 (52)	1.9953 (75)
300	$B_{\parallel}$ quenching	3030 (220)[a]	

[a] From Andrianov *et al.* (1978b).

2. Materials with no muonium centers

The alternatives to paramagnetic muonium signals are a large diamagnetic μ^+ signal or a large "missing fraction" of the muon polarization. A diamagnetic μ^+ state can represent either (a) a positively charged muon state such as a free μ^+ that has failed to bind an electron, or a singly ionized muonium center such as Mu^{*+}; (b) a negatively charged muon state with an extra electron such as Mu^-; or (c) a paramagnetic muonium state in which the electron is effectively decoupled from the muon, for example, by rapid electron spin flipping in the Nosov-Yakovleva model (see Sec. II.B.1). A large missing fraction implies the formation of an unobserved paramagnetic state, since only the coupling of the muon to an unpaired electron can depolarize the muon rapidly on the time scale of its lifetime. The failure to observe coherent precession of the paramagnetic state may be due to many causes (see Sec. II.B). An intermediate case between a large diamagnetic signal and a large missing fraction is the observation of a rapidly damped μ^+ signal. Rapid μ^+ relaxation has been observed above 450 K in Si, above 300 K in Ge (see Sec. V.G), and above 200 K in tellurium (Gurevich *et al.*, 1979). Like the missing fraction, this relaxation must involve the formation of a paramagnetic state.

The low-temperature formation probabilities of muon states in the diamond and zincblende materials were presented in Table VIII. The materials in which experiments show *no* muonium precession are α—Sn, GaSb, InP, InAs, InSb, CdS, and CdTe. Those with a large μ^+ signal ($>80\%$) at low temperature are α—Sn, InAs, and CdS. In addition, a single-crystal sample of the (I,III)-VI chalcoginide $\mathrm{AgGaSe_2}$, whose structure is a generalization of the zincblende structure, showed a large μ^+ signal at 15 K [$f_{\mu^+}=82\ (12)\%$, $f_{\mathrm{missing}}=18\ (12)\%$] in a high-transverse-field experiment at 1.1 T (unpublished result of the Zurich group). The materials in Table VIII with a large missing fraction ($>20\%$) are GaSb, InP, InSb, ZnS, ZnSe, and CdTe.

The presence of Mu* precession in GaAs and GaP and its absence in InP has a perhaps interesting parallel in the proton and deuteron implantation experiments of Newman and Woodhead (1980). Whereas the implanted GaAs and GaP samples show Ga—H and Ga—D stretching modes in their infrared absorption spectra, presumably from hydrogen trapped at an anion vacancy, no analogous In-related modes are seen in InP.

VI. DISCUSSION OF THEORETICAL MODELS

A. Mu, Mu*, and hydrogen sites

Before any reasonably detailed model of the muonium states in semiconductors can be formulated, the *sites* of the states in the host lattice must be determined or assumed. Until now, only the channeling and blocking techniques have produced any direct, experimental information on the site of the muon in the lattice, and this is still quite incomplete. In this section a brief review of *theoretical calculations* of the muonium or hydrogen sites in semiconductor hosts is presented. The results of these calculations are summarized in Table XXII, and the sites involved are defined in Fig. 89, which shows a [110] projection of the silicon lattice.

The channeling determination of the position of implanted deuterium in silicon by Picraux and Vook (1978) yielded the "D" site, 1.6 Å from a silicon ion in the [111] antibonding direction. More recent experiments by Nielsen (1986) with a smaller dose of implanted deuterium showed simultaneous occupation of the tetrahedral ("T") and bond-center ("BC") sites, with predominantly bond-center occupation below approximately 130 K and above approximately 430 K, and a preference for the tetrahedral site in the intermediate temperature region. The muon-decay-blocking experiments by Patterson *et al.* (1984a) indicated tetrahedral occupation, presumably next to an oxygen impurity, in Czochralski silicon and were compatible with a site on the [111] axis, 0.9 Å from a lattice site, in high-purity float-zone material. This float-zone result can be interpreted in terms of the four different sites, two of them near a vacancy, labeled "Ch" in Fig. 89. Note that one of these agrees well with the formation of a Si—H-like bond ("SiH") near a vacancy. Patterson (1984b), formulated an argument based on incomplete blocking data in favor of the D site for Mu*, but this model was retracted when more data became available (see the Note Added in Proof to this reference).

Using the extended Hückel technique, Singh *et al.* (1977) treated several silicon clusters with dangling bonds at the surface and with unperturbed ion positions. In both a 30-ion and a 38-ion cluster, they found a stable hydrogen position at the tetrahedral site. In a 35-ion cluster with a vacancy, they discovered that hydrogen sits in a dangling bond 0.8 Å from an ion that neighbors the va-

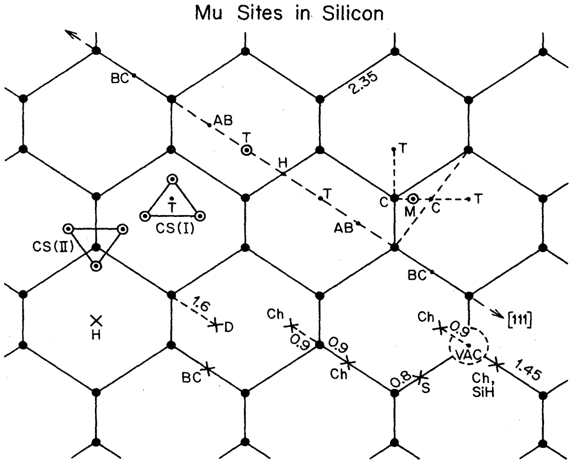

FIG. 89. A [110] projection of silicon showing the muonium sites indicated by channeling and blocking experiments and predicted by various theoretical investigations. The open circles represent candidates for the isotropic Mu state, and the crosses are candidates for anisotropic Mu*.

TABLE XXII. Experimental and theoretical site determinations of muonium in silicon, diamond, and germanium.

Site	Technique	Remarks	Reference
Silicon			
D	Channeling	Radiation damage (?)	Picraux and Vook (1978), Patterson (1984b)
T	e^+ blocking	*O* trapping (?)	Patterson *et al.* (1984a)
Near *AB*,*BC*, or vacancy	e^+ blocking	("Ch")	Patterson *et al.* (1984a)
T	Channeling	Tetrahedral interstitial site	Nielsen (1986)
BC	Channeling	Bond center	Nielsen (1986)
T	Hückel cluster		Singh *et al.* (1977)
near vacancy	Hückel cluster	Single bond ("S")	Singh *et al.* (1977)
D	Pseudopotential		Rodriguez *et al.* (1979)
H	Electronic arguments		Estle (1981)
M	MNDO cluster	Between 2 "C" sites	Corbett *et al.* (1983)
T	CNDO cluster	Mu unbound	Mainwood and Stoneham (1984)
Near vacancy	UHF cluster	Mu^{++}, single bond (Si—H)	Sahoo *et al.* (1985), Estreicher and Marynick (1986a)
D	Tight binding	Acceptor site	Johnson *et al.* (1986)
CS(I),*CS*(II)	Chemical arguments	Tunneling states	Cox and Symons (1986)
T	UHF cluster		Sahoo *et al.* (1986a)
BC	PRDDO cluster		Estle *et al.* (1986)
Diamond			
H	Electronic arguments		Estle (1981)
T	UHF cluster		Sahoo *et al.* (1983), Estreicher *et al.* (1985)
T	INDO, MINDO clusters		Patterson (1984a)
H	UHF cluster	Mu^{++}	Sahoo *et al.* (1984)
Near *H*	CNDO cluster	Mu unbound	Mainwood and Stoneham (1984)
Near vacancy	INDO cluster	C—H	Patterson (1984a)
Near vacancy	UHF cluster	Mu^{++}, triple bond	Sahoo *et al.* (1985), Estreicher and Marynick (1986a)
CS(I),*CS*(II)	Chemical arguments	Tunneling states	Cox and Symons (1986)
BC	PRDDO cluster		Estle *et al.* (1986)
Germanium			
H	Electronic arguments		Estle (1981)
CS(I),*CS*(II)	Chemical arguments	Tunneling states	Cox and Symons (1986)
Near vacancy	UHF cluster	Mu^{++}, single bond	Sahoo *et al.* (1986b)

cancy (the "S" site in Fig. 89). In all cases they obtained a hydrogen level that was either within or close to the edge of the energy gap, and they made predictions of the hydrogen vibrational frequencies.

Rodriguez *et al.* (1979) used a pseudopotential method without consideration of lattice relaxation and found a stable hydrogen site in silicon very close to the D site of Picraux and Vook. Johnson *et al.* (1986) performed an empirical tight-binding calculation of hydrogen in pure silicon, in which they also obtained an energy minimum at the D site. The resulting center was predicted to be an acceptor. Estle (1981) presented an argument based on general electronic considerations in favor of the hexagonal site ("H") for Mu* and the tetrahedral site for Mu in all the group-IV semiconductors.

With the "modified neglect of diatomic overlap" (MNDO) approach, Corbett *et al.* (1983) considered a 14-ion silicon cluster with 20 surface hydrogen atoms and found a stable hydrogen position at the so-called "M" site. This site is midway between two neighboring "C" sites, which are in turn at the centers of rhombuses formed by three silicon atoms and a tetrahedral site. The barrier for diffusion away from this site was found to be 0.3 eV, in fair agreement with the high-temperature diffusion data of van Wieringen and Warmoltz (1956) ($E_a = 0.48$ eV). In a cluster with 16 silicon ions plus a vacancy and 36 hydrogen atoms, they found that hydrogen saturates a dangling bond near the vacancy.

A first-principles calculation of the site and electronic structure of muonium in the 10 carbon + 16 hydrogen atom cluster shown in Fig. 90 was performed by Sahoo *et al.* (1983) for hydrogen in diamond. They employed an unrestricted Hartree-Fock (UHF) self-consistent-field approach, and for muonium sites on the [111] symmetry axis, they found an energy minimum at the tetrahedral site (see Fig. 91). Relaxation of the carbon atom posi-

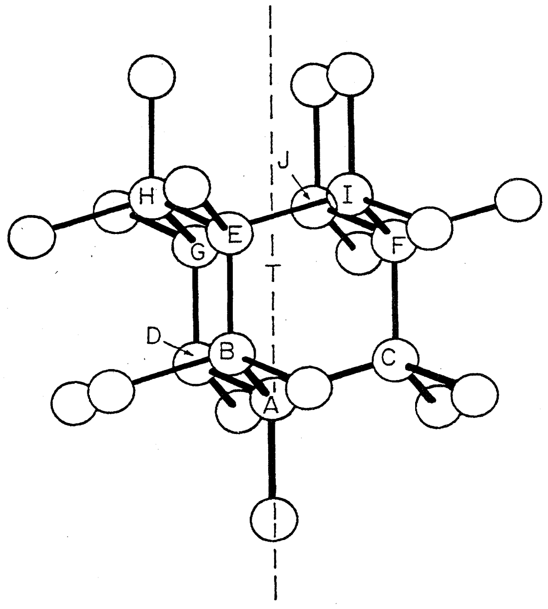

FIG. 90. The 10 carbon + 16 hydrogen cluster used by Sahoo *et al.* (1983) for their unrestricted Hartree-Fock (UHF) calculation of interstitial Mu. The lettered circles are the carbon atoms, and the muonium atom was moved along the dashed line. From Sahoo *et al.* (1983).

tions was not taken into account. The sensitivity of the energy profiles obtained to the C—H bond distance used for the surface hydrogens, as well as the effect of increasing the cluster size, was investigated by Estreicher *et al.* (1985) using both the UHF method and that of partial retention of diatomic differential overlap (PRDDO). PRDDO was used with diamond clusters of up to 30 carbon + 40 hydrogen atoms, and results have also been published on the lattice relaxation around Mu at the tetrahedral and hexagonal interstitial sites (Estreicher and Marynick, 1986b). A UHF calculation similar to that performed in diamond was recently made by Sahoo *et al.* (1986a) for the case of silicon, where a somewhat flatter tetrahedral energy minimum was found.

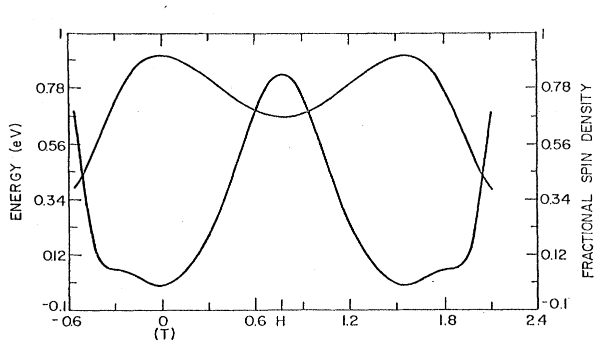

FIG. 91. The calculated [111] energy profile (curve peaking at the hexagonal site *H*) and the fractional spin density [equal to A/A (vacuum)] from a UHF calculation of the 10 C + 16 H cluster of Fig. 90. The experimental value of A/A (vacuum) for Mu in diamond is 0.832. From Sahoo *et al.* (1983).

The UHF results of Sahoo *et al.* (1983) in a diamond are well reproduced by my INDO (intermediate neglect of differential overlap) and MINDO (modified intermediate neglect of differential overlap) calculations of the same 10 carbon + 16 hydrogen cluster (Patterson, 1984a; see Fig. 92). The INDO and MINDO programs have been described by Pople and Beveridge (1970) and by Bischof (1976), respectively. Both employ empirical constants that have been adjusted to reproduce the positions of atomic energy levels, in the case of INDO, and molecular heats of formation, in the case of MINDO. In both calculations, the C—H distance was set to the 1.09 Å typical of hydrocarbons. With INDO, I fixed the positions of the carbon ions, while with MINDO the carbon ions, but not the surface hydrogen atoms, were allowed to adjust their positions. With the muonium at the hexagonal position, MINDO yielded a 1% increase in the C—C bond length of the hexagon.

Mainwood and Stoneham (1984) used the complete neglect of differential overlap (CNDO) technique to compute the energy profile of muonium in diamond and silicon using the 30-atom cluster shown in Fig. 93. The dangling bonds of the cluster were saturated not with hy-

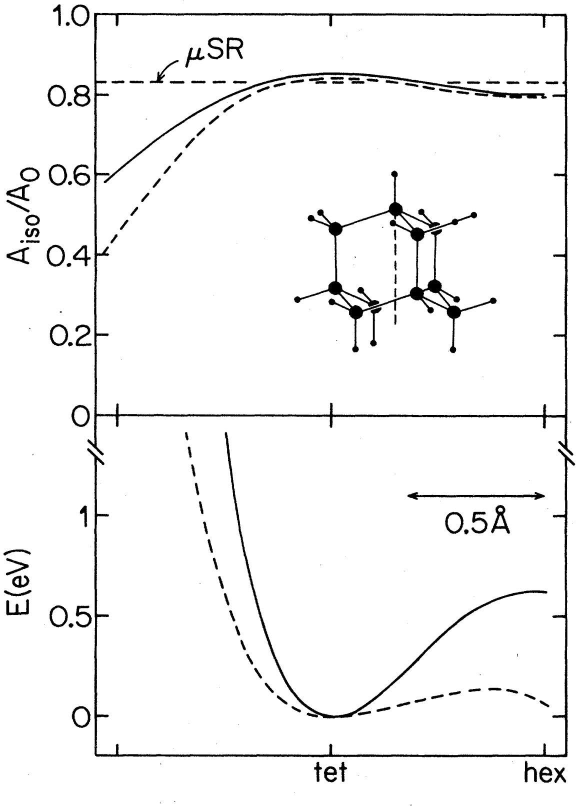

FIG. 92. The [111] energy profile and isotropic hyperfine frequency (relative to vacuum) for the 10 C + 16 H diamond cluster calculated using INDO on a rigid cluster (solid curves) and MINDO on a flexible cluster (dashed curves). The dashed line labeled μSR represents the measured value of A/A (vacuum) in diamond of 0.832. From Patterson (1984a).

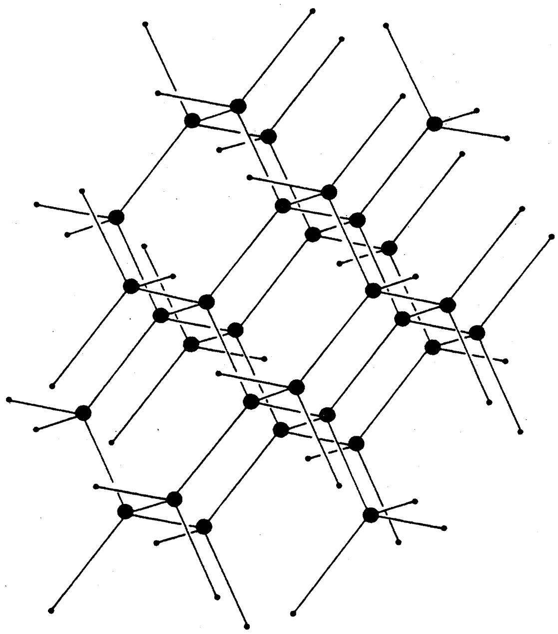

FIG. 93. The 30-atom cluster used by Mainwood and Stoneham (1984) for their CNDO calculations of Mu in diamond and silicon. The small dots represent terminating sp^3 host-ion orbitals. From Mainwood and Stoneham (1984).

drogen, however, but with "partial atoms," i.e., single sp^3 host orbitals. The result in diamond was a very flat potential surface with minima near the hexagonal site. In silicon, they obtained the profile shown in Fig. 94, with a minimum at the tetrahedral site. They further noted that, when lattice relaxation is taken into account, the hexagonal Si—Si bonds stretch by 1% of a lattice spacing and the potential barrier at the hexagonal site falls virtually to zero. Their conclusion is that Mu is *unbound* in both diamond and silicon.

As a candidate for Mu*, Sahoo *et al.* (1984) studied the result of making the muonium defect center doubly positively charged in their 10 carbon + 16 hydrogen atom cluster (Fig. 90). Using the UHF method, they found a pronounced energy minimum at the hexagonal site, with a secondary minimum 0.4 Å from the tetrahedral site toward a neighboring carbon ion.

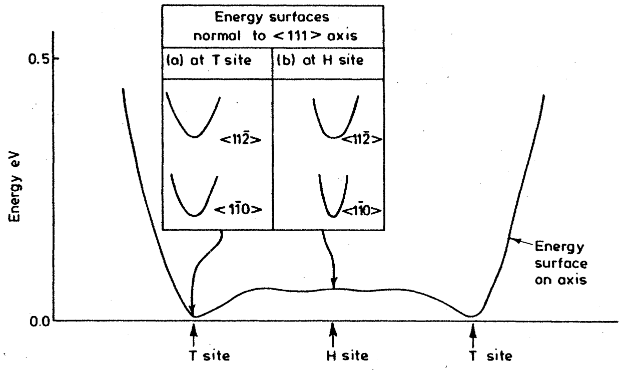

FIG. 94. The energy profiles calculated with CNDO for Mu in silicon using the cluster shown in Fig. 93. From Mainwood and Stoneham (1984).

My attempt to explain Mu* was to place a neutral muonium atom near a vacancy in the very small 4 carbon + 12 hydrogen diamond cluster shown in Fig. 95 (Patterson, 1984a). Using the INDO program, a rigid cluster, and a C—H bond distance of 1.09 Å, I found the [111] energy profile shown in the figure, which simply demonstrates the tendency of muonium to form a C—H bond. A slightly lower energy results from moving the muonium 0.15 Å off of the [111] axis from the C—H bond site, a consequence of a Jahn-Teller distortion. More sophisticated UHF calculations of the 4 host-atom + 12 hydrogen vacancy cluster were presented for diamond and silicon (Sahoo *et al.*, 1985) and later extended to germanium (Sahoo *et al.*, 1986b) by the very active SUNY group. They again chose their muonium defect to be doubly positively charged (to avoid the Jahn-Teller effect), and as in my neutral calculation, they found energy minima along the [111] axis on each side of the vacancy (see Fig. 96). For silicon and germanium, the minimum close to the single lattice ion neighboring

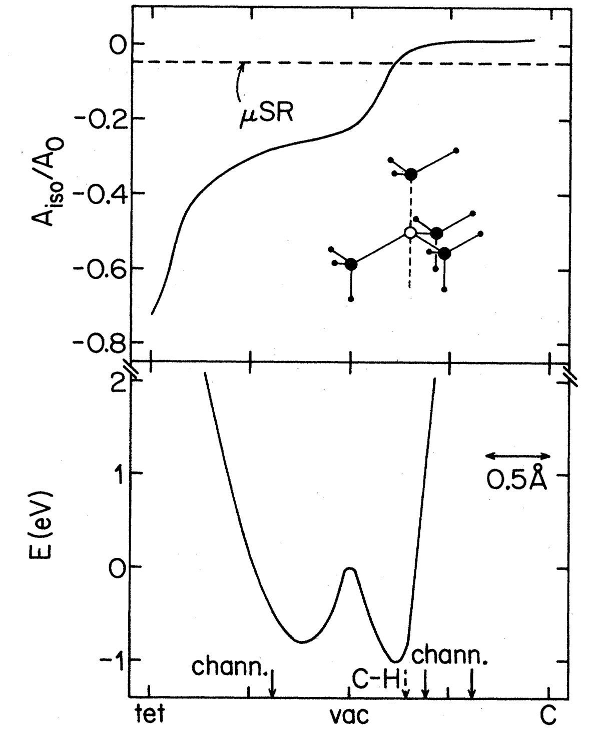

FIG. 95. The [111] energy profile and isotropic hyperfine frequency A_s (relative to the value for vacuum Mu) calculated for the diamond vacancy cluster indicated. C—H indicates the position of a muon which forms a hydrocarbon C—H bond to a carbon ion neighboring the vacancy, and "chann." indicates the muon site positions determined using muon-decay blocking (Patterson *et al.*, 1984a) (scaled from silicon). The dashed line indicates the experimentally determined value for Mu* in diamond [A_s/A (vacuum) $= -0.0461$]. From Patterson (1984a).

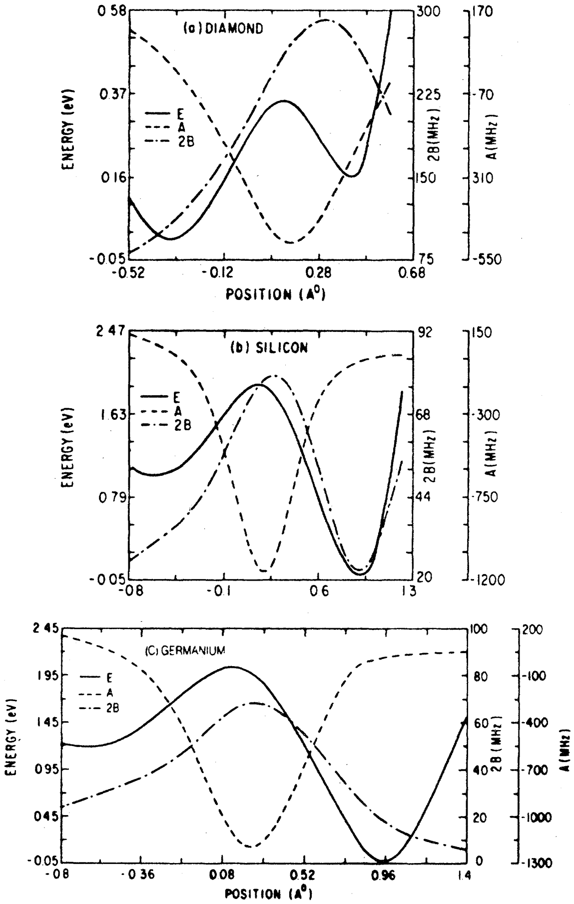

FIG. 96. The [111] energy profiles and hyperfine constants $A_s = A$ and $A_p = B$ calculated for a doubly positively charged muonium defect in the 4 host-atom + 12 hydrogen-vacancy cluster using the UHF technique. The vacancy position is defined as zero, and a single host atom neighboring the vacancy is to the right. From Sahoo *et al.* (1986b).

the vacancy is the deepest, while "Mu^{++}" in diamond prefers the minimum closer to three lattice-ion neighbors. Several comments on these calculations have been made by Estreicher and Marynick (1986a).

Novel models for Mu and Mu* in all semiconductors were recently proposed by Cox and Symons (1986) based on chemical considerations. For isotropic Mu they argued that by analogy with the chemical reaction

$$\mathrm{H}^{\cdot} + (\mathrm{CH_3})_3\mathrm{Si}-\mathrm{Si}(\mathrm{CH_3})_3 \rightarrow \mathrm{H}-\mathrm{Si}(\mathrm{CH_3})_3 + {}^{\cdot}\mathrm{Si}(\mathrm{CH_3})_3 \,, \tag{6.1}$$

Mu approaching a silicon lattice ion will fasten to the antibonding side and will partially disrupt the Si—Si bond. It is as if the reaction (6.1) is prevented from going to completion by the constraints imposed by the lattice. Having established the antibonding site as a candidate [remember that similar sites were found in the calculations of Rodriguez *et al.* (1979) and Johnson *et al.* (1986)], Cox and Symons go on to propose two possible modes of rapid local tunneling, the result of which is an isotropic averaging of the hyperfine interaction. The tunneling mode that I have labeled "CS(I)" in Fig. 89 involves motion among the four antibonding sites surrounding a tetrahedral interstitial site, and in the "CS(II)" mode, motion occurs about a lattice ion. Cox and Symons argued that in the III-V and II-VI compounds, antibonding sites surrounding the anions will be preferred, but suggest cation preference in the cuprous halides. The two isotropic Mu states observed in CuCl and CuBr were tentatively ascribed to the CS(I) and CS(II) (around the Cu ion) tunneling modes.

In the same publication, Cox and Symons (1986) suggested that Mu* occupies the bond-center site in the group-IV materials and a site slightly displaced from the bond center in the III-V materials. Preliminary calculations by Estle *et al.* (1986) supported this site assignment in diamond and silicon. These authors used PRDDO on a diamond cluster with 36 C + 36 H atoms and an unspecified silicon cluster. By allowing the two nearest-neighbor ions to relax, they found dramatic reductions in the energy of muonium at the bond center, leading to a stable site. The relaxation was large: the resulting muon-neighbor distances were 1.09 and 1.59 Å in diamond and silicon, respectively, implying a 41% (35%) increase in the C—C (Si—Si) distance.

During the final stages of the writing of this review, a calculation by Claxton *et al.* (1986) was published which lent strong support to the bond-center site for Mu* and which directly treated the Mu→Mu* transition observed in diamond (see Sec. V.F). Like Sahoo *et al.* (1983), these authors performed UHF calculations of the 10 C + 16 H diamond cluster in Fig. 90 using the bulk diamond C—C distance and the hydrocarbon C—H bond length. Unlike the previous investigators, however, Claxton *et al.* moved the muonium atom from the tetrahedral site to a neighboring bond-center site and allowed the C—C bond to stretch (see Fig. 97). Their energy profiles for different C—C distances, shown in Fig. 98, demonstrate that Mu at the T site and Mu* at the BC site can be simultaneously stable. The equilibrium C—C distance is increased by the Mu* by 39%. The Mu→Mu* barrier height from the figure is approximately 2.2 eV [compared with the experimental values of 0.476 and 0.569 eV in Eqs. (5.24) and (5.25)].

The evidence for extremely fast Mu motion at low temperatures presented in Sec. V.E contrasts strongly with the high-temperature permeability study of van Wieringen and Warmoltz (1956), which yielded an activation for hydrogen diffusion in silicon of 0.48 eV. Theorists disagree on the possibility of rapid or athermal Mu motion at low temperature. The hydrogen vibration frequencies predicted by Singh *et al.* (1977) indicate a localized state in silicon, as do the deep potential wells found by Rodriguez *et al.* (1979) and Corbett *et al.* (1983) in silicon and by Sahoo *et al.* (1983), Estreicher and Marynick (1986b), Claxton *et al.* (1986), and myself in diamond.

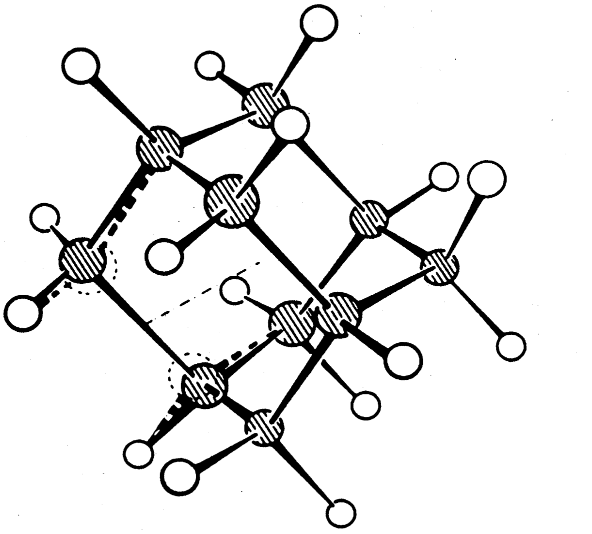

FIG. 97. The 10 C + 16 H diamond cluster used in the UHF calculations of Claxton *et al.* (1986). The muonium atom was moved along the weakly dashed line, and the two carbon atoms forming the bond-center site were allowed to relax their positions. From Claxton *et al.* (1986).

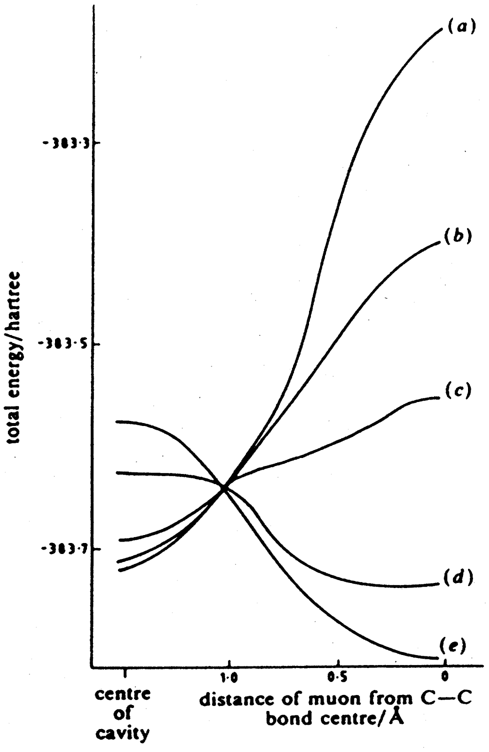

FIG. 98. The "tetrahedral to bond-center" energy profiles calculated for the diamond cluster in Fig. 97 using the UHF technique. The curves (a)–(e) refer to different extensions of the C—C bond: (a) 0.0 Å; (b) 0.1 Å; (c) 0.2 Å; (d) 0.4 Å; (e) 0.6 Å. From Claxton *et al.* (1986).

On the other hand, the CNDO calculations of Mainwood and Stoneham (1984) show low or nonexistent barriers for Mu motion in silicon and diamond.

B. The electronic structure of isotropic Mu

The theoretical attempts to account for the observed hyperfine frequency A of Mu in semiconductors are summarized in Table XXIII. All of the entries refer to the vicinity of the tetrahedral interstitial site. The theoretical predictions are to be compared with the experimental values cited at the top of the table.

The cavity model of Reiss (1956) and Kaus (1958) describes the electric potential near a point charge by the r-dependent dielectric function

$$\begin{aligned}\varepsilon(r) &= R\varepsilon_0/[(R-r)\varepsilon_0+r] \quad r<R\\ &= \varepsilon_0 \quad r>R\ ,\end{aligned} \tag{6.2}$$

where ε_0 is the bulk dielectric constant and R is a "cavity radius." Wang and Kittel (1973) found that by choosing the cavity radius equal to that of an interstitial sphere at the tetrahedral site in a lattice of touching hard spheres and by assuming an r-independent electron mass equal to its free value, they could account for the trend, if not the exact values, of A in silicon and germanium. Their plot of A/A(vacuum) as a function of the cavity radius R is shown in Fig. 99. Holzschuh *et al.* (1982) verified these results, but, upon extending the calculations to diamond, found an A value in diamond smaller than that for both silicon and germanium, in disagreement with experiment (see Table XXIII).

Wang and Kittel (1973) also suggested an alternative dielectric function approach in which $\varepsilon(r)$ was derived from the wave-vector-dependent dielectric function obtained from the band structure of the host material. With the free-electron mass, they found encouraging agreement with experiment for silicon and germanium. Later work by Varisov (1982) and Holzschuh *et al.* (1982) verified these results, but the latter authors again found that the trend to diamond is incorrect. The simultaneous use of a dielectric function and the free-electron mass has been criticized by Pantelides (1979).

Using the self-consistent charge extended Hückel procedure on a cluster of 30 host ions, Coker *et al.* (1978) obtained strong reductions in the hyperfine frequency at Mu in silicon and germanium, but the A values again followed an incorrect trend.

The question of why Mu forms a deep donor was addressed in the work of Pickett *et al.* (1979), Altarelli and Hsu (1979), and Resca and Resta (1980). The self-consistent pseudopotential calculation by Pickett *et al.* was based on a supercell of one hydrogen atom and 54 germanium ions. They found that the effect of intra-atomic correlation is to produce a singly occupied deep donor state in the valence band of germanium. A contour plot of the total valence "pseudocharge" density is shown in Fig. 100. Atarelli and Hsu, on the other hand,

TABLE XXIII. Calculations of the electronic structure of isotropic Mu at the tetrahedral interstitial site in diamond, silicon, and germanium.

Host	A (MHz)	Method	Reference
C	3711 (2)	Experiment	Sec. V.A
Si	2006.3 (2.0)	Experiment	Sec. V.A
Ge	2359.5 (2)	Experiment	Sec. V.A
Si	(3736, 3722)	Cavity model	Wang and Kittel (1973), Holzschuh *et al.* (1982)
Ge	(3838, 3820)	Cavity model	Wang and Kittel (1973), Holzschuh *et al.* (1982)
C	1871	Cavity model	Holzschuh *et al.* (1982)
Si	(1906, 1915)	Dielectric functions	Wang and Kittel (1973)
	(2026, 2038)	Dielectric functions	Varisov (1982)
	(1910, 759)	Dielectric functions	Holzschuh *et al.* (1982)
Ge	(2022, 2133)	Dielectric functions	Wang and Kittel (1973)
	(2127, 2236)	Dielectric functions	Varisov (1982)
	(2173, 781)	Dielectric functions	Holzschuh *et al.* (1982)
C	(1700, 509)	Dielectric functions	Holzschuh *et al.* (1982)
Si	3303	Hückel cluster	Coker *et al.* (1978)
Ge	2856	Hückel cluster	Coker *et al.* (1978)
Ge	Deep donor	Self-consistent supercell	Pickett *et al.* (1979)
Si,Ge	Interstitial Deep donor	Intervalley mixing	Altarelli and Hsu (1979)
Si,Ge	Position-independent Deep donor	Intervalley mixing	Resca and Resta (1980)
C,Si,Ge	490–3750	Density functional, zero-point motion	Manninen and Meier (1982)
C	3347	UHF cluster, motional average	Sahoo *et al.* (1983), Estreicher *et al.* (1985)
Si	2900	UHF cluster, motional average	Sahoo *et al.* (1986a)
Si	1812	LCAO Green's function, static	Katayama-Yoshida and Shindo (1983)
C	(3790, 3750)	INDO, MINDO clusters	Patterson (1984a)
Si	Hyperdeep level	Multiple scattering cluster	Assali and Leite (1985)
C,Si,Ge	Tunnel states	Chemical arguments	Cox and Symons (1986)
C	4900	UHF cluster	Claxton *et al.* (1986)

attributed the formation of a deep donor in silicon and germanium to the valley-orbit interaction of the distinct conduction-band minima, an effect, they stated, that is only of importance for interstitial impurities like Mu. Resca and Resta found that the valley-orbit interaction causes a deep level for a screened point-charge potential, regardless of its location in the host lattice.

Until 1982, little or no mention was made of the effect of the zero-point motion of Mu on its hyperfine frequency. Manninen and Meier (1982) used the density-functional formalism, the host pseudopotential, and an approximate dielectric function to obtain a screened pseudopotential that was a function of the Mu site in the lattice. The spin density at the muon was then computed self-consistently. They obtained very small hyperfine frequencies [$A/A(\text{vacuum})\simeq 0.1$] for Mu at rest at the tetrahedral interstitial site in diamond, silicon, and germanium. The assumption of zero-point motion of Gaussian width 1–1.5 atomic units, however, led to *motionally averaged* hyperfine frequencies comparable with experiment (see Fig. 101).

Instead of an *increase* in A with Mu motion, the unrestricted Hartree-Fock self-consistent-field calculation by Sahoo *et al.* (1983) of the 10 C + 16 H diamond cluster showed a *decrease*. Their [111] energy profile is shown in Fig. 91 along with the normalized spin density at the muon. Whereas Mu at rest at the tetrahedral energy minimum yields $A/A(\text{vacuum})=0.90$, the inclusion of zero-point motion decreases this to 0.75, compared with the experimental value of 0.832. Preliminary results for a silicon cluster gave a motionally averaged A value somewhat larger than experiment (Sahoo *et al.*, 1986a). My (nonmotionally averaged) results for the same diamond cluster (Fig. 92) are 0.849 and 0.840 for the INDO and MINDO calculations, respectively.

The local spin-density-functional formalism combined with the linear combination of atomic orbitals and Green's function method was used by Katayama-Yoshida and Shindo (1983) to compute the electronic structure of Mu at the tetrahedral site in silicon. The change in the number of states below a given energy E for the isotropic A_1 representation caused by the presence of the muon is shown in Fig. 102. Note the important changes at energies far below the valence-band edge. The reduced

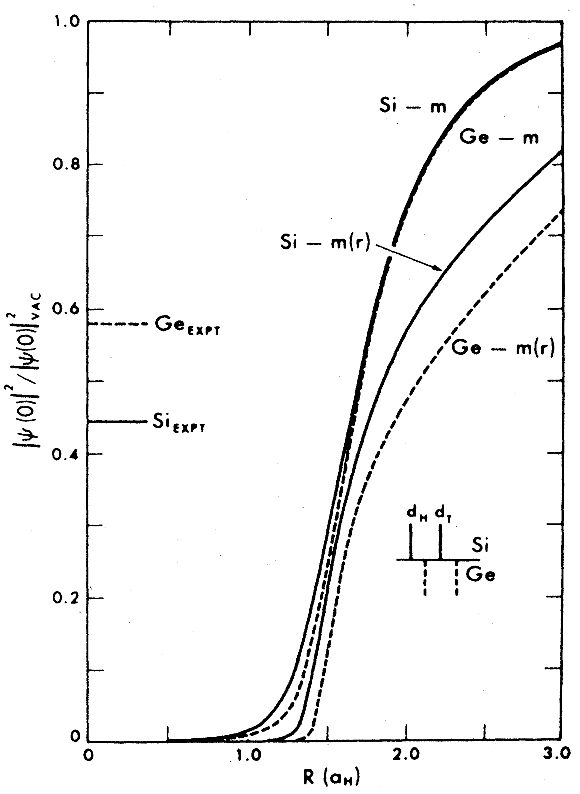

FIG. 99. Reduced hyperfine frequencies for Mu in silicon and germanium, as a function of the cavity radius R, calculated using cavity models for the position-dependent dielectric constant [Eq. (6.2)]. The labels m and $m(r)$ refer, respectively, to calculations in which the bound-electron mass was taken to be the free mass for all radii and taken to be the free mass within the cavity and the bulk effective mass m^* outside. The touching-sphere cavity radii d_H and d_T for the hexagonal and tetrahedral sites are indicated. From Wang and Kittel (1973).

hyperfine frequency $A/A(\text{vacuum})=0.406$ found assuming that the muon is at rest is in good agreement with the experimental value (0.449).

A "hyperdeep" atomic-like 1s level was also found by Assali and Leite (1985) for hydrogen at the tetrahedral site in silicon. These authors used the Watson-sphere terminated molecular cluster model in the framework of the self-consistent-field multiple-scattering X_α theory. Qualitative chemical arguments for the dependence of A on the host in elemental and compound semiconductors are given by Cox and Symons (1986). The hyperfine frequency found for tetrahedral Mu at rest in diamond by Claxton *et al.* (1986) exceeds the vacuum value, but motional averaging will cause a decrease (see Fig. 103).

C. The electronic structure of anisotropic Mu*

Many models have been suggested for the anisotropic Mu* state in semiconductors (see Table XXIV). At the time of its discovery, Mu* was believed to be an isotropic

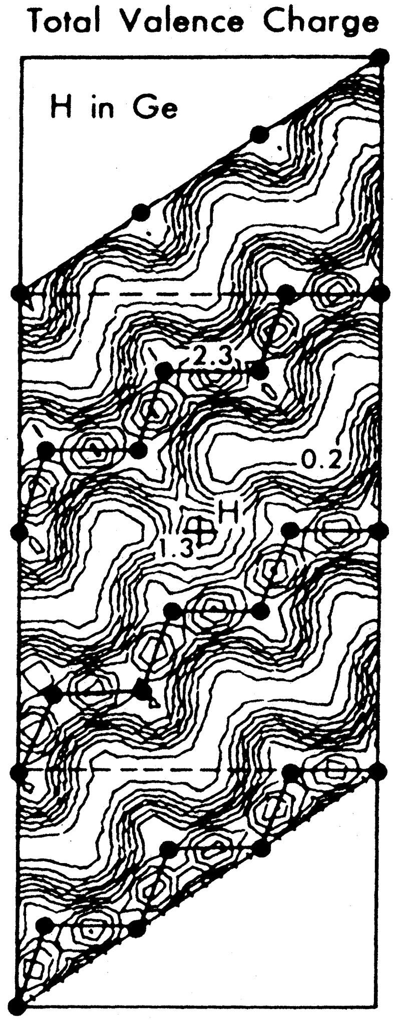

FIG. 100. A (110) cross section of a 54 Ge + 1 Mu supercell showing the total valence "pseudocharge" density. From Pickett *et al.* (1979).

state with a very large electronic g value, and it was proposed that a tumbling excitonic molecule ($\mu^+ e^- e^- h^+$) or an excited state of Mu was involved (Brewer *et al.*, 1973). These models are incompatible with the relatively large Mu* hyperfine interaction and with the observation in diamond that Mu* is more stable than Mu.

The hexagonal interstitial site (Belousov *et al.*, 1978a, 1978b, 1981; Estle, 1981) would have the correct [111] symmetry for Mu*. Sahoo *et al.* (1984) found an energy minimum at the hexagonal site for a doubly positively charged muonium defect using the UHF method on the 10 C + 16 H diamond cluster of Fig. 90. The resulting values for A_s and A_p were -3.5 and 32.0 MHz, i.e., much smaller in magnitude than the experimental values (see Table XXIV). A doubly charged hexagonal cluster with 6 C + 12 H produced the values -10.3 and 35.0 MHz. No neutral cluster calculation has yielded a stable muon position at the hexagonal site. Furthermore, although a "pancake-shaped" electronic cloud at such a

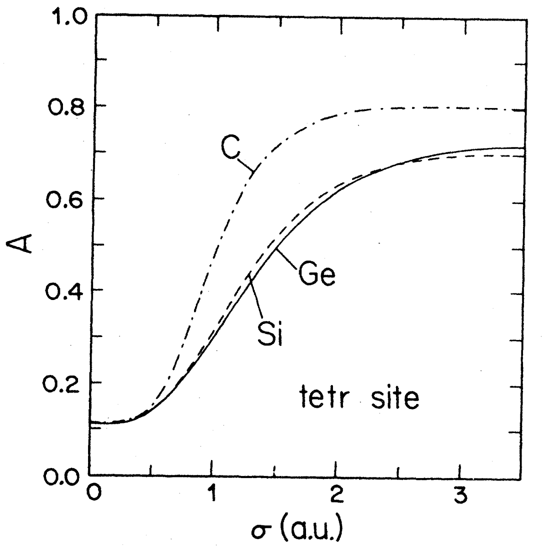

FIG. 101. The reduced hyperfine frequency for Mu in diamond, silicon, and germanium as calculated by Manninen and Meier with the density-functional formalism as a function of the Gaussian width σ of the Mu zero-point motion. The experimentally determined reduced hyperfine frequencies are 0.832, 0.449, and 0.529 for diamond, silicon, and germanium, respectively. From Manninen and Meier (1982).

site would give a [111]-symmetric hyperfine interaction, it would require $A_s > 0$ and $A_p < 0$, in disagreement with experiment (see Sec. V.F).

Estle (1984) mentions the possibility that Mu* in silicon is a [111]-oriented molecule consisting of muonium bound to an interstitial silicon atom. It is known that in a radiation environment such interstitial atoms are mobile at 4.2 K. This model has received little attention to date.

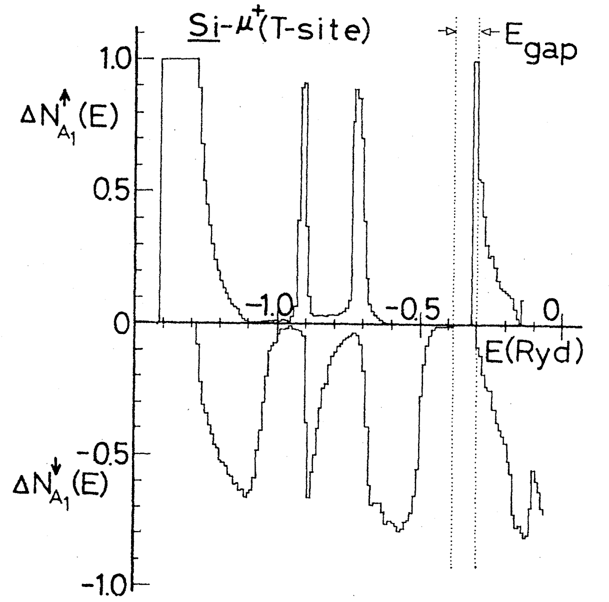

FIG. 102. The change in the number of states below a given energy E for the isotropic A_1 representation caused by the presence of the muon at the tetrahedral site in silicon. From Katayama-Yoshida and Shindo (1983).

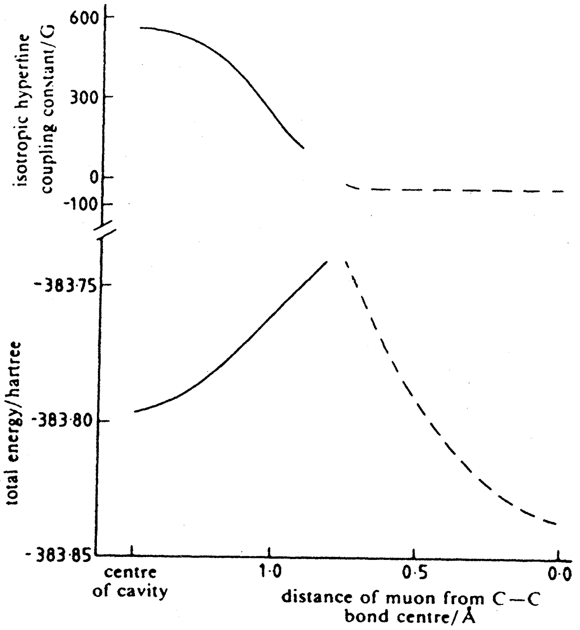

FIG. 103. The "tetrahedral to bond-center" energy profiles and isotropic hyperfine parameter calculated with the UHF technique for the diamond cluster shown in Fig. 97. The solid curves refer to zero extension of the C—C bond, and the dashed curves correspond to an extension by 0.68 Å. The hyperfine parameter scale refers to the equivalent coupling in Gauss for a proton $[=hA/(g_e\mu_B)\times g_p\mu_N/g_\mu\mu_\mu = A\times 0.1211$ G/MHz]. The experimental values in these units for Mu (vacuum), Mu (diamond), and Mu* (diamond) are 540.5, 449.4, and -24.91 G, respectively. From Claxton *et al.* (1986).

The final two Mu* models I shall mention now appear to be the major contenders. These are the vacancy model, in which muonium either finds or creates a host-ion vacancy and satisfies one or more of the dangling bonds, and the bond-center model, in which muonium inserts itself between two neighboring host ions.

The Mu* hyperfine parameters in GaP and GaAs agree to within 10% (see Table IX). This close similarity has been cited by Kiefl *et al.* (1985) in support of a model in which muonium occupies a phosphorous or arsenic-ion vacancy and hence experiences the same nearest-neighbor environment in both materials.

My INDO calculation (Patterson, 1984a) of the diamond vacancy cluster in Fig. 95 shows good agreement with the experimental A_s value for muonium which forms a C—H bond in the vacancy (see also Table XXIV). The anisotropic interaction A_p was not evaluated in detail, but a crude point dipole model gave a positive value. As noted in the previous section, the energy minimum found in this calculation is slightly displaced from the [111] axis, hence rapid motion about the six equivalent sites is required in order to produce the ob-

TABLE XXIV. Theoretical calculations of the electronic structure of anisotropic Mu* in diamond, silicon, and germanium.

Host	A_s[a] (MHz)	A_p[a] (MHz)	Method (site)	Reference
C	-205.730 (41)	186.856 (26)	Experiment	Sec. V.A
Si	-67.333 (34)	25.257 (17)	Experiment	Sec. V.A
Ge	-96.448 (23)	34.589 (12)	Experiment	Sec. V.A
C	(-3.5, -10.3)	(32.0, 35.0)	UHF cluster (Mu^{++}, H)	Sahoo *et al.* (1984)
	-661	727	UHF cluster (BC, unstable)	Sahoo *et al.* (1986b)
C	-250	>0	INDO cluster (C—H near vacancy off [111])	Patterson (1984a)
C	-85	69.5	UHF cluster (Mu^{++}, near vacancy)	Sahoo *et al.* (1985), Estreicher and Marynick (1986a)
Si	-55	16	UHF cluster (Mu^{++}, near vacancy)	Sahoo *et al.* (1985), Estreicher and Marynick (1986a)
Ge	-70	12.5	UHF cluster (Mu^{++}, near vacancy)	Sahoo *et al.* (1986b)
C,Si,Ge	<0	>0	Chemical arguments (BC)	Cox and Symons (1986)
C	-800	>0	PRDDO cluster (BC)	Estle *et al.* (1986)
Si	<0	>0	PRDDO cluster (BC)	Estle *et al.* (1986)
C	-320		UHF cluster (BC)	Claxton *et al.* (1986)

[a] The relative sign between A_s and A_p is known from experiment, as are the absolute signs for C. The absolute signs for Si and Ge are assumed to be the same as for C.

served [111] symmetric hyperfine interaction.

Sahoo *et al.* (1985, 1986b) used the same type of cluster for UHF calculations of muonium-vacancy centers in diamond, silicon, and germanium. In these calculations, however, they avoided the problem of the Jahn-Teller distortion by making the cluster doubly positively charged. The values for A_s and A_p as a function of muon position are shown for the three hosts in Fig. 96. The values are somewhat smaller in magnitude than experiment, but the signs and the trend of A_s are correctly reproduced (see Table XXIV).

The first suggestion that Mu* could represent a muonium state situated at the center of a Si—Si bond was made by A. M. Portis (private communication) soon after the discovery of Mu*. His argument was that a positive muon should be attracted to the concentration of negative charge in the bond. An alternative picture is that of Barsov *et al.* (1979, 1980), in which the muon breaks a Si—Si bond and forms a Si—Mu* bond. Symons (1984) offered chemical arguments for the bond-center model for Mu* in silicon and germanium and proposed that Mu* in diamond is at a C—N bond between carbon and a substitutional nitrogen impurity. A possible test of the latter hypothesis would be to look for the ^{14}N nuclear hyperfine interaction. More detailed chemical arguments on the hyperfine interaction expected at the bond-center site in elemental and compound semiconductors appeared in the work of Cox and Symons (1986).

Several cluster calculations of bond-centered Mu* have now appeared. Sahoo *et al.* (1986b) found an unstable site using the UHF technique on an unrelaxed diamond cluster and hyperfine parameters that have the correct signs but are substantially larger than experiment (see Table XXIV). Stoneham (1984) found that CNDO calculations of relaxed diamond and silicon clusters failed to show a stable bond-center site. Like the unstable site of Sahoo *et al.*, the stable bond-center sites found by Estle *et al.* (1986) using PRDDO on strongly relaxed diamond and silicon clusters also have the correct signs for the hyperfine parameters. Finally, the recent UHF calculation of Claxton *et al.* (1986) found an isotropic hyperfine parameter for Mu* in the center of a stretched bond which has the correct sign and approximately the correct magnitude (see Fig. 103).

Estle, Rudaz *et al.* (1984) produced what they called a "crude" but quite model-independent picture of Mu* in germanium from their analysis of the nuclear hyperfine broadening of the Mu* lines in natural and isotopically enriched samples. Assuming that the electronic wave function of Mu* is primarily made up of sp^3 atomic orbitals of the host ions, they found that the Mu* electron is distributed among approximately 10 host ions, each with 6% of the spin density, and 50 ions, each with 0.8%.

The vacancy-related models for Mu* draw support from the observations of vacancy-associated hydrogen states, the similarity of the hyperfine constants in GaAs and GaP, and the results of cluster calculations. Further support of these models can be found in several correlations between the temperatures of vacancy annealing and Mu* disappearance. Vacancies become unstable in silicon between 130 and 180 K (Frank, 1975), which correlates well with the disappearance of Mu* in this material above 165 K. In germanium, vacancies disappear above 65 K in unperturbed material and above 27 K when carriers are created with band-gap light (Bourgoin *et al.*, 1981), in approximate agreement with the disappearance of Mu* above 85 K in pure germanium and above 20 K in doped samples (Fig. 78). Finally, vacancies in diamond are stable up to at least 700 °C (Loubser and van Wyk, 1978), as is Mu*.

As discussed in Sec. IV.A the principal problem with vacancy-related models for Mu* is the source of the vacancy. Vacancies are unstable in silicon and germanium at room temperature, and, even assuming motion of Mu at the adiabatic limit, its trapping rate at vacancies, both accumulated from previous muons and produced by the stopping muon itself, is much smaller than the muon-decay rate. A possible way out is the ionization-enhanced vacancy production mentioned in Sec. IV.A.

Intrinsic-defect models for Mu* such as the bond-center model are supported by the observation of a thermally activated Mu→Mu* transition in diamond. As discussed in Sec. V.F the large Arrhenius frequency factor found for the transition rate $\Lambda(T)$ indicates that Mu requires only a single hop in order to form Mu*. A time-consuming search for preexisting vacancies is ruled out.

The interesting observation has been recently made by J. U. Andersen (private communication) that with sufficient nearest-neighbor relaxation, the bond-center site for Mu* begins to resemble a vacancy-related model for Mu* with an interstitial host ion nearby. This "close Frenkel pair" model for Mu* is reminiscent of the $E3'$ electron trap seen with DLTS upon proton irradiation of silicon (Irmscher *et al.*, 1984; see Sec. IV.B) and may warrant further consideration.

VII. CONCLUSIONS

The central problem in investigations of muonium in semiconductors is still to construct realistic microscopic models of the three states μ^+, Mu, and Mu* and to relate them to the states pertinent to hydrogen.

Existing spin Hamiltonians adequately describe the spectroscopy of these states. What is still needed here is an efficient, accurate method of simulating the nuclear hyperfine interaction of a muonium state with many inequivalent nuclear spins. Moreover, the dynamics of muonium in semiconductors is reasonably well treated with existing theories of depolarization and interstate transitions. A very convenient calculation method has turned out to be the jump model of Celio, which can include the effects of Nosov-Yakovleva electron spin flips, persistent modulation of the hyperfine interaction, and irreversible changes of state, both with and without conservation of the electron spin polarization.

The transverse-field μSR technique is and will remain the preferred method for studying muonium states, by virtue of its simplicity and the spectroscopic information it supplies. The somewhat more involved high-field, high-time-resolution variation of this technique allows the experimenter to quench the nuclear hyperfine interaction and hence to study systems with concentrated nuclear spins. The quenching of relaxation with the time-differential longitudinal-field technique should be able to deliver important information on the processes responsible for relaxation. The limited contribution made by this method to date is probably due to the lack of *coordinated* experiments which identify the relaxing state with transverse-field μSR and which determine the cause of the relaxation with longitudinal-field quenching.

As the intensity of polarized muon beams increases, the time-integral techniques, which place no restriction on the number of muons simultaneously present in the sample, will gain in importance. These include time-integral radio-frequency and microwave resonance techniques and the new avoided-level-crossing technique. The sensitivity of these methods to the nuclear hyperfine interaction will hopefully permit them to make definite statements about the local geometry of the Mu and Mu* sites. Still more direct site information for *all* the muon states (including the "missing fractions") is potentially accessible with the muon-decay-blocking technique, particularly when it is used in conjunction with transverse-field μSR at various sample temperatures. Like the time-integral μSR techniques, muon-decay blocking places no limit on the muon beam intensity.

The muon-stopping process in a semiconductor is very complex, particularly in the important radiation chemistry regime. It is established, I believe, that the effects on the muon polarization of pre-formed vacancies from the muon implantation, both those from the accumulated muon dose and those created during the deceleration of a particular muon, are negligible. What happens, however, in the ionization cloud surrounding the stopped muon, both at $t=0$ and during the muon lifetime, is not at all clear. It is probably the μSR experiments themselves that will yield the most information on this complex interplay of processes.

We turn now to the experimental results obtained to date on muon states in semiconductors. The muon- and pion-decay-blocking data are at present inadequate and somewhat contradictory. The two pion-decay experiments in germanium yielded different [110] channeling patterns, and the muon-decay experiments in germanium and silicon were complicated by impurity trapping. More muon-decay-blocking studies are required to elucidate the sites of the three observed states and that of any missing fraction. These should be performed as a function of temperature in both high-purity and well-characterized doped samples in conjunction with transverse-field μSR.

The existing measurements of the electronic g factors for Mu and Mu* can certainly be improved upon, but there is apparently little theoretical motivation for such improvements.

It is well established that isotropic Mu is extremely mobile at low temperature in silicon and germanium. In view of the vastly slower motion of hydrogen, it is challenging for theorists to explain this mobility, which is perhaps due to a "delay to self-trapping." Future experiments in these materials could search for macroscopic diffusion to the surface of powder grains or thin films.

The situation in diamond is unclear due to conflicting, sample-dependent results. Little is known about Mu motion in the compound semiconductors, but there are already interesting disrepancies. In GaAs, the apparent rapid motion inferred from the trapping in low-resistivity material conflicts with the slow motion inferred from both the nuclear hyperfine linewidth and the failure to find neutron-induced defects. Also intriguing is the apparent sudden onset of rapid diffusion of the Mu^{I} center in CuCl below 10.5 K.

The thermally activated transition from Mu to Mu* in diamond is now well documented, both in terms of the disappearance of Mu and the appearance of Mu*. The transition has allowed a determination of the sign of the hyperfine parameters of Mu*: The isotropic part A_s is negative, and the anisotropic part A_p is positive, indicating that indirect polarization transfer is active. The observation of a $\mathrm{Mu}\rightarrow\mathrm{Mu}^*$ transition also in irradiated silicon raises the question of the fate of Mu in semiconductors in general; does it, on its way to the μ^+ state, intermittently form Mu*?

Muonium dynamics in Si, Ge, and GaAs is clearly complex, but happily similar. In high-purity samples at low temperature, the three states Mu*, Mu, and μ^+ are formed. As the temperature is increased, Mu* first disappears, to reappear as μ^+, followed by a thermally activated $\mathrm{Mu}\rightarrow\mu^+$ transition. Each of these transitions makes itself apparent in a stepwise increase in the μ^+ amplitude. Two features of the transitions are unclear. The first is the discrepancy in the activation energies for muonium disappearance and μ^+ appearance, and the second, perhaps related point, is the cause of the electron spin flipping that accompanies the transition. In all three materials, the μ^+ state becomes unstable at the highest temperatures investigated, presumably due to repeated charge exchange with a paramagnetic state. Experiments at still higher temperatures are called for.

Doping Si, Ge, and GaAs generally increases the relaxation rates of Mu and Mu*. Sample-dependent effects, even in nominally high-purity material, indicate that mobile Mu traps at impurities at low temperatures. The immobile Mu* state, on the other hand, is relaxed by spin collisions with the free carriers introduced by doping. The striking onset of room-temperature relaxation of the μ^+ state with n doping in silicon is not understood, nor is the observation that doping moves the increase in λ_{μ^+} in germanium to higher temperatures. In oxygen-doped silicon, the absence at all temperatures of a μ^+ signal indicates that the μ^+ state to which Mu* jumps is highly mobile and can find the dilute oxygen impurities. The existing longitudinal-field quenching data in silicon and germanium present a puzzle whose solution requires measurements at more temperatures in conjunction with transverse-field work.

Although electric-field and optical-illumination experiments appear to be a dead end, investigations of electron- and neutron-irradiated samples are both interesting and informative. Irradiation defects in silicon serve as trapping centers for mobile Mu. The failure of these preformed vacancies to increase the initial Mu* amplitude in electron-irradiated silicon argues against the vacancy model for this state. But the observation upon irradiation of a $\mathrm{Mu}\rightarrow\mathrm{Mu}^*$ transition at 20 K indicates that Mu* formation is promoted by lattice disorder. The trapping of free electrons by radiation defects effectively transforms n-doped silicon into high-purity material, as far as the relaxation of Mu* at higher temperature is concerned. Although neutron irradiation has the same effect as electron irradiation in silicon, it has the opposite effect in GaAs, namely, of killing Mu* and leaving Mu unchanged.

We consider now the other zincblende materials. The two isotropic Mu states in the cuprous halides are an unexpected mystery. Luckily their low hyperfine frequencies will permit detailed studies with the avoided-level-crossing technique. Further study of the interesting material β—SiC should be made on a high-quality single crystal. The large missing fractions seen in many III-V and II-VI compounds indicate still undiscovered paramagnetic muonium states, and the large μ^+ fractions seen in others invite site studies with muon-decay blocking and perhaps measurements of a paramagnetic or diamagnetic shift in the μ^+ frequency.

The progress made in the theoretical understanding of muonium states in semiconductors in the last four years, particularly with the molecular cluster approaches, is very gratifying. It is fair to say that the isotropic Mu state at low temperature in diamond and silicon, if it indeed occupies the tetrahedral interstitial site, is quite well understood. The changes in hyperfine frequency as one raises the temperature and as one moves to germanium and the compounds still need to be addressed. The very rapid motion of Mu at low temperature also requires a theoretical explanation.

The path to understanding the Mu* state has undergone many twists and turns since it began 14 years ago, and the long list of proposed models is a testament to the imagination of those involved. Two candidates are now clearly in the lead: the vacancy-associated model and the bond-centered model. Speaking for the vacancy model are (1) the vacancy-associated hydrogen states seen with infrared absorption in elemental and compound semiconductors, (2) the similarities between the Mu* hyperfine parameters in GaP and GaAs, (3) the good agreement between the observed and calculated Mu* hyperfine frequencies for this model, and (4) the correlations between the vacancy annealing temperatures and the temperatures at which Mu* disappears. Speaking against vacancy association are (1) the unavailability of pre-formed vacancies in sufficient concentration, (2) the failure of electron irradiation to increase the initial Mu* amplitude, and (3) the ability in diamond of Mu to change into a Mu* state in a *single* overbarrier jump. The bond-centered model overcomes all of the objections to the vacancy model, although the theoretical stability of the site may still be questioned by some groups. The recent bond-centered molecular cluster calculations are very convincing, but the severe stretching of the bond calls for a treatment of the relaxation of more distant neighbors using larger clusters. I find the compromise solution appealing in which a bond becomes so elongated that one is really dealing with a close Frenkel pair. In the end it will probably be the avoided-level-crossing and muon-decay-blocking experimenters who will have the last say.

Finally, one should address the question "What have muons taught us about hydrogen in particular and about defects in general in semiconductors?" The electronic similarity of muonium and hydrogen argues strongly that an implanted muon and an implanted proton should behave at least qualitatively similarly. This implies the the existence of isotropic H and anisotropic H*, perhaps with different rates of interconversion and motion, but with basically the same structure as Mu and Mu*. In the theoretical calculations made for these states to date, little consideration if any has been taken of the muon mass. Why then do not electron spin resonance studies of proton irradiated silicon show these paramagnetic states?

As we have seen, both Mu and Mu* are unstable at elevated temperatures. In order to have any chance of success, an ESR search for hydrogen states must be performed on samples irradiated and kept at low temperature. A more severe restriction, however, involves the time scale of the experiments. A μSR experiment only tells us what occurs during the first few microseconds following the muon implantation. It may be impossible to construct an ESR experiment which collects enough signal strength soon enough after the proton implantation without requiring excessive levels of radiation damage. The absence of observable paramagnetic hydrogen states has an interesting parallel in the observed tendency of Mu and Mu* to decay to the diamagnetic μ^+ state.

Further parallels cannot presently be drawn between muonium and hydrogen states in semiconductors, because too little is known about hydrogen. More heartening are the unexpected features which the study of these muonium states have contributed to the field of defects in semiconductors in general. The most significant of these, in my opinion, are the following: (1) the strong reduction in the electron spin density at the nucleus of an isotropic hydrogenlike impurity (isotropic Mu) upon introducing it into a semiconductor host, and the systematic dependence of the spin density on the host ionicity, (2) the motion of such a center through the host at a jump rate approximately equal to the Debye frequency, and (3) the simultaneous existence of a second, strongly anisotropic paramagnetic center (Mu*) possibly representing a hydrogenlike atom in a highly distorted bond-center environment.

ACKNOWLEDGMENTS

The μSR group of the Physics Institute of the University of Zurich (the so-called "Zurich group"), of which I have the pleasure of being a member, has aided me substantially in the writing of this review by supplying numerous published and unpublished results, participating in helpful discussions, and showing great patience. The group is ably led by W. Kündig, and past and present members include Hp. Baumeler, M. Celio (now at TRIUMF, Vancouver, Canada), J. Felber, E. Holzschuh, H. Keller, R. F. Kiefl (now at TRIUMF), P. F. Meier, W. Odermatt, M. Richner, J. W. Schneider, U. Seifert, and H. Simmler. I should also like to thank our collaborators: K. W. Blazey (IBM, Rüschlikon, Switzerland), T. L. Estle (Rice University, Texas), I. M. Savic (Belgrade, Yugoslavia), C. Schwab (Strasbourg, France), J. P. F. Sellschop (Johannesburg, South Africa), and M. C. Stemmet (Johannesburg, South Africa). The University of Zurich channeling group has made possible the construction and operation of the muon-decay-blocking apparatus. Its members include A. Bosshard, U. Straumann, P. Truöl, Th. Wichert (University of Konstanz, West Germany), and A. Wüest. The μSR and muon-decay-blocking experiments performed by the Zurich group were only possible with the excellent technical assistance and the support of the Swiss Institute for Nuclear Research (SIN) under the direction of J. P. Blaser. I also acknowledge pleasant and enlightening discussions on the early history of μSR with V. L. Telegdi (ETH, Zurich). F. Waldner of the University of Zurich provided the key for our understanding of the anisotropic spin Hamiltonian of Mu*. I also want to acknowledge both the assistance with the molecular cluster calculations and the many fruitful ideas regarding the chemical nature of muonium which were provided by H. Fischer, M. Heming, and E. Roduner of the Physical Chemistry Institute of the University of Zurich. I should like to thank J. F. Ziegler of IBM, Yorktown Heights, New York, for kindly supplying me with the TRIM program for simulating the muon-stopping process and R. E. Pixley of the University of Zurich for help running the program. I am indebted to several research groups for helpful discussions and their permission to present unpublished material. These include the μSR group at the University of Konstanz, West Germany (A. Weidinger and E. Albert), the pion-channeling group at the Max Planck Institute for Metals Research, Stuttgart, West Germany (A. Seeger and K. Maier), and the channeling group at the University of Aarhus, Denmark (B. B. Nielsen and J. U. Andersen).

REFERENCES

Abragam, A., 1961, *The Principles of Nuclear Magnetism* (Oxford University Press, Oxford), p. 439.

Abragam, A., 1984, C. R. Acad. Sci. Ser. 2 **299**, 95.

Albert, E., 1986, doctoral thesis (University of Konstanz).

Albert, E., A. Möslang, E. Recknagel, and A. Weidinger, 1983, Hyperfine Int. **15-16**, 525.

Albert, E., A. Möslang, E. Recknagel, and A. Weidinger, 1984, Hyperfine Int. **17-19**, 611.

Albert, E., S. Barth, A. Möslang, E. Recknagel, A. Weidinger, and P. Moser, 1985a, Appl. Phys. Lett. **46**, 759.

Albert, E., A. Möslang, E. Recknagel, and A. Weidinger, 1985b, in *Proceedings of the 17th International Conference on the Physics of Semiconductors,* edited by J. D. Chadi and W. A. Harrison (Springer, New York), p. 693.

Anderson, C. D., and S. H. Neddermeyer, 1937a, Phys. Rev. **50**, 263.

Anderson, C. D., and S. H. Neddermeyer, 1937b, Phys. Rev. **51**, 884.

Anderson, C. D., and S. H. Neddermeyer, 1938, Phys. Rev. **54**, 88.

Andrianov, D. G., L. A. Goncharov, E. V. Minaichev, G. G. Myasishcheva, Yu V. Obukhov, V. S. Roganov, G. I. Savel'ev, V. G. Firsov, and V. I. Fistul, 1976, Fiz. Tekh. Poluprovodn. **10**, 1167 [Sov. Phys. Semicond. **10**, 692 (1976)].

Andrianov, D. G., E. V. Minaichev, G. G. Myasishcheva, Yu. V. Obukhov, V. S. Roganov, G. I. Savelev, V. G. Firsov, and V. I. Fistul, 1970, Zh. Eksp. Teor. Fiz. **58**, 1896 [Sov. Phys. JETP **31**, 1019 (1970)].

Andrianov, D. G., G. G. Myasishcheva, Yu. V. Obukhov, V. S. Roganov, V. G. Firsov, and V. I. Fistul, 1969, Zh. Eksp. Teor. Fiz. **56**, 1195 [Sov. Phys. JETP **29**, 643 (1969)].

Andrianov, D. G., G. G. Myasishcheva, Yu. V. Obukhov, V. S. Roganov, G. I. Savelev, V. G. Firsov, and V. I. Fistul, 1978a, Fiz. Teckh. Poluprovodn. **12**, 161 [Sov. Phys. Semicond. **12**, 92 (1978)].

Andrianov, D. G., G. G. Myasishcheva, Yu. V. Obukhov, V. S. Roganov, G. I. Savelev, V. G. Firsov, and V. I. Fistul, 1978b, Fiz. Teckh. Poluprovodn. **12**, 202 [Sov. Phys. Semicond. **12**, 118 (1978)].

Arseneau, D. J., D. M. Garner, M. Senba, and D. G. Fleming, 1984, J. Phys. Chem. **88**, 3688.

Assali, L. V. C., and J. R. Leite, 1985, Phys. Rev. Lett. **55**, 980.

Altarelli, M., and W. Y. Hsu, 1979, Phys. Rev. Lett. **43**, 1346.

Balzer, G., H. Graf, E. Recknagel, A. Weidinger, and Th. Wichert, 1981a, Hyperfine Int. **8**, 393.

Balzer, G., H. Graf, E. Recknagel, A. Weidinger, and Th. Wichert, 1981b, Hyperfine Int. **9**, 603.

Barsov, S. G., A. L. Getalov, V. A. Gordeev, R. F. Konopleva, S. P. Kruglov, V. I. Kudinov, L. A. Kuzmin, S. M. Mikirtychyants, E. V. Minaichev, G. G. Myasishcheva, Yu. V. Obukhov, G. I. Savelev, V. G. Firsov, and G. V. Shcherbakov, 1979, Zh. Eksp. Teor. Fiz. **76**, 2198 [Sov. Phys. JETP **49**, 1110 (1979)].

Barsov, S. G., A. L. Getalov, V. A. Gordeev, R. F. Konopleva, S. P. Kruglov, V. I. Kudinov, L. A. Kuzmin, S. M. Mikirtychyants, E. V. Minaichev, G. G. Myasishcheva, Yu. V. Obukhov, G. I. Savelev, V. G. Firsov, and G. V. Shcherbakov, 1980, Zh. Eksp. Teor. Fiz. **79**, 1461 [Sov. Phys. JETP **52**, 738 (1980)].

Barsov, S. G., A. L. Getalov, V. A. Gordeev, V. A. Evseev, R. F. Konopleva, S. P. Kruglov, V. I. Kudinov, L. A. Kuzmin, S. M. Mikirtychyants, E. V. Minaichev, G. G. Myasishcheva, Yu. V. Obukhov, G. I. Savelev, V. G. Firsov, and G. V. Shcherbakov, 1982, Pis'ma Zh. Eksp. Teor. Fiz. **37**, 40 [JETP Lett. **37**, 48 (1983)].

Barsov, S. G., A. L. Getalov, V. A. Gordeev, V. A. Evseev, R. F. Konopleva, S. P. Kruglov, V. I. Kudinov, L. A. Kuzmin, S. M. Mikirtychyants, E. V. Minaichev, G. G. Myasishcheva, Y. V. Obukhov, G. I. Savelev, V. G. Firsov, and G. V. Shcherbakov, 1984a, Hyperfine Int. **17-19**, 551.

Barsov, S. G., A. L. Getalov, V. A. Gordeev, S. P. Kruglov, V. I. Kudinov, L. A. Kuzmin, S. M. Mikirtychyants, E. V. Minaichev, G. G. Myasishcheva, Y. V. Obukhov, G. I. Savelev, V. G. Firsov, and G. V. Shcherbakov, 1984b, Hyperfine Int. **17-19**, 635.

Barsov, S. G., A. L. Getalov, V. A. Gordeev, V. A. Evseev, R. F. Konopleva, S. P. Kruglov, V. I. Kudinov, L. A. Kuzmin, S. M. Mikirtychyants, E. V. Minaichev, G. G. Myasishcheva, Y. V. Obukhov, G. I. Savelev, V. G. Firsov, and G. V. Shcherbakov, 1985, Pis'ma Zh. Eksp. Teor. Fiz. **42**, 424 [JETP Lett. **42**, 525 (1985)].

Baryshevskii, V. G., S. A. Kuten, and V. I. Rapoport, 1982, Phys. Lett. A **88**, 289.

Baumeler, Hp., R. F. Kiefl, H. Keller, W. Kündig, P. F. Meier, W. Odermatt, B. D. Patterson, J. W. Schneider, T. L. Estle, S. P. Rudaz, D. P. Spencer, and K. W. Blazey, 1987, unpublished.

Baym, G., 1978, *Lectures on Quantum Mechanics* (Benjamin-Cummings, London/Amsterdam; Don Mills, Ontario/Sydney/Tokyo), p. 237.

Beck, R., P. F. Meier, and A. Schenck, 1975, Z. Phys. B **22**, 109

Belousov, Yu. M., V. N. Gorelkin, and V. P. Smilga, 1978a, Zh. Eksp. Teor. Fiz. **74**, 629 [Sov. Phys. JETP **47**, 331 (1978)].

Belousov, Yu. M., V. N. Gorelkin, and V. P. Smilga, 1978b, Zh. Eksp. Teor. Fiz. **75**, 1999 [Sov. Phys. JETP **48**, 1007 (1978)].

Belousov, Yu. M., V. N. Gorelkin, and V. P. Smilga, 1981, Zh. Eksp. Teor. Fiz. **81**, 642 [Sov. Phys. JETP **54**, 3431 (1981)].

Bischof, P. K., 1976, J. Am. Chem. Soc. **98**, 6844.

Blazey, K. W., J. A. Brown, D. W. Cooke, S. A. Dodds, T. L. Estle, R. H. Heffner, M. Leon, and D. A. Vanderwater, 1981, Phys. Rev. B **23**, 5316.

Blazey, K. W., T. L. Estle, E. Holzschuh, P. F. Meier, B. D. Patterson, and M. Richner, 1984, Hyperfine Int. **17-19**, 595.

Blazey, K. W., T. L. Estle, E. Holzschuh, W. Odermatt, and B. D. Patterson, 1983, Phys. Rev. B **27**, 15.

Blazey, K. W., T. L. Estle, E. Holzschuh, P. F. Meier, B. D. Patterson, and M. Richner, 1986a, Phys. Rev. B **33**, 1546.

Blazey, K. W., T. L. Estle, S. L. Rudaz, E. Holzschuh, W. Kündig, and B. D. Patterson, 1986b, Phys. Rev. B **34**, 1422.

Boekema, C., 1983, Philos. Mag. B **47**, 331.

Boekema, C., E. Holzschuh, W. Kündig, P. F. Meier, B. D. Patterson, W. Reichart, and K. Rüegg, 1981, Hyperfine Int. **8**, 401.

Bourgoin, J. C., and J. W. Corbett, 1975, in *Lattice Defects in Semiconductors 1974,* Institute of Physics conference series No. 23 (IOP, London), p. 149.

Bourgoin, J. C., P. M. Mooney, and F. Poulin, 1981, in *Defects and Radiation Effects in Semiconductors,* edited by R. R. Hasiguti, Institute of Physics conference series No. 59 (IOP, Bristol), p. 33.

Brewer, J. H., 1979, discussion comment, Hyperfine Int. **6**, 153.

Brewer, J. H., D. S. Beder, and D. P. Spencer, 1979, Phys. Rev. Lett. **42**, 808.

Brewer, J. H., and K. M. Crowe, 1978, Annu. Rev. Nucl. Part. Sci. **28**, 239.

Brewer, J. H., K. M. Crowe, F. N. Gygax, R. F. Johnson, B. D. Patterson, D. G. Fleming, and A. Schenck, 1973, Phys. Rev. Lett. **31**, 143.

Brewer, J. H., K. M. Crowe, F. N. Gygax, and A. Schenck, 1975, in *Muon Physics,* edited by V. Hughes and C. S. Wu (Academic, New York/San Francisco/London), Vol. III, p. 3.

Brewer, J. H., D. G. Fleming, and P. W. Percival, 1982, in *Fourier, Hadamard, and Hilbert Transforms in Chemistry,* edited by A. G. Marshall (Plenum, New York), p. 345.

Brewer, J. H., and P. W. Percival, 1981, Eds., *Proceedings of the Second International Topical Meeting on Muon Spin Rotation* (North-Holland, Amsterdam).

Brice, D. K., 1978, Phys. Lett. A **66**, 53.

Brown, J. A., R. H. Heffner, M. Leon, S. A. Dodds, T. L. Estle, and D. A. Vanderwater, 1983, Phys. Rev. B **27**, 3980.

Bucci, C., R. De Renzi, G. Guidi, P. Podini, R. Tedeschi, and L. O. Norlin, 1981, Hyperfine Int. **8**, 385.

Burkhard, P., E. Roduner, J. Hochmann, and H. Fischer, 1984, J. Phys. Chem. **88**, 773.

Cahn, J. H., 1959, J. Appl. Phys. **30**, 1310.

Calvo, R., and R. Orbach, 1967, Phys. Rev. **164**, 284.

Celio, M., and P. F. Meier, 1983, Phys. Rev. B **28**, 39.

Celio, M., 1985, unpublished.

Chappert, J., and R. I. Grynszpan, 1984, Eds., *Muons and Pions in Materials Research* (North-Holland, Amsterdam/Oxford/New York/Tokyo).

Chen, Y., and J. W. McKay, 1968, Phys. Rev. **167**, 745.

Choyke, W. J., and L. Patrick, 1972, Phys. Rev. Lett. **29**, 355.

Clawson, C. W., E. E. Haller, K. M. Croew, S. S. Rosenblum, and J. H. Brewer, 1981, Hyperfine Int. **8**, 417.

Clawson, C. W., K. M. Crowe, E. E. Haller, S. S. Rosenblum, and J. H. Brewer, 1984, Hyperfine Int. **17-19**, 603.

Claxton, T. A., A. Evans, and M. C. R. Symons, 1986, J. Chem. Soc. Faraday Trans. 2 **82**, 2031.

Coffin, T., R. L. Garwin, S. Penman, L. M. Lederman, and A. M. Sachs, 1958, Phys. Rev. **109**, 973.

Coker, A., T. Lee, T. P. Das, and A. Glodeanu, 1978, Hyperfine Int. **4**, 821.

Corbett, J. W., J. C. Bourgoin, L. J. Cheng, J. C. Corelli, Y. H. Lee, P. M. Mooney, and C. Weigel, 1977, in *Radiation Effects in Semiconductors,* Institute of Physics conference series No. 31 (IOP, London), p. 1.

Corbett, J. W., S. N. Sahu, T. S. Shi, and L. C. Synder, 1983, Phys. Lett. A **93**, 303.

Cox, S. F. J., and M. C. R. Symons, 1986, Chem. Phys. Lett. **126**, 516.

de Launay, J., 1956, in *Solid State Physics,* edited by F. Seitz and D. Turnbull (Academic, New York), Vol. 2, p. 219.

De Renzi, R., G. Guidi, and L. Oddi, 1981, Hyperfine Int. **8**, 389.

Dolling, G., and R. A. Cowley, 1966, Proc. Phys. Soc. London **88**, 463.

Döring, K. P., N. Haas, E. E. Haller, D. Herlach, W. Jacobs, M. Krauth, H. Orth, J. Rosenkranz, A. Seeger, J. Vetter, K. P. Arnold, Th. Aurenz, and H. Bossy, 1983, Physica B **116**, 354.

Döring, K. P., K. P. Arnold, M. Gladisch, N. Haas, E. E. Haller, D. Herlach, W. Jacobs, M. Krause, M. Krauth, H. Orth, and A. Seeger, 1984, Hyperfine Int. **17-19**, 629.

Doyle, W. T., and A. B. Wolbarst, 1975, J. Phys. Chem. Solids **36**, 549.

Ehrlich, R. D., H. Hofer, A. Magnon, D. Y. Stowell, R. A. Swanson, and V. L. Telegdi, 1972, Phys. Rev. A **5**, 2357.

Eisenstein, B., R. Prepost, and A. M. Sachs, 1966, Phys. Rev. **142**, 217.

Emin, D., 1981, Hyperfine Int. **8**, 515.

Estle, T. L., 1981, Hyperfine Int. **8**, 365.

Estle, T. L., 1984, Hyperfine Int. **17-19**, 585.

Estle, T. L., K. W. Blazey, C. Boekema, and R. H. Heffner, 1984, Hyperfine Int. **17-19**, 615.

Estle, T. L., S. Estreicher, and D. S. Marynick, 1986, Hyperfine Int. **32**, 637.

Estle, T. L., S. L. Rudaz, E. Holzschuh, R. F. Kiefl, B. D. Patterson, W. Kündig, and K. W. Blazey, 1984, Hyperfine Int. **17-19**, 623.

Estle, T. L., and D. A. Vanderwater, 1983, Phys. Rev. B **27**, 3962.

Estle, T. L., M. E. Warren, and B. D. Patterson, 1984, Hyperfine Int. **17-19**, 589.

Estreicher, S., and D. S. Marynick, 1986a, Phys. Rev. Lett. **56**, 1511.

Estreicher, S., and D. S. Marynick, 1986b, Hyperfine Int. **32**, 613.

Estreicher, S., A. K. Ray, J. L. Fry, and D. S. Marynick, 1985, Phys. Rev. Lett. **55**, 1976.

Favart, D., P. M. McIntyre, D. Y. Stowell, V. L. Telegdi, R. DeVoe, and R. A. Swanson, 1971, Phys. Rev. Lett. **27**, 1336.

Feher, G., R. Prepost, and A. M. Sachs, 1960, Phys. Rev. Lett. **5**, 515.

Felber, J., 1984, diploma thesis (University of Zurich).

Ferrel, R. A., Y. C. Lee, and M. K. Pal, 1960, Phys. Rev. **118**, 317.

Fleming, D. G., R. J. Mikula, and D. M. Garner, 1982, Phys. Rev. A **26**, 2527.

Flik, G., J. N. Bradbury, D. W. Cooke, R. H. Heffner, M. Leon, M. A. Paciotti, M. E. Schillaci, K. Maier, H. Rempp, J. J. Reidy, C. Boekema, and H. Daniel, 1986, Phys. Rev. Lett. **57**, 563.

Frank, W., 1975, in *Lattice Defects in Semiconductors,* Institute of Physics conference series No. 23 (IOP, London), p. 23.

Frank, R. C., and J. E. Thomas, 1959, Bull. Am. Phys. Soc. Ser. 2 **4**, 411.

Friedmann, J. I., and V. L. Telegdi, 1957a, Phys. Rev. **105**, 1681.

Friedmann, J. I., and V. L. Telegdi, 1957b, Phys. Rev. **106**, 1290.

Gardner, E., and C. M. G. Lattes, 1948, Science **107**, 270.

Garwin, R. L., L. M. Ledermann, and M. Weinrich, 1957, Phys. Rev. **105**, 1415.

Gemmel, D. S., 1974, Rev. Mod. Phys. **46**, 129.

Goltzene, A., B. Meyer, C. Schwab, S. G. Greenbaum, R. J. Wagner, and T. A. Kennedy, 1984, J. Appl. Phys. **56**, 3394.

Gordeev, V. A., S. P. Kruglov, V. I. Kudniov, L. A. Kuzmin, S. M. Mikirtychyants, E. V. Minaichev, Yu. V. Obukhov, G. I. Savelev, V. G. Firsov, and G. V. Shcherbakov, 1978, Pis'ma, Zh. Eksp. Teor. Fiz. **27**, 420 [JETP Lett. **27**, 394 (1978)].

Gurevich, I. I., I. G. Ivanter, L. A. Makariyna, E. A. Meleshko, B. A. Nikolsky, V. S. Roganov, V. I. Selivanov, V. P. Smilga, B. V. Sokolov, V. D. Shestakov, and I. V. Jakovleva, 1969, Phys. Lett. B **29**, 387.

Gurevich, I. I., I. G. Ivanter, E. A. Meleshko, B. A. Nikolsky, V. S. Roganov, V. I. Selivanov, V. P. Smilga, B. V. Sokolov, and V. D. Shestakov, 1971, Zh. Eksp. Teor. Fiz. **60**, 471 [Sov. Phys. JETP **33**, 253 (1971)].

Gurevich, I. I., B. A. Nikolskii, V. I. Selivanov, and B. V. Sokolov, 1975, Zh. Eksp. Teor. Fiz. **68**, 806 [Sov. Phys. JETP **41**, 401 (1976)].

Gurevich, I. I., I. G. Ivanter, B. A. Nikolsky, A. N. Ponomarev, V. S. Roganov, V. I. Selivanov, and V. A. Suetin, 1979, Hyperfine Int. **6**, 175.

Gurevich, I. I., and B. A. Nikolskii, 1981, in *Physics Reviews,* edited by I. M. Khalatnikov, Soviet Scientific Reviews Sec. A (Harwood Academic, Chur, Switzerland), Vol. 3, p. 89.

Gygax, F. N., W. Kündig, and P. F. Meier, 1979, Eds., *Proceedings of the First International Topical Meeting on Muon Spin Rotation* (North-Holland, Amsterdam).

Haller, E. E., G. S. Hubbard, W. L. Hansen, and A. Seeger, 1971, in *Radiation Effects in Semiconductors,* Institute of Physics conference series No. 31 (IOP, London), p. 309.

Haller, E. E., B. Joos, and L. M. Falicov, 1980, Phys. Rev. B **21**, 4729.

Hartmann, O., E. Karlsson, R. Wäppling, D. Richter, R. Hempelmann, K. Schulze, B. Patterson, E. Holzschuh, W. Kündig,

and S. F. J. Cox, 1983, Phys. Rev. B **27**, 1943.
Hartmann, O., E. Karlsson, B. Lindgren, and R. Wäppling, 1986, Eds., *Proceedings of the 4th International Conference on Muon Spin Rotation, Relaxation and Resonance* (Baltzer, Basel).
Haynes, J. R., and J. A. Hornbeck, 1953, Phys. Rev. **90**, 152.
Heming, M., E. Roduner, and B. D. Patterson, 1986, Hyperfine Int. **32**, 727.
Heming, M., E. Roduner, B. D. Patterson, W. Odermatt, J. Schneider, Hp. Baumeler, H. Keller, and I. M. Savic, 1986, Chem. Phys. Lett. **128**, 100.
Hensel, J. C., T. G. Phillips, and G. A. Thomas, 1977, in *Solid State Physics,* edited by H. Ehrenreich, F. Seitz, and D. Turnbull (Academic, New York/San Francisco/London), Vol. 32, p. 87.
Hintermann, A., P. F. Meier, and B. D. Patterson, 1980, Am. J. Phys. **48**, 956.
Holzschuh, E., 1982, doctoral thesis (University of Zurich).
Holzschuh, E., 1983, Phys. Rev. B **27**, 102.
Holzschuh, E., H. Graf, E. Recknagel, A. Weidinger, and Th. Wichert, 1979, Phys. Rev. B **20**, 4391.
Holzschuh, E., and W. Kündig, 1984, Hyperfine Int. **17-19**, 939.
Holzschuh, E., W. Kündig, P. F. Meier, B. D. Patterson, and J. P. F. Sellschop, M. C. Stemmet, and H. Appel, 1982, Phys. Rev. A **25**, 1272.
Holzschuh, E., W. Kündig, B. D. Patterson, 1981a, Hyperfine Int. **8**, 819.
Holzschuh, E., W. Kündig, B. D. Patterson, 1981b, Helv. Phys. Acta **54**, 552.
Hughes, V. W., D. W. McColm, K. Ziock, and R. Prepost, 1960, Phys. Rev. Lett. **5**, 63.
Ichimiya, T., and A. Furuichi, 1968, Int. J. Appl. Radiat. Isot. **19**, 573.
Irmscher, K., H. Klose, and K. Maass, 1984, J. Phys. C **17**, 6317.
Ivanov, Yu. M., B. A. Nikolskii, B. M. Smirnov, and L. V. Surkova, 1962, Zh. Eksp. Teor. Fiz. **43**, 337 [Sov. Phys. JETP **16**, 241 (1963)].
Ivanter, I. G., 1969, Zh. Eksp. Teor. Fiz. **56**, 1419 [Sov. Phys. JETP **29**, 761 (1969)].
Ivanter, I. G., 1977, Zh. Eksp. Teor. Fiz. **73**, 1639 [Sov. Phys. JETP **46**, 861 (1977)].
Ivanter, I. G., B. A. Nikolskii, A. N. Ponomarev, V. I. Selivanov, and V. A. Suetin, 1978, Zh. Eksp. Teor. Fiz. **75**, 376 [Sov. Phys. JETP **48**, 189 (1978)].
Ivanter, I. G., and V. P. Smilga, 1968a, Zh. Eksp. Teor. Fiz. **54**, 559 [Sov. Phys. JETP **27**, 301 (1968)].
Ivanter, I. G., and V. P. Smilga, 1968b, Zh. Eksp. Teor. Fiz. **55**, 1521 [Sov. Phys. JETP **28**, 796 (1969)].
Ivanter, I. G., and V. P. Smilga, 1971a, Zh. Eksp. Teor. Fiz. **60**, 1985 [Sov. Phys. JETP **33**, 1070 (1971)].
Ivanter, I. G., and V. P. Smilga, 1971b, Zh. Eksp. Teor. Fiz. **61**, 2176 [Sov. Phys. JETP **34**, 1167 (1972)].
Iwasaki, M., 1974, J. Mag. Res. **16**, 417.
Johnson, N. M., C. Herring, and D. J. Chadi, 1966, Phys. Rev. Lett. **56**, 769.
Johnson, N. M., and S. K. Hahn, 1986, Appl. Phys. Lett. **48**, 709.
Johnson, R. F., 1976, doctoral thesis (University of California, Berkeley, LBL Report No. 5526).
Katayama-Yoshida, H., and K. Shindo, 1983, Phys. Rev. Lett. **51**, 207.
Kaus, P. E., 1958, Phys. Rev. **109**, 1944.
Kiefl, R. F., 1986, Hyperfine Int. **32**, 707.
Kiefl, R. F., E. Holzschuh, H. Keller, W. Kündig, P. F. Meier, B. D. Patterson, J. W. Schneider, K. W. Blazey, S. L. Rudaz, and A. B. Denison, 1984, Phys. Rev. Lett. **53**, 90.
Kiefl, R. F., S. Kreitzman, M. Celio, R. Keitel, G. M. Luke, J. H. Brewer, D. R. Noakes, P. W. Percival, T. Matsuzaki, and K. Nishiyama, 1986, Phys. Rev. A **34**, 681.
Kiefl, R. F., W. Odermatt, Hp. Baumeler, J. Felber, H. Keller, W. Kündig, P. F. Meier, B. D. Patterson, J. W. Schneider, K. W. Blazey, T. L. Estle, and C. Schwab, 1986, Phys. Rev. B **34**, 1474.
Kiefl, R. F., B. D. Patterson, E. Holzschuh, W. Odermatt, and D. R. Harshman, 1984, Hyperfine Int. **17-19**, 563.
Kiefl, R. F., J. W. Schneider, H. Keller, W. Kündig, W. Odermatt, B. D. Patterson, K. W. Blazey, T. L. Estle, and S. L. Rudaz, 1985, Phys. Rev. B **32**, 530.
Kinchin, G. H., and R. S. Pease, 1955, Rep. Prog. Phys. **18**, 1.
Kitaoka, Y., M. Takigawa, H. Yasuoka, M. Itoh, S. Takagi, Y. Kuno, K. Nishiyama, R. S. Hayano, Y. J. Uemura, J. Imazato, H. Nakayama, K. Nagamine, and T. Yamazaki, 1982, Hyperfine Int. **12**, 51.
Kittel, C., 1968, *Introduction to Solid State Physics,* 3rd edition (Wiley, New York/London/Sydney), p. 324.
Kleinhenz, R. L., Y. H. Lee, Vijay A. Singh, P. M. Mooney, A. Jaworowski, L. M. Roth, J. C. Corelli, and J. W. Corbett, 1979, in *Defects and Radiation Effects in Semiconductors,* edited by J. H. Albany, Institute of Physics conference series No. 46 (IOP, Bristol; AIP, New York), p. 200.
Kudinov, V. I., E. V. Miniachev, G. G. Myasishcheva, Yu. V. Obukhov, V. S. Roganov, G. I. Savelev, V. M. Samoilov, and V. G. Firsov, 1975, Pis'ma Zh. Eksp. Teor. Fiz. **21**, 49 [JETP Lett. **21**, 22 (1975)].
Kudinov, V. I., E. V. Miniachev, G. G. Myasishcheva, Yu. V. Obukhov, V. S. Roganov, G. I. Savelev, V. M. Samoilov, and V. G. Firsov, 1976, Zh. Eksp. Teor. Fiz. **70**, 2041 [Sov. Phys. JETP **43**, 1065 (1976)].
Kudinov, V. I., E. V. Miniachev, G. G. Myasishcheva, Yu. V. Obukhov, V. S. Roganov, G. I. Savelev, and V. G. Firsov, 1977, Pis'ma Zh. Eksp. Teor. Fiz. **25**, 331 [JETP Lett. **25**, 307 (1977)].
Kündig, W., E. Holzschuh, P. F. Meier, B. D. Patterson, K. Rüegg, J. P. F. Sellschop, M. Stemmet, and H. Appel, 1980, Helv. Phys. Acta **53**, 611.
Lee, Y. H., and J. W. Corbett, 1973, Phys. Rev. B **8**, 2810.
Lindhard, J., 1965, K. Dan. Vidensk, Selsk. Mat. Fys. Medd. **34**, No. 14.
Loubser, J. H. N., and J. A. van Wyk, 1978, Rep. Prog. Phys. **41**, 1201.
Maier, K., 1984, Hyperfine Int. **17-19**, 3.
Mainwood, A., and A. M. Stoneham, 1984, J. Phys. C **17**, 2513.
Mann, A., and W. Brandt, 1981, Phys. Rev. B **24**, 4999.
Manninen, M., and P. F. Meier, 1982, Phys. Rev. B **26**, 6690.
Mariam, F. G., W. Beer, P. R. Bolton, P. O. Egan, C. J. Gardner, V. W. Hughes, D. C. Lu, P. A. Souder, H. Orth, J. Vetter, U. Moser, and G. zu Putlitz, 1982, Phy. Rev. Lett. **49**, 993.
Meier, P. F., 1980, in *Exotic Atoms '79,* edited by K. Crowe, J. Duclos, G. Fiorentini, and G. Torelli (Plenum, New York/London), p. 331.
Meier, P. F., 1981, unpublished.
Meier, P. F., 1987, Phys. Rev. B **35**, 5257.
Meier, P. F., 1982, Phys. Rev. A **25**, 1287.
Molière, G., 1947, Z. Naturforsch. A **2**, 133.
Morin, F. J., and J. P. Maita, 1954a, Phys. Rev. **96**, 28.
Morin, F. J., and J. P. Maita, 1954b, Phys. Rev. **94**, 1525.

Myasishcheva, G. G., Yu. V. Obukhov, V. S. Roganov, and V. G. Firsov, 1967, Zh. Eksp. Teor. Fiz. **53**, 451 [Sov. Phys. JETP **26**, 298 (1968)].

Newman, R. C., 1982, Rep. Prog. Phys. **45**, 1163.

Newman, R. C., and J. Woodhead, 1980, Radiat. Eff. **53**, 41.

Nielsen, B. B., 1986, doctoral thesis (University of Aarhus, Denmark).

Nishiyama, K., Y. Morozumi, T. Suzuki, and K. Nagamine, 1985, Phys. Lett. A **111**, 369.

Nosov, V. G., and I. V. Yakovleva, 1962, Zh. Eksp. Teor. Fiz. **43**, 1750 [Sov. Phys. JETP **16**, 1236 (1963)].

Nosov, V. G., and I. V. Yakovleva, 1965, Nucl. Phys. **68**, 609.

Odermatt, W., Hp. Baumeler, H. Keller, W. Kündig, B. D. Patterson, J. W. Schneider, J. P. F. Sellschop, M. C. Stemmet, S. Connell, and D. P. Spencer, 1986, Hyperfine Int. **32**, 583.

Orear, J., G. Harris, and E. Bierman, 1957, Phys. Rev. **107**, 322.

Palmer, D. W., 1977, in *Radiation Effects in Semiconductors*, Institute of Physics conference series No. 31 (IOP, London), p. 144.

Pantelides, S. T., 1979, Hyperfine Int. **6**, 145.

Particle Data Group, 1984, Rev. Mod. Phys. **56**, No. 2, Part II.

Patrick, L., and W. J. Choyke, 1973, Phys. Rev. B **8**, 1660.

Patterson, B. D., 1980, Am. J. Phys. **48**, 945.

Patterson, B. D., 1984a, unpublished.

Patterson, B. D., 1984b, Hyperfine Int. **17-19**, 517.

Patterson, B. D., 1984c, in *Muons and Pions in Materials Research*, edited by J. Chappert and R. I. Grynszpan (North-Holland, Amsterdam/Oxford/New York/Tokyo), p. 161.

Patterson, B. D., 1987, in *Relativistic Channeling*, edited by R. A. Carrigan and J. A. Ellison (Plenum, New York), p. 459.

Patterson, B. D., Hp. Baumeler, H. Keller, R. F. Kiefl, W. Kündig, W. Odermatt, J. W. Schneider, W. J. Choyke, T. L. Estle, D. P. Spencer, K. W. Blazey, and I. M. Savic, 1986, Hyperfine Int. **32**, 625.

Patterson, B. D., C. Boekema, and P. F. Meier, 1981, Hyperfine Int. **8**, 811.

Patterson, B. D., A. Bosshard, U. Straumann, P. Truöl, A. Wüest, and Th. Wichert, 1984a, Phys. Rev. Lett. **52**, 938.

Patterson, B. D., A. Bosshard, U. Straumann, P. Truöl, A. Wüest, and Th. Wichert, 1984b, Hyperfine Int. **17-19**, 965.

Patterson, B. D., A. Hinterman, W. Kündig, P. F. Meier, F. Waldner, H. Graf, E. Recknagel, A. Weidinger, and Th. Wichert, 1978, Phys. Rev. Lett. **40**, 1347.

Patterson, B. D., E. Holzschuh, R. F. Kiefl, K. W. Blazey, and T. L. Estle, 1984, Hyperfine Int. **17-19**, 599.

Patterson, B. D., E. Holzschuh, W. Kündig, P. F. Meier, W. Odermatt, J. P. F. Sellschop, and M. C. Stemmet, 1984, Hyperfine Int. **17-19**, 605.

Patterson, B. D., W. Kündig, P. F. Meier, F. Waldner, H. Graf, E. Recknagel, A. Weidinger, and Th. Wichert, 1978, Helv. Phys. Acta **51**, 442.

Percival, P. W., and H. Fischer, 1976, Chem. Phys. **16**, 89.

Percival, P. W., J. C. Brodovitch, and K. E. Newman, 1984, Hyperfine Int. **17-19**, 721.

Philips, J. C., 1970, Rev. Mod. Phys. **42**, 317.

Pickett, W. E., M. L. Cohen, and C. Kittel, 1979, Phys. Rev. B **20**, 5050.

Picraux, S. T., 1976, in *Ion Beam Surface Layer Analysis*, edited by O. Meyer, G. Linker, and F. Käppeler (Plenum, New York/London), Vol. 2, p. 527.

Picraux, S. T., and F. L. Vook, 1978, Phys. Rev. B **18**, 2066.

Picraux, S. T., F. L. Vook, and H. J. Stein, 1979, in *Defects and Radiation Effects in Semiconductors*, edited by J. H. Albany, Institute of Physics conference series No. 46 (IOP, Bristol; AIP, New York), p. 31.

Pooley, D., 1966, Proc. Phys. Soc. London **87**, 257.

Pople, J. A., and D. L. Beveridge, 1970, *Approximate Molecular Orbital Theory* (McGraw-Hill, New York).

Qi, M. W., G. R. Bai, T. S. Shi, and L. M. Xie, 1985, Mater. Lett. **3**, 466.

Reiss, H., 1956, J. Chem. Phys. **25**, 681.

Resca, L., and R. Resta, 1980, Phys. Rev. Lett. **44**, 1340.

Richner, M., 1982, diploma thesis (University of Zurich).

Rodriguez, C. O., M. Jaros, and S. Brand, 1979, Solid State Commun. **31**, 43.

Roduner, E., and H. Fischer, 1981, Chem. Phys. **54**, 261.

Ross, G. G., and B. Terreault, 1986, Nucl. Instrum. Methods **B15**, 61.

Sahoo, N., K. C. Mishra, and T. P. Das, 1985, Phys. Rev. Lett. **55**, 1506.

Sahoo, N., K. C. Mishra, and T. P. Das, 1986a, Hyperfine Int. **32**, 601.

Sahoo, N., K. C. Mishra, T. P. Das, and P. C. Schmidt, 1986b, Hyperfine Int. **32**, 619.

Sahoo, N., Santosh K. Mishra, K. C. Mishra, A. Coker, T. P. Das, C. K. Mitra, L. C. Snyder, and A. Glodeanu, 1983, Phys. Rev. Lett. **50**, 913.

Sahoo, N., Santosh K. Mishra, K. C. Mishra, A. Coker, T. P. Das, C. K. Mitra, L. C. Snyder, and A. Glodeanu, 1984, Hyperfine Int. **17-19**, 525.

Schenck, A., 1976, in *Nuclear and Particle Physics at Intermediate Energies*, edited by J. Warren (Plenum, New York/London), p. 519.

Schenck, A., 1977, in *Exotic Atoms*, edited by G. Fiorentini and G. Torelli (Frascati National Laboratory, Frascati, Italy), p. 355.

Schenck, A., 1985, *Muon Spin Rotation Spectroscopy* (Adam Hilger, Bristol/London).

Schneider, J. W., 1984, diploma thesis (University of Zurich).

Schneider, J. W., Hp. Baumeler, H. Keller, R. F. Kiefl, W. Kündig, W. Odermatt, B. D. Patterson, T. L. Estle, S. P. Rudaz, K. W. Blazey, and C. Schwab, 1986, Hyperfine Int. **32**, 607.

Schwab, C., 1986, unpublished.

Schwab, C., and A. Goltzene, 1982, Prog. Crystal Growth Charact. **5**, 233.

Seeger, A., 1984, Hyperfine Int. **17-19**, 75.

Seifert, U., 1981, diploma thesis (University of Zurich).

Shi, T. S., S. N. Sahu, G. S. Oehrlein, A. Hiraki, and J. W. Corbett, 1982, Phys. Status Solidi A **74**, 329.

Sieverts, E. G., 1983, Phys. Status Solidi B **120**, 11.

Sigle, W., H. D. Carstanjen, G. Flik, D. Herlach, G. Jünemann, K. Maier, H. Rempp, and A. Seeger, 1984, Nucl. Instrum. Methods Phys. Res. B **2**, 1.

Simánek, E., and R. Orbach, 1966, Phys. Rev. **145**, 191.

Simmler, H., 1986, unpublished.

Singh, V. A., C. Weigel, J. W. Corbett, and L. M. Roth, 1977, Phys. Status Solidi B **81**, 637.

Spencer, D. P., D. G. Fleming, and J. H. Brewer, 1984, Hyperfine Int. **17-19**, 567.

Stoneham, M., 1984, discussion comment, Hyperfine Int. **17-19**, 782.

Street, J. C., and E. C. Stevenson, 1937, Phys. Rev. **52**, 1003.

Swanson, R. A., 1958, Phys. Rev. **112**, 580.

Symons, M. C. R., 1984, Hyperfine Int. **17-19**, 771.

Thompson, P. A., J. J. Amato, P. Crane, V. W. Hughes, R. M. Mobley, G. zu Putlitz, and J. E. Rothberg, 1969, Phys. Rev. Lett. **22**, 163.

Van Wieringen, A., and N. Warmoltz, 1956, Physica **22**, 849.

Varisov, A. Z., 1982, Fiz. Tekh. Poluprovodn. **16**, 516 [Sov. Phys. Semicond. **16**, 330 (1982)].

Vook, F. L., 1963, in *Radiation Damage and Defects in Semiconductors,* Institute of Physics conference series No. 16 (IOP, London), p. 60.

Wang, J. S., and C. Kittel, 1973, Phys. Rev. B **7**, 713.

Warren, J. L., J. L. Yarnell, G. Dolling, and R. A. Cowley, 1967, Phys. Rev. **158**, 805.

Watkins, G. D., 1973, in *Radiation Damage and Defects in Semiconductors,* Institute of Physics conference series No. 16 (IOP, London), p. 228.

Watkins, G. D., 1975, in *Lattice Defects in Semiconductors,* Institute of Physics conference series No. 23 (IOP, London), p. 1.

Weber, E. R., and J. Schneider, 1983, Physica B **116**, 398.

Weidinger, A., G. Balzer, H. Graf, E. Recknagel, and Th. Wichert, 1981, Phys. Rev. B **24**, 6185.

Weidinger, A., E. Albert, A. Möslang, and E. Recknagel, 1983, unpublished.

Westhauser, E., E. Albert, M. Hamma, E. Recknagel, A. Weidinger, and P. Moser, 1986, Hyperfine Int. **32**, 589.

Woods, G. S., and A. T. Collins, 1983, J. Phys. Chem. Solids **44**, 471.

Yamazaki, T., and K. Nagamine, 1984, Eds., *Muon Spin Rotation and Associated Problems* (Baltzer, Basel/Osaka).

Ziegler, J. F., J. P. Biersack, and U. Littmark, 1985, *The Stopping and Range of Ions in Solids* (Pergamon, New York/Oxford/Toronto/Sydney/Frankfurt/Tokyo), Vol. 1.